UNIVERSIDADE FEDERAL DO RIO GRANDE DO SUL
INSTITUTO DE INFORMÁTICA
PROGRAMA DE PÓS-GRADUAÇÃO EM COMPUTAÇÃO

VITOR FERNANDO PAMPLONA

Interactive Measurements and Tailored Displays for Optical Aberrations of the Human Eye

Thesis presented in partial fulfillment
of the requirements for the degree of
Doctor of Computer Science

Prof. Dr. Manuel Menezes de Oliveira Neto
Advisor

Porto Alegre, July 2012

CIP – CATALOGING-IN-PUBLICATION

Pamplona, Vitor Fernando

Interactive Measurements and Tailored Displays for Optical Aberrations of the Human Eye / Vitor Fernando Pamplona. – Porto Alegre: PPGC da UFRGS, 2012.

159 f.: il.

Thesis (Ph.D.) – Universidade Federal do Rio Grande do Sul. Programa de Pós-Graduação em Computação, Porto Alegre, BR–RS, 2012. Advisor: Manuel Menezes de Oliveira Neto.

1. Computational diagnostics. 2. Computational ophthalmology. 3. Subjective refraction. 4. Ophthalmatics. 5. Tailored displays. 6. Hardware apps. 7. Mobile mates. 8. Light-field displays. 9. Interactive diagnostics. 10. Visual optics. I. Oliveira Neto, Manuel Menezes de. II. Título.

“If the research does not change the way people think, the project is a failure.”
— GEORGE M. WHITESIDES, PHD

Thanks everybody. You are awesome. I have learned so much from you guys. It is a great pleasure to share credits of this work with all of you. Your ideals, values and excitement have had and will continue to have a remarkable influence on my entire career.

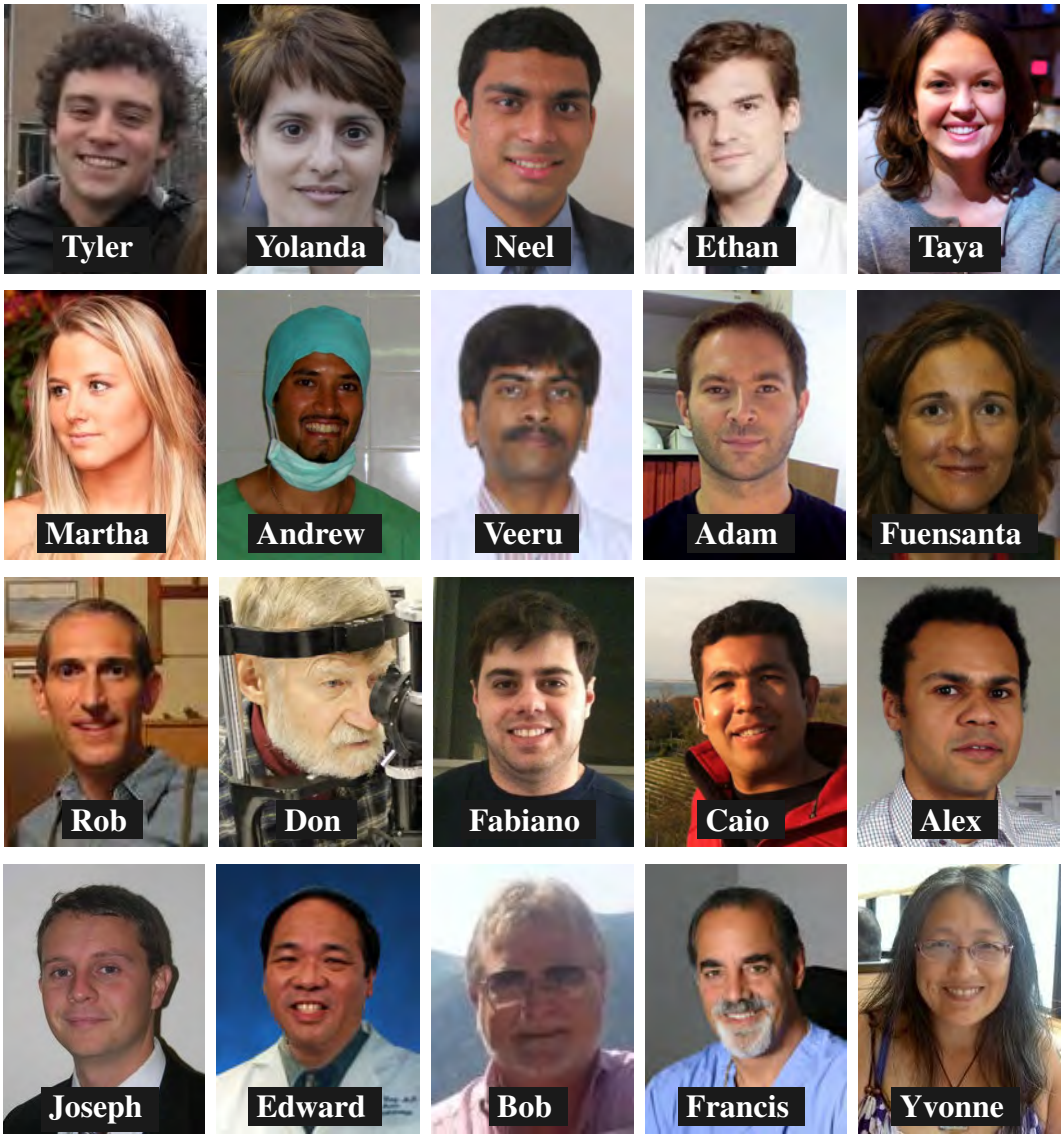

Thanks for the great work and valuable advises. Our extensive discussions around this work and interesting explorations in operations have been very helpful for this study. I really appreciate sharing experiences with all of you.

I have received tremendous support, friendship and encouragement from numerous colleagues in the Computer Graphics Group at UFRGS and Camera Culture Group at MIT. Special acknowledgment for CNPq-Brazil fellowships 142563/2008-0 and 200763/2009-1. Samsung provided additional support.

CONTENTS

LIST OF FIGURES

LIST OF TABLES

ABSTRACT

This thesis proposes *light-field pre-warping methods* for measuring and compensating for optical aberrations in focal imaging systems. Interactive methods estimate refractive conditions (*NETRA*) and model lens opacities (*CATRA*) of interaction-aware eyes and cameras using cost-efficient *hardware apps* for high-resolution screens. *Tailored displays* use stereo-viewing hardware to compensate for the measured visual aberrations and display in-focus information that avoids the need of corrective eyeglasses. A light-field display, positioned very close to the eye, creates virtual objects in a wide range of predefined depths through different sectors of the eye's aperture. This platform creates a new range of interactivity that is extremely sensitive to spatially-distributed optical aberrations. The ability to focus on virtual objects, interactively align displayed patterns, and detect variations in shape and brightness allows the estimation of the eye's point spread function and its lens' accommodation range. While conventional systems require specialized training, costly devices, strict security procedures, and are usually not mobile, this thesis simplifies the mechanism by putting the human subject in the loop. Captured data is transformed into refractive conditions in terms of spherical and cylindrical powers, axis of astigmatism, focal range and aperture maps for opacity, attenuation, contrast and sub-aperture point-spread functions. These optical widgets carefully designed to interactive interfaces plus computational analysis and reconstruction establish the field of *computational ophthalmology*. The overall goal is to allow a general audience to operate portable light-field displays to gain a meaningful understanding of their own visual conditions. Ubiquitous, updated, and accurate diagnostic records can make private and public displays show information in a resolution that goes beyond the viewer's visual acuity. The new display technology is able to compensate for refractive errors and avoid light-scattering paths. Tailored Displays free the viewer from needing wearable optical corrections when looking at it, expanding the notion of glasses-free multi-focus displays to add individual variabilities. This thesis includes proof-of-concept designs for ophthalmatic devices and tailored displays. User evaluations and validations with modified camera optics are performed. Capturing the daily variabilities of an individual's sensory system is expected to unleash a new era of high-quality tailored consumer devices.

Keywords: Computational diagnostics, computational ophthalmology, subjective refraction, ophthalmatics, tailored displays, hardware apps, mobile mates, light-field displays, interactive diagnostics, visual optics.

Medidas Interativas e Telas Ajustáveis para Aberrações Ópticas em Olhos Humanos

RESUMO

Esta tese descreve métodos interativos para estimar e compensar erros de refração (NETRA) e opacidades ópticas (CATRA) em sistemas de imageamento usando telas de campos de luz programáveis, de alta resolução e alto contraste. Os novos métodos para oftalmologia computacional descritos aqui podem avaliar câmeras e olhos se o usuário do sistema estiver consciente do modelo de interação. A solução combina elementos ópticos baratos, interfaces interativas e reconstrução computacional. Uma tela de campos de luz, posicionada perto do olho, cria objetos virtuais em profundidades pré-definidas através de várias seções do olho. Via esta plataforma, cria-se uma nova gama de aplicações interativas que é extremamente sensível a aberrações ópticas. A capacidade de focar em um objeto virtual, alinhar padrões exibidos na tela e detectar suas variações de forma e brilho permite ao sistema estimar a função de propagação de ponto de luz para o olho e a acomodação da lente. Enquanto os sistemas convencionais requerem formação especializada, dispositivos caros, procedimentos de segurança sensíveis e normalmente não são móveis, esta tese simplifica o mecanismo, colocando o paciente no centro do teste. Ao final, a resposta do usuário calcula a condição de refração em termos de poderes esférico e cilíndrico, o eixo de astigmatismo, o poder de acomodação da lente e mapas para a opacidade, atenuação, contraste e função de espalhamento de um ponto de luz. O objetivo é permitir que o público em geral opere um sistema de iluminação portátil e obtenha uma compreensão de suas próprias condições visuais. Esta tese apresenta projetos ópticos para software e hardware para oftalmologia computacional. Avaliações com usuários e com câmeras com lentes modificadas são realizadas. Os dados compilados são usados para reconstruir visão afetada do indivíduo, oferecendo uma nova abordagem para capturar informações para o rastreio, diagnóstico e análises clínicas de anomalias visuais.

Palavras-chave: Oftalmologia computacional, hardware apps, telas de campo de luz, interação humano computador, óptica visual, erros de refração, cataratas, acomodação visual.

1 INTRODUCTION

Uncorrected eye aberrations decrease one's visual capabilities, creating sub-optimal and inconsistent user experiences. The lack of accurate, low-cost and massive eye health diagnostics create illusions of truth that blind the search for better visual performance. For instance, some remote villages in India still believe that cataracts, or white blindness as they call, are an unavoidable stage of life instead of a simple visual condition that can be solved with a three-dollar surgery. Refractive errors, or the lack of sharp vision, are accepted as a natural limitation by every child until they try eyeglasses and discover a new world. Specialized centers for eye exams are scarce and often viewed as overpriced services and superfluous goods by underserved communities. By allowing the measurement and real-time correction of refractive conditions at the patient's reach, this thesis aims to increase the worldwide standards for vision quality and content accessibility.

Today, the majority of acuity measuring devices use sophisticated hardware to precisely estimate optical aberrations. Acuity enhancement options range from simple eyeglasses to prosthetic optical components and expensive cumbersome relays for adaptive optics. Emerging trends in portable light-field displays provide new opportunities for user-friendly and inexpensive instruments that capture reliable medical data to measure and neutralize optical aberrations. This thesis presents three disruptive innovations that utilize cutting-edge optical and display technology to provide a simple tools for managing ocular health. Specifically, it proposes pre-warping methods for light-field displays to estimate refractive conditions (*NETRA*), model lens opacities (*CATRA*) and compensate for an individual's optical aberrations (*Tailored Displays*). NETRA and CATRA have the potential to raise awareness of visual conditions by creating inexpensive computational ophthalmology tools. Tailored displays enhance visual acuity, freeing the viewer of inconvenient corrective wearables and postponing the need for optical replacements and unnecessary incisions in the eye.

Since the introduction of the Scheiner disk in 1619 - two pinholes in a disk where distant objects duplicate when refractive errors are present - ophthalmic tools have evolved to costly, highly accurate, automatic but cumbersome instruments designed for clinicians with four-plus years of training. This thesis goes back to the beginnings of ophthalmology and retrofits an ubiquitous computational power to create XXI-century versions of the Scheiner's test. Lasers and high-resolution sensors are replaced by user interaction procedures. By using the patient's involvement on the test, the proposed tools allow a person to take eye care measurements by himself and export the data to clinical centers that can provide solutions for his condition. *NETRA* and *CATRA* measure spatially-distributed optical aberrations using programmable anisotropy. These hardware apps can be built by repurposing widely available smart phones (Figure 1.1). Instead of an automated system, the proposed methods involve the subject in the diagnostic process. The user looks into the display in close range and marks, matches or aligns a series of programmed patterns several times. The procedure returns quantitative values for refractive aberrations in terms of sphere, cylinder, axis of astigmatism and accommodation range, and four 2D graphical

(a) Nairoby periphery - Kenya

(b) Hyderabad - India

(c) Teresina periphery - Brazil

(d) NASA's Kennedy Space Center - USA

Figure 1.1: NETRA being tested in (a) Kenya, (b) India (c) Brazil and (d) at NASA's Kennedy Space Center. This prototype is a clip-on eyepiece that goes on top of a cell phone. The user looks through it and interactively aligns red and green rings by clicking on the phone's keypad. Number of clicks required to align indicates the refractive error.

representations for lens occluders: opacity, attenuation, contrast and point spread functions maps. These patient-run tests eliminate the need for a trained clinician to measure the visual conditions.

The key enabling factor is the ever-increasing pixel resolution of modern screens, which are now down to $26\mu m$ (single color channel of Apple's $326dpi$ display). This is close to the $10\mu m$ resolution of optical sensors in ophthalmic instruments (*e.g.,* Shack-Hartmann). At this pixel pitch, the screens on modern phones can be re-purposed to achieve accuracy comparable to robust scientific instruments. Although the proposed measuring methods are designed for ubiquity, they are not intended to replace the need for optometrists or ophthalmologists. Instead, the goal is to build portable screening and measuring tools (Figure 1.1), similar to modern electronic devices used to measure body temperature, blood oxygenation, or blood sugar. The new instruments are similarly intended to promote health through self-awareness. NETRA and CATRA cost as low as $3,00$ USD to manufacture, which could make mobile devices one of the most viable options to scale for visual diagnostic services worldwide. Since eyes provide a window into the health of the rest of the body and eyesight measurements can change on a daily basis, from a public health perspective, the new low-cost easy-to-use techniques and the ability to quantitatively track the evolution of eye disorders over time provides a wave of additional data for correlating risk factors, predicting the evolution of deformations, and preventing future complications for individuals.

The knowledge of the optical properties of an eye allows traditional electronic displays go beyond an individual's visual acuity. Current high-resolution screens switch the upper bound limits of the visual performance from the up-until-recently display's pixel density to the viewer's visual acuity. Further improvements on the resolution of display

technologies are ineffective because they only benefit a small fraction of the population: those with vision quality above the current meaning of corrected eyesight. The same hardware available on glasses-free 3D televisions can be utilized to project an in-focus image for an individual with myopia or warp an image according to a specific eye condition and thus to compensate for bad eyesight. Tailored Displays compute light-fields that are pre-warped to account for aberrations and deviate from opacities or scattering sites in the viewer's eye(s). The procedure uses aberration and scattering maps as inputs (*e.g.,* from NETRA and CATRA). It splits an object's light field into multiple instances that are each in-focus for a given eye sub-aperture. The display then projects the computed anisotropic illusions at many depths in a holographic style. Their integration on the retina results in an enhanced clarity and sharpness in projection. The use of multiple depths to render each point of focus creates multi-focus, *multi-depth* displays. Tailored displays have common application for completing daily tasks where eyeglasses are not desired or when multi-focus function is necessary (*e.g.,* driving), offering a comfortable and convenient alternative to corrective eye wear. Future medical record systems will be updated constantly and will be essential to drive future tailored tools and materials. User operation features should be designed for people of diverse abilities, not merely the average person.

Although the majority of this thesis deals with focusing range, opacities, and aberrations in the human eye, the proposed methods are also applicable to other optical systems such as photographic and video cameras, telescopes, microscopes, and light-field cameras. The reader from the optical/computer science world can understand the eye as a camera with flexible but aberrated lenses. Terminology, diagrams and analysis are intentionally similar to traditional camera and rendering materials in computer graphics and optics. For the sake of simplicity, the discussion uses 2D geometric optics (1D sensor and 2D ray space) but they apply to 3D without major changes.

1.1 Problem Statement

Measuring and neutralizing optical aberrations in living eyes are challenging processes that usually require sophisticated sensors and high-quality optics. Focusing abilities, refractive conditions and overall clearness within all possible light paths strongly affects the sharpness of the image being viewed. Optical parts in imaging systems (i.e. lenses and surrounding media) can have aberrations up to the point where their summation is equal to the smallest variation detected by their sensor, which is defined by the density and optical performance of the sensor's photoreceptors. As the optical quality requirement for seeing a clear image increases, the resolution for measuring devices must also increase. The cone density in the *fovea centralis* of a tipical human retina admits variation of ≈ 1 arc minute with no perceivable difference (SCHWIEGERLING, 2004), which means that ideal measuring devices must estimate optical properties in steps of ≈ 1 arc minute (≈ 0.25 diopters, assuming a pupil radius of $1.2mm$) without changing, unassembling, or mechanically interfering with the living visual system. The pupil radius is directly proportional to the required step size. Counteracting an individual's optical aberrations requires the same resolution.

Currently, there is no tool for massive, accurate self-evaluation of eye refractive disorders or cataracts. Measuring technologies can be divided in three groups, based on the applied subjective determinations: (i) patient-centric tecniques require patients to adjust their own view using optical elements (a trial set of lenses or phoropter) while looking at a target (Snellen/reading chart), e.g. visual acuity tests and subjective refraction; (ii) in clinician-centric techniques, clinicians use diagnostic tools to focus their eye and/or a light source on the eyes of their patients to see and rate deformations based on their subjective opinion (e.g. retinoscopy, slit-lamps); and (iii) objective methods use a ma-

Figure 1.2: This thesis proposes two new patient-centric subjective methods to measure optical parameters of optical system. In this prototype, the cell phone clip-on (left) creates a limited light-field display designed for measurement of refractive errors in terms of spherical, cylindrical and axis of astigmatism (right). Photo by Jonathan Williams.

chine to capture images under controlled illumination and compile the measured data (e.g auto-refractors, Shack-Hartmann sensors, photorefractors, retro-illumination-based image processing). Both subjective approaches require graduate-level training to operate tools, to rate deformations and to apply psychological tricks to make sure the measurements are accurate. On the other hand, the more accurate objective solutions that are more expensive and rely entirely on the physical realm of the system, which may not represent the perceptual and neural nature of the problem. Although refractive errors are accurately expressed with a wavefront map, there is no equivalent quantitative mapping system for opacities and scattering media. Cataract assessment requires a clinician on site, which may not be available in remote parts of the world. This thesis presents two patient-centric, subjective methods using easy-to-learn objective tasks. The combination of patient-centric subjective and objective methods incorporates the perceptual nature of the problem in a objective task.

Acuity enhancement options range from simple eyeglasses to optical replacements and expensive relays for adaptive optics. They are grouped by the correction holder. Eyeglasses with simple, bifocal, and multi-focal lenses, contact lenses, LASIK and cataract surgeries can be used to enhance visual acuity. However, all of these require wearing prosthesis, which can be uncomfortable and inconvenient, or incisions in the eye, which is painful for patients and involves risk. Multi-focus displays and holograms can enhance visual acuity by projecting images on the subject's range of accommodation. However, these techniques, while less invasive, do not account for the subject's individual variability. This thesis suggests a new type of display that adjusts itself to compensate for the subject's eye refractive errors (*e.g.*, myopia, hyperopia, presbyopia, astigmatism, and keratoconus) and avoids light scattering on the optical path, such as cataracts. The display is to some extent similar to an adaptive optics-based contact lens which is still being researched (LIANG; WILLIAMS; MILLER, 1997), but is applied to the device rather than the eye.

1.2 Proposed Approaches

This thesis proposes pre-warping methods for *light-field displays* to measure and neutralize optical aberrations in imaging systems. Novel interactive methods estimate refrac-

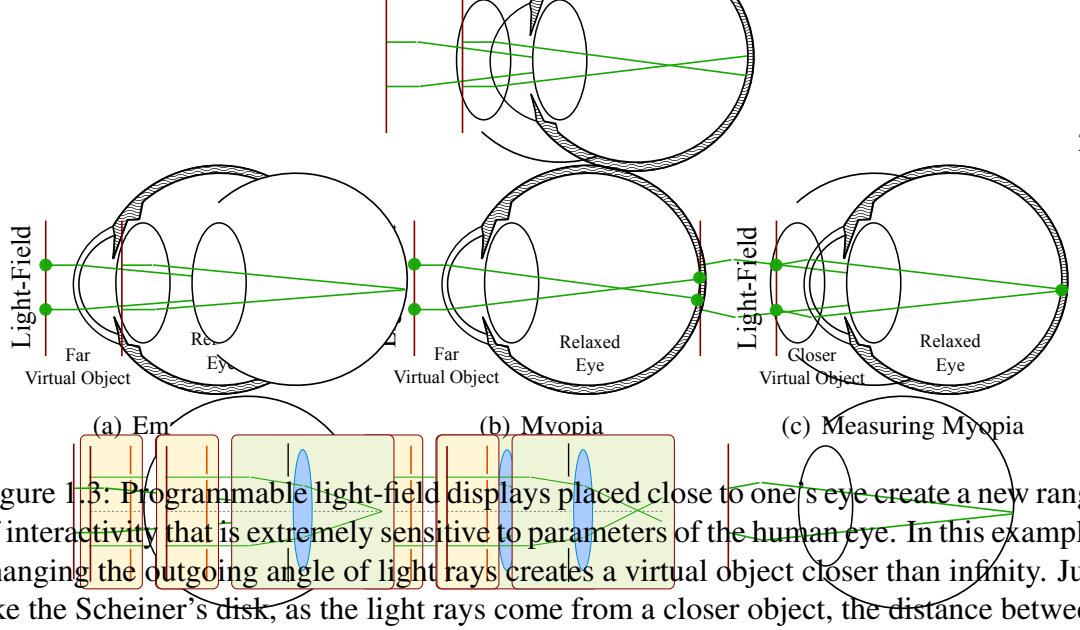

(a) Em (b) Myopia (c) Measuring Myopia

Figure 1.3: Programmable light-field displays placed close to one's eye create a new range of interactivity that is extremely sensitive to parameters of the human eye. In this example, changing the outgoing angle of light rays creates a virtual object closer than infinity. Just like the Scheiner's disk, as the light rays come from a closer object, the distance between copies of the object (green points) for a myopic subject decreases. When the two points overlap, the virtual object's depth is the farthest point in focus for an individual. The inverse of this distance is the optical power required on her eyeglasses.

tive conditions and lens opacities of imaging systems using high-resolution programmable displays and user feedback (Figure 1.2). The *Tailored Display* is the first display device ever to use measured data for enhancing visual acuity, pre-warping virtual objects according to the user's visual needs. This innovative application of individual optical variability to 3D technology extends the current state-of-the-art in computer graphics to be used as tools for ophthalmology. It creates a new family of diagnostic tools that leverage the advanced display resolution of ubiquitous general-purpose mobile devices making eye care more accessible. This patient-centric, low-cost approach is also coupled with interactive technology allowing for accurate quantitative self-evaluation of eye refractive disorders. In addition, this work introduces new quantitative representations for a cataract-effected eye and a simple method to measure focal range; both using the same accessible platform. The data is captured and processed to simulate an individual's vision including all refractive defects. This technology could redefine the doctor-patient relationship to one of increased understanding through shared experience. Optical diagrams and equations appear throughout the thesis to describe optimization models along with implementation instances to assess their functionality.

1.2.1 Computational Ophthalmology: Hardware Apps for Mobile Diagnostics

All solutions developed throughout this work combine optically anisotropic hardware (*i.e.,* light-field displays) and interactive software. The solution's ability to control the direction of individual light rays allows for the division of the eye's pupil into testing sectors and, with user feedback, measurements of its optical aberrations. High resolution displays generate multi-focus holograms for each eye. This allows for the projection of virtual objects at varying depths and provides an opportunity to explore the user's focusing abilities (Figure 1.3). By testing each sector of the eye individually, interactive light-field displays guided by custom software are intriguingly fit for capturing data for eye care. This thesis studies geometric optics and user-interaction concepts to optimize overall usability and viability in hardware and software for measuring techniques.

Since such high-resolution light-field technology is not available yet, the creation of optical attachments for standard displays is required (Figure 1.2). These optical setups are essentially a type of high-resolution light-field displays intended for specific tasks. Because they are designed to be held up to the eye, they reach an ideal tradeoff of brightness and angular resolution found on mobile phones (300 dots per inch). These attachments are not intended to create full-fledged light-field displays, but rather multi-focus displays

optimized for a specific purpose. These *hardware apps* are passive, or non-electronic, snap-on attachments that that utilize the technology of the devices on which they are placed to provide functions that are impossible when disjoint. Analogous to open source software development, the recent advances of the 3D printing technology allows for anyone, anywhere to provide customized solutions for local needs.

1.2.2 A Thermometer for Visual Performance

The field of ophthalmology today reflects photography during the mid-1960s when taking pictures required expensive and bulky equipment. Maintenance costs were high, measurements repeated many times, and pictures could take a week to be printed. The photographer had to double as a chemist, using dark room chemicals to adjust color, brightness and contrast. Customers had to visit specific sites to be photographed. Advances in photography through the past decades have led to a much more convenient and affordable practice, and portable cameras are everywhere. Professional photographers are not obsolete, but this transition has narrowed the profession to full-time artists who deal primarily with illumination, framing, and digital processing. Camera users in the general population have taken on the role of capturing the raw data anywhere. Professionals are only used for high quality measurements driven by their interpretation of what information is going to be captured and its usage.

More broadly and related to the topic at hand, the field of medicine has followed the same trend (HUGHES; JOSHI; WAREHAM, 2008; BELT et al., 2010). Most practitioners already believe that their main impact is on interpreting data instead of capturing it (KOCH, 2006). However, the field itself still holds possession over imaging devices which are bulky, expensive, and require special training to operate. This leads to a public reliant on hospitals and health centers for important screenings. And those individuals in need of screenings are often those who are least mobile and for whom visits impose significant inconveniences. This thesis aims to accelerate the popularization of medical imaging tools by using widespread general purpose devices as the platforms for scientific instruments. NETRA does not replace current devices but rather allows for one to target and measure refractive errors anywhere, increasing the growing body of solutions for home care. A hardware app creates proper light-fields to automate Scheiner's disk and the mobile phone computes refractive data in terms of spherical and cylindrical powers, and axis of astigmatism. By relying on interactive tests of *Vernier Acuity* (LEVI; KLEIN; CARNEY, 2000; DROVER et al., 2010) - alignment of lines rather than discerning blur - NETRA measures are remarkably accurate below the phone's resolution. Just like a thermometer that measures corporal temperature and does not prescribe medicines, NETRA measures the refractive error for eyeglasses (imaging) but does not prescribe a correction, or in other words, it does not interpret the data. Like the thermometer, NETRA provides a tool for individuals to assess their own health. Specifically, it allows individuals to monitor ocular conditions so they can seek medical care if numbers exceed a critical point. With about two billion people worldwide using glasses and six hundred million people with uncorrected refractive errors (WHO, 2005), these simple and low-cost optical attachments that collect accurate and quantifiable medical data help tackle a global health problem, and are ideal tools for remote parts of the world.

1.2.3 A Radar for Eye Opacities

CATRA introduces modeling and measuring procedures to produce quantitative maps of opacity, attenuation, contrast, and point-spread functions (PSF) of the eye. Techniques to identify cataracts assign a rough subjective score that ranges from *low/early cataracts* to *completely blocked/white vision*. The proposed representation is equivalent to a radar for the cloud cover of the eye. Instead of subjectively grading cataracts' severity, the

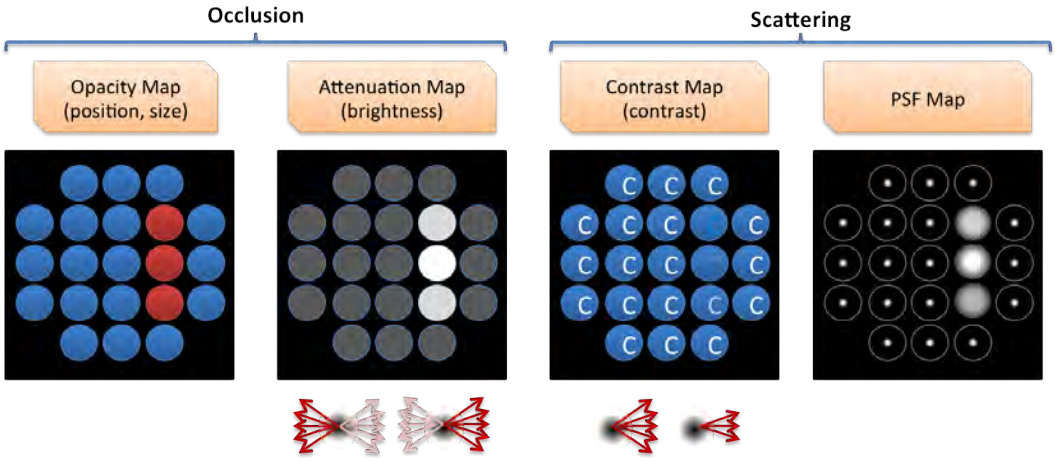

Figure 1.4: Four proposed maps to characterize scattering media into the eye. Each circle represents one subaperture of the pupil. From left to right: (i) opacity maps assess the position and size of the cataract (red circles show affected subapertures); (ii) attenuation maps estimate the density of the scattering material for each subaperture, which determine the amount of forward-scattered light; (iii) contrast maps estimate how wide is the scattering's light-spreading angle; and (iv) subaperture point spread functions are computed by adjusting a gaussian-like scattering profile for every affected subaperture.

software presents quantitative, spatial, and density information to keep track of occluders over time (Figure 1.4). Opacity map is a binary map that shows size and position of cataracts while the attenuation map displays it's subaperture densities. Contrast and local point spread functions model how light is being scattered by the affected subapertures. The proposed interactive procedure navigates these maps to reduce the search space for the full point spread function of the eye. Together, these new maps encode the required information to estimate an individual's cataract-affected view, a feature never found before.

Surgery is the only solution for cataracts and thus clinicians usually face a dilemma of: whether or not to surgically remove the lens of the eye. In their current iteration, the proposed maps contain more information than what clinicians need to make this decision. However, the Shack-Hartmann wavefront sensor to map high-order optical distortions of the human eye also had no practical application twenty years ago. Today, the high accuracy of these devices provides the only reliable data for LASIK surgery. A widespread availability of devices like the one proposed, which generate quantitative data of a cataract-affected eye, may benefit the future of diagnostic and surgical practice as well as increase health-awareness.

1.2.4 Tailored Displays to Compensate for Visual Aberrations

Tailored displays enhance visual acuity with no moving parts by pre-warping virtual objects in a wide range of depths according to the user's visual needs (Figure 1.5). This thesis proposes adjustable displays to avoid the need of wearable optical corrections when looking at them. Just like any visual correction, compiled refractive data (*i.e.,* from NETRA and CATRA) are essential to this approach. Aberration and scattering maps are used to pre-warp a light field which virtually places the distorted anisotropic images into in-focus sub-aperture-dependent depths. As a single point of focus can be distributed into many depths, it creates multi-focus multi-depth displays. The result is an enhanced projection onto the retina, which significantly decreases out-of-focus blur. Tailored displays are suggested for use in daily tasks where eyeglasses are not desired (*e.g.,* when

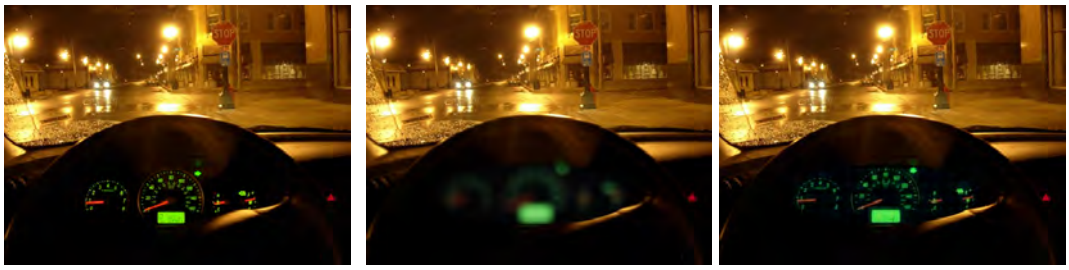

(a) Input Image (b) Regular Dashboard (c) Tailored Dashboard

Figure 1.5: Difference in the view of a presbyopic subject when driving using a regular display (b) and a tailored display (c) on the dashboard of the car. (a) how a emmetrope would see the same view. Picture (b) shows how the subject sees the dashboard of (a) without wearing correction. The tailoring display restores visual acuity without needing eyeglasses or contact lenses. The dashboard of (b) is a photograph with a presbyopic camera looking to a regular display and (c) is a photograph using a presbyopic camera on a tailored display.

using electronic gadgets for sports, work, reading, etc.) or when a multi-focus function is required (*e.g.,* driving, meetings, classes, etc). Convergence-based 3D displays with multi-focus and tailoring features can explore the limits of an individual's visual performance and lead to a new ultra-resolution acuity-enhancing 3D technology.

1.3 Thesis Statement

This thesis demonstrates that eye optical aberrations can be estimated and neutralized using light-field displays and carefully designed interactive methods and optics. Currently available 300-dots-per-inch mobile phone displays have resolution to achieve such accurate ophthalmic measurements, and 1800-dots-per-inch LCD displays can create holographic-style imagery at many depths and with a resolution around 1-arc minute (the eye's standard acuity).

1.4 Contributions

The proposed interactive methods use programmable light-field displays to estimate refractive conditions (*NETRA*) and lens opacities (*CATRA*) of imaging systems. Both solutions trade mechanically moving parts for moving patterns on a screen and forgo the need to use external light sensors.

NETRA measures focusing abilities by exploiting *alignment* rather than *blur* as an indicator of misfocus. The main contributions include:

- A co-design of optics and software to create an effective, low-cost interface sensitive to refractive parameters of the human eye. NETRA creates an unusual optical configuration for a programmable anisotropic display, which is the *dual of a Shack-Hartmann system*;

- *An interactive method to project virtual objects at desired depths*, adapted to eye aberrations, which allows one to indirectly measure refractive errors (myopia, hyperopia and astigmatism). Patterns drawn on screen and user interfaces are designed to provide visual stimuli for measurement and accommodation;

- An interactive method to move virtual objects in depth to *estimate the eye's focal range* providing a measurement for presbyopia. NETRA enables the measurement

of the farthest and closest point in focus by changing patterns on the screen. A user study determines which patterns are best for alignment and for accommodation control.

Nine evaluations (six times in the USA, twice in Brazil, one in India) for the optical and interactive procedures were performed with and without the use of eye drops to relax the eye. Results state an accuracy of $0.3D$ and precision of 0.18 on smartphone-based designs.

NETRA is the only method that measures accommodation without a mechanically moving device or creating a virtual light source inside the eye, thus it is safer and more mobile. It replaces lasers or lights focusing into an eye with a method that relies on user feedback, allowing for self-assessment. The Vernier alignment task guarantees superior performance. The technique goes beyond traditional lens aberration measurement and can also estimate range of focus for eyes and cameras.

CATRA is a novel optical design combined with an interactive technique to scan and measure the *forward scattering* of a cataract-affected lens without moving the users' visual point of reference. The mechanism creates *steady images in the center of the fovea* to avoid gazing and misalignments while mapping the eye. The main contributions include:

- A co-design of optics and user interaction that creates an *effective solution to measure optical scattering* inside the human eye. Off-the-shelf display and simple optical components make the device safe, cheap, and compact;
- *Five interactive measurement techniques* used to assess the presence, size and position, attenuation, contrast, and point-spread function of scattering spots in imaging systems;
- *Four new maps to quantify the scattering behavior* inside the eye. Together they estimate the eye's point spread function (PSF). An image-based technique uses the eye's PSF to simulate an individual's eyesight.

Evaluations in the US and Mexico recorded 85% correlation between CATRA and the clinician's subjective evaluation (LCOS III) and precision error rates of 1%, 3%, 3% for the values of attenuation, contrast and PSF maps. The proposed interactive technique reduces the search space for the PSF of the viewer's eye. The subject can stop the interactive flow at any time, with more information being measured as they proceed. The captured data, displayed in the form of maps, is more detailed than techniques currently used and there is no established quantitative "gold standard" for in-vivo accuracy comparison. CATRA is the first method to interactively measure a sub-aperture PSF map of an eye, the first to measure sub-aperture contrast sensitivities, and the first to explore an individual's cataract-affected view.

Tailored displays pre-warp light-field images to *compensate for spatially-distributed optical distortions on the human eye*. Every sector of the eye's aperture can focus at a different depth. The displaying solution *projects images in the accommodation range of an aperture sector* instead of relying on multi-focus or convergence clues of standard light-field renderers. The main contributions include:

- Novel *multi-depth displays* that compensate for aberrated vision and enhance uncorrected visual acuity. They support time-varying optical corrections with no moving parts and use off-the-shelf components. These displays exploit accessible inexpensive technology to provide resolution that approaches, and sometimes exceeds a standard retinal resolution;

- A real-time rendering procedure for 3D displays which *distributes virtual objects and their light fields* into many focal depths according to the wavefront aberrations of the eye's aperture. Virtual objects placed inside one's accommodation range are tailored to compensate for cataract, low-order, and higher-order refractive effects. An extension to support multi-focus is also presented.

Tailored displays are evaluated their effectiveness in measuring for nearsightedness, farsightedness, astigmatism, presbyopia (reading glasses), keratoconus and any type of cataracts. This is the first validated display technique that uses measurements of refractive error (NETRA) and cataract maps (CATRA) to make optical corrective wear optional when looking at displays. It is also the first consistent solution to compensate for the visual effects created by cataracts.

From a practical perspective, the quantitative output nature of the measuring methods, the absence of sometimes hazardous instruments, and the creation of highly mobile prototypes promote periodic eye tests and have the potential to increase health awareness. New 3D displays with multi-focus and tailoring features can explore the limits of an individual's visual performance and lead to a new ultra-resolution acuity-enhancing display technology.

2 HUMAN EYE AND VISUAL OPTICS

The human eye is a sophisticated imaging system capable of dynamically adjusting its refractive power to focus at a wide range of depths. Figure 2.1 shows a cross section of the eye. Light enters through the cornea, an elliptic transparent layer that, together with the crystallin lens, focuses images onto the retina. The cornea is a thin $\approx 0.5mm$ negative meniscus - a steeper concave lens, thinner at the center than at the periphery - of $\approx 7.8/6.5mm$ radii. Just behind it, a thick watery substance called aqueous humour transports nutrients and filters light wavelengths between 220 to $980nm$. The pupil, the iris-controlled rounded aperture, determines the amount of light that reaches the retina and the eye's depth of focus. The crystallin lens is a transparent, bi-convex and flexible lentil-shaped structure made of thousands of roughly concentric layers. It has from 7 to $9mm$ of diameter and from 2 to $4.5mm$ of thickness (SCHACHAR, 2005). Its curvature and thickness are changed by the ciliary muscle to adjust to the desired focal distance (accommodation). Located in the posterior part of the eye, the retina is a sensory element consisting of approximately 130 million $2.5\mu m$-diameter photo-receptors (rods and cones) distributed in a gaussian shape around the fovea. It converts visible light, already disturbed by other tissues of the eye, to neural action potentials[1] who are sent to the brain through the optic nerve. The object being seen by the subject is projected on the fovea. The optic disc, the eye's blind spot, is placed 3 to $4mm$ to the nasal side of the fovea.

Cataracts and refractive errors are the main causes of loss of *visual acuity*. Today, approximately two billion people need eyeglasses (WHO, 2005) and the prevalence of both conditions are expected to grow with the increasing life-span and rise in "near work", such as the use of electronic gadgets (NIH-EDPRSG, 2004; SCHAEFFEL, 2006). Visual

[1] Neural action potentials, in neurophysiology, is a pulse-like wave of voltage that travels along several types of cell membranes inside the optic nerve.

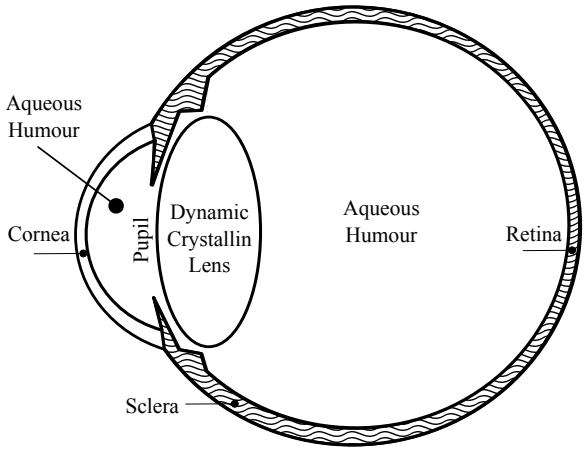

Figure 2.1: Cross section of a human eye.

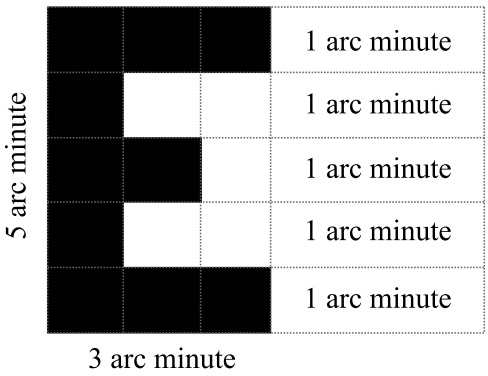

Figure 2.2: Optotype calibrated for a 1 arc-minute resolution reading chart. These charts have to be placed at the calibrated depth and also work best under controlled illumination.

acuity is a measurement of the smallest discernible feature of an imaging system. The **standard visual acuity for humans is 1 arc minute**. In the ophthalmology field, it is represented by the ratio of an eye chart's depth over a depth at which the pixel pitch of the chart's minimum readable line matches the arc minute resolution of one's eye. The term $20/20$ vision is the standard for emmetropes or the absence of refractive errors and cataracts (*i.e.,* normal vision) means that for a chart that is 20 feet away, an emmetrope reads the line in which the letters are printed with a pixel pitch of 1 arc minute (Figure 2.2). In other words, emmetropes read at 20 feet the same line the standard eye would read. Since visual acuity is a perceptual measurement, the only way to fully measure it is to interactively ask the subject to read or identify patterns, such as Snellen charts and trial set of lenses. Theoretical limits on the human foveal vision are found to be between 0.6 $(20/12)$ and 0.25 $(20/5)$ arc minutes (SCHWIEGERLING, 2000). By increasing the optical quality of the image reaching the retina, even emmetropes could potentially double their visual performance. Over the years, researchers have sought a way to overcome the current acuity of human vision. This thesis propose a new path of research using anisotropic displays that could achieve this aim in the future.

2.1 The Eye: A Focal Imaging System

An imaging framework (*e.g.,* a camera or an eye) consists of an enclosed hollow with an opening entrance called *aperture* and a sensing surface for *capture*. Aperture determines *circle of confusion*, a region in the sensor plane where the energy from a point source spreads. The more narrow the aperture, the darker and sharper the image. Circle of confusion r in small-aperture systems is always present and its size is dominated by aperture a:

$$r = \frac{(E+S)a}{E} \tag{2.1}$$

where E is the distance from the aperture to the sensor and S the object's depth (Figure 2.3(a)). Since sharpness is defined by photoreceptor density, blurriness is not perceived when the circle of confusion is smaller than individual photoreceptors.

Focal imaging systems use lenses to overcome the darkness of a high-resolution pin-hole system. Lenses are optical elements which ideally have perfect axial symmetry, converging and diverging light beams. Collimated beams of light traveling parallel to the lens optical axis converge (or focus) to a spot on the axis at a certain distance behind the lens. This property is known as *focal length* (f) and is defined by the curvature of the lenses and the refractive power of the material. The focal length is positive for converging lenses and negative for diverging ones. Uncollimated beams of incoming light rays from

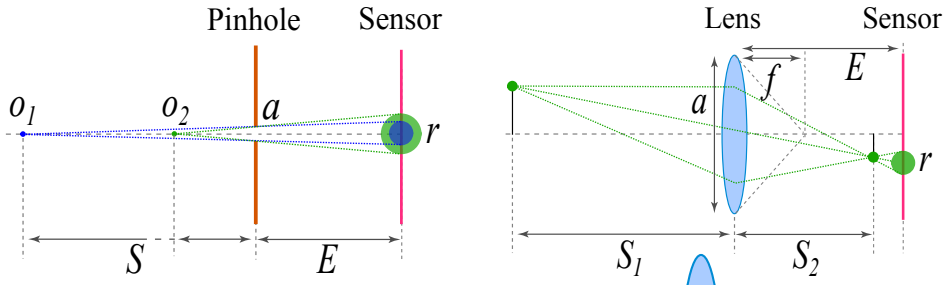

(a) Pinhole Systems (b) Focal Systems

Figure 2.3: Circle of confusion on imaging systems. On pinhole systems (a), placing the sensor closer to the pinhole mask decreases blurriness but does not bring images into focus; Focal systems (b) uses a lens to converge a given depth (S) to the sensor position (E). Circle of confusion is adjusted to the minimum by changing the sensor plane E. Captured image is brighter in focal than pinhole systems.

an object S_1 away from a lens with focal length f are gathered and focused at an image plane placed S_2 away on the other side of the lens:

$$\frac{1}{S_1} + \frac{1}{S_2} = \frac{1}{f}, \tag{2.2}$$

where magnification of M is given by:

$$M = -\frac{S_2}{S_1}. \tag{2.3}$$

By including lenses in imaging systems and allowing focusing by moveming the sensor plane close and far from the lens, the circle of confusion r becomes null for any aperture when the sensor position E matches the image plane S_2:

$$r = \frac{(S_2 - E)a}{S_2} \tag{2.4}$$

The out-of-focus blur created by misplacing E is called spherical aberration.

2.2 Accommodation and Refractive Powers

Refractive power is the reciprocal of the lens' focal length f in meters ($D = 1/f$). It is additive and expressed in *diopters* (D). Human-manufactured lenses are static for f. The sensor position E on cameras changes to the respective S_2 in order to sharply capture objects at S_1. In the human eye, however, the sensing position E (*i.e.,* the eye axial length) does not change. Just like a camera focuses at a specific depth to attain keen visual perception, the crystallin changes its power f with accuracy and rapidity by what is called the faculty of *accommodation*. The crystallin shape changes from more planar (when the eye is focusing at a far object) to more spherical (when focusing at a near object), increasing the refractive power as it does so. It is said that the subject's eye accommodates when focusing closer and relaxes when focusing far. Accommodation is by definition a function of distance, and its accuracy is conditioned by the experience of the acquired clues, consciously or unconsciously (MARK, 1962).

The image quality of a focal system is given by its *point spread function* (PSF). PSF describes an integration of all optical interferences that affects the projection of a given point source on the sensor. The degree of spreading (blurring) of a point is directly correlated with visual acuity. It is a spatial domain version of the modulation transfer function, a Fourier transform of the eye's aperture. For incoherent light, an object's projection is a convolution of the object image by the PSF.

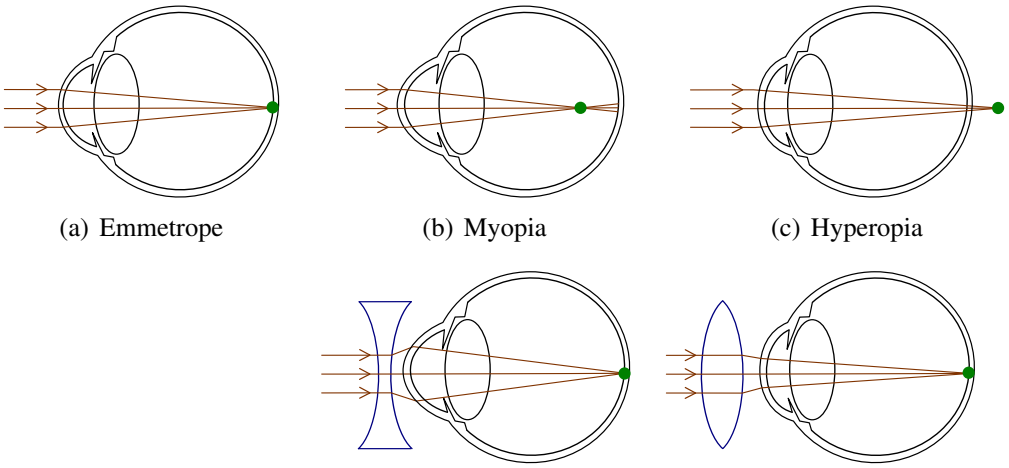

(a) Emmetrope (b) Myopia (c) Hyperopia

(d) Corrected Myopia (e) Corrected Hyperopia

Figure 2.4: The human eye and some refractive disorders and corrections. (a) A perfect eye focuses parallel rays to a single point on the retina; (b) a myopic eye has an elongated eye ball or a bumped cornea, and parallel rays focus to a point before the retina; (c) myopia can be corrected with a diverging lens (negative diopters); (d) a hyperopic eye has a shallow eye ball or a flatter cornea, and parallel rays focus to a point after the retina; (e) hyperopia can be corrected with a converging lens (positive diopters).

There are two main sources for loss of visual acuity in the human eye: (i) refractive errors when the crystallin is not able to adjust f for S_1 (low order aberrations) or in absence of axial symmetry (third and higher-order aberrations), and (ii) opacities (cataracts), where scattering occluders are present in the lens and code the aperture.

2.3 Refractive Errors and Focusing Inabilities

The eye's refractive power comes from two sources: the shape of the air-cornea interface, which is almost constant, and the crystallin lens, which provides additional and adjustable power. Figure 2.5 illustrates focal ranges for individuals with farsightedness (*myopia*), nearsightedness (*hyperopia*), loss of accommodation power (*presbyopia*), astigmatism (also on Figure 2.6) and higher order aberrations. The space ranging between the farthest and nearest point of focus archive clear vision via the process of accommodation. Optical aberrations shift the accommodation range closer and farther from the eye. To obtain maximum efficiency, the far point (optical infinity) should conjugate to the retina when the eye is unaccommodated. The use of corrective lenses shifts the accommodation range to mimic the normal eyesight. In case of asymmetric refractive errors the shift varies spatially.

Nearsightedness and farsightedness are characterized by radially symmetric aberrations caused by a mismatch among the eye's focal length and axial length when the crystallin lens is fully relaxed. Both are corrected by moving the eye's farthest point of focus to optical infinity. Figure 2.4(a) shows a schematic representation of a perfect human eye. The cornea and crystallin together have focal length equal to the eye's axial length, projecting an object at infinity onto the retina. Figure 2.4(b) demonstrates a myopic eye where the image is focused before it reaches the retina due to the lens' focal length being smaller than the eye's axial length. This aberration is caused by an excess of corneal refractive power (refractive myopia) or by an elongated eye ball (axial myopia). Corrective devices such as divergent lenses, contact lenses, or refractive surgery decrease the refractive power (Figure 2.4(d)).

Hyperopia is exhibited in Figure 2.4(c) where the combined focal length of the cornea

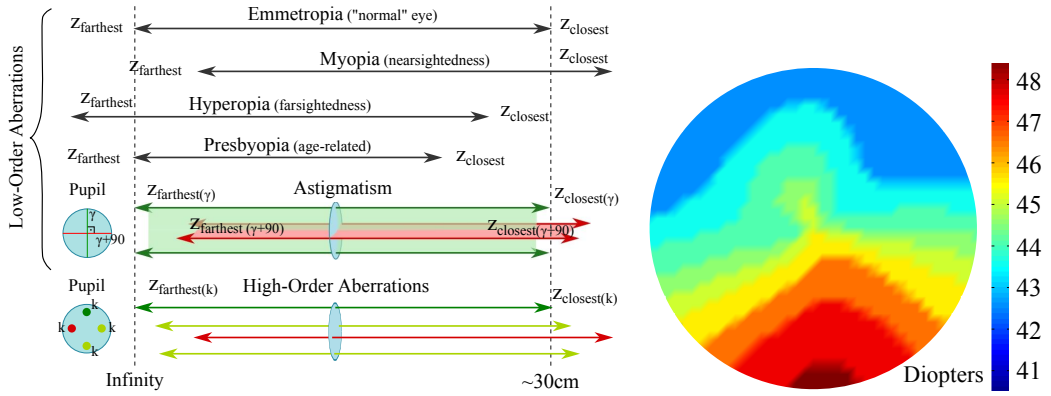

Figure 2.5: (a) Range of focus for various eye refractive conditions and (b) a wavefront aberration map best fitted with Zernike polynomials. The wavefront map represents all refractive errors in the cornea, vitreous and crystalline lens. Myopia shifts the focal range closer, causing bad far sight. Hyperopia shifts the focal range farther, causing bad near sight and lens fatigue since the crystalline lens does not relax even when looking at infinity. Presbyopia reduces the focal range and moves the nearest plane of focus away from the eye. Astigmatism, first described by Young (1801), has two principal focal lengths in perpendicular meridians due to a toric curvature of the cornea or lens (Figure 2.6). Higher order aberrations, such as Keratoconus (b), present non-symmetric variations on refractive powers. Colored height map represent refractive powers in diopters.

and crystallin is bigger than the eye's axial length. This condition is caused by insufficient corneal refractive power (refractive hyperopia), or by a short ocular globe (axial hyperopia). Hyperopia is corrected by adding refractive power through the use of convergent lenses (Figure 2.4(e)), contact lenses, or refractive surgery. Hyperopes can see optical points "beyond infinity", but since there is not such an object, their accommodation range is refined - from infinity to the closest point. Hyperopes use accommodation to focus at infinity which, in long exposures can create headaches and fatigue.

Presbyopia reduces the accommodation range over time due to muscle fatigue related to aging. It is corrected by the use of bi-focal and multi-focal lenses or reading glasses.

Astigmatism (Figure 2.6) is a refractive condition caused by a toric curvature in the cornea or crystallin. The eye has different curvatures along two perpendicular meridians and it cannot sharply focus an image onto the retina. Sphero-cylindrical lenses, contact lenses, or refractive surgery can correct astigmatism.

Higher order aberrations, such as optical coma and keratoconus, present many focal lengths distributed in the aperture map (Figure 2.5(b)). They shift the accommodation range according to sectors of the lens and are not easily corrected or treated. Just like astigmatism, higher-order aberrations cannot project sharp images onto the retina, and blur objects even inside the subject's focal range.

2.3.1 Measuring Refractive Errors

Measuring refractive errors consists of determining the distance from optical infinity to the farthest point in focus for an individual. The distance is converted to the optical power needed in the eyeglasses. Low-order aberrations (myopia, hyperopia, and presbyopia) are described in terms of spherical powers (S) for symmetric errors (*i.e.,* myopia, hyperopia, presbyopia); and cylindrical powers (C) with an axis (γ) for astigmatism. Higher-order aberrations are described using a spatial distribution of focal lengths called *wavefront map*. Low-order aberrations can be converted to wavefront maps by fitting Zernike polynomials. Alternatively, the refractive power from diopters, associated with a given eye meridian θ can be estimated as $P(\theta) = S + C\,sin^2(\gamma - \theta)$. There are four tech-

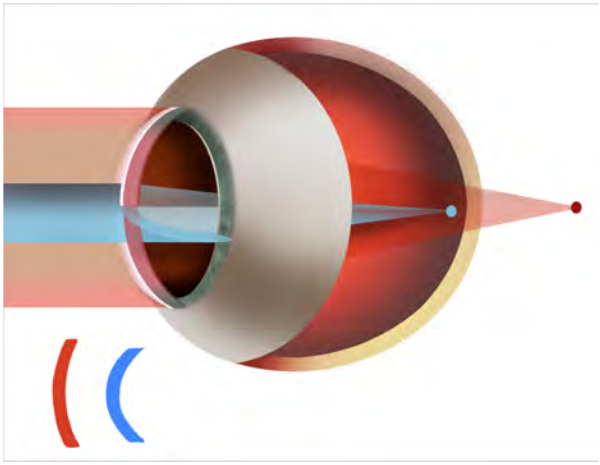

Figure 2.6: Astigmatism is the non-symmetric variance of refractive power between two meridians. In this example, the horizontal power is stronger than the vertical, characterizing astigmatism of 90 degrees. Illustration courtesy of Yolanda Spínola Elías.

niques to measure refractive error: (i) Snellen charts with trial set of lenses, in which the optometrist looks for improvements in visual acuity made by adding corrective lenses; (ii) retinoscopy, arguably the gold standard for refractive measurements where highly skilled optometrists analyze the changes of the light pattern being reflected into the retina as they add corrective lenses; (iii) auto-refractors, which automate the Scheiner's test with a lens and fundus camera; and (iv) the Shack-Hartmann device for wavefront sensing, which analyzes the distortions which appear in a known light pattern when reflected onto a human retina and creates a complete and accurate wavefront map (LIANG et al., 1994)

All measuring devices only work if the subject's eye lens is relaxed, focusing as far as it can. Two common techniques to induce eye relaxation while clinicians take measurements are *fogging* and *cycloplegia*. To fog, the clinician, who already has a first approximation for the required correction, applies lenses on the idle eye (or the one not being tested) and moves a virtual object just beyond the farthest focal point that the eye can see. Even if the image is never in focus, the visual cortex adjusts accommodation to the sharpest image, relaxing the eye. As both eyes are synchronized, the testing eye will also relax. Cycloplegia induces paralysis of the ciliary muscle of the eye, resulting in loss of accommodation. It is performed through the use of cycloplegic drugs, *i.e.,* atropine, cyclopentolate, homatropine, scopolamine and tropicamide. These drops can cause dilation of the pupil for several days and thus practitioners rarely use them, relying entirely on the fogging procedure.

These measuring technologies vary most because they are based on subjective determinations (Figure 2.7): (i) patient-centric subjective approaches require the patient to adjust their own view using optical elements (a trial set of lenses or phoropter) while looking at a target (Snellen/reading chart), e.g. visual acuity tests and subjective refraction; (ii) clinician-centric subjective techniques use diagnostic tools to focus the clinician's eye and/or a light source and subjectively rate deformations (e.g. retinoscopy, slit-lamps); and (iii) objective methods use a machine to capture images under controlled illumination and compile the measured data (e.g auto-refractors, Shack-Hartmann sensors, retro-illumination). Both subjective approaches require graduate-level training to operate tools, to rate deformations and to apply psychological tricks to make sure the measurements are accurate. Highly-accurate expensive objective solutions, on the other hand, rely entirely on the physical aspects of the system, which may not represent the perceptual nature of the problem.

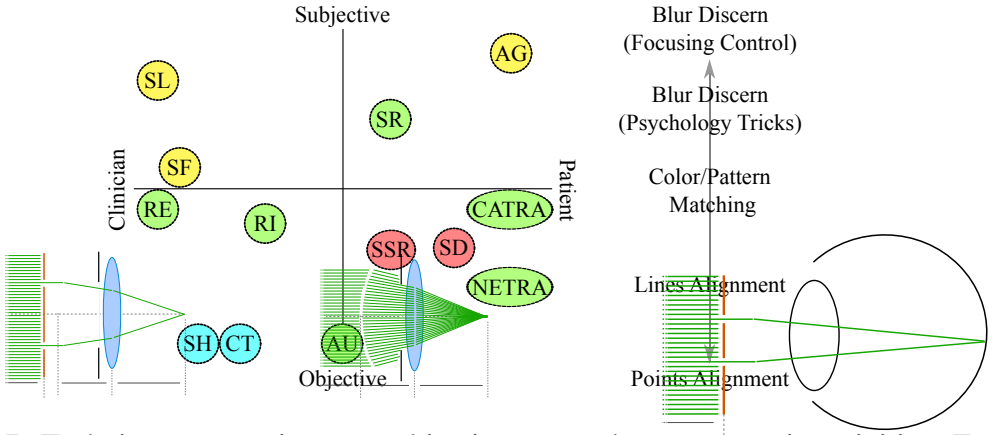

Figure 2.7: Technique comparison on subjectiveness and person centric activities. From left to right: slit-lamp (SL), retinoscop[y] (R[etinoscopy]), impflug photography ([Scheimpflug] Shack-Hartmann wavefront sensor (SH), cornea[l] [topography] (CT), retro-illumin[ation] [tech]ues (RI), auto-refraction (AU), subjective re[fraction] patially-resolv[ing] ers (SSR), Scheiner's disk (SD) and self-adju[sting] (AG). Co[lo]rs r[epresent] [accu]cy, from highly accurate (cyan) to good enough [to] reproducibility iss[ues].

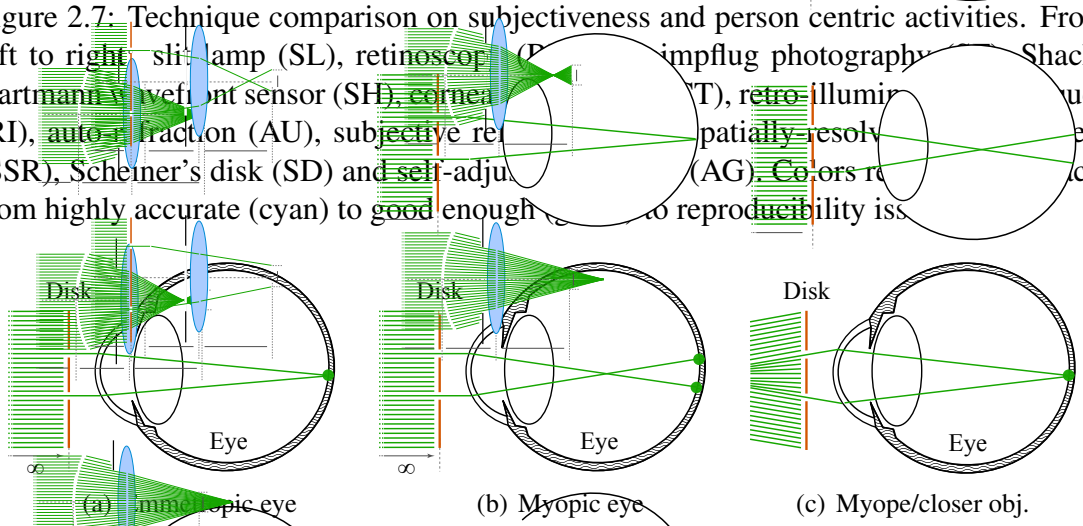

Figure 2.8: Cross-section diagram showing effects of Scheiner's disk held up to the eye with the viewer looking to an object at infinity. (a) Emmetropes (normal eyesight) converge light rays going through the pinholes to a point on the retina. (b) Myopic eyes converge light rays before the retina creating a circle of confusion coded by the disk. The distance between viewed copies is the size of the out-of-focus blur for an aperture with size equal to the distance between pinholes. (c) Bringing the object closer moves copies towards each other. When they overlap, the farthest point in focus is the object depth.

2.3.2 Patient-Centric Subjective Approaches

Scheiner's Disk is the simplest test for measuring refractive aberrations. A disk with two pinholes held up to the eye converts the viewers' unfocused blur into a spatial distance between two copies of a target object (Figure 2.8). By moving the object towards the eye, the distance between perceived images decreases. When they match, the inverse of the object's depth from the eye (d) is the refractive correction required by that individual ($1/d$). This method could only diagnose myopic cases, however, its basic principle is applied in most modern refractive error measurement strategies. It is applied in ours as well.

Badal's optometer (BADAL, 1876; ATCHISON et al., 1995) consists of a single positive lens and a movable target. With the lens up to the eye, the patient moves the target towards the lens until the target becomes clear. The position of the target in diopters minus the power of the lens represents the refraction of the patient's eye. This optometer is an inaccurate instrument in which results are affected by accommodation, the variation in retinal image size with target distance, the large depth of focus and the non-linearity of the scale. Badal's improvement to the original optometer was to place the lens so that its focal point coincides with the nodal point of the eye, thus overcoming the problems of the

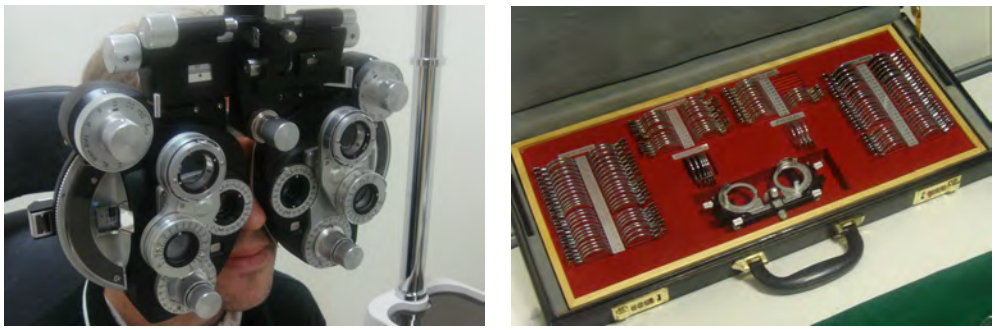

(a) Phoropter (b) Set of Trial Lenses

Figure 2.9: Patient-centric subjective solutions: (a) phoropter, a fast-to-manipulate set of trial lenses with head support and (b) a trial lens set and frame, the mobile version of the phoropter. Snellen Charts are used as a target and to measure visual acuity while testing lenses.

non-linear scale and the changing retinal image size. [2]

Young's optometer (YOUNG, 1801) consists of a single positive lens and uses the Scheiner's disc principle. The target is either a single point of light or a pattern, which is moved back and forth until it is seen singly by the observer. When the target is out of focus, it is seen doubled and slightly blurred.

Subjective Refraction is the standard "which is better, one or two?" procedure. The patient sits behind a phoropter (Figure 2.9(a)) or uses a trial set of lenses (Figure 2.9(b)) while looking at a reading chart. A clinician carefully adjusts the combination of lenses to optimize visual acuity – measured by the smallest line in the chart legible to the patient. Patient feedback is crucial for this process. As the patient reads the eye chart, she may use prior knowledge to "guess" letters that are not clearly visible. Charts are often calibrated and use specific typefaces to take remove the impact of guessing but clinicians still have to repeat measurements several times using psychological tricks to make sure readings accurately reflect patient visual acuity. Further, the amount of illumination in the room also affects visual acuity and may change results.

Laser Speckle Pattern Refraction uses the interference pattern of the laser beam to screen for and measure for eye aberrations. When a laser beam strikes a matte surface, a speckle pattern is seen by viewers. The perceived pattern does not change as the viewer moves around if he is emmetropic. Myopic and hyperopic individuals will see the pattern moving with and against their movement respectively. The clinician inserts lenses in front of the patient up to the moment the that pattern stops changing. A significant amount of observers, though, are unable to perform the task due to the slight irregularities of their eye, thus making the procedure to become unviable in practice.

Spatially Resolved Refractometry (WEBB; PENNEY; THOMPSON, 1992) is a very rare procedure that measures eye aberrations based on subjective alignments from the patient. A cross pattern (usually laser) is projected into the subject's retina. Several light beams are then projected, one at a time, through different points on the pupil. For each beam, the user moves a projected pattern to the center of the cross pattern (2D search). The difference between the initial angle of a beam and the adjusted angle gives the local wavefront derivative. Typically, a matrix of 37 points, or 37 alignments, is projected in a $6mm$ pupil. The subject's head/eye and the optical apparatus should remain stationary with respect to each other during the measurements.

[2] The nodal point is the point in the eye where light entering or leaving the eye and passing through the nodal point, is undeviated.

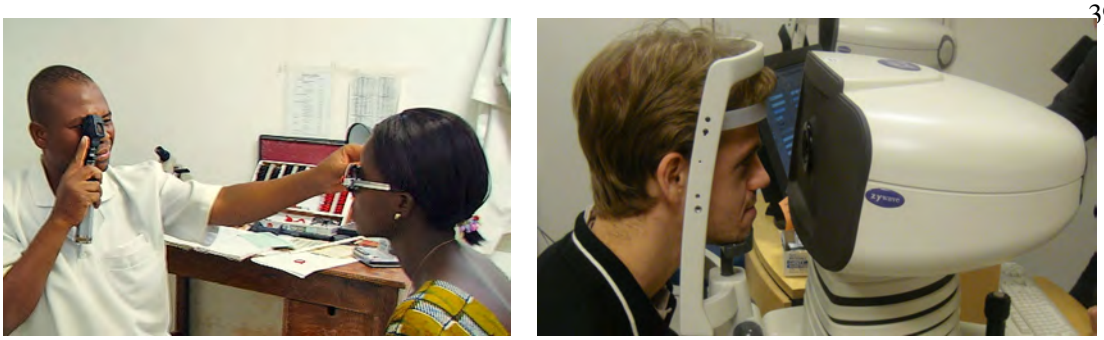

(a) Retinoscopy (b) Shack-Hartmann

Figure 2.10: Gold standard methods when used with cycloplegia: (a) Retinoscopy, where clinicians use *retinoscopes* to project focused light on subject's retina and check for its reflex direction of movement (photo courtesy of Community Eye Health Journal) and (b) shack-hartmann devices, objective methods which compute refraction maps of the entire optical system in a single shot.

2.3.3 Clinician-Centric Subjective Approaches

Retinoscopy (CORBOY, 2003) is a subjective technique in which a highly-skilled clinician uses a streak retinoscope to shine focused light in the form of a slit into the patient's eye (Figure 2.10(a)). The relative movement of the light reflection off the patient's retina, while manually sweeping the device throughout the pupil, indicates the presence of refractive errors. Myopes display a light reflex in which it moves opposite the direction of the sweeping of the light beam. Hyperopes, on the other hand, display a reflex that moves with the same direction the light beam is swept. The clinician's goal is to neutralize the movement of the reflex by adding and removing lenses to the light beam. Astigmatism can be measured by changing the angle of the slit and the movement of the retinoscope. Retinoscopy is considered the gold standard for measuring refractive errors when taken under cycloplegic conditions, but its accuracy is highly dependent on the clinician's manual skills.

The *Fincham Coincidence Optometer* (FINCHAM, 1937) forms the image of an illuminated fine line target on the retina by passing through a the periphery of the pupil. The examiner looks through a telescope with a split-prism focusing screen, similar to old cameras in which the photographer uses alignment to discern focus (KER, 2005). The split-prim system splits the visual field into two. If the incident beam of light is not in focus on the retina, the two parts of the visual field are seen out of alignment. Adjusting the dioptric value of the target in order to obtain alignment gives a measure of the ametropia.

2.3.4 Objective Approaches

Wavefront-sensing Techniques measure the total amount of aberration in the images formed on the subject's retina, and therefore accounts for the eye's entire optical path (LIANG et al., 1994). All of them require a high-quality fundus camera to capture the retina or a reflected pattern on it. *Tscherning aberrometry* (TSCHERNING, 1894) uses collimated beams of laser light passing through a regular array of (hundreds of) pinholes and, if the subject has no refractive error, focuses to a single point on the human retina. By putting additional positive lenses on the light path, a grid of bright spots is projected onto the retina. Aberrations in the optical components distort the light path, shifting the spots on the retina. *Laser Raytracing* (NAVARRO; LOSADA, 1997) is a similar technique but it replaces the mask for a narrow, moving laser beam that scans the pupil. For both methods, a fundus camera captures retinal images of the spot diagram projected on the retina and builds an aberration map. The *Shack-Hartmann wavefront sensor* (J,

(a) Auto-Refractor (b) Scheimpflug/Topographer (c) Adjustable Glasses

Figure 2.11: (a) An auto-refractor, which measures spherical and cylindrical refractive errors in a single shot; (b) Placido Scheimpflug/Topographer to compute the corneal shape and its refractive power among other measurements, and (c) Adjustable glasses that allow an individual to adjust the power of the lens, measuring spherical conditions and providing a solution at the same time (DOUALI; SILVER, 2004);

1904; SHACK; PLATT, 1971) analyzes the distortions observed in a known reflected light pattern (Figure 2.10(b)). A narrow infrared beam produced by a super-luminescent diode is projected into the subject's retina. This projection is back-reflected through the eye lenses and after a fixed monolithic microlens array, produces an image of bright spots on a camera. The lenslet simulates apertures in the Hartmann disc located in front of the eye that isolate a narrow pencil of light emerging through different parts of the cornea. The relative displacements of these spots are proportional to the local wavefront aberrations which are fitted using Zernike polynomials. Shack-Hartmann is used for characterizing imaging distortions ranging from atmospheric turbulence, telescopes, cameras, and the human eye. Shack-Hartmann's resolution is much higher than the required to prescribe glasses and contact lenses (SALMON TO; A, 1998; MORENO-BARRIUSO et al., 2001). Given its cost, Shack-Hartmann is rarely found in clinics and it is mostly used for accurate refraction maps before a LASIK surgery.

Auto-refraction uses infrared sensors and auto-focus to measure nearsightedness, farsightedness, and astigmatism with a high degree of accuracy and repeatability (Figure 2.11(a)) (DAVE, 2004; ATCHISON et al., 1995). Results are usually used as a first approximation for a posterior Subjective Refraction to fine-tune the measurements. Auto-refractors automate the Scheiner disk test, accessing the image quality of a projected source on the subject's retina (Badal Lens). Either way, auto-refractors are composed by a set of moving lenses and slits, but together with wavefront sensing techniques, can measure refractive errors for any eye (including blind ones). They do not check for the retinal perception and therefore their results do not necessarily correlate with visual acuity.

Photorefraction is the measurement of refractive error by photography in long working distances (usually a meter or more). The discovery that the vertebrate eye can be considered a reflector led to the conclusion that its double-pass point spread could be used to compute its degree of defocus. Photoretinoscopy uses an eccentric light source to automate retinoscopy (HOWLAND B, 1962). The clinician can correct the reflex by adding lenses in front of the camera or a computer can process the image and retrieve the amount of refractive aberrations (ROORDAA; BOBIERA; CAMPBELLA, 1998). All of the photorefractive techniques allow refractions from both eyes to be recorded simultaneously. Some techniques also record the refraction of multiple meridians of the same eye at the same time (HOWLAND, 2009).

Corneal Topography (Figure 2.11(b)) techniques can be classified into Placido systems, triangulation-based systems, and keratometry. In *Placido systems*, a known pat-

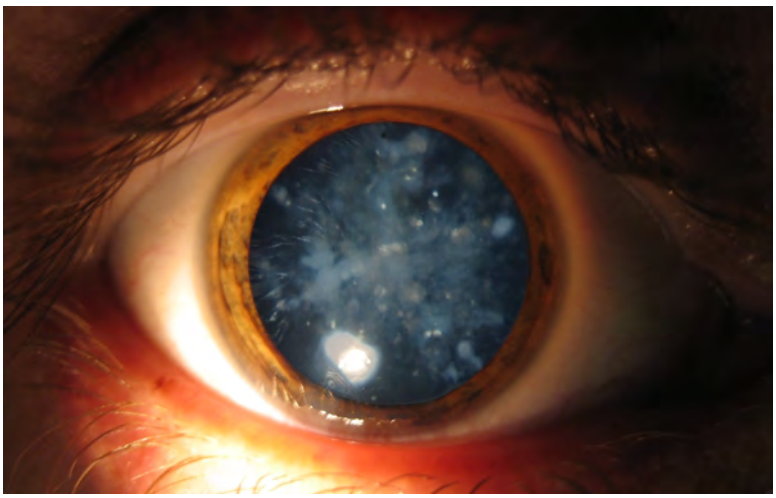

Figure 2.12: Cataracts clouds the eye, scattering light when it goes through the white blobs on the pupil. The image represents an advanced case of the disease, where the subject may not differentiate objects in front of him and when it is possible to see scattering spots even with nude eyes or cameras. Image for illustrative purposes only.

tern containing black and white concentric circles (Placido's disks) is projected onto the cornea. The reflection of the pattern is captured by a camera through a pinhole at the center of the pattern. The captured picture is the first Purkinje image, and from where the shape of the cornea can be reconstructed along with its refractive errors. *Triangulation-based systems* use structured light, moving cameras, and capture a diffuse image of the cornea. Corneal shape is estimated by triangulation. Placido and triangulation-based systems use ultraviolet light, fluorescent dyes, or narrow light beams. *Keratometry* measures the corneal curvature by processing an image of a reflected light ring (LIUA; HUANGA; PFLUGFELDERA, 1999). In the case of an astigmatism, the ring becomes elliptical and it is possible to measure the maximum and minimum optical powers in orthogonal meridians (DOUTHWAITE; EVARDSON, 2000). These techniques are non-invasive, but can only capture aberrations in the cornea. Since crystallin aberrations can enhance or compensate for some corneal aberrations, or even cancel some out, information about corneal topography alone cannot be used for prescribing corrective lenses (ARTAL et al., 2001).

Several commercial products (such as the Nikon Retinomax), and research prototypes of portable and handheld optometers and auto-refractometers exist. They are, however, very limited in accuracy, portability, safety and cost compared to the solutions described in this thesis.

2.4 Cataracts and Light Scattering Media

Cataracts are light scattering proteins that opacify the crystallin in certain regions, deforming the eye's point spread function and reducing retinal illumination (Figure 2.12). The multi-layered crystallin is a very unique structure. It has no blood vessels to transport nutrients, no neural nerves and it is completely clear in its healthy state. The inner body, called the nucleus, is surrounded by the cortex and the epithelium, the skin of the lens. A clear capsule holds the lens in place. With the continuos production of lens fibers through life, the lens becomes thicker and more compact. This is a major cause of the loss of optical clarity, called cataracts (ASBELL et al., 2005).

Cataracts can form in the nucleus (Nuclear Cataract - NC), on the cortex (Cortical Cataract - CC) or under the capsule (Sub-capsular Cataract - SC) of the lens (Figure 2.13). Nuclear cataracts are the most common (LI et al., 2010). A nuclear cataract starts

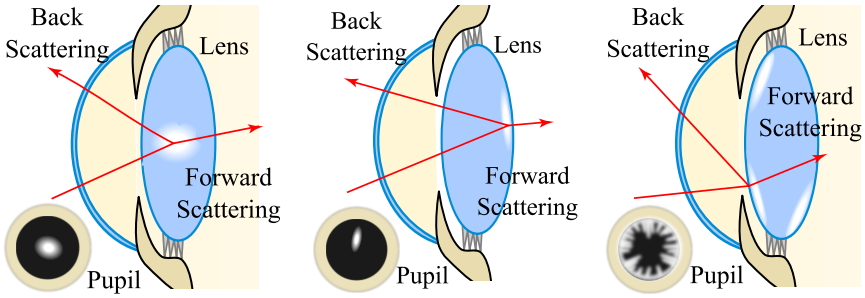

(a) Nuclear (b) Subcapsular (c) Cortical

Figure 2.13: Most common types of cataracts: (a) Nuclear forms on the center of the crystallin, grows towards the periphery, and is strongly related to the aging process; (b) Sub-capsular starts on the back of the crystallin, mostly due to diabetes. (c) Cortical starts on the periphery, and grows inwards towards its center. Back scattering reduces the visual acuity by partially blocking light. Forward scattering blurs the retinal image, decreasing contrast. Pupil size determines the strength of the effects. For nuclear and sub-capsular, the smaller the pupil size, the bigger the effects, while for cortical cataracts the bigger the pupil size, the worse the effect.

at the center and moves towards the surface. The lens becomes hard, the subject looses accommodation power and the vision becomes hazy with triplopia, diffraction rings and radial light needles (CAMPBELL, 1999). Cortical cataracts starts on the periphery and grow toward the center. They produce water droplets and gray cloud effects. Sub-capsular cataracts form on the back of the lens and are associated mainly with diabetes and injuries. 50% of their prevalence are an affect of post-cataract surgery complications when residual lens epithelial cells migrate to the posterior capsule (CAMPARINI et al., 2000). Sub-capsular cataracts produces glare, distortions and blurry images. For nuclear and sub-capsular cataracts, the smaller the pupil size, the bigger the effects, while for cortical the bigger the pupil size, the more perceivable the effects.

Cataracts can be assessed by *back scattering* or *forward scattering*. Back scattering reduces visual acuity by decreasing the amount of light reaching the retina while forward scattering adds noise to the retinal image, decreasing contrast. Back scattering can be misleading as it does not account for what the patient actually sees. It is widely known that the presence of black reflex on retinal images or white structures in corneal images may not affect visual acuity given differences in back and forward scattering. The correlation of backscattering with visual acuity is strong for nuclear but weak for sub-capsular and cortical cataracts(WAARD; IJSPEERT; BERG, 1992). In the end, visual acuity tests with Snellen charts are required to confirm the practical effects of loss of contrast and glare.

Current methods for cataract detection require costly equipment and highly trained clinicians. They are usually detected subjectively by finding a white reflex on the slit lamp or in an ophthalmoscope and subjectively rating the aberration. Nuclear cataracts are best diagnosed by Scheimpflug slit-lamp photography while cortical and sub-capsular by analyzing retro-illumination images (LI et al., 2010; CAMPARINI et al., 2000). Since the exact position of the cataract is unknown, the ability to operate devices and manually focus to scan the eye lens is essential.

2.4.1 Back Scattering Examinations

The Slit-lamp Microscope is used to backscatter light from cataract spots. It shines focused slit of light that reflects back from the cornea and goes through a stereo microscope with Koehler illumination and a variable-width slit as a light source (Figure 2.14). Changing illumination makes it possible to estimate the corneal thickness, defects and an-

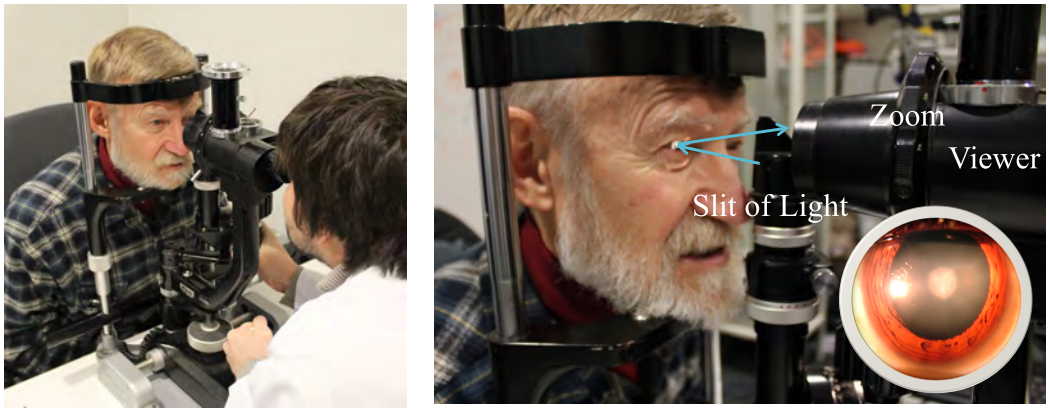

Figure 2.14: Slit-lamp microscopes provide many focusing and angling options to manually find deformations and cloudiness in the eye. A slit of light is focused into the cornea, which reflects back and reaches the viewer's microscope.

terior chamber depth, and view crystallin lens opacities. Clinicians manipulate numerous focusing magnifications, angles and lighting in order to manually search for the cataract. Early opacities are difficult to detect. The method's reproducibility among clinicians is very poor (DONNELLY et al., 2004);

Scheimpflug Slit-lamp Photography tilts the camera's depth of field to consistently get transversal sharp focused images of the lens. Cataracts appear as varied elevations in accordance to location and severity. This technique estimates the density of the crystallin lens opacities and can capture enough information to recreate the internal eye geometry (KORETZ et al., 2004). The Scheimpflug strategy has the disadvantage of requiring numerous pictures from various meridians to reliably estimate the size of the opacity (HAYASHI et al., 1998; LASA et al., 1995). Recently, Tkaczyk et. al (2011) used a circular photodetector technique to measure the fraction of light scattered backwards by the cataract when illuminated by a laser diode. Initial clinical results show that the back scattering attenuation coefficient correlates with clinical examination and Scheimpflug photography.

Purkinje images are a set of four back reflection images from the human eye: outer corneal surface, inner corneal surface, outer crystalline lens surface, inner crystalline lens surface. These reflections can be used to check for opacities, measure the curvature radii of the crystalline and corneal surfaces (SMITH; GARNER, 1995; ROYSTON; DUNNE; BARNES, 2007), and estimate the axes of alignment of the human eye (DEUBEL; BRIDGEMAN, 1995). The drawback of this method is that the gradient index distribution of the crystalline is unknown, causing errors when predicting its radii. Moreover, a stable view of the subject's eye, as well as mechanisms for independently moving the light source and the camera are required. The use of sodium fluorescein improves the contrast of epithelial defects and abrasions and can be used to improve the performance of those algorithms. Unfortunately, it makes these techniques invasive.

2.4.2 Forward Scattering Examination

Retro-illumination techniques flood the retina with light. Their reflex reaches the crystallin and the cataracts from behind, propagating the scattering properties to the camera, which captures the cataracts as dark blobs. The images are compared and ranked according to a grading system, such as Chylark et al. (1993). Mean gray level, best fitting polynomials, feature extraction, etc are used to automatically measure size and the shape of the cataract (LI et al., 2010).

Research alternatives such as femtosecond lasers, and optical coherence tomography

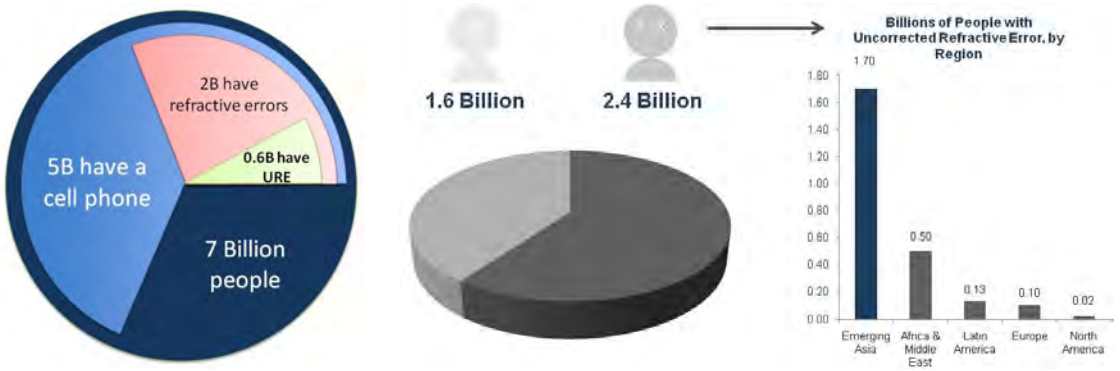

(a) WHO Report (b) Essilor Estimatives

Figure 2.15: Uncorrected refractive aberrations as seen by the World Health Organization (a) and by the largest lens manufacture worldwide (b). NETRA and CATRA uses the ubiquity of mobile phones to create a massive a scientific tool and spread awareness that mostly impacts underserved populations.

(PALANKER et al., 2010) may provide new high-quality tools to estimate the size and position of a cataract. Using Shack-Hartmann, the coherent light ray hits the crystallin from behind and reaches the sensor. Blur captured by each lenslet is a sub-aperture PSF of the lens (DONNELLY et al., 2004). Shack-Hartmann uses infrared light, which may scatter differently than visible light. Cataracts can also be detected at the molecular level using dynamic light scattering (ANSARI; DATILES; KING, 2000). Although some of these techniques have been successfully used in a few clinics (KIM; BRESSLER, 2009), their high costs limit their adoption for diagnostic purposes.

2.5 The Global Impact of Vision Loss

Loss of vision is a key driver of poverty carrying with it not only physical limitations which hinder education, certain types of work, and increase the risk of personal injury, but significant social stigmas as well. Vision losses severely limits children's ability to learn and become literate, contributing to the vicious cycle of poverty and abysmal standards of living. According to AMD Alliance International, the global cost of vision loss in 2010 was nearly $\$3$ trillion dollars ($2,954$ billion USD) for 733 million people living with poor vision and treatable blindness (Access Economics, 2010). Almost 90% of these people come from low and middle income countries. According to the World Health Organization(2005), at least 500 million people suffer from uncorrected refractive conditions and 2 billion people worldwide are known to have refractive errors (HOLDEN, 2007). Essilor (one the world's leading lens manufacture) frequently states that there are $2.4B$ underserved people, mostly living in developing parts of Asia, whose vision could be improved with corrective eyewear (ESSILOR, 2009) (Figure 2.15). In the United States, 9% of school age children have uncorrected refractive conditions and 60% of the so-called "problem learners" are merely suffering from undetected vision problems. Less than 50% of the children diagnosed with treatable eye and vision problems ever receive care, and of those who do, the average time between the screening and the examination is 18 months (American Optometric Association, 2010). The prevalence of refractive conditions is expected to grow with the increasing longevity (NIH-EDPRSG, 2004) and heavy "near work", such as the use of electronic gadgets (SCHAEFFEL, 2006). For instance, in urban areas in East Asian countries, $80-90\%$ of children completing high school are now myopic (LL et al., 2004; MORGAN; OHNO-MATSUI; SAW, 2012).

Despite the fact that eyeglasses cost as little as $\$3$ to manufacture; automatic examina-

tion, measuring, and massive screening of refractive errors is still very challenging. The low and middle income countries do not have easy access to reliable, affordable diagnostic tools to perform the necessary tests and collect minimum data for the prescription. The World Health Organization confirms that quality eye-care is rare because existing solutions are both expensive and require a trained technician/optometrist, unavailable in smaller cities (WHO, 2005). This is especially prohibitive in countries like India where there are only $9,000$ optometrists for a country of 1.2 billion people, or in many African countries, where there is only one ophthalmologist per million people (Ethiopia has only 95 ophthalmologists for a population of 75 million). Even where optometrists and diagnostic facilities are available, it may cost anywhere from $\$5$ to up to $\$200$ for a standard visit to an optometrist, a severe limitation for the majority who live on less than $\$2$ dollars a day. Without access to accurate and affordable eye tests, the second cause of preventable blindness in the world, uncorrected refractive errors, will continue to go undiagnosed and untreated. Millions will go without knowing that they even have a curable condition, let alone receive glasses or surgery to treat them: the economic and social cost of uncorrected vision conditions will only continue to rise without a proper solution (Access Economics, 2010).

Cataracts are the leading cause of avoidable blindness worldwide ($\approx 40\%$ of all cases) and are highly related to the aging process (WHO, 2005). Over 100 million suffer from cataracts. India, with 32% of cataract blindness cases, and Sub-Saharan Africa, with 20% of cataract blindness cases, account for the majority of cataract cases in the World. 17% of Americans over 40 have cataracts, 50% of those over 75 have had cataracts, and its incidences are expected to grow as longevity increases (NIH-EDPRSG, 2004; LI et al., 2010; ASBELL et al., 2005). Yet, while often related to aging, cataracts can develop at any age, even in infancy, causing amblyopia, the suppression of the visual signals from one eye to prevent double vision. There are no efficient methods to prevent them or to halt their growth, however, the expansion can be controlled through early diagnostics (FOSTERA et al., 2003). The elective surgical replacement of the biological lens to a synthetic lens is the only cure for cataracts. The patient's visual needs determines when to operate (ASBELL et al., 2005). Easy-to-use, accurate methods to detect early cataracts and assess their progression over time would be helpful for the development and testing of treatments.

The proposed inexpensive, hardware apps for measuring cataracts and refractive errors drastically decrease the cost of screening and eliminate the need for trained clinicians on the ground. Each app's small dimensions, ease-of-use design and low cost enable at-home and remote location use, thus permitting penetration into remote villages of less developed nations. Similar to a home pregnancy test, the people can test for cataracts themselves after reading basic pictorial instructions. NETRA and CATRA have the potential to make the measurements of eye disorders affordable for the masses and empower people to act proactively and detect cataracts early, thereby enabling early treatment and the prevention of avoidable blindness.

3 NEAR EYE TOOL FOR REFRACTIVE ASSESSMENT

Measuring refractive properties of imaging systems is a common task in many fields ranging from astronomy to optometry. The majority of applications use sophisticated hardware to precisely estimate aberrations. This chapter explores novel estimation techniques for refractive aberrations based on interaction with a view-dependent display. Instead of an automated system, the proposed method (NETRA) involves the user in the process. NETRA is based on the Schneier's principle (WEBB; PENNEY; THOMPSON, 1992) and Spatially Resolved Refractometers (PORTERFIELD, 1759), using currently available cell phone displays as light sources to create the inverse of Shack-Hartmann techniques (LIANG et al., 1994). The inversion is obtained by placing a microlens or a pin-hole array over a high-resolution LCD display instead of a camera sensor. The key idea relies on pre-warping the position and angle of ray-beams to counteract the effect of eye lens aberrations and overlap sharp images on the retinal plane. In practice, the user looks into this display at a very close range and aligns displayed patterns (Figure 3.1). Light rays refract according to the local optical power in different sections of the cornea/crystalline. The number of steps required to align indicates the local refractive error. By repeating this procedure a few times, lens aberrations are compiled and translated into optical corrections in terms of sphere, cylinder and axis of astigmatism. By changing the pattern on the screen, NETRA can also measure focal range and speed by driving the lens accommodation.

At least two billion people worldwide have refractive errors. Uncorrected refractive

Figure 3.1: Can a person look at a portable display, click on a few buttons and recover his refractive fidelity? NETRA combines inexpensive optical elements, programmable display and interactive software components to create the equivalent of a parallax barrier display that interfaces with the human eye. This platform creates a new range of interactivity for measuring optical parameters of the human eye, such as refractive errors, focal range, and focusing speed.

errors are the second leading cause of avoidable blindness (HOLDEN, 2007). 87% of these individuals live in developing countries. From those, 517 million suffer from near-vision impairment (WHO, 2005). Current means of measuring refractive eye conditions include Snellen charts, phoropters, retinoscopes, and refractometers. The operation of such devices require a trained clinician, and none of them allow for self evaluation. This chapter proposes a simple, low-cost measuring tool that enables self-awareness of refractive conditions such as myopia, hyperopia and astigmatism. It is ideal for remote areas, where even such resources as electricity might not be consistently available. Design parameters of these novel devices are explored as well as smart patterns to maximize their usability. Optical probes are validated on modified camera optics and subject evaluations.

3.1 Major Contributions

NETRA – *Near Eye Tool for Refractive Assessment* – is a novel device based on a view-dependent display to measure focusing abilities of an optical system. NETRA exploits *alignment rather than blur* as an indicator of misfocus. The major contributions of this method include:

- A co-design of optics and software to create an effective, low-cost interface sensitive to refractive parameters of the human eye. NETRA creates an unusual optical configuration for a programmable anisotropic display, which is the *inverse of a Shack-Hartmann system*;
- *An interactive method to create virtual objects at desired depths*, adapted to eye aberrations, which allows one to indirectly measure refractive errors (myopia, hyperopia and astigmatism). Patterns drawn on the screen and user interfaces are designed to provide cues for measurement and accommodation;
- An interactive method to move virtual objects in depth to *estimate the eye's focal range*, providing a measurement for presbyopia. NETRA enables the measurement of the closest and farthest point in focus by changing patterns on the screen. A user study determines which patterns are best for alignment and to ensure accommodation control.

Evaluations for the proposed optical and interactive procedures are performed with and without the use of eye drops (clycloplegia) to relax the eye. NETRA is the only method that measures refractive errors without a mechanically moving device or the creation of a virtual light source inside the eye, thus making it safer and more mobile. It uses moving patterns on a digital screen rather than mechanically moving parts. The method relies on user feedback (subjective method) of an objective task and allows for self-assessment. The technique goes beyond traditional lens aberration measurement and also estimates the range of accommodation for eyes and cameras. NETRA *employs an alignment task instead of a blur discern test*. This differs from the common practice in optometry today.

3.2 Inverting Shack-Hartmann

The work on NETRA is inspired by recent developments in shaping light rays by light-field techniques in computer graphics (NG; HANRAHAN, 2006; LEVOY; ZHANG; MCDOWALL, 2009). Surprisingly, there has been little discussion of the connection between light field capture and the Shack-Hartmann technique in optics. The Shack-Hartmann test involves measuring the phase of the aberrated wavefront from a (distant)

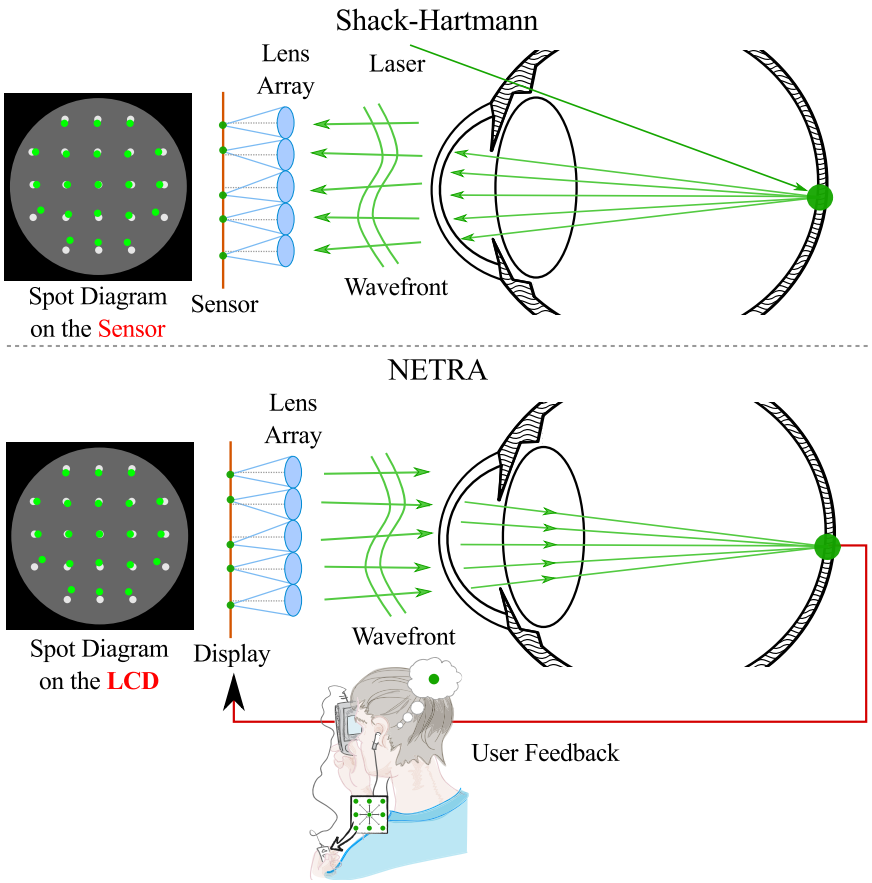

Figure 3.2: Shack-Hartmann method (top) creates a virtual point source into the eye and captures wavefront slopes with a light-field fundus camera. The difference among the expected position of focused light (grey dots) and the captured one (green dots) is mapped to wavefront aberrations. NETRA (bottom) replaces the sensor by the display and ask the subject to align the spot diagram. In the end, both produce the same output, a slope map.

point source by placing a microlens array in front of a digital sensor (Figure 3.2(top)). Light passes through the optical setup whose performance is being assessed. The modified wavefront is then captured by a Shack-Hartmann sensor - essentially a light-field fundus camera. The phase information captured is used to understand the optical system under study. The displacement of the images under each lenslet indicates phase changes, which are converted to turbulence or lens aberrations $W(x, y)$ by:

$$\frac{\partial W(x,y)}{\partial x} = \frac{\Delta x}{f} \quad \text{and} \quad \frac{\partial W(x,y)}{\partial y} = \frac{\Delta y}{f} \tag{3.1}$$

where $W(x, y)$ is the wavefront error, Δx and Δy are shifts on the sensing plane and f is the focal length of the lenslet. The longer f, the greater the resolution in terms of diopters per shifted pixel and the smaller the range of measurement. The wavefront is then approximated by the J orthogonal set of basis functions V_i through a system of

linear equations over N slope measurements:

$$\begin{bmatrix} \partial V_1(x_1,y_1)/\partial x & \partial V_2(x_1,y_1)/\partial x & \cdots & \partial V_J(x_1,y_1)/\partial x \\ \partial V_1(x_2,y_2)/\partial x & \partial V_2(x_2,y_2)/\partial x & \cdots & \partial V_J(x_2,y_2)/\partial x \\ \vdots & \vdots & \ddots & \vdots \\ \partial V_1(x_N,y_N)/\partial x & \partial V_2(x_N,y_N)/\partial x & \cdots & \partial V_J(x_N,y_N)/\partial x \\ \partial V_1(x_1,y_1)/\partial y & \partial V_2(x_1,y_1)/\partial y & \cdots & \partial V_J(x_1,y_1)/\partial y \\ \partial V_1(x_2,y_2)/\partial y & \partial V_2(x_2,y_2)/\partial y & \cdots & \partial V_J(x_2,y_2)/\partial y \\ \vdots & \vdots & \ddots & \vdots \\ \partial V_1(x_N,y_N)/\partial y & \partial V_2(x_N,y_N)/\partial y & \cdots & \partial V_J(x_N,y_N)/\partial y \end{bmatrix} \begin{bmatrix} h_1 \\ h_2 \\ \vdots \\ h_J \end{bmatrix} = \begin{bmatrix} \partial W(x_1,y_1)/\partial x \\ \partial W(x_2,y_2)/\partial x \\ \vdots \\ \partial W(x_N,y_N)/\partial x \\ \partial W(x_1,y_1)/\partial y \\ \partial W(x_2,y_2)/\partial y \\ \vdots \\ \partial W(x_N,y_N)/\partial y \end{bmatrix}, \tag{3.2}$$

where h represents polynomial coefficients. The reconstructed wavefront becomes a weighted linear combination of these polynomials:

$$W(x,y) = \sum_{j=1}^{J} h_j V_j(x,y) \tag{3.3}$$

The Zernike polynomials are a standard for ophthalmic representations of wavefront aberrations $W(x,y)$ in the eye. They are a sequence of polynomials that are orthogonal on the unit disk and defined in the polar coordinates (ρ,θ) as a normalized product of a radial-dependent component and an azimuthal-dependent component. The radial component is a polynomial, whereas the azimuthal component is sinusoidal:

$$Z_n^m(\rho,\theta) = \begin{cases} N_n^m R_n^{|m|}(\rho)\cos\, m\theta & \text{if } m \geq 0, \\ -N_n^m R_n^{|m|}(\rho)\sin\, m\theta & \text{if } m < 0; \end{cases} \tag{3.4}$$

where n is order of the polynomial ($n \geq 0$) and m is the angular component ($m = -n + 2i$ for $i = [0,n]$). $N_n^m = \sqrt{2(n+1)/(1+\delta_m)}$ is a normalization factor and function $R_n^{|m|}(\rho)$ is given by:

$$R_n^{|m|}(\rho) = \sum_{k=0}^{(n-|m|)/2} \frac{(-1)^k\,(n-k)!}{k!\,((n+|m|)/2-k)!\,((n-|m|)/2-k)!}\,\rho^{n-2\,k}, \tag{3.5}$$

where δ_m is 1 for $m = 0$ and 0 for $m \neq 0$. The second order Zernike polynomials can be converted into a sphero-cylindrical representation through:

$$\begin{aligned} M &= \frac{-Z_2^0\; 4\sqrt{3}}{p^2} \\ J_0 &= \frac{-Z_2^2\; 2\sqrt{6}}{p^2} \\ J_{45} &= \frac{-Z_2^{-2}\; 2\sqrt{6}}{p^2}, \end{aligned} \tag{3.6}$$

in cross-cylinder convention, where p is the pupil size and V_n^m is the n^{th} order Zernike coefficient of meridional frequency m. In the minus-cylinder convention:

$$\begin{aligned} S &= M + \sqrt{J_0 + J_{45}} \\ C &= -2\sqrt{J_0 + J_{45}} \\ \alpha &= 0.5\tan^{-1}(J_0/J_{45}), \end{aligned} \tag{3.7}$$

where sphere S, cylinder C and axis of astigmatism α are the optical powers used in prescriptions.

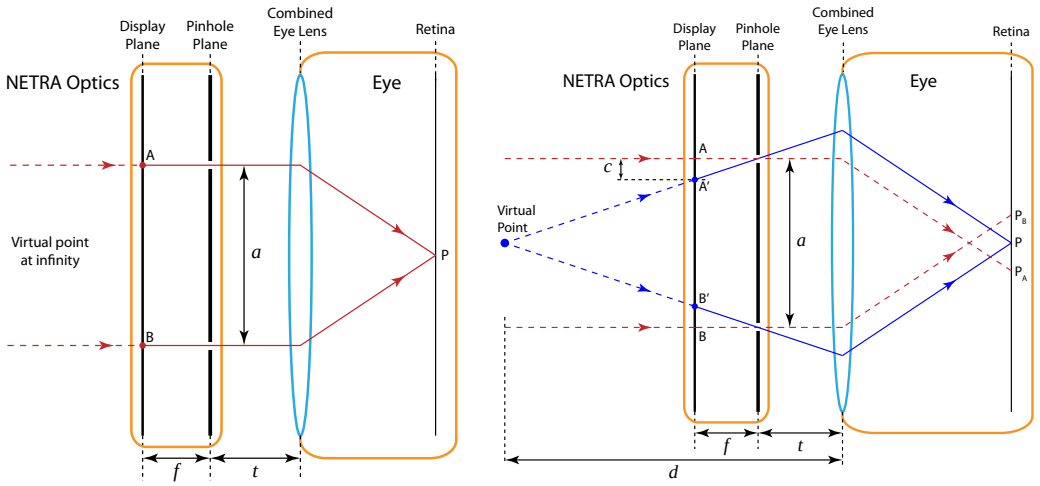

(a) Perfect Eye (b) Myopic Eye

Figure 3.3: NETRA optical setup: (a) The NETRA optical system using a pinhole array. A perfect eye converges parallel rays onto a point on the retina. (b) A myopic eye converges a set of parallel rays before the retina (red arrows). By shifting points A and B to A' and B', respectively, the resulting rays focus on the retina at point P (blue arrows). The amount of shift required to move A to A' allows us to compute refractive error.

Based on the principle of ray reversibility of geometric optics (Fermat's principle[1]), NETRA swaps the sensor for a digital display, inverting all light paths (Figure 3.2(bottom)). While Shack-Hartmann measures the localized slope of the wavefront in the sensor plane, NETRA makes the user interactively shift the spots on the screen until they are aligned. The slope computed by NETRA is exactly the same as the Shack-Hartmann's $\Delta(x, y)$ and thus all the theory for Shack-Hartmann also applies to NETRA. Knowledge of this shift provides data to estimate parameters through Equations 3.3 and 3.2 such as the radius of curvature and hence any errors resulting from defocus and other aberrations.

3.3 Creating Programmable Depth Perception

The intuition behind inverting Shack-Hartman relies on the concept of a virtual point source at a given depth created by a carefully designed light-field display. Figure 3.3 shows the basic optical setup. A microlens array or a pin-hole array is placed over a controllable high-resolution display. The viewer holds this setup next to the eye being tested. The image formed on the viewer's retina depends on the local refractive properties of the tested section in the lens. Using a simple interaction scheme, the viewer modifies the displayed patterns until the perceived image closely matches a specified result. This procedure is repeated for a few sections of the eye. Based on this interaction, NETRA estimates the viewer's refractive conditions, such as myopia, hyperopia, and astigmatism.

Figure 3.3(a) shows a simplified ray diagram for NETRA with two pinholes in 2D. As the system illuminates one point directly under each pinhole (points A and B), two parallel rays enter the eye, simulating a virtual point at infinity. If the eye is not focused at the virtual depth, two copies of the virtual object appear. An eye that can focus at infinity converges these rays, which meet at a single spot P on the retina. A *myopic* eye (farsightedness), however, is unable to focus at infinity and converges these incoming rays before they reach the retina, producing two distinct spots (P_A and P_B on Figure 3.3(b)).

Changing the position of point A (or B) changes the vergence of the rays produced

[1]Principle of Reversibility: Any light ray in an optical system, if reversed in direction, retraces the same path backward, obeying Fresnel and Snell equations as well as Fermat's principle of least time.

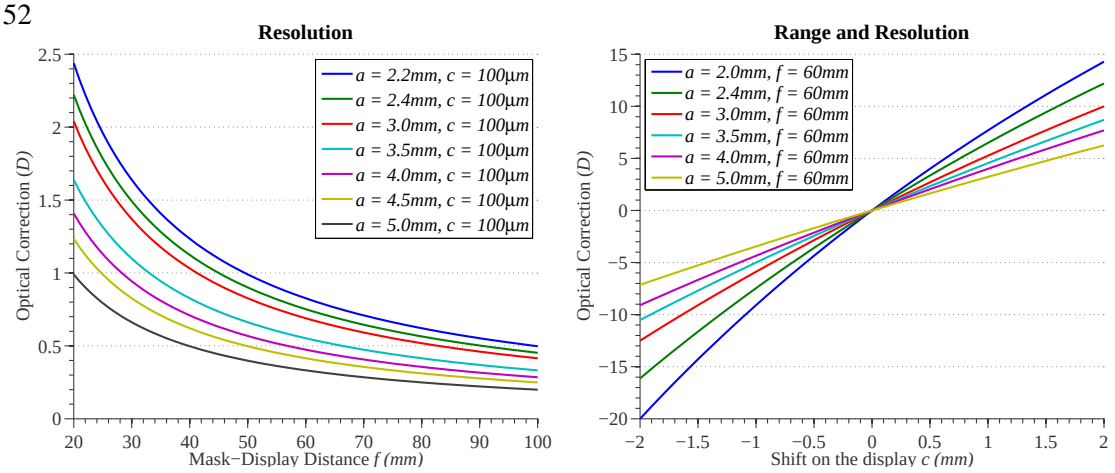

Figure 3.4: (left) Resolution of the first $100\mu m$ shift on the display and (right) range per resolution trading by changing a. The Bigger a, the bigger resolution, however a is limited by pupil diamenter.

by the pinholes. For instance, moving points A and B closer to each other on the display plane causes the corresponding rays to diverge, progressively moving the virtual point closer to the viewer. Likewise, moving these points apart, causes the associated rays to converge, moving the virtual point away from the observer. For a myopic eye, as points A and B get closer, the two imaged spots overlap on the retina at P (Figure 3.3(b)). The amount of shift applied to A and B is converted to the depth at which the subject is focusing. The case for hyperopia (near-sightedness) is similar: as points A and B move further apart on the display plane, the resulting rays converge. To match their accommodation range, the system is able to create a virtual object "beyond infinity".

The amount of shift c to create a virtual source at a distance d from the eye is:

$$c = \frac{fa}{2(d-t)}, \tag{3.8}$$

where t is the distance from the pinhole array to the eye, a is the spacing between the pinholes, and f is the distance between the pinhole array and the display plane. Moving A and B on screen, one can arbitrarily vary the distance between the virtual scene point and the eye without any moving parts. This is an equivalent procedure to varying the power of a lens placed in front of the eye. From Equation 3.8, the power of a diverging lens required to fix spherical aberrations is given (in diopters) by

$$D = \frac{1000}{d} = \frac{1000}{\frac{fa}{2c} + t}, \tag{3.9}$$

where all distances are in mm. Positive values for c and D represent myopia, while negative values represent hyperopia. Figure 3.4 illustrates how Equation 3.9 progresses for a few parameters. One can trade step resolution for range of correction by changing f and a. As the pixel resolution (the measuring step size - c) doubles, the final resolution in diopters also doubles.

3.3.1 Alignment Instead of Blur

Unlike a real light point that creates a blurred circle of confusion in the retina, the system projects discontinuous sets of rays into the eye, producing a coded circle of confusion for a point that is out of focus. The number of rays emanating from the virtual point is limited to the number of pinholes. In the case of two pinholes, two points P_1, P_2 are captured by the retina (Figure 3.3). The distance $P_A - P_B$ is proportional to the circle of

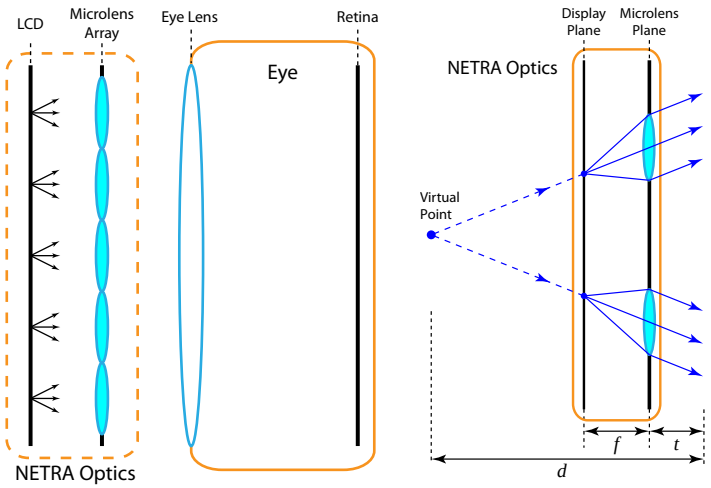

(a) NETRA Optical System (b) Microlens design

Figure 3.5: NETRA optical setup with microlens array: (a) a microlens array placed over a high-resolution display is held right next to the eye. For simplicity, the diagram uses a single lens to represent the combined refractive power of the cornea and the crystalline. (b) Microlens design of the system improves the light throughput.

confusion's diameter (r): $P_A - P_B = ar/p$, where p is the pupil diameter. This subtle difference allows the *conversion of a blur estimation problem into an simpler alignment task*.

The human eye can align objects with remarkable accuracy. Visual acuity is related to the smallest visible feature one can discern and it is limited by the cone size in the retina. Hyperacuity, or Vernier acuity, is the human ability to detect the proper alignment of two line segments and is about 5-10 times greater than visual acuity (WESTHEIMER, 1975; DROVER et al., 2010). Under optimal conditions of good illumination, high contrast, and long line segments, the limit to hyperacuity is about 8 arc seconds or 0.13 arc minutes, compared to the visual acuity's limit of about 1 arc minute. Because the limit of hyperacuity is well below the size of the human photoreceptors, it is accepted as a feature of the visual cortex rather than the retina. Hyperacuity is the secret behind the precision of a sliding caliper and, of course, of NETRA, which relies on the alignment abilities to enhance accuracy even on low resolution devices.

3.3.2 Microlens Setup and Focus Ambiguity

Microlens arrays enhance an image being formed through an array of pinholes in the same way that a single lens serves a pinhole camera. With the freedom of wider apertures, focal systems can capture more light than pinhole system while preserving sharp focus. In the lens-based setup, the pinhole array is replaced by a microlens array at a distance f from the display equal to its focal length. Instead of a single ray coming from each pinhole in one direction, the sensor receives a focused bundle of parallel rays, as shown in Figure 3.5(b). This introduces *focus ambiguity*: the eye can focus (or accommodate) either at the virtual point at a distance d, or at infinity to sharp focus each parallel bundle of rays onto the retina. Forced focus at infinity is required for measuring myopia, while accurate measurement of hyperopia requires accommodation to completely relax the eyes (focus beyond infinity). These concepts will be further discussed in Section 3.5.2, which describes variability on the focus cue strength by varying the displayed patterns and Section 3.5.1, which discusses alternatives for eye relaxation.

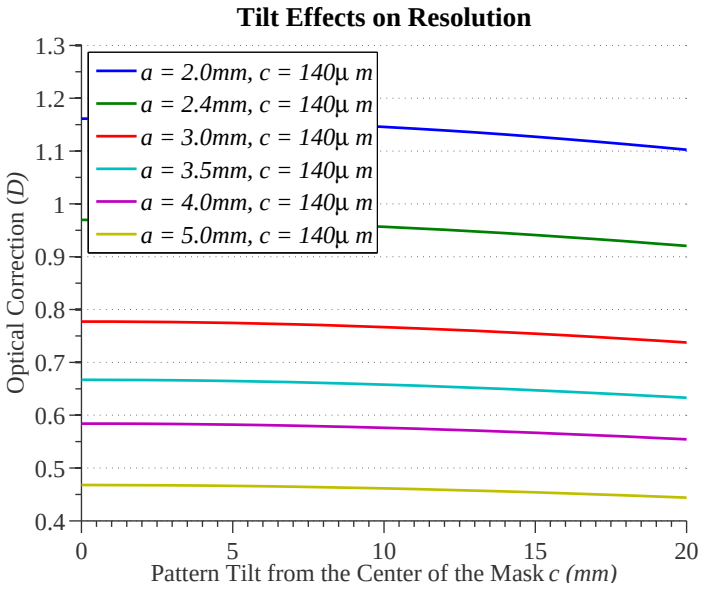

Figure 3.6: Small effects created by misaligning the display and the mask. Given that lenses come in steps of 0.25 diopters, issues with hardware alignment can be ignored.

3.3.3 Alignment of the Display and Mask Optical Axis

Incorrect alignment between the display and pinhole mask changes m and introduces variations in accuracy. m is the distance light travels from the virtual object to the center of the mask. In tilted setups, m increases and if not adjusted, each pixel c represents less or more than what the system is calibrated to measure. Figure 3.6 how this results in misalignment by the eye. In practice, with $a = 2.4mm$, $t = 10mm$ and $f = 60mm$ a difference of $50mm$ creates an error smaller than $0.25D$. Any value smaller than $50mm$ does not significantly change the results.

3.3.4 Maximum Reliable Resolution

The diopter resolution of NETRA is limited by the size of the cone cells of the eye (effectively the pixel size of the retina), $p_e \sim 4\mu m$, and eye's focal length, $f_e \sim 24mm$. The human user can resolve misalignments of a single pixel (cone cell). With the pixel size of the display as p, the smallest shift ($c = p$) and assuming $t \sim 0$, the maximum resolution of the setup (in diopters) from Equation 3.8 is

$$D_{min} = 2000 \max\left(\frac{p}{fa}, \frac{p_e}{f_e a}\right). \tag{3.10}$$

With a pin-hole spacing of $a = 3mm$, D_{min} becomes 0.15 diopters according to the upper bound set by p_e. This is further reduced by diffraction in the eye and the NETRA optics.

The pupil size limits the maximum spacing between lenslets (distance *a* in Figure 3.3), which affects the achievable range of corrective powers. Also, the granularity of the microlens array cannot always match the pin hole spacing and affects the accuracy for the cylindrical axis in the case of measuring astigmatism.

3.3.5 Ideal Pinhole Size

Pinhole size (h) is defined by the accepted signal-to-noise-ratio of the aberrations created by each pattern from the screen onto the retina. With a subject looking at infinity ($f = E$), the pinhole diameter h for a circle of confusion with the size of a single retinal photoreceptor ($r \approx 2.5\mu m$) is given by the following derivation.

The pattern on the screen is $m + t$ away from the eye, where m is again the distance from the display to the mask and t is the distance form the mask to the observer's eye.

The light from the screen goes through the aperture, reaches the lens and converges to a point S_2 that is computed by:

$$\begin{aligned} S_1 &= (m+t) \\ \frac{1}{S_2} &= \frac{1}{f} - \frac{1}{m+t}. \end{aligned}$$

Observing that the pinhole h is placed t away from the lens and thus decreases the aperture size a to h' by

$$h' = \frac{hm}{m+t},$$

the relation between pinhole diameter h' and circle of confusion c is (Equation 2.4)

$$\begin{aligned} r &= \frac{(S_2 - E)h'}{S_2} \\ \frac{1r}{\frac{1}{f} - \frac{1}{m+t}} &= \left(\frac{1}{\frac{1}{f} - \frac{1}{m+t}} - E \right) h', \end{aligned}$$

where E is the eye axial length. With the subject looking at infinity ($f = E$), the equation reduces to

$$h' = \frac{r(m+t)}{E}. \tag{3.11}$$

Assuming $E = 24mm$ (standard eye), an eye focusing at infinity ($f = E = 24mm$), receiving light from a pattern $m + t = 60mm$ away, cannot perceive the blur up to a pinhole diameter of $h = 6.25\mu m$. A single pixel on the same setup has a width of $p \approx 141\mu m$ and is magnified by 0.71 to $100\mu m$ on the retina, creating a signal 40 times bigger than the out-of-focus blur created by a pinhole size of $h = 6.25\mu m$. As most of the perceived pattern is the line (signal), these parameters have a good signal to noise ratio.

The ideal pinhole size h is computed to a desired signal to noise ratio. Given an acceptable blur b as a factor of the pattern size p, h is found from:

$$h' = \frac{pb(m+t)}{E}, r = pb \tag{3.12}$$

For instance, a factor of 35% blur for each side of the pattern gives b=0.7 and the ideal pinhole diameter is $h = 247\mu m$ for $m + t = 60mm$, $p = 141\mu m$ and $E = 24mm$.

This complements Rayleigh's equation (STRUTT; RAYLEIGH, 1891) for the pinhole size:

$$h = 1.9\sqrt{f\lambda}, \tag{3.13}$$

where f is the eye's focal length (assuming the mask is close and centered to the lens) and λ is the wavelength of light. A yellow-green band (550 nm) should yield optimum results for white illumination. The prototypes developed during this thesis use $h \approx 250\mu m$.

3.4 Measuring Astigmatism and Focal Range

The correction for any refractive error is the shift on accommodation range that places the farthest point in focus to infinity. Assuming that the eye is relaxed (focusing at the farthest focal point), NETRA measures myopia and hyperopia using the alignment technique described in Section 3.3. The viewer looks close on the display and sees partially overlapping patterns. The viewer proceeds with a 1D search (moving them towards of away from each other) to align patterns by moving them on the display. The spacing between the patterns c when they appear perfectly aligned (as seen by the user through the

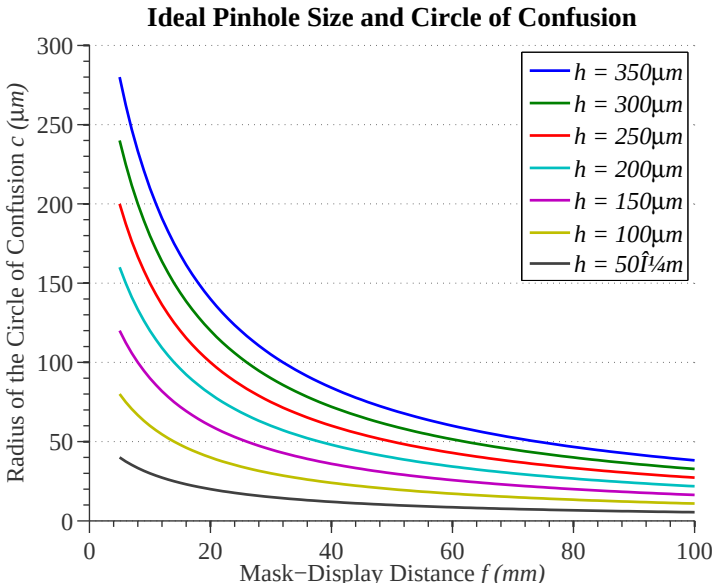

Figure 3.7: (left)Radius of the circle of confusion (r) as a function of the distance display-mask (m) for many pinhole diameters. $E = 24mm$ and $t = 10mm$. (right) Tilt effects by misaligning the display and the mask.

probe) gives the position of the farthest focal point that subject can clearly see. Equation 3.9 gives the required corrective power to the desired shift in the accommodation range. NETRA takes advantage of the freedom of patterns to optimize this process. Section 3.5.2 discusses some of the patterns used in this work, and Figure 3.8(right) shows a sequence of images seen by a camera with simulated myopia.

The analogy of generation of a virtual point by the NETRA optics is intuitive and works well with spherical lenses, but is inadequate for non-radially symmetric or higher-order aberrations.

3.4.1 Measuring Astigmatism

Astigmatism is a common refractive error resulting from an irregularly shaped cornea and/or the crystallin. The analogy of moving a virtual point, employed earlier as a mental device to understand NETRA for myopia and hyperopia, unfortunately, does not extend to astigmatism. An astigmatic eye is often modeled as a toric (sphero-cylindrical) patch, and its refractive power $P(\theta)$ along a meridian with direction θ is characterized as

$$P(\theta) = S + C\, sin^2(\alpha - \theta), \tag{3.14}$$

where S is the eye's spherical power, C is its cylindrical power, and α is the angle of the cylinder axis (THIBOS; BRADLEY, 1997). It follows that $min(P(\theta)) = S$, and $max(P(\theta)) = S + C$.

Cylindrical eye aberrations, as shown in Figure 3.8(middle), make it incredibly difficult for individuals with astigmatism to align even the most general patterns (such as a cross). Unlike the spherical case, moving two dots along the radial direction produces a spiral in their observed positions, and they may never converge. Lines aligned with the cylindrical axis (vertical axis in Figure 3.8) are collinear but lines at any other orientation do not become collinear. Since the astigmatism axis is not known a-priori, it is challenging to design patterns and their program movement for optimal alignment strategies. Allowing a 2D search, moving the pattern in the x and y axis instead of just moving closer of farther from each other, works but the process is slow, tedious, and error prone (WEBB; PENNEY; THOMPSON, 1992).

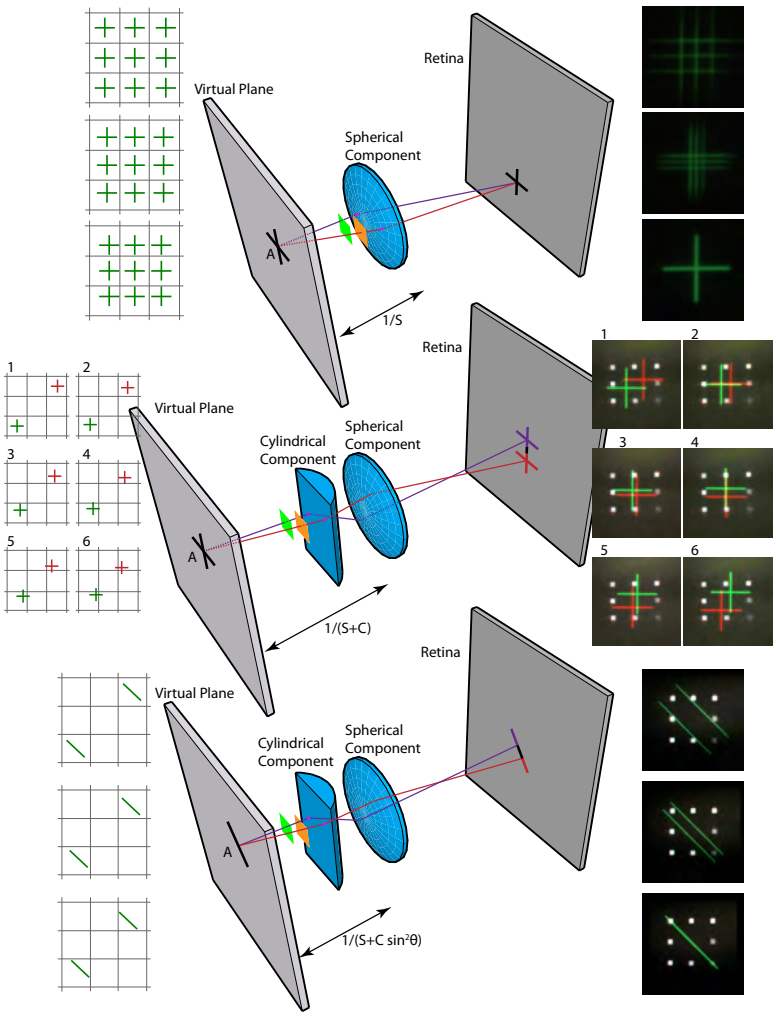

Figure 3.8: Alignment challenges in the context of astigmatism aberrations. Small images on the left show the patterns displayed on the screen as the viewer moves them closer to each other. Each cell on the grid represents the display under a pinhole/lenslet. Images on the right show how the viewer sees the respective image on left. (Top) For an eye with only spherical aberrations, the spherical power S is measured by displaying a cross pattern under the green and orange lenslets. The user then moves the patterns until they align on the retina. This alignment happens when the virtual cross A is at distance $1/S$ from the lens. Rays become parallel after passing by the spherical aberrated component of the myopic eye and naturally converge at a point. (Middle) Unfortunately, virtual points in the focal plane of the sphere-cylindrical lens at $1/(S + C)$ do not assist with alignment when cylindrical aberrations are present. Unlike in the spherical case, the cross sign centers do not necessarily meet if one simply moves them toward or away from the center. (Bottom) The solution involves moving line segments oriented perpendicular to the line joining the two lenslets. The spacing at which these lines are perceived by the user as overlapping gives the power along the corresponding meridian.

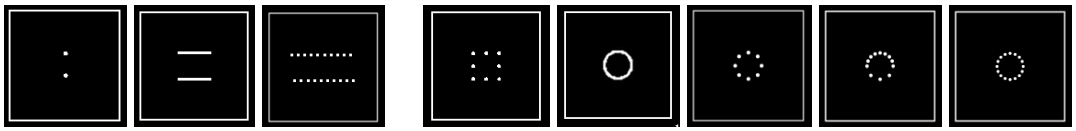

(a) (b) (c) (d) (e) (f) (g) (h)

Figure 3.9: A set of tested masks on NETRA: (a) two pinholes replicates the Scheiner test and results in the power required on the measuring meridian; (b) lines allow the user to place his eye at any part of the mask to perform the test. This mask is designed to avoid the search for patterns on screen and to avoid having a bi-ocular design with adjustable interpupillary distances; (c) dashed offsetted lines are ideal for Vernier alignment; (d) Pinholes in a square were used on the first tests for astigmatism. The test is comprised of aligning the two squares of dots, one square for each pattern on screen. (e) The circle creates a continuous but blurred circle in the retina; (f) pinholes in circle are best for the interaction procedure. Subjects easily understand the task; (g) by increasing the amount of pinholes, one can increase the accuracy for the measurements of the axis of astigmatism; (h) using more pinholes may confuse the viewer. All masks support a minimum pupil size of 2.4mm

The solution involves exposing two lenslets at a time oriented at angle θ (Figure 3.8(bottom)). Notice that a line segment placed at orientation $(\theta + \pi/2)$ only becomes collinear when the virtual image is created in the front focal plane at a distance $1/(S + C\ sin^2(\alpha - \theta))$ from the lens. The diopter at this meridian is calculated by computing the number of steps required while moving these two parallel line segments perpendicular to each other. All other line segment orientations and counted steps lead to incorrect results. By evaluating the eye's refractive errors along $\theta \in [0, \pi)$, NETRA obtains the values for the eye's S, C, and α parameters. In practice, a collection of small number of such measurements along equally-spaced meridians are used to optimize (in the least squares sense) the eye's parameters - spherical (S) and cylindrical (C) powers, as well as the axis (α) of the cylinder.

3.4.2 Choosing the Appropriate Mask

Figure 3.9 shows a set of masks used on top of the display during this thesis: (a), (b) and (c) measure in a given meridian only, a quick test to estimate spherical powers in the absence of astigmatism. (d) was the first mask for astigmatism tested on NETRA. Measured meridians are computed as a unique combination of pinhole pairs. The theoretical resolution is ± 11.5 degrees in the axis of astigmatism. Since the two patterns on screen create two squares made from eight copies of the displayed pattern (cross-talk[2]), the observer must overlap the first line of each square. (e) is designed to increase the accuracy of the axis, being able to measure virtually any meridian. However, given that this is a continuous mask - without any pinholes - the image observed by the viewer blurs. (f) has a theoretical accuracy of ± 11.5 in the axis of astigmatism with an easier training procedure than (d): touching circles instead of overlapping the first line of each square. (g) is an optimized mask to measure with ± 5.5 degrees in accuracy. (h) is a higher resolution of (f) to increase accuracy to ± 2.5 degrees.

Masks (a), (b) and (c) can rotate to test different meridians. The current rotation of the mask can be captured through a picture from the device or by mechanically inserting the testing axis. The software must align its patterns with the pinholes or lines in the mask. In a alternative implementation, the display can rotate with the mask. The software can

[2]Cross-talk is the perception of a duplication of the screen pattern created by the mask and due to the lack of ability to use only one pinhole of the mask at a time or per pattern on screen.

then use other sensors, such as accelerometers, to compute the measuring meridian. All of the measurements are executed horizontally on the screen space. In this case, one can use color channels to triple the current display resolution, increasing overall accuracy.

Figure 3.9(c) is a mask with two sequences of pinholes forming two dashed lines that have an offset by one pinhole from one line to the other. It allows the creation of Vernier tasks and super-resolution. Each point on the screen turns into a dashed line on the retina. When aligned, the dashed lines turn into a single solid line. Since lines are off-set from each other, the subject has a clear sense of the accuracy of the alignment. Small errors in the alignment are easily noticed.

Figure 3.9(g) increases accuracy for the angle of astigmatism. Using this mask, the algorithm runs as follows: (i) test at 0-degree meridian; (ii) test at 90-degree meridian; (iii) if they have difference in power less than 0.25 diopters, test at 45-degree; (iv) if they still have a difference in power less than 0.25 diopters, the subject does not have an astigmatism; (v) test at 45 plus the current axis of astigmatism; (vi) test at 56 plus the current axis of astigmatism; (vii) test at 34 plus the current axis of astigmatism; (viii) test the current axis of astigmatism. For every step, compute the best fitting procedure to discover new powers and angles of the astigmatism. For every step, measure the meridian 90 degrees away from the current meridian to balance the data making the fitting more accurate. This procedure decreases the error to around 5.5 degrees.

3.4.3 Dealing with Cross-talk

Cross-talk between microlenses or pinholes may occur when the pattern meant for one lenslet is visible through an adjacent lenslet. This produces additional images of the overlapping patterns on the viewer's retina, which might be confusing. Although one can easily build blocking walls to avoid cross-talk, NETRA addresses this problem by skipping every alternate lenslet and using carefully designed patterns and detailed interactive procedures. The pinhole mask of Figure 3.9(f) is an example of a mask designed for the interaction. It is easier to understand the alignment of circles than random pinholes, for instance. Blocking walls would decrease the overall range of corrections and require precise display-mask alignment. One may also take advantage of cross-talk by using jittered pinholes as discussed in Section 3.5.2.

Another way to remove cross-talk is to use colored masks and assign distinct colors for the mask patterns, and the figures and animations used to create the setting. Figure 3.10 shows how the crosstalk problem can be solved with these color masks. A similar idea assigns a distinct level of polarization for each feature or pinhole in the mask in such a way that the polarized light from the screen passes mostly through one feature. In this case one may need to change the polarization state of the light on the screen by adding polarizers or polarization rotors.

Chromatic aberration in the eye and microlens may produce virtual points at different depths, making the use of colored patterns difficult. However, color patterns increase the effective display resolution with reasonable success. The interaction with colored patterns is also easier to explain to users.

3.4.4 Eye-device Alignment

NETRA optics allow for the measurement of virtual points without the need to precisely align the eye with the apparatus. The center of the optical setup does not need to be aligned with the eye's optical axis. Spherical aberration is uniform on the lens and thus all light reaching the lens at the same incoming angle focus to the same spot on the focal length of the eye. Since the user may tremble or have shaky hands, light rays from points A and B on the screen can intersect with many sectors of the cornea/crystallin during a single alignment. Under spherical conditions, the distance between projected points in

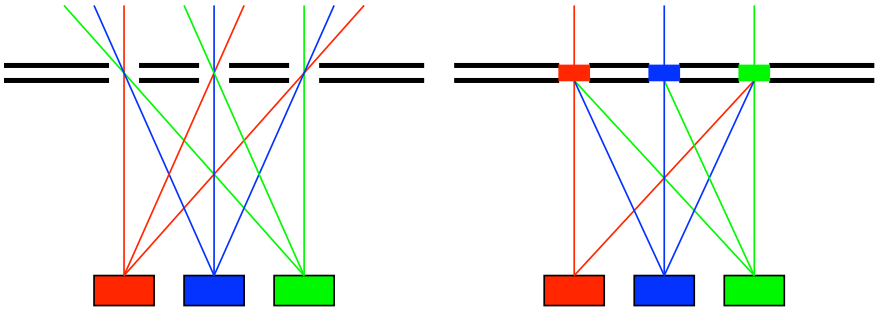

Figure 3.10: Cross-talk happens because each pinhole is assigned to only one pattern on screen. In practice, light from a pattern passes though all pinholes, creating copies of the image. By assigning color masks to each pin-hole, one can avoid the cross-talk and better control what is shown to the user.

the retina ($P_A - P_B$) remains steady if the displayed testing patterns do not move. For astigmatism, the distance ($P_A - P_B$) also remains steady if the subject does not rotate the display – keeping the measuring angle of astigmatism. Considering a cross-section of a myopic eye, a triangle with a base a and height S_2 (image plane) builds an equivalent triangle for the circle of confusion which has a base of $P_A - P_B$ and height of E - S_2, where E is the eye's axial length. $P_A - P_B$ is then

$$P_A - P_B = \frac{a(E - S_2)}{S_2} \tag{3.15}$$

for any S_2. The eye-pinhole distance t is usually very small with respect to the distance to the virtual point d, and can be safely ignored for low powers.

3.5 Measuring Accommodation Range

NETRA provides two distinct focus cues for the viewer - one at infinity due to lenslet bundles and another at a finite depth due to the overlapping of different lenslet beams. The strength of one focus cue over the other is controlled by the displayed pattern under each lenslet. The ability to switch these patterns on screen provides greater flexibility in measuring refractive errors and accommodation range.

A full exam is a two step process consisting of measurements for astigmatism and accommodation range. After the far field eyesight measurements are taken, symmetric accommodation patterns are projected along the cylindrical axis to test for presbyopia. These patterns are carefully placed to create a virtual object at the farthest point in focus for a user. As the user moves these patterns closer or further from each other, her eye refocuses to the given virtual object depth. Moving them apart assesses if the subject was at her farthest focal point and moving them closer makes the subject accommodate even more. The user indicates to the software when she no longer sees a single object which, by that point, the software has found the closest and/or farthest focal points.

NETRA assesses the closest distance in focus by moving the virtual point closer until the eye stops focusing on it. This gives a measure of the accommodation range and *presbyopia* (near-sightedness related to the aging process), where the lens has a reduced accommodation range. To control accommodation, NETRA changes the displayed pattern. While sharp patterns allow for one to move them without changing accommodation,

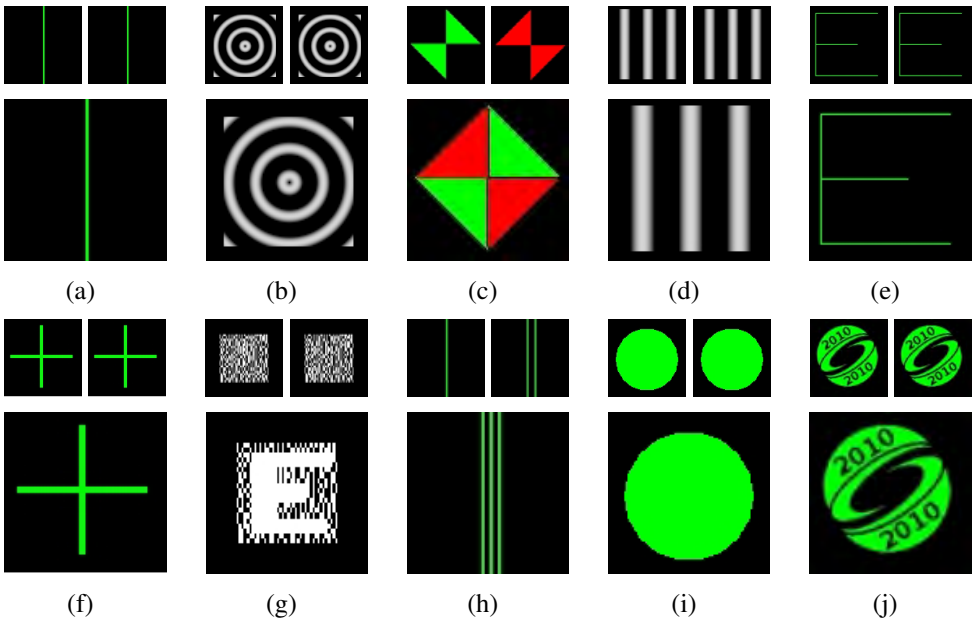

Figure 3.11: Patterns evaluated by users sorted by the standard deviation (diopters) of the differences between 18 alignments for each. For pattern, the top row shows pairs of shapes used for alignment while the bottom presents the pattern obtained after the corresponding shapes are perfectly aligned. The standard deviation of repeating the alignment several times are (the smaller the better): (a) Pair of single lines (0.10); (b) Concentric sinusoidal rings (0.13); (c) Crosshair (0.14); (d) Sinusoidal bars (0.16); (e) Letter E (0.17); (f) Cross (0.24); (g) VCS (0.26); (h) 2 lines $\times$ 1 line (0.28); (i) Circle (0.28); (j) SIGGRAPH logo (0.34).

soft blurred patterns allow for accommodation control over the eye.

3.5.1 Controlling Accommodation Far Vision Measurements

All measurements for refractive corrections (myopia, hyperopia and astigmatism) must be taken on a relaxed eye – accommodation on the farthest possible focal point. With NETRA, instead of using a distant scene or cycloplegic eye drops to suspend accommodation, one can use three main techniques: (i) lenslets with or without the pinhole mask; (ii) using a single lens on top of the pinhole pattern; or (iii) using accommodation control patterns.

Using lenslets (i), one can rely on the bundle of parallel rays coming from each lenslet to fix eye focus at infinity (for a perfect eye) or close to infinity (for a myopic eye). The bundle of collimated rays produced from each lenslet makes myopes try to focus at infinity, which is beyond their farthest focal point. The eye relaxes in the search of the best (least blurred) image. The second technique (ii) uses the same theory, but with one bigger lens and masks that do not resemble pinholes. Even though certain pinholes can be used for the alignment task, other mask shapes can be used for accommodation control at the same time the alignment is taken.

Accommodation patterns (iii) can continuously shift the virtual point away from the eye, causing the lens to adjust the focus until it is completely relaxed. This trick can operate in accommodation ranges even beyond infinity and it is not dependent on the positioning of the lenslets. Moving the virtual point any farther results in multiple overlapping images easily identified by the user. The distance at which the eye is no longer able to focus on the pattern gives farthest point of focus for myopia, hyperopia and astigmatism.

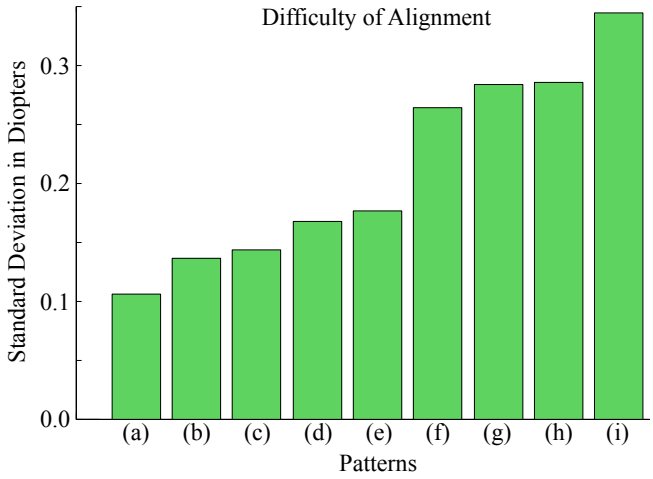

Figure 3.12: Standard deviation (in diopters) of the differences among three consecutive alignments of the same pattern for all users. The pair of single lines produce the most consistent alignments (most repeatable).

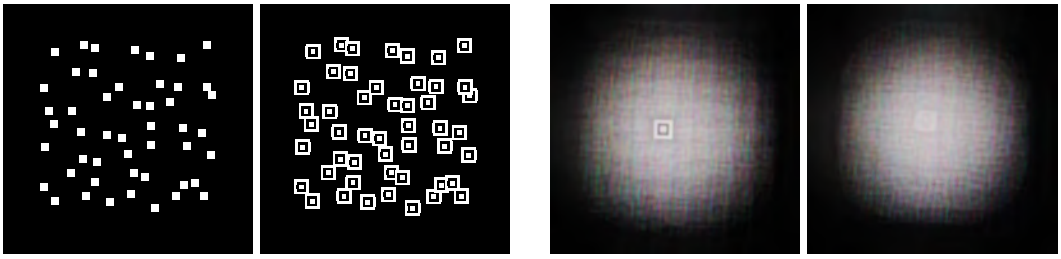

Figure 3.13: (Left) Jittered pinhole pattern (h) and corresponding display mask (p) for 0 diopters; (right) a normal eye sees a distinct pattern (g) in the middle, while a myopic eye sees a blurred image.

3.5.2 Choosing the Best Patterns

Figure 3.11 shows the functionality of various tested patterns for performing alignments on a user evaluation.

Subjects are asked to align the pairs of patterns shown in Figure 3.11 while observing them through the probe. Each pair of patterns was aligned three times by each subject. The subjects were constrained to move the patterns only horizontally (1D translation). For subjects requiring refractive correction, the experiment was performed without corrective lenses. The time subjects took to align each pattern was recorded, as well as the error (measured in diopters) between repetitions. While the average alignment time was approximately the same for all patterns (about 10 seconds), the pair of line segments produced the most consistent results in terms of repeatability (Figure 3.11(a)). In all evaluations written in this thesis, line segments are used as the pattern for measuring myopia, hyperopia and astigmatism.

3.5.2.1 Patterns for Accommodation

The eye focuses at the virtual point produced by NETRA's optical setup which uses a smooth sinusoidal pattern (Figures 3.11(b) and 3.11(d)). Such patterns are useful for measuring accommodation range and speed of accommodation, and presbyopia. The 1D sinusoid (Figure 3.11(d)) is used for the range test and symmetrically project it along the axis of the cylindrical power.

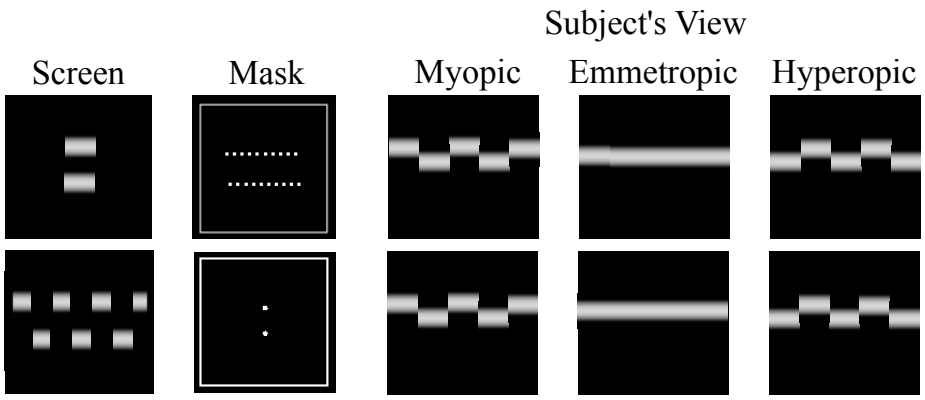

Figure 3.14: Creating super-resolution with vernier tasks. The sinusoidal patterns are dupplicated on the subject's view to allow vernier acuity. The top part uses a coded mask, while the bottom uses a traditional mask with duplicated patterns on sreen.

3.5.2.2 Hybrid Patterns

Some patterns allow for both accommodation and alignment. Smooth transitions in the pattern encourage accommodation, while sharp edges allow the user to easily judge when the images are misaligned or out of focus. An example of a pattern which enables both outcomes is a combination of the sinusoidal pattern with the line pattern. This pattern can be used to test whether the user is focusing at infinity, and to measure accommodation range. The sinusoidal pattern is displayed under several lenslets, and the lines are displayed only under the extreme lenslets; the lines overlap when the image is in focus and split when the patterns misalign.

3.5.2.3 Visual Cryptography (VCS)

Visual Cryptography patterns (NAOR; SHAMIR, 1994) rely on the human perception framework to decode information contained on them (Figure 3.11(g)). Two parts of a pattern are placed under separate lenslets with additional noise. The hidden pattern is revealed when they perfectly align. Unfortunately these patterns do not offer any indication of how far the viewer is from the alignment until it is achieved.

3.5.2.4 Jittered Patterns

The View-Master setup (Figure 3.16(right)) reduces the constraint from regularly spaced pinholes by jittering each pinhole by a small amount. The corresponding pattern behind each pinhole in the display is also jittered as shown in Figure 3.13. The jittered pattern converts the crosstalk between pinholes into random noise. This is useful when pinhole spacing is minimum (more light throughput) or the distance between the pattern to the pinhole is significant (increased power resolution) and structured crosstalk may confuse the viewer. Due to the irregular arrangement, these patterns are harder to use with microlens arrays.

Given a desired pattern, g, and a jittered pin-hole array, h, placed at distance f from pattern p, the pattern p is obtained by convolution, $p = h \otimes g$. Eye, when focused at infinity, integrates all the parallel rays into a single spot, and the intensity of the parallel ray in angular direction β is given by $h(x)p(x - f\beta)$. Thus, the generated image is given by $I(\beta) = \sum_x (h(x)p(x - f\beta)) = h \star p$, where $\star$ implies cross-correlation. Thus, $I = h \star h \otimes g$. It is clear that to present image g to a human eye, one must use a jittered pinhole pattern h, whose autocorrelation is a delta function.

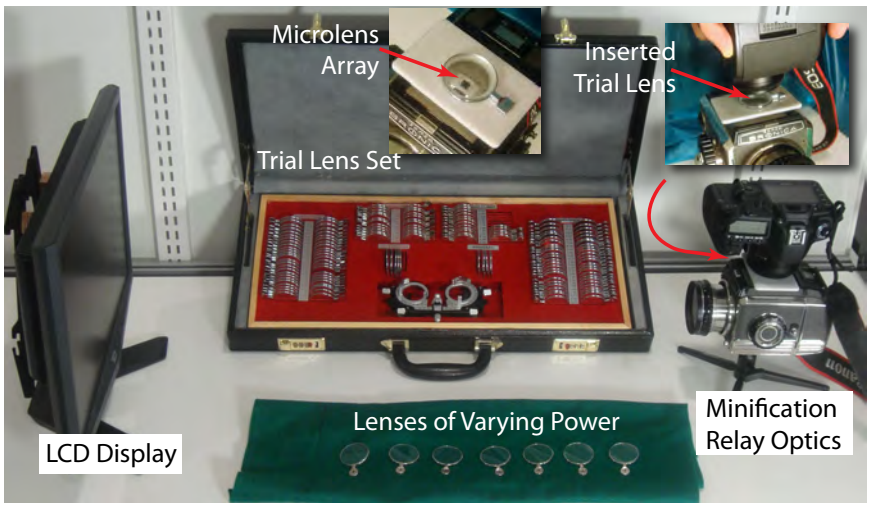

Figure 3.15: Evaluation setup and trial lens set.

3.5.2.5 *Vernier Patterns*

Vernier Patterns are lines with sinusoidal pixel intensities in width (Figure 3.14). These are drawn perpendicular to the current meridian being measured. As usual, the software draws two patterns on the screen, one behind each pinhole of the mask, and the user aligns them.

The sin pattern can be duplicated, resembling a dashed line. The pattern can be drawn duplicated on the screen (Figure 3.14(bottom)) or a dashed mask can be used to create the same effect (Figure 3.14(top)). The dashed patterns must be offset, such that they create solid sinusoidal line when overlapped.

3.5.2.6 *Super Resolution*

Super-resolution increases the accuracy of the device by allowing sub-pixel displacements of c. For instance, one can create a sinusoidal pattern with ten times more pixels than the resolution on the screen. Every ten pixel square of the pattern forms a single pixel on the screen. They can be averaged or the procedure can pick a representative pixel on the pattern to be draw. The test pattens move by 0.1 screen pixels. The pattern pixel value is averaged or picked every tenth of a displacement and the subject notices a change in the appearance of the pattern. This procedure creates super resolution that is suitable for measuring with Vernier acuity.

3.6 Prototypes and Evaluations

A few prototypes and proof-of-concept designs were developed to validate NETRA. They are described below along with their respective evaluation procedures. The collected data shows that even extremely low-cost phone clip-ons can reach accuracy below $0.5D$.

For easy of creation, the first prototype is based on an LCD screen with minimizing relay optics (Figure 3.15). This setup uses a 24" Dell 2407WFP LCD display (1920×1200 pixels) coupled with an optical minification system (factor of 1/35.8), and an array of 20×20 500-microns lenslets with a focal length of $12.5mm$ (Edmund Optics part number NT64-479). The minification system creates a virtual display of 3,320 DPI on the focal plane of the micro lenses, which is equivalent to a $7.5\mu m$ pixel-pitch display. As per Equation 3.8, $a = 3.5mm$, and $c = 0.0075 \times$ *number of displaced pixels*. An eyepiece guarantees that $t = 15mm$, giving approximately ± 0.16 diopters per displaced pixel on the LCD. This setup closely approaches to being limited by the size of the cone cells in the eye.

Figure 3.16: Three of the first prototypes: (left) cell phone, (center) high-resolution display, (right) View-Master. Variables f and a are measured in mm while D is in diopters.

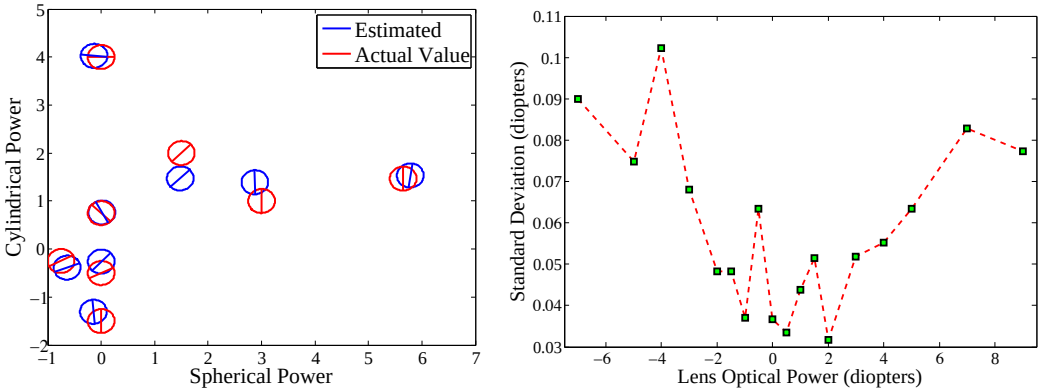

Figure 3.17: Estimating lens parameters. Left: Parameters estimated with NETRA and the actual values for several sphero-cylindrical lenses. The circles are centered at the corresponding spherical (S) and cylindrical (C) values. The line segments inside the circles are the cylindrical axes. Blue represents estimated values, and red represents actual values. Right: Standard deviation in diopters of a six round estimation of the power for a set of spherical lenses in the $[-7, 9]$ diopters range.

Several prototypes were built during the development of NETRA (Figure 3.16). They span across size and interface, but mainly screen resolution (pixels per inch). In the head-mounted display (HMD) prototype (Figure 3.16(center)), a Vuzix iWear VR 920 HMD (1806 DPI) with a 500-microns lenslet with a focal length of $12.5mm$ (Edmund Optics part number NT64-479) results in $\pm$ 0.35 diopters per displaced pixel ($a = 3.5mm$). The View-Master setup uses jittered patterns and a translating mask instead of an LCD display (Figure 3.16(right)). All cell phone setups use a Samsung Behold II (Figure 3.16(left)), which has a display of 180 DPI (or 540 DPI with three color channels in 1D), and the Google Nexus One phone, which has a display of 250 DPI (or 750 DPI with three color channels in 1D). Using a pinhole mask with a $3mm$ hole pitch and a distance $f = 20mm$, these prototypes provide approximately 0.71 diopter and 0.4 diopter per displaced pixel, respectively. The pinhole array pattern is a regular 3×3 grid where each squared pinhole has a width of $0.5mm$.

3.6.1 Controlled Evaluation

The accuracy of the evaluation prototype was measured using a camera focused at infinity with an additional lens of known power in front of it. An operator manually shifts the patterns shown through a live-view on a computer connected to the camera and finds the shift required for optimal alignment. The power of the additional lens is then compared with the computed refractive power.

Figure 3.17(left) compares the estimated results with the actual lens parameters for a set of sphero-cylindrical lenses. The circles are centered at the corresponding spher-

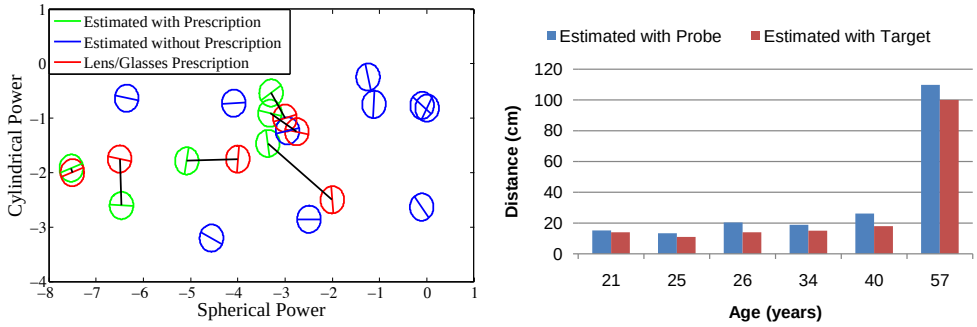

Figure 3.18: User evaluation. Left: Refractive errors estimated for several subjects using NETRA. Green represents estimated values for subjects with known prescription, which are shown in red and connect to the corresponding estimates by a line segment. Blue shows measurements made with NETRA system for patients with unknown prescriptions. Right: Closest focal distance (in cm) estimated for a group of subjects of different ages estimated using both NETRA (blue) and a reading target (red).

ical (S) and cylindrical (C) power values. The line segments inside the circles are the cylindrical axes. For this experiment, the average absolute errors for the spherical power, cylindrical power, and cylindrical axis were 0.09 diopters (standard deviation $\sigma = 0.056$ diopters), 0.23 diopters ($\sigma = 0.19$ diopters), and 8.43 degrees ($\sigma = 6.16$ degrees), respectively. Figure 3.17(right) shows the absolute errors in the measurements performed during six rounds of estimating the power for a set of spherical lenses in the $[-7, 9]$ diopters range.

3.6.2 Prescription-Matching User Evaluation

A group of 13 volunteers (ages 21 to 57) evaluated the first prototype (Figure 3.15). For each subject, the software estimates their spherical (S) and cylindrical (C) refractive errors, as well as the corresponding cylindrical axis (α). Figure 3.18(left) shows the estimated refractive error for each volunteer. The blue and green circles represent the results obtained with NETRA. The values estimated for subjects with known prescriptions are shown in green. Red circles indicate the actual prescriptions, and are connected to the corresponding estimated values with a line segment. For subjects with known prescriptions, there are results for both eyes. For the others, only the results for one eye are displayed. The small line segments inside the circles represent the orientations of the cylindrical axis. The estimated values using NETRA are reasonably close to the actual prescriptions. The average absolute error from the known prescriptions were under 0.5 diopter ($\sigma = 0.2$) for both cylindrical and spherical powers. The average absolute error of NETRA's estimates of the cylindrical axis was under 6 degrees. The differences between NETRA and the actual prescriptions possibly results from imperfect calibration and other physical limitations of the prototype, inadequate directions to the volunteers on how to interact with the proposed system, and subject exhaustion during the experiment. Also, while optometrists use some methods which could hinder accuracy, such as prescribing in multiples of 0.25 diopter, and 10 degrees axis, they also have the opportunity to incorporate subjective factors such as patients' comfort level and age before making the final prescription. The prescription for glasses is sometimes under-corrected in 0.5 diopter in comparison to contact lenses. Thus, the automatically estimated corrections do not necessarily match optometrists' prescriptions exactly.

Deviations in the actual spacing between the eyeball and the probe from the assumed value of $t = 15mm$ can introduce a small variation in the recovered power. Higher powers are more sensitive to these variations in t. For instance, a deviation in t of $\pm 10mm$ results in an absolute variation of zero for a perfect eye focused at infinity, a variation as small

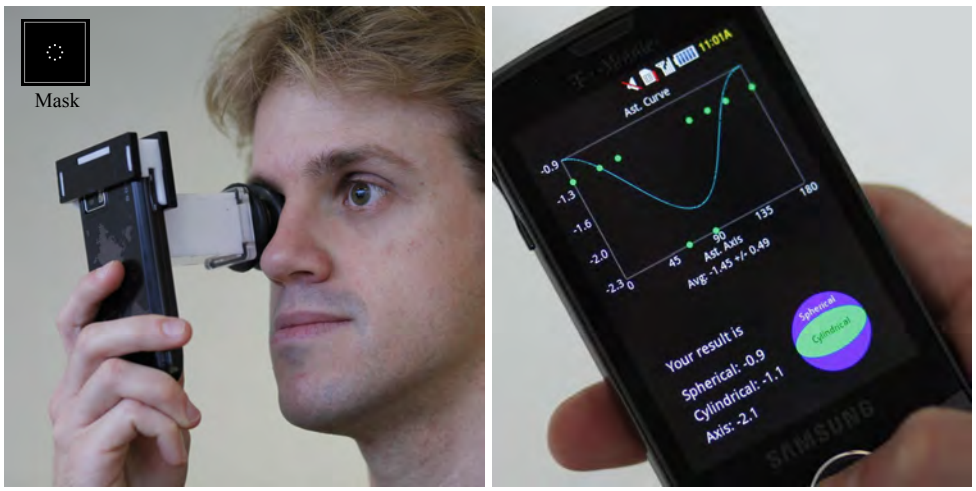

Figure 3.19: Cell phone prototype and mask used in all cycloplegic clinical evaluations.

as 0.1 diopter for an eye with power ± 3 diopters, and a variation about 0.5 diopter for an eye with power ± 7 diopters. These variations are not very critical though; as shown in Figure 3.18, even people with power as high as -8 diopters obtained accurate results with NETRA's prototype.

3.6.3 Eye Accommodation Range Evaluation

The closest focal distance of an eye was measured using NETRA and then compared with ground measurements. According to previous experiments, sinusoidal patterns are the most appropriate for inducing accommodation changes. Therefore, the NETRA system projects a $1D$ sinusoid along the axis of the cylindrical power for those with an astigmatism. Patterns containing only sharp edges were not very effective for inducing changes in accommodation states when viewed through the eyepiece. These findings seem to be supported by findings in the opthalmology literature (DAY et al., 2009) which show that square waves of any spatial frequencies could not cause changes in accommodation micro-fluctuations. On the other hand, sine waves both at small and large spatial frequencies can induce significant changes in accommodation micro-fluctuations. NETRA projects a sinusoidal pattern at various distances, ranging from the already measured farthest focusing point to the closest one. Subjects were asked to let the eye focus on the pattern. Accommodation occurred almost automatically. An object falling outside a subject's accommodation range perceived as a blurred image. Figure 3.18(right) shows the closest distances at which a group of subjects with various ages (21 to 57) could focus at, and the corresponding distances estimated using a reading target. During the user evaluation, 2 of the 13 test subjects experienced difficulties in changing accommodation with the patterns being used. Thus, further research is required to identify intelligent patterns that can induce accommodation changes in those individuals. All procedures were executed at the MIT Media Lab in Cambridge, USA and no ophthalmologists or optometrists were involved.

In a similar evaluation, the subjects' accommodation range was determined using the sliding transparent masks prototype (Figure 3.16(right)), but with a wider range of diopter values. Starting at $+5$ diopters and going all the way up to -10 diopters, each subject was asked to identify for which diopter value (s)he could clearly see a small light square with a black dot in the center (Figure 3.13). Although the author's experience reveals that the approach works for spherical cases, time requirements and low priorities have prevented a careful data collection and thus data analysis was compromised.

3.6.4 Phone Prototype and In-house Prescription-Matching User Evaluation

A Samsung Behold II prototype (Figure 3.19) was compared with current user's prescription data. The phone display has 180 DPI or 540 DPI with three color channels in 1D (Figure 3.16(a)). A pinhole mask with a pitch of $2mm$ and diameter of $0.25mm$ at a distance of $f = 60mm$ and $t = 15mm$ was used. This provided approximately 1.2 diopters per displaced pixel. A grid of 8 pinholes (3×3 grid without the central one) was used to test 8 meridians for the astigmatism case.

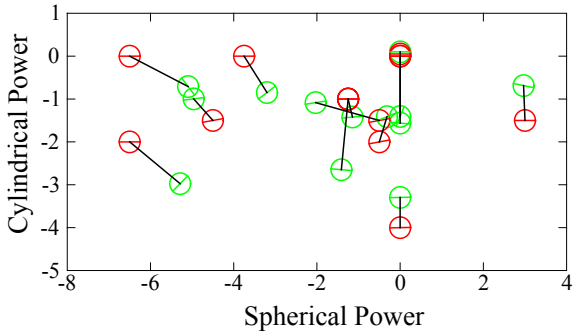

Figure 3.20: User evaluations of the cell phone prototype. Refractive errors are estimated for 13 eyes. Green represents estimated values for subjects with known prescriptions. Current subject prescriptions are shown in red and are connected to their corresponding NETRA estimates by a line segment. The angle of the circle's central line is the angle of astigmatism.

This prototype was tested on 13 eyes (ages 19 to 30) and the results were compared against the subjects' current prescriptions. For this experiment, the mean absolute error was $0.49D$ ($\sigma = 0.08$D) for spherical correction, 0.67 ($\sigma = 0.029$D) for cylindrical correction, and 9.17 ($\sigma = 0.75$) for the axis of astigmatism. The mean absolute error of the spherical equivalent ($S_{eq} = S + C/2$) was 0.55 diopters ($\sigma = 0.02$D). Figure 3.20 shows detailed results. No eye drops for relaxing accommodation were used. Instead, the subjects were instructed to look at far objects in the beginning of each meridian test. Intriguingly, the error was smaller on non-dominant eyes: $S_{eq} = 0.36$ diopters ($\sigma = 0.007$D). This could be due to the dominant eye being more efficient at stabilizing accommodation. All procedures were executed at the MIT Media Lab in Cambridge, MA, USA without the involvement of ophthalmologists or optometrists(PAMPLONA et al., 2010a).

3.7 Smartphone Prototype Clinical Trials

Results from the cell-phone prototype (Figure 3.19) were compared with methods used in current practices, including the opthalmology gold standard, during three clinical trials in three different countries. These trials were conducted independently and executed by different researchers. All of them had on-the-ground ophthalmologists and optometrists and were approved by the internal review boards at each university/hospital, and followed the Declaration of Helsinki.

3.7.1 User Evaluation Procedures and Software

The application starts with colored lines on the screen (Figure 3.22(left)). The administrator of the test plugs the clip-on and looks through the eye piece. He sees eight lines for each color (Figure 3.21). DOWN and UP buttons (LEFT and RIGHT have similar behaviors) move the eight lines towards or away from each other. The MIDDLE button changes the measurement angle. The alignment task is composed of sixteen tests in eight

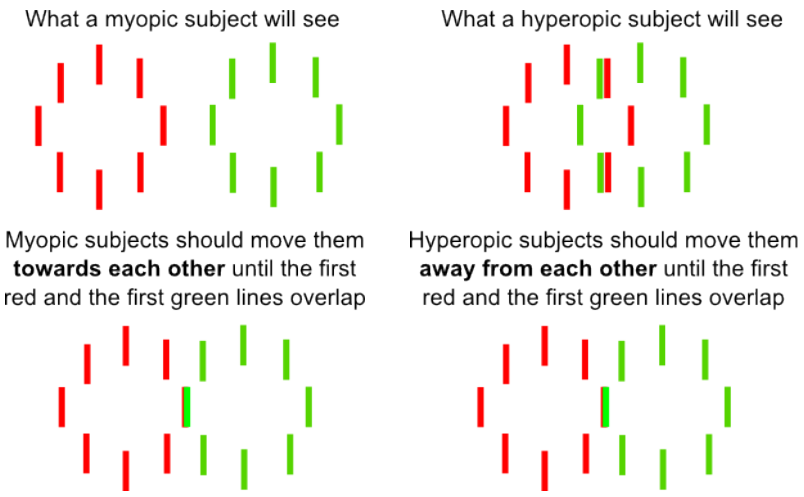

Figure 3.21: What a myopic (left) and hyperopic (right) individual sees through the eye piece. Their task is to make the circles touch. This illustration is shown to the patient in a training session before the test.

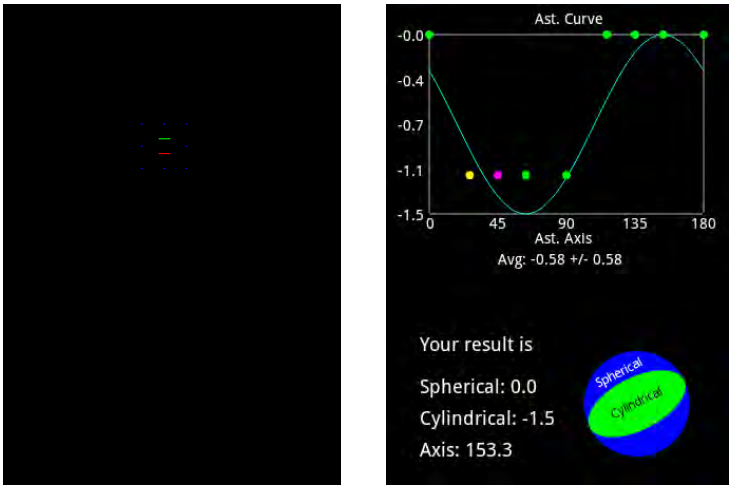

Figure 3.22: Lines presented without the eye-piece onto the phone and the phone's resulting screen. The lines are aligned with the mask used. The top part of the results screen shows a chart of the refractive error per angle of measurement. A best fitting procedure plots the sinusoidal curve. On the bottom part, an estimation for the subject's prescription.

angles and the cell phone vibrates when they are completed. Although the test ends when the cell phone vibrates, this does not finish the application. The patient can go one more round to check to see if everything is aligned.

When the subject finishes the test (cell phone vibrates), the cell phone is returned to the administrator. He presses MENU to compute the results and removes the eye piece. The results appear after the best fitting processing over Equation 3.14 (usually takes 2 seconds). The result screen shows a chart of the measured values for each angle, an estimated prescription and a small drawing showing what the subject's eye looks like. Each dot on the chart represents a measured value. Figure 3.22(right) shows 4 readings needing 0 diopters of correction and 4 readings around -1.1 diopters. Negative values signify myopia while positive ones signify hyperopia. The dot color represents the strength of each measurement. Green dots reflect that there was no doubt when the patient tried to touch circles. Yellow and magenta show low and high imprecision respectively. Doubt is shown in situations when the patient does not know which position is the best alignment for the meridian. As the less precise data points, magenta and yellow dots are less reliable

than green ones for the fitting curve. The prescription estimation is based on the best fitting curve over the data collected. On Figure 3.22, the subject does not have myopia or hyperopia (Spherical = $0D$) but has an astigmatism of $-1.5D$ in an angle of 153 degrees. The software does not round the results to steps of 0.25 diopters and angles of 1 degree.

Before the measurements, the patient undergoes a training section. With the subject seated, the administrator explains the measurement procedure walking through a digital tutorial on the phone. Administrators are instructed to do the following:

- Go to the first page of the digital tutorial and say: "First of all, I will attach this plastic piece on the cell phone and you will look inside it. Placing it very close to the eye."

- Change to page 3 of the digital tutorial (patterns) and say: "When you look inside, you will see these groups of green and red lines (pointing to the screen). Your task is to align or overlap the first green and the first red lines that you see. Use UP and DOWN buttons to move the lines in order to align them. Do not align all of the lines, only the first green and the first red that you see there." Press the RIGHT button on the keypad of the phone to go on the tutorial and show them how the alignment will occur.

- Say: "When the alignment is done, the color of the aligned line can change to yellow. You must press the MIDDLE button to change the angle of alignment and start aligning again. You will perform this alignment 16 times. Before starting each alignment, you should open the idle eye, relax for a few seconds, close the eye and start aligning the lines. The cell phone will vibrate when you finish the test."

- Give the device to the patient and ask him to find the circles. Don't worry if it takes a while for them to find the lines. This is typical. The angle at which they look into the device changes what they see.

- Now that they have the device, explain again. Tell them that they can move the lines by pressing the UP and DOWN buttons on the phone and they can change the angle pressing the MIDDLE button. Let them practice for up to 5 minutes.

The examinations begin immediately following the training section. The most common question at this stage is whether the lines should be on top of each other or just barely touching (side-by-side). Subjects must be instructed to place them on top of each other as best as they can. The subjects for our experiment provided free and informed consent, and the studies were approved by the Institutional Review Board of every partner institution.

3.7.2 American Subjective-Refraction-Matching Clinical Trial

In this study, refractive errors are estimated for 14 eyes (6 astigmatic) using the Samsung Behold II cell phone prototype and compared with Subjective Refraction (SR). All procedures were executed at the MIT Media Lab in Cambridge, USA [3]. Patients were instructed by the inventors of the system on how to use NETRA. A non-inventor optometrist took their Subjective Refraction using a trial set of lenses and a standard Snellen chart. Inventors, doctors, and subjects did not exchange measure information during the test so as not to bias measurements.

The experiment was conducted in two rounds with two clip-ons: (i) using a $a = 2.4mm$ pinhole mask with no cycloplegia (dry); and (ii) a $a = 4mm$ pinhole mask clip-on with cycloplegia (wet - tropicamide 1%, phenylephrine 2.5%, and cyclopentolate 1%).

[3] Collaboration with Vicki Chen, Nicole Quinn, Yos Priestley, Jay Duker, Jordana F Goren and Mitchell B Strominger from Tufts University and New England College of Optometry.

Cycloplegia dilates the pupil and thus a, which is limited by pupil size, can be bigger when eyes are cyclopleged. Each pixel shift results in $\approx 1D$ for the 2.4mm mask and in $\approx 0.6D$ for the $4.0mm$ mask. For the dry procedure, subjects were asked to take the test with both eyes opened while looking at a gray wall ≈ 7 meters away in order to handle accommodation and relax their eyes. Procedures were executed in this sequence: SR dry, NETRA dry, SR wet and NETRA wet.

Table 3.1 and Figure 3.23 compare results from the experiment. NETRA measurements are repeated twice per person. Average absolute difference was 0.30D ($\sigma = 0.39$D) for the spherical component of the prescription. Repeatability was 0.32D ($\sigma = 0.43$D) for dry tests and 0.21D ($\sigma = 0.32$D) for wet tests. The NETRA did not deliver accurate measurements for dry tests on this experiment. Figure 3.23(red line) intersects Y at $-1.66D$, meaning that most subjects accommodated on NETRA. Figure 3.24 shows raw data for all subjects of this test. Surprisingly, the measurements for wet NETRA are better correlated with dry refraction than to wet refraction. Another intriguing result is the difference between the cylindrical component for wet and dry. Although cylinder is not affected by cycloplegia, their mean absolute errors are 0.25D ($\sigma = 0.35$D) for subjective refraction, 0.43D ($\sigma = 0.28$D) for NETRA between wet and dry tests.

The best fitted trending line between wet SR and wet NETRA (orthogonal linear regression: $NETRA = m * Subjetive + b$) on spherical values (Figure 3.23(blue)) had a constant bias of $b = -0.44D$ and a slope of $m = 0.76$, which means that NETRA was overcorrecting. In the best scenario $b = 0$ and $m = 1$. This variation can be treated as an unknown shift on the computed NETRA values. Thus, the linear equation that can take NETRA readings as close as possible to the measured Subjective Refraction of this experiment is

$$NETRA_{improved} = \frac{NETRA_{current} + 0.44}{0.76} \tag{3.16}$$

Then the absolute average difference of $NETRA_{improved}$ and Subject Refraction is 0.27D ($\sigma = 0.26$D), Which means that the readings may have an error between $0D$ and $0.53D$ for 68% of the cases. In this case, the correlation is 0.98 and T-test probability is 1.00, which means the difference is unlikely to be smaller than 0.27, an expected value

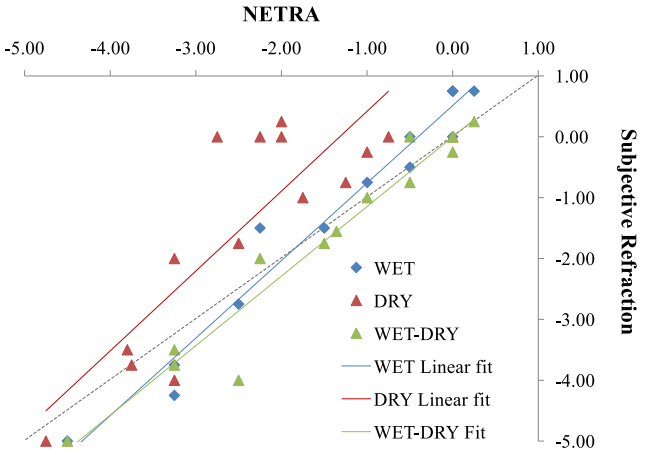

Figure 3.23: Spherical values for NETRA vs Subjective Refraction for Dry and Wet cases. The dashed line represents the ideal case. NETRA clearly takes advantage of cycloplegic drops to relax accommodation. Asking subjects to look at a wall 6 meters away reduces accommodation (by experience, results are usually $4D$ off if the test is taken without any method to relax the eye). Lines are linearly fitted in a least squares sense. A comparison of wet NETRA with dry subjective refraction (WET-DRY) achieves the closest matching for an ideal case.

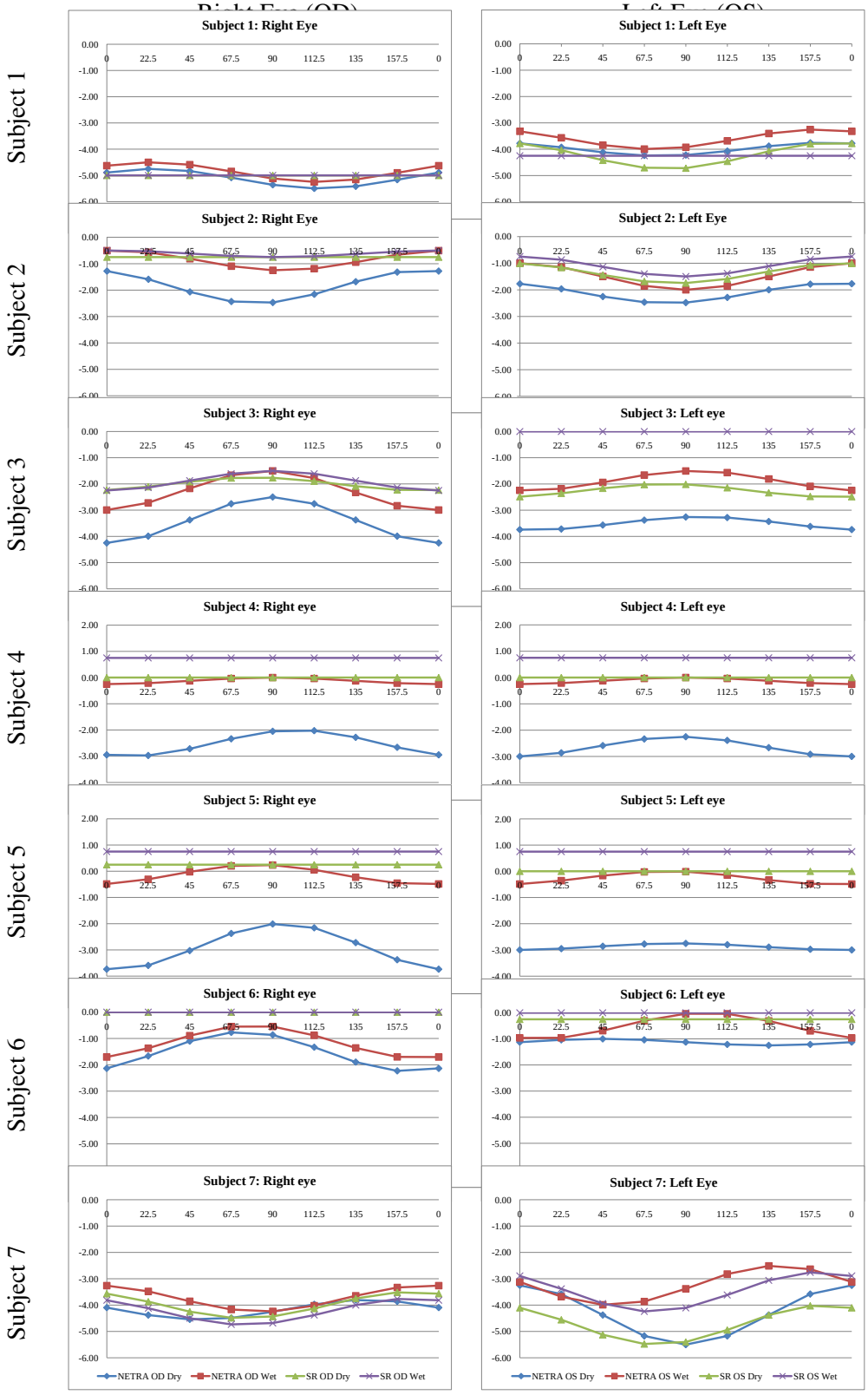

Figure 3.24: Optical correction (y-axis) by measured meridian (x-axis) comparing NETRA with Subjective Refraction. The resolution of $0.6D$ per pixel shifted on the screen makes NETRA very susceptible to errors on emmetropes. Notice how the angle of astigmatism matches in all readings.

Comparison	Sph. ($n = 14$)	Cyl. ($n = 6$)	Axis ($n = 6$)	Sph. Eq. ($n = 14$)
Wet-Wet Mean Abs Error	0.46 ± 0.32	0.25 ± 0.32	9.17 ± 8.59	0.61 ± 0.31
Wet-Wet Correlation (r)	0.98	0.65	0.46	0.98
Wet-Wet T-Test (P)	0.36	0.11	0.29	0.023
Wet-Wet Significant Diff.	No	No	No	Yes
Dry-Dry Mean Abs Error	1.09 ± 0.87	0.46 ± 0.49	12.65 ± 7.81	1.35 ± 1.04
Dry-Dry Correlation (r)	0.84	0.45	0.25	0.85
Dry-Dry T-Test (P)	0.004	0.47	0.35	0.001
Dry-Dry Significant Diff.	Yes	No	No	Yes
Wet-Dry Mean Abs Error	0.30 ± 0.39	0.29 ± 0.37	9.33 ± 8.07	0.40 ± 0.42
Wet-Dry Correlation (r)	0.97	0.29	0.22	0.96
Wet-Dry T-Test (P)	0.14	0.29	0.32	0.78
Wet-Dry Significant Diff.	No	No	No	No

Table 3.1: NETRA vs Subjective Refraction for Wet NETRA with Wet SR, Dry NETRA with Dry SR, and Wet NETRA with Dry SR. The convergence clue of opening both eyes and looking straight ahead to the wall while taking the test helps, but cycloplegic (WET) results are significantly better. Dry results may also be affected by the radius of the pinhole mask that was 60% smaller in radius than on the wet test, providing only 60% of the WET resolution. Green cells highlight when NETRA closely matches other methods, while red cells highlight cases for improvement.

since the step is $0.6D$ and thus uncertainty is $\pm 0.3D$.

3.7.3 Indian Retinoscopy-Matching Clinical Trial

This trial was conducted at the L.V. Prasad Eye Institute in Hyderabad, India without inventors present[4]. Refractive errors were estimated using the cell phone prototype with a $2.4mm$ pinhole mask. Captured data was compared with measurements taken by Retinoscopy and Auto-Refractors. In this study, cycloplegic spherical refractive errors of the dominant eye of 29 adults (mean + SD age: 23.1 ± 2.6yrs), with best-corrected visual acuity of $20/20$, were measured three times using NETRA and then were averaged. The

[4]Collaboration with Veerendranath Pesala, Sangeetha Srinivasan, Ethan Solomon and Shrikant Bharadwaj from Hyderabad Eye Research Foundation, Bausch and Lomb School of Optometry, Prasad Eye Institute, and MIT Media Lab

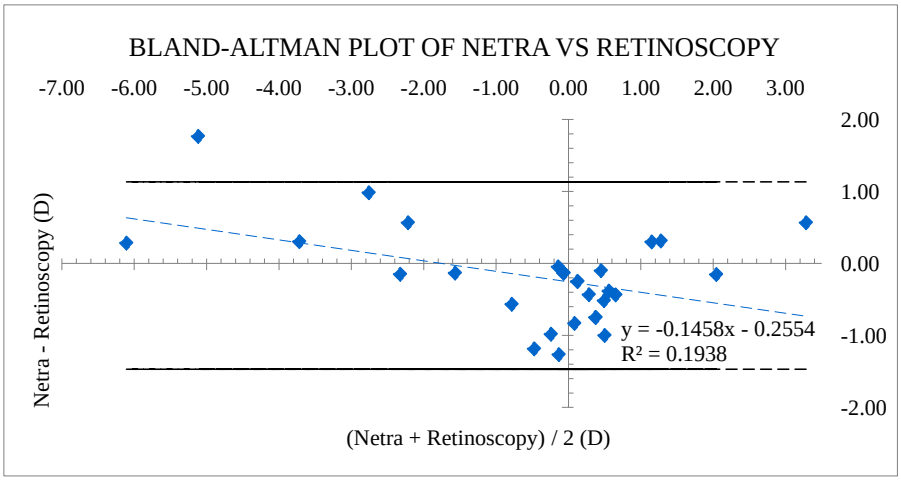

Figure 3.25: Bland-Altman chart of NETRA VS Retinoscopy. Data captured using a 1D-resolution cell phone prototype.

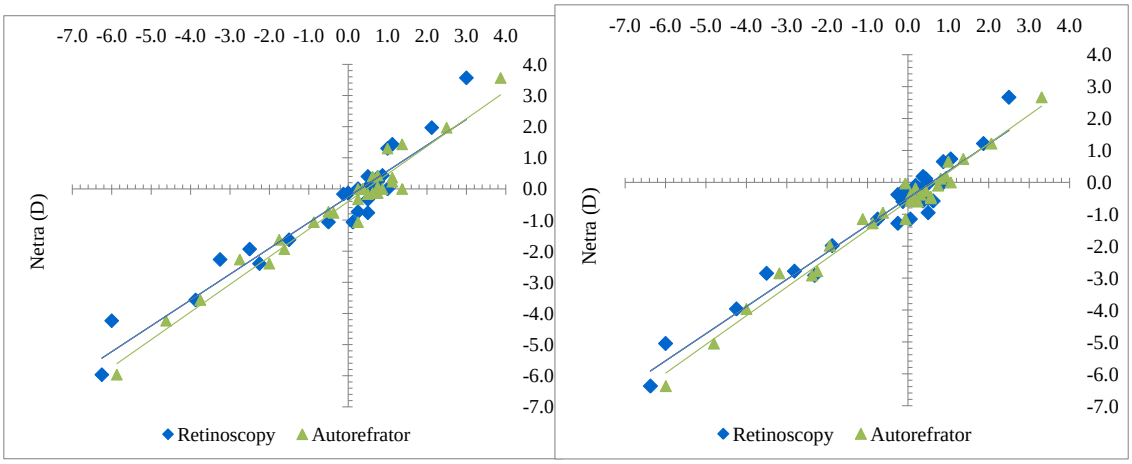

(a) Spherical Only (b) Spherical Equivalent

Figure 3.26: (a) NETRA vs Retinoscopy (blue) vs Auto-refractor (green) for spherical powers and (b) spherical equivalents. Data captured using a 1D-resolution cell phone prototype.

spherical equivalent of the same eye is also determined using objective retinoscopy performed by an experienced optometrist. Cycloplegic refractive errors of subjects ranged from -6.25D to $+3.00$D.

Refraction determined by NETRA correlated strongly with that of objective retinoscopy ($r = 0.96$) and the variation between the two measures was not statistically different ($p = 0.14$) (Figure 3.25). Orthogonal linear regression fit to the plot of NETRA against retinoscopy had a slope of $m = 0.86$ and a y-intercept of $b = -0.22$D (Figure 3.26). These values were close to the US-based test (Section 3.7.2). More results are shown on Table 3.2. Average absolute errors were $0.54D$ for NETRA vs Retinoscopy and 0.49**D** for NETRA vs Auto-Refractor. Repeatability for the three measures determined by NETRA across all subjects was 0.18**D** ($\sigma = 0.15$D) for spherical and 0.26 ($\sigma = 0.20$D) for cylindrical. Each pixel shift on this prototype was equivalent to ≈ 1D. When compared to objective retinoscopy, NETRA slightly underestimated the myopic and hyperopic cycloplegic refractive errors and had a small myopic offset of 0.22D (PESALA et al., 2011).

Applying Equation 3.16, the absolute average difference between NETRA and Retinoscopy grows to 0.60 ($\sigma = 0.48$D) and between NETRA and Auto-Refractors it drops to 0.46D ($\sigma = 0.41$D). In the same way, applying $m = 0.86, b = -0.22$ to the previous US-based experiment data, the wet-wet spherical comparison drops to 0.32D ($\sigma = 0.26$D).

3.7.4 Brazilian Auto-Refractor-Matching Clinical Trial

For this cross-sectional study, patients were examined from May to August 2011 at the Hospital Nossa Senhora da Conceição, Porto Alegre, Brazil with the help of inventors [5]. 16 volunteers (29 eyes - mean + SD age: 30 ± 11 yrs) with ages from 14 to 61 with best-corrected visual acuity of $20/40$ tested cycloplegic NETRA. Cycloplegic refractive errors of subjects ranged from -3.75D to $+1.25$D. Captured data was compared with Auto-Refractors (Topcon RM8800). Average absolute error is $0.64D$ ($\sigma = 0.39$D) for spherical, $0.59D$ ($\sigma = 0.64$D) for cylindrical and 27.19 degrees ($\sigma = 23.86$) for axis of astigmatism.

After a complete eye examination, patients underwent dry (non-cycloplegic) and wet (cycloplegic) data capture (in that order) using auto-refraction and NETRA for each eye

[5] Collaboration with Gabriela Unchalo Eckert, Martha Lang, Patricia Ioschpe Gus and Anelise Dutra Wallau from Grupo Conceição

Comparison	Sph. ($n = 29$)	Cyl. ($n = 29$)	Axis ($n = 24$)	Sph. Eq. ($n = 29$)
Ret-NET Mean Abs Error	0.54 ± 0.42	0.58 ± 0.42	29.06 ± 26.56	0.55 ± 0.40
Ret-NET Correlation (r)	0.96	0.24	0.83	0.97
Ret-NET T-Test (P)	0.14	0.000	0.998	0.000
Ret-NET Significant Diff.	No	Yes	No	Yes
AR-NET Mean Abs Error	0.49 ± 0.34	0.49 ± 0.37	35.91 ± 33.65	0.54 ± 0.36
AR-NET Correlation (r)	0.98	0.31	0.77	0.99
AR-NET T-Test (P)	0.00	0.005	0.965	0.000
AR-NET Significant Diff.	Yes	Yes	No	Yes
Ret-AR Mean Abs Error	0.43 ± 0.31	0.30 ± 0.19	20.92 ± 22.36	0.40 ± 0.29
Ret-AR Correlation (r)	0.97	0.48	0.93	0.97
Ret-AR T-Test (P)	0.038	0.036	0.019	0.000
Ret-AR Significant Diff.	Yes	Yes	Yes	Yes

Table 3.2: NETRA under cycloplegia vs Retinoscopy vs Auto-Refractor. Since the masks were smaller ($a = 2.4mm$), resolution was also smaller ($\approx 1D$/pixel). Thus a bigger average absolute error is expected when compared to Table 3.1. Even with a bigger step size, NETRA reaches an average error close to that of Retinoscopy vs Autorefractor. Green cells highlight when NETRA closely matches other methods, while red cells highlight cases to improve.

condition in a random order. 2 drops of tropicamine were instilled within 5 minutes and test was finished about 25 minutes after the last drop.

Refraction determined by NETRA is correlated more with auto-refractors ($r = 0.98$) than with subjective refraction ($r = 0.85$). However, NETRA is significantly different from Auto-Refractors ($p = 0.00$) and not significantly different from subjective refraction. Figure 3.27 (left) compares cycloplegic NETRA with two readings of Auto-Retractors (AR1 and AR2). Figure 3.27 (right) shows no significant variability among accuracy of the young and elderly. The dashed line represents the ideal case. Although these results are about $0.5D$ bigger than what is ideally desired ($0.15D \pm 0.15$, since lenses come in steps of 0.25 diopters), the comparison of Auto-Refractors with Subjective Evaluation is also high 0.71D ($\sigma = 0.45$D) (Table 3.3).

The orthogonal linear regression fit to the plot of NETRA had a slope of $m = 1.02$ and a y-intercept of $b = 0.12$D for subjective refraction, $m = 1.17$ and $b = -0.53$D for auto-refractor 1, and $m = 1.2$ and $b = -0.46$D for auto-refractor 2. Applying Equation 3.16, the absolute average difference between NETRA and Subjective Refraction drops to 0.39D ($\sigma = 0.98$D) and between NETRA and Auto-Refractors grows to 0.86D ($\sigma = 0.65$D).

3.7.5 Conclusion

These three studies all demonstrated that NETRA's measurements were very much in agreement with other current examinations of patients under cycloplegia. NETRA could measure cycloplegic subjective refraction within a 1 diopter of spherical equivalent difference from auto-refraction and 0.5D spherical difference from subjective refractions. Due to accommodation, this version of NETRA lacks precision in determining refractive errors in dynamic examination. With assessment and adjustments of the accommodation issues, NETRA has good potential of becoming an inexpensive, simple, and portable alternative for assessing refractive errors.

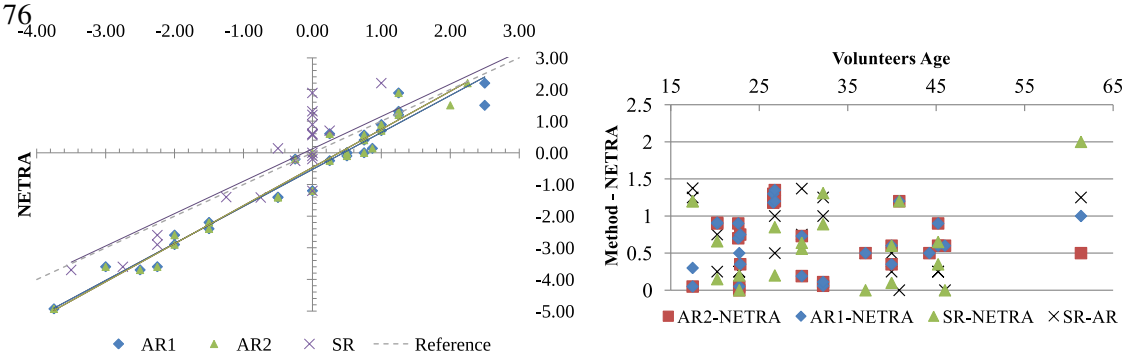

Figure 3.27: (left) Cycloplegic NETRA against two readings of auto-refractors (AR1 and AR2) and subjective refraction (SR). The dashed line represents the ideal result for the experiment. (right) The difference between methods in a function of age. No correlation between accuracy and age was found: $r = 0.15$, $r = 0.08$, $r = 0.13$, $r = -0.23$ for accuracy of AR1-NETRA, AR2-NETRA, SR-NETRA and SR-AR respectively. This suggests that NETRA is not generation-y limited.

Comparison	Sph. ($n = 29$)	Cyl. ($n = 29$)	Axis ($n = 21$)
AR1-NET Mean Abs Error	0.64 ± 0.39	0.59 ± 0.64	27.19 ± 23.86
AR1-NET Correlation (r)	0.98	0.43	0.88
AR1-NET T-Test (P)	0.00	0.001	0.67
AR1-NET Significant Diff.	Yes	Yes	No
AR2-NET Mean Abs Error	0.60 ± 0.41	0.61 ± 0.63	27.35 ± 24.58
AR2-NET Correlation (r)	0.98	0.44	0.89
AR2-NET T-Test (P)	0.00	0.001	0.604
AR2-NET Significant Diff.	Yes	Yes	No
SR-NET Mean Abs Error	0.72 ± 0.58	0.61 ± 0.48	21.71 ± 21.70
SR-NET Correlation (r)	0.85	0.68	0.92
SR-NET T-Test (P)	0.58	0.001	0.23
SR-NET Significant Diff.	No	Yes	No
AR1-SR Mean Abs Error	0.71 ± 0.45	0.21 ± 0.24	24.29 ± 38.24
AR1-SR Correlation (r)	0.91	0.94	0.92
AR1-SR T-Test (P)	0.00	0.06	0.22
AR1-SR Significant Diff.	Yes	No	No

Table 3.3: NETRA under cycloplegia vs Auto-Refractor vs Subjective Refraction. Notice that the absolute average error of an auto-refractor compared with subjective evaluation is as high as any other. Green cells highlight when NETRA closely matches other methods, while red cells highlight cases to improve.

3.8 Optical Solutions for Accommodation Control

Methods for relaxing the crystalline lens while assessing refractive aberrations through NETRA are key for the practical usage of the device. Optical relaxation channels can be built on top of the testing channel to make the eye focus as far as possible. Since accommodation, convergence and pupil light reflex of both eyes are under the control of the Edinger-Westphal nucleus, the relaxation stimulus can be targeted to the any of the viewer's eyes that other eye will follow. Also, convergence in general rules accommodation (MADDOX, 1886). As the viewer converge his eyes to a given depth, the accommodation of both eyes will follow and focus at the same point. By making the viewer look straight, converging at infinity, his accommodation will relax to focus as close to infinity as possible.

On NETRA, the optical relaxation channel in a monocular design uses a beam splitter

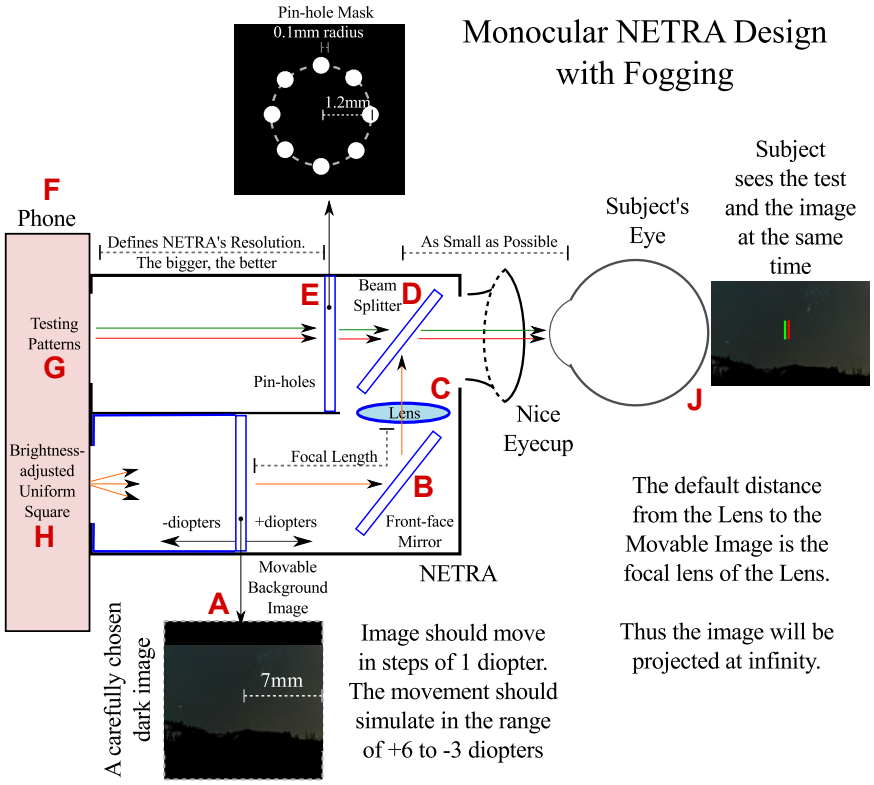

Figure 3.28: NETRA h-shaped design with eye relaxation technique. Two light paths, the former for the test and the latter for fogging, are blended into the retina. The design includes a steady or movable relaxation image (A), a mirror (B), a beam splitter (C) and lens (D). The NETRA mask is placed on (E) and the display (F) is placed on the back. (G) is the available area on the phone to show the test and (H) is the area which shows a pattern to illuminate the film (A). In this example, the subject's eye (J) sees the test (green arrows) with the film (A), that comes from the eye relaxation path (red arrows), as a background. (A) is positioned the close depth of one focal length away from (C). As (A) moves closer to (B), the subject focuses closer (accommodates). If (A) moves away from (B), the subject focuses far (relaxing the eye). Fogging image is printed on a transparency, allowing the screen to control its brightness (H).

to fuse the testing and relaxation stimulus before reaching the testing eye (Figure 3.28). In a bi-ocular setup, the optical relaxation stimulus targets the idle eye (Figure 3.36(a)). The testing and relaxation stimulus are fused by using stereoscopy. Convergence cues from stereo images can also help the viewer to relax his eyes. Since the testing eye observes images through a pinhole-based mask, everything is in focus and the accommodation fluctuates (ONG, 1968). As the idle eye is being stimulated to relax, the measuring eye reacts by relaxing as well.

This section presents relaxation techniques based on a set of optical components that are placed on top of the display. For all the methods, the visuals cast to the idle eye can be duplicated for the testing eye to create a stereo view, relaxing the lens through convergence.

3.8.1 Eye Relaxation in a Monocular H-Shape Design

Figure 3.28 shows an optical design that adds an eye relaxing technique into a monocular eye piece for the NETRA procedure. The device is composed by two light channels. The top channel encloses the NETRA alignment test as described in Section 3.3 and the bottom optical path is used for eye relaxation techniques. An adjustable background image (A) is placed around one focal length away from the lens, creating a relaxation

stimulus virtually anywhere. The beam splitter (C) integrates both light paths on the viewer's retina. The relaxation procedure can be conducted in two ways: (i) the image does not change in position and stays at one focal length from (C); and (ii) the subject has to mechanically move the background image as far as he can, keeping the image in sharp focus. (i) works for all subjects that need correction (q in diopters) from -20 to $q = 1/f - 1/d$, where f is the focal length of (C), and d is a fixed distance from (A) to (C). For instance, if d equals f, the image is virtually at infinity and the relaxation procedure will successfully affect all myopic individuals (-10 to 0). If d is bigger than f, hyperopes can be measured. (ii) works for all powers since the subject can adjust d to the smallest distance at which he can see the film in focus. The risk is that the subject might be able to see the image in sharp focus throughout his accommodation range. Indeed, there is no guarantee that he positioned the film at the farthest distance in focus. The eye easily accommodates to the depth in which the stimulus is cast.

The following procedure is required to allow subjects to adjust d: (i) the subject puts the device very close to the eye; (ii) the subject moves the film away from the lens, up to the point the film blurs; (ii) the subject moves the film closer to the lens up to the point where the image is in focus; (iii) the subject moves the film away from the lens up to the point the film is blurred; (iv) the subject takes the test. This method is similar to the procedure for computing the best optical power successfully tested with adaptive eyeglasses (SUGIURA; MORITA, 1993; DOUALI; SILVER, 2004).

In alternative versions of this design, the film (A) can be replaced by an image on the screen. The distance from the screen to the lens (C) must be close to the lens focal length. The lens (C) can be exchanged for lenses of varying power to create a similar effect of adjusting the image depth d. In a third version of this design, an additional lens can be inserted on top of (C). The device must have a lens holder around (C). In this case, (A), (C) and the additional lens does not need to move. A positive lens moves the point at which the subject is focusing farther. A negative lens moves the point in focus closer. The test then starts with the subject choosing the strongest lens in which he still sees images in focus or only slightly blurred.

The lens (C) can also change its shape to simulate the movement and the creation of virtual objects closer or far from the viewer. There are a few options to make this happen: (i) liquid lenses increase and decrease the optical power by changing the amount of liquid inside; (ii) electro-wetting lenses work on the surface tension of liquids to produce the desired lens curvature and thus control the optical power; (iii) electro-active lenses change the refractive index of liquid crystals inside the lens, changing its power; and (iv) Alvarez lenses slide on top of each other to produce the desired optical power. The lens (C) can also be changed to an adaptive optics device which can create the given optical power via software.

The pattern (H) is drawn on the display to light up the film. It can be a simple white steady square or up to a dynamic image. The brightness of the pattern drawn on (H) is used to adjust the brightness of the film so that the lines remain clearly visible. H's colors change viewer's perception of the pattern. For instance, given that most people focus on wavelengths around the green color, one may illuminate the film with only green pixels to better control accommodation. (H) can assume many patterns according to the design and film. The subject ends up seeing a convolution of the colored images (H) and (A), just like the jittered pinholes setup.

3.8.2 Eye Relaxation in a Bi-ocular Design

While one eye is being measured, the idle eye is stimulated to relax (Figure 3.29). This is similar to the two-channels monocular design, but with the eye relaxation applied to the idle eye instead of the one being measured. Figure 3.29 shows the optical diagram

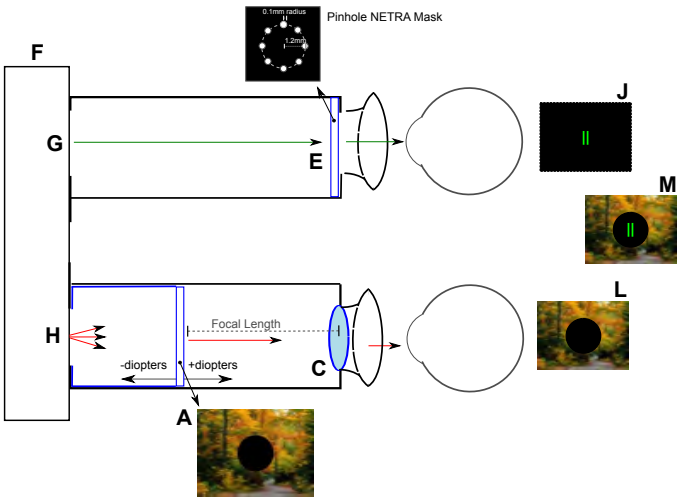

Figure 3.29: Apparatus for a bi-ocular design that relaxes the left eye while the right eye takes the test. The NETRA mask is placed on (E) and the display (F) is place on the back. (G) is the area on the phone to show the test and (H) is the area on the phone that shows a pattern to illuminate the film. In this example, the subject's right eye (J) sees the test (green arrows) while the subject's left eye sees the film (L). When both eyes are open, the test is seen on a background given by the film (M). (A) is positioned close to the depth that is one focal length away from (C). As (A) moves, the subject focuses farther or closer.

that is relaxing the left eye and engaging the second eye for the test. The NETRA mask is placed on (E) and the display (F) is place on the back. (G) is the area on the phone to show the test and (H) is the area on the phone that shows a pattern to illuminate the film. The subject's right eye (J) sees the test (green arrows) while the subject's left eye sees the film (L). When both eyes are open, the test is seen surrounded by the film (M). (A) is positioned close to the depth that is one focal length away from (D). Just like the previous design, (A) can be steady or movable. As (A) moves closer to the lens, the subject focuses closer. This setup also reduces shuddering and positioning the device incorrectly.

The design of the bi-ocular also induces the subject to look straight, controlling convergence. Since convergence affects accommodation and pupil size, when looking straight, the subject's eye is more open to relax and increase the pupil size. As both eyes are connected to the autonomous nervous system, the accommodation of the testing eye follows the stimulated eye. The result is a more accurate eye relaxation and a more stable measurement. This setup also reduces shuddering and incorrect device positioning.

The test is performed with the image placed at one focal length away from the lens. In case of hyperopia or strong myopia, the following procedure is undertaken: the subject puts the device very close to their eye and moves the film away from the lens up to the point at which the film is blurred. The subject moves the film closer to the lens up to the point where the image is in focus and moves the film away from the lens again up to the point where the film is blurred. Then the subject starts the test. The search for the blurred view is conducted twice to guarantee that the subject's crystallin is in the most relaxed state (DOUALI; SILVER, 2004).

Alternatively, instead of moving the image, an additional lens can be placed on top of (C). In this case, the overall test is taken several times using through the following procedure: (i)the subject takes the test in one eye; (ii) the subject or technician checks the result and sums 1 or 2 diopters to the resulting spherical power; (iii) A lens with the computed power is placed in front of (C) and the procedure is repeated. The test finishes when there is no difference between consecutive results.

3.8.2.1 *Evaluation*

A user study was conducted to assess the performance of the eye relaxation technique without using cycloplegia or fogging procedures. This study is meant to determine the accuracy of this section's prototype in measuring refractive error in comparison to non-cycloplegic Nidek AR-310A auto-refractor (AR) and retinoscopy-based subjective refraction (SR).

Refractive errors are estimated for the 90^{th} degree meridian for 13 eyes (9 astigmatic - mean age 29.79 ± 11.32) using a Samsung Galaxy S smartphone (233PPI) taking place from Apr 29 to May 16 2012. The device is bi-ocular with the fellow eye viewing an object at infinity (film steady at one focal length away from the lens). The testing eye looks trought a double slit mask (Figure 3.9(b)), $2.4mm$ apart, with color filters (red and green). The subject aligns red and green lines from the screen with the translation on screen proportional to refractive error. There is no cross-talk on this model.

The 13 subjects underwent AR, SR, and NETRA refractive tests. Subject's refractive errors ranged from $+0.5D$ to $-7.5D$ (mean + SD refraction $-3.00 \pm 2.21D$). All procedures were executed at the New England College of Optometry in Boston, USA[6]. No cycloplegia or fogging was applied. Patients were instructed by inventors on how to use NETRA. A non-inventor optometrist took their Subjective Refraction using a trial set of lenses and a standard Snellen chart. There was no interchange of the measured information among inventors, doctors and patients during the test.

Results 1 For all 13 subjects, the average difference between NETRA and SR is 0.56 ± 0.64. The refraction determined by NETRA correlates closely with that of SR $r = 0.98$ and the two measures were not statistically significantly different from each other ($p > 0.05$). *Orthogonal linear regression fit* presented a slope of 0.92 and a y-intercept of $-0.19D$. The average difference between NETRA and AR is 0.56 ± 0.61 (correlated $r = 0.99$).

Results 2 2 subjects were removed due to the exclusion criteria (bad eyes), which includes amblyopia, color blindness and exophoria. The results of the 11 remaining subjects showed mean absolute errors of $0.35 \pm 0.23D$ for NETRA vs auto-refractor, $0.34 \pm 0.29D$ for NETRA vs subjective refraction and 0.37 ± 0.28 for auto-refractor vs subjective refraction. Table 3.4 summarizes this result. Orthogonal linear regression fit presented a slope of 0.99 and a y-intercept of $-0.18D$ (Figure 3.30).

When compared to SR, NETRA slightly overestimated the myopic refractive errors and had a small myopic offset of $\approx -0.18D$. NETRA is about $0.3D$ off on average from both methods, which is similar to the difference from the Nidek auto-refractor to subjective refraction. According to the results, if we remove bad eyes, 71% of the measurements have a max error of $0.5D$. This value increases to 81% if we apply the linear shift of $0.18D$ (half of our resolution per pixel). On the same subjects, the Nidek Auto-refractor results in 70% of the measurements with max error of $0.5D$. The results show that NETRA is an effective tool for non-eyecare professionals to rapidly estimate refractive errors. While other eye conditions affected these results, in the future they could be detected through new screening methods.

3.8.3 Fiber-optics-based Fogging in Software

This implementation uses fiber optics as a stimulus for relaxing the eye. The user looks into the display at close range, focuses on the fibers, and marks, matches or aligns patterns for a several times. Figure 3.31 illustrates the process in 2D. The NETRA mask is placed on (E) and the display (F) is placed on the back of the device. (G) is the area on the phone which shows the test and (H) is the area on the phone that shows patterns which

[6]Collaboration with Bruce More and Nadin Solaka from the New England College of Optometry.

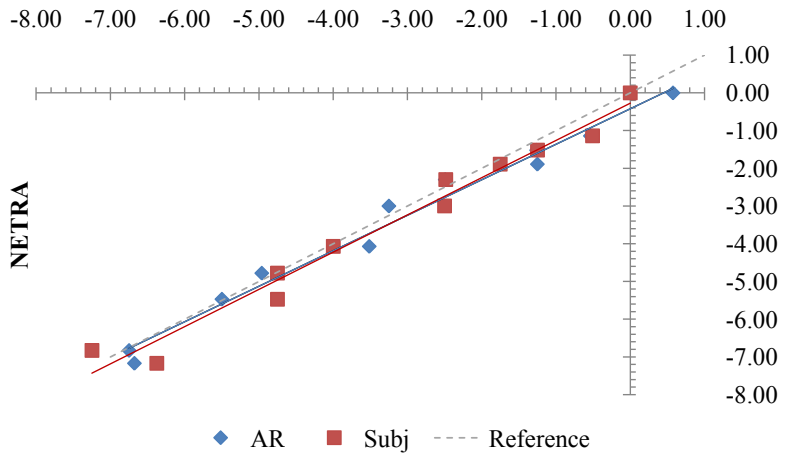

Figure 3.30: Spherical values for NETRA (y-axis) vs Subjective Refraction (x-axis) and Auto-refractor (x-axis) with no cycloplegia. The dashed line is the ideal case. NETRA clearly relaxes accommodation while taking the measurements in bi-ocular designs. Lines are linear fits in a least squares sense.

Comparison	Power at 90 degrees ($n = 11$)
SR-NET Mean Abs Error	0.34 ± 0.29
SR-NET Correlation (r)	0.99
SR-NET T-Test (P)	0.0978
SR-NET Significant Difference	No
AR-NET Mean Abs Error	0.35 ± 0.23
AR-NET Correlation (r)	1.00
AR-NET T-Test (P)	0.0121
AR-NET Significant Difference	Yes
SR-AR Mean Abs Error	0.37 ± 0.28
SR-AR Correlation (r)	0.99
SR-AR T-Test (P)	0.5984
SR-AR Significant Difference	No

Table 3.4: NETRA with no cycloplegia vs Subjective Refraction vs Auto-Refractor. NETRA reaches an average error pretty close that of Retinoscopy vs Auto-Refractor. Green cells highlight when NETRA closely matches other methods, while red cells highlight cases for improvement.

illuminate the fibers. Fibers are divided into clusters that have a given height. (C) makes each cluster of fibers create an illusion of an object at a different depth from the eye. Only one cluster is turned on at a time. There is an option to place parts of a film (A) on the tip of each cluster such that the user sees a more interesting pattern than the fibers tips. The user focus on the cluster that is being illuminated by the phone. In the illustration, the subject's right eye is receiving the test while the subject's left eye is receiving clues to control accommodation. On this design none of the components move.

Fiber optics are placed from the screen and extend up to close to one focal length of a lens (C). This creates a virtual depth around infinity which can be controlled by software. One or more fibers are placed for each depth to create clusters of fibers. The activation of each cluster independently creates a visual stimulus for a desired depth. When the cluster ends exactly at the focal length of the lens, that cluster is generating a stimulus of an object at infinity. As the subject starts the test, the phone illuminates the cluster that is closest to the user. Via an interactive procedure the subject changes the illuminating cluster, moving it further from the eye up to the point he cannot focus sharply anymore.

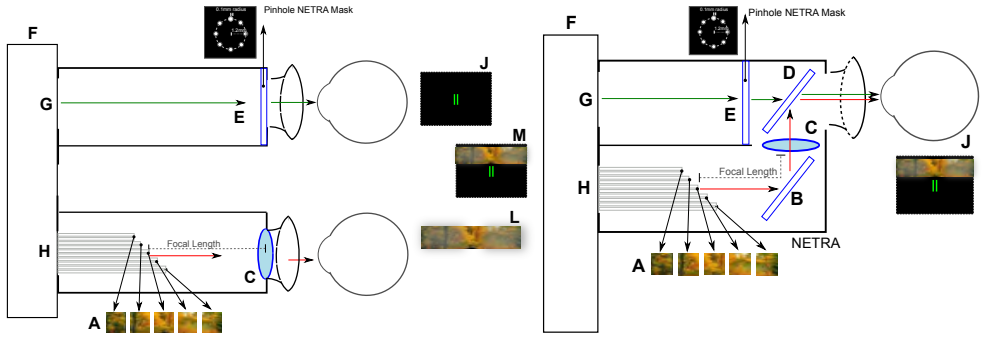

Figure 3.31: (left) Design using optical fibers for relaxing one eye (left eye in this illustration) while the visual acuity of the right eye is being measured. The NETRA mask is placed on (E) and the display (F) is place on the back of the device. (G) is the area on the phone designated for showing the test and (H) is the area on the phone that shows a pattern to illuminate the fibers. Fibers are divided into clusters and each cluster has a given height. Each cluster of fibers creates an illusion of an object at a different depth from the eye. Clusters can be turned on and off by the display (software). On the tip of each cluster, one can choose to put a film (A) so that the user has a more interesting view of the fiber bundles. The user focuses on the cluster that is being illuminated by the phone. (right) This diagram shows visual stimulus from the fiber optics design being ported to a monocular design. Beam splitters (D) and a mirror (B) are used to show the relaxation stimulus to the same eye.

To change the illuminating cluster, the software running on the phone turns regions on the screen that were previously calibrated for given clusters on and off.

Fibers from many clusters can combine at the point closest to the eye to enhance the visual stimulus. Also, the fibers can be placed in such a way that they form a pattern on both sides. Mixing the fibers increase the feeling of depth. They begin in pre-defined clusters on the screen and end in a different distribution on the other extremity of the system.

Figure 3.31(right) shows the additional optics used to create this monocular version. The relaxation stimulus is transferred to the testing eye through a mirror and a beam splitter.

In the first part of the test, the viewer looks through the device and adjusts for the maximum point at which he can see the fibers or the film on top of them (A) in sharp focus. In the latter, he runs the test. To adjust for the maximum point, the software illuminates clusters with expected depths from close to far. Throughout this process, the viewer's eye is focused as close to infinity as it can get (completely relaxed state).

3.8.4 Progressive-lens-based Fogging in Software

Figure 3.32 shows a design in which a progressive lens is used to relax the eye. The pattern drawn on screen (H) illuminates parts of the film (A) and that produces a given depth illusion that is only seen trough the right part of the lens. There must be a set of blockers (N) to prevent light from part of the film from reaching a non-desired. The width and number of blockers is the same as the size and number of the multiple lenses that compose a progressive lens.

The test is performed in two steps: accommodation calibration and the test. First, the subject chooses what is the least sharp film part that he can see while the software illuminates one part at a time. Each part renders a stimulus at a different depth. The software illuminates from the closest stimulus to the farthest. The subject stops when he sees the first slightly blurred image. With the accommodation calibrated, the subject takes

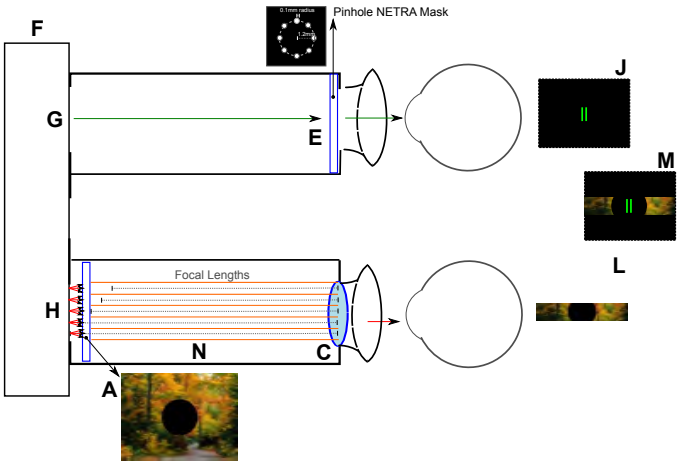

Figure 3.32: A bi-ocular design where the lens (C) is a linear progressive lens. In this design, all elements remain static throughout the test. The pattern drawn on screen (H) illuminates the portion of the film (A) that can produce a given depth illusion. In this illustration, the right eye sees the test while the left eye sees part of the film that is making his eye relax.

the test. Alternatively, a an operating person, such as a technician, can help the subject find the first slightly blurred image.

Adjusting Lenses. In alternative versions of this design, each power of the progressive lens (C) can change to make the subject focus even closer or even farther. For instance: (i) liquid lenses increase and decrease power by changing the amount of liquid inside each power section; (ii) Electro-wetting lenses work on the surface tension of each section to produce the desired lens curvature and thus optical power; and (iii) electro-active lenses change the refractive index of liquid crystals inside the section, changing their power. The lens (C) can also be generated by an adaptive optics device or a holography.

3.8.5 Open-view Eye-Relaxation Design

On monocular designs, to relax accommodation the person can take the test with the idle eye open, looking to a wall 6 meters away in a slightly dark room. Figure 3.33 shows a bi-ocular open-view implementation for relaxing one eye while the visual acuity of the second eye is being measured. The subject must point the device to a far object and focus there. Eyes will blend the test and the wall into one perceived image. The NETRA mask is placed on both channels (E) and the display (F) is placed on the back of the device, oriented in portrait and aligned with the subject's nose. (G) are areas on the phone to show the test, one for each eye. Only one eye is being tested at a time. Polarizers (P) decrease the light intensity of the real world, allowing the subject to see the patterns from the screen. The mirror (B) and the mostly reflective beam splitter (D) form the optical path from the screen to the subject's eye.

3.8.6 Light-field-based Fogging in Software

Figure 3.34 shows a light-field implementation for relaxing the eye using holography style stimulus. The subject executes the test with his right eye while his left eye views a virtual object (holography-style) at a given depth. The film (A) is a precomputed mask that works as a filter for what is drawn on the screen (H). If the image (H) and film (A) are the same, the software can change the scale of the image (H) to change the depth of the virtual object. As the (H) grows, the subject focuses farther.

The test is an interactive process as follows: (i) the subject sees only the holographic

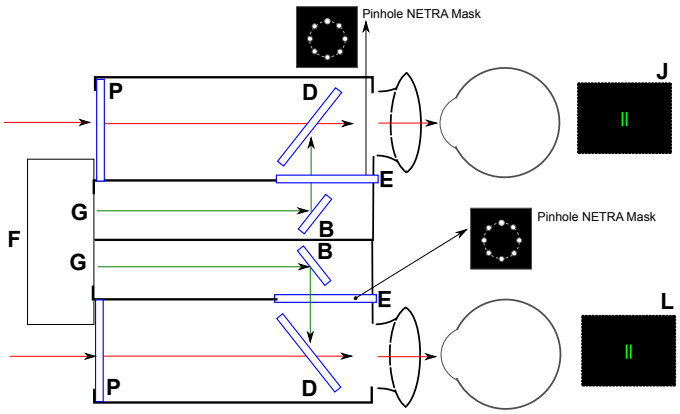

Figure 3.33: An open-view implementation for relaxing one eye while the visual acuity of a second eye is being measured. The NETRA mask is placed on both channels (E) and the display (F) is placed on the back of the device, oriented in portrait and aligned with the subject's nose. (G) are areas on the phone to show the test, one for each eye. Only one eye is being tested at a time. Polarizers (P) decrease the light intensity of the real world, allowing the subject to see the patterns from the screen. The mirror B and the mostly reflective beam splitter (D) form the optical path from the screen to the subject's eye.

image; (ii) the software moves it away from the eye up to the point that the image disappears; (iii) software comes back to a previous stage where the subject still sees the image; (iv) the subject takes the NETRA test on the other eye.

Given a regularly spaced pinhole mask, a computation relaxes the constraint of regularly spaced pinholes by jittering each pinhole by a small amount. The corresponding pattern behind each pinhole in the display is also jittered. The jittered pattern converts the crosstalk between pinholes into random noise. A similar technique using jittered pinholes was described on the NETRA patent to measure the aberration. This current version uses a similar strategy but applied to eye relaxation/accommodation control.

3.8.7 Film-based Relaxation on the Testing Channel

On the testing channel, a two lens system may be added on top of the NETRA mask to enhance the eye relaxation system (Figure 3.35). Lenses are 2 focal lengths away from each other, one focal length from each lens. A film can be placed exactly at the junction of focal lengths (in between the lens) to generate a stimulus of an object far away (virtually at infinity). The film must receive illumination: from the phone, or from ambient light through an opening on the device. The film can be made of a non-attenuating material at the center, creating a pinhole for the testing patterns and prevent their attenuation. This concept can be applied to all other film-based designs.

Figure 3.35 shows a design where fibers illuminate the film (A). Fibers here are optional to increase the amount of light reaching the film. The NETRA mask is placed on (E) and the display (F) is placed on the back of the device. The film (A) is illuminated via the (H) sections on screen.

3.8.8 Lens-based NETRA

For all designs discussed, the testing procedure can be done with an additional lens on top of the mask (Figure 3.36). This setup is similar to the original mask-only test, but the shift c to compute the refractive error is measured from the center of the mask instead of from a point on the screen behind the respective mask's pinhole. To keep the same equations from NETRA, (V)'s focal length must be equal to the distance from the lens to the display. On this design there is no difference between the results for measuring myopia

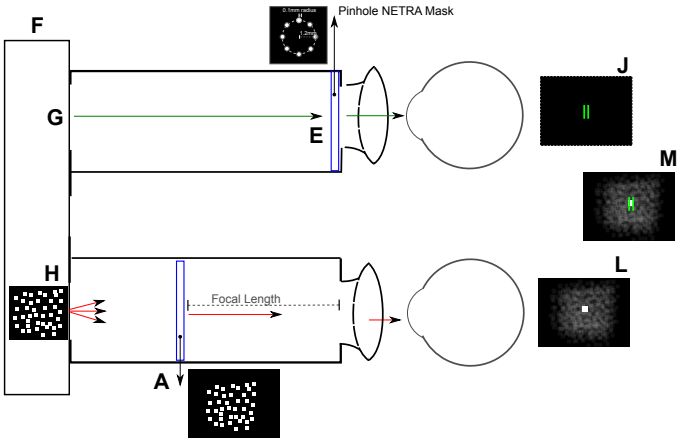

Figure 3.34: A light-field implementation for relaxing one eye while the visual acuity of a second eye is being measured. The NETRA mask is placed on (E) and the display (F) is placed on the back of the device. On the right eye, the subject executes the test while on the left eye, he sees a virtual object (holography-style) at a given depth. The film (A) is then a precomputed mask that works as a filter for drawings on the screen (H). For instance, if the image (H) and film (A) are the same, the software applies a scale on the image (H) to change the depth of the virtual object. As the (H) grows, the subject focuses further.

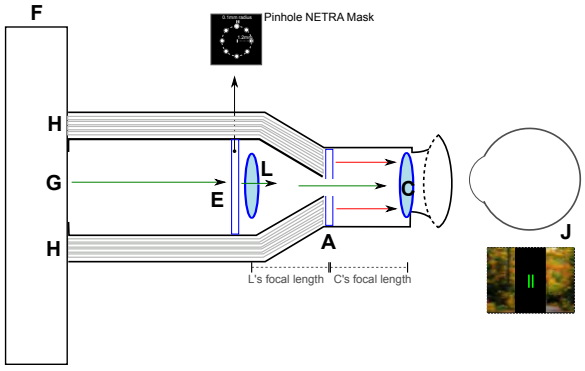

Figure 3.35: A monocular version with a 2f system in which the relaxing film (A) is being illuminated by fibers. Fibers here are optional to increase the amount of light reaching the film. The NETRA mask is placed on (E) and the display (F) is placed on the back of the device. The film (A) is illuminated by the sections of screen (H).

(usually represented by a minus sign) and hyperopia (usually represented by a plus sign). To differentiate among them, lines must have two colors and the eye-piece must have color filters on the pinholes, removing cross-talk. The wavelengths being cast by the display should match only its respective pinhole or feature on the mask. In alternative versions of this design, the mask can also be built inside the lens. However, the testing procedure remains the same.

3.8.8.1 Early Evaluation

16 nearly emmetropic subjects tested an version of this device with no cycloplegia. Results were compared against subjective refraction. This trial was conducted at the Conceição Hospital in Porto Alegre, Brazil with the help of inventors [7]. The average difference between subjective refraction and binocular NETRA was $1.27D \pm 1.07$ on the

[7]Collaboration with Gabriela Unchalo Eckert, Martha Lang, Patricia Ioschpe Gus and Anelise Dutra Wallau from Grupo Conceição

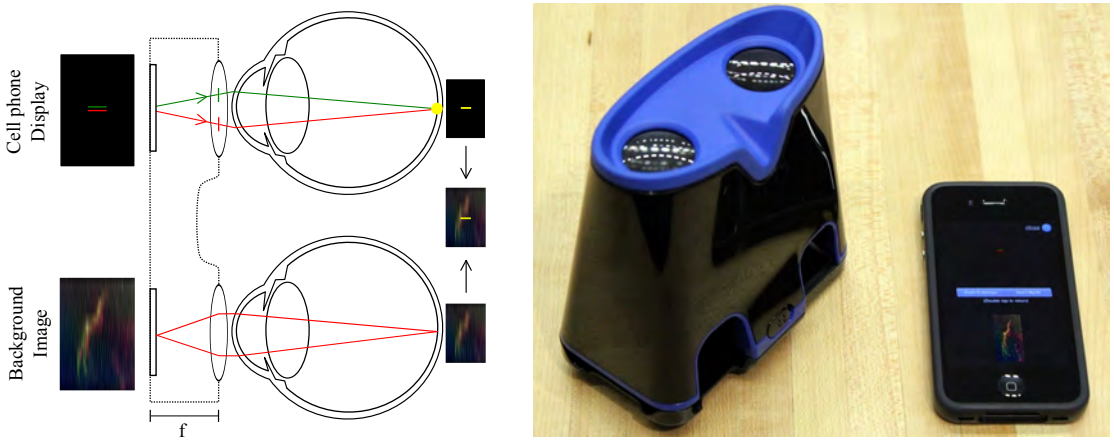

(a) Binocular With-Lens (b) Lens-based NETRA Prototype

Figure 3.36: NETRA binocular designs with object-at-infinity eye relaxation technique. The right eye is being tested while the left eye relaxes. Color-filtered pinholes on the lens avoid crosstalk among the testing lines. The subject sees a sum of both visuals and is able to do the alignment test, while focusing far. On the right, our prototype for this design using a modified Hasbro My3D.

first round and $1.36D \pm 1.10$ on the second. A non-cycloplegic monocular NETRA (no lens and no solution for accommodation) compared with subjective refraction for another 16 volunteers reaches a difference of $2.5D \pm 1.41$ on average. This initial trial shows that the setup has potential to remove accommodation issues. Accuracy of the readings is expected to improve as technology evolves.

3.9 Digital Camera Applications

NETRA has a time dimension and is also useful for estimating speed of accommodation. This approach is suitable to detect healthy conditions of the ciliary muscles, temporary tiredness, or intoxication. The virtual pattern can change depth from frame to frame. A young subject takes approximately 350ms to re-accommodate. While this thesis does not evaluate these applications, the author checked the focusing speed of a consumer video camera. In Figure 3.37(left), a virtual object at infinity is shown and, in the very next frame, a virtual object at 20 cm appears. The camera has to immediately refocus.

The evaluation of *focusing range and speed* for various digital cameras is done by dynamically changing the distance of the virtual pattern for the camera. An adaptation to the software evaluates the auto-focus speed by recording the number of frames required for the camera to bring image into sharp focus. Figure 3.37(right) shows the results for identifying the closest distance at which a camera can focus using an optical bench (Figure 3.37(center)). The probe creates a virtual pattern at a certain distance from the camera and then moves the pattern closer. At each distance, it checks whether the camera-lens configuration can still focus on the virtual pattern. The final recorded data is shown in Figure 3.37(right).

3.10 Discussion and Conclusion

This chapter presented an interactive technique based on a novel near-eye optical probe and high-resolution display. This is the only wavefront aberration estimation method without moving parts or retinal illumination (Table 3.5). Substituting mechanically moving parts with moving patterns on a digital screen requires careful consideration of the

Figure 3.37: Our probe is used to test refocusing speed (left) and focus range (center). Closest distance at which different camera-lens configurations can focus at (right). The blue bars are estimated distances with our probe. The red bars are estimates obtained using an optical bench.

impact of asymmetric aberrations, such as astigmatism. The designed 2D patterns and their movements mimic virtual sources and allow intuitive manipulation by the users. The adaptive two-step process allows the estimation or calibration of the relaxed state aberration via alignment as well as the focusing range via accommodation cues. This chapter described four different prototypes of the system: (i) using lenslet arrays on a magnification system, (ii) using pinhole masks on a smartphone, (iii) controlling accommodation when using masks; and (iv) a simple series of sliding masks. The use of different patterns and interaction strategies to estimate refractive errors, and accommodation range and speed was analyzed. The unusual configuration leads to the exploration of a variety of patterns, and the signal processing approach provides greater freedom to create view-masks and patterns. This method can also estimate focusing range and speed, features which are not available in other devices. Several evaluations and clinical trials were conducted (170 eyes were measured in 7 experiments) to assess the accuracy and usability of prototypes. The accuracy was accessed by estimating the refractive power of corrective lenses from a lens trial set, by comparing refractive errors in human subjects, and by analyzing the optical performance of digital cameras.

Based on this trials, the accuracy of the probe in NETRA is comparable to the state of the art optometry devices. Studies demonstrated very good agreement of NETRA with the current practice in patients. NETRA could measure cycloplegic refraction within a 0.3 diopters difference on spherical power from subjective refractions and within a 0.37 diopters difference from subjective refractions without cycloplegia or fogging. Repeatability among alignments was $0.18D$. A difference of $0.3D$ was found between commercially available auto-refractors and subjective evaluations. With 81% of the measurements displaying a maximum error of $0.5D$, NETRA is an effective tool for rapidly estimating refractive errors without eye care professionals. Furthermore, the precision of the evaluated NETRA prototypes was high even without eye drops or fogging techniques.

3.10.1 Limitations

Since NETRA relies on subjective feedback, it cannot be used by individuals who cannot reliably perform the user-required tasks, such as very young children. Other eye conditions such as glaucoma, color blindness, amblyopia may create difficulties when using the system. The accuracy of the measurements is limited by the focal length of the microlens array (or pinhole mask) and by the dot pitch of the underlying display. Accuracy, however, is expected to improve as technology (pixel pitch of current displays) evolves. Changes in pupil diameter smaller than the distance between pinholes used in the mask may create issues to see the displayed patterns.

Techniques	Objectivity	Speed	Accuracy Reliability	Astigmatism	Mobility	Training	Cost bracket	Self-Evaluation	Data-Capture
Retinoscopy	Obj	Med.	$\pm 0.25D$	Yes	Good	High	$\$2K$	No	No
Subj. Refr.	Subj	Slow	$\pm 0.25D$	Yes	Good	High	$\$1K$	No	No
Auto Refr.	Obj	Fast	$\pm 0.25D$	Yes	No	Basic	$\$15K$	No	Comp.
Portable AR	Obj	Fast	$\pm 0.50D$	Yes	Good	Basic	$\$20K$	No	Comp.
Focometer	Subj	Med.	$\pm 0.75D$	Yes	Good	Med.	$500	Yes	No
Optiopia	Subj	Med.	–	–	Good	Med.	$200	Yes	No
EyeSite	Subj	Med.	–	–	No	Med.	$200	Yes	Comp.
iTest	Subj	Med.	$\pm 0.5D$	No	Excel	Med.	$120	Yes	No
NETRA	Subj	Med.	$< 0.50D$	Yes	Excel	Basic	$3	Yes	Phone

Table 3.5: Comparison of NETRA against current available technologies and research tools. Costs were extracted from the (WHO, 2005) report. Some cheaper options may exist - for instance, authors were able to acquire a set of trial lenses for $300. Note that simple reading charts are expensive because they must be used under optimal lighting conditions and need a set of trial lenses. Since NETRA in the future will be able to retrofit the billion phones out there, the phone is not included in its cost.

3.10.2 Future Works

Matching convergence and accommodation for displayed imagery is achieved using multi-focus displays (AKELEY et al., 2004; HOFFMAN et al., 2005). Liu and Hua (2009) have shown that a liquid-based lens solution can change the plane of focus inside a head mounted display (HMD). Rolland et al. (2000) showed a multi-planar volumetric display based on a stack of laminated planes that are selectively illuminated inside a Head Mounted Display (HMD). NETRA achieves multi-focus without additional depth layers or mechanically moving lenses or lights. Thus, it could also be used to create novel multi-focus HMDs, although at significantly reduced spatial resolution.

Computer graphics techniques can greatly benefit from a multi-focus display. Although the spatial resolution is diminished in the proposed display, a dynamic parallax barrier created with two LCD screens can trade frame rate for spatial resolution by sequentially exposing different pin-holes. The current approach emphasizes accommodation and leaves convergence measurements for future exploration.

This new measuring display is 4D plus time. Experiments with color and time-based patterns (blinking) have not demonstrated any qualitative differences in the results. This, however, remains an interesting area for future research. Diagnosing other diseases such as cataract, retinal stray light and amblyopia (also known as lazy eye) could potentially be achieved through this new measuring display. Finally, it was a surprise to achieve 0.3 diopter accuracy on a mobile phone display. Mobile-phone-based distribution and the view-master inspired probe have a lot of potential for helping developing regions.

It is important to reinforce that NETRA provides a measurement of the refractive error, and does not provide a complete prescription. Optometrists use several subjective factors in addition to the physical measurement to decide on their final prescriptions. The art of prescribing correcting lenses is qualitatively complex and often does not exactly match the measured refractive errors from any technique (THIBOS et al., 2002). NETRA is not meant to replace eye care specialists, but rather is proposed as a self-awareness tool for use at home (to monitor refractive error over time), or in certain areas of developing

countries where optometrists might not be available. Hopefully, this work will spur new research in using modern interactive displays, imaging techniques, and visually interactive procedures to create a new class of self-evaluation probes.

4 CATARACTS MEASURING AND MODELING

This chapter introduces an interactive method to assess cataracts in the human eye by crafting an optical solution that measures the perceptual impact of forward scattering on the foveal region. Current solutions rely on highly-trained clinicians to check the back scattering in the crystallin lens and test their predictions on visual acuity tests. In the proposed approach, close-range parallax barriers create collimated beams of light to scan through sub-apertures, scattering light as it strikes a cataract. User feedback generates maps for opacity, attenuation, contrast and sub-aperture point-spread functions. The goal is to allow a general audience to operate a portable high-contrast light-field display to gain a meaningful understanding of their own visual conditions. User evaluations and validation with modified camera optics have been performed and will be discussed in this section. The technique's captured data is used to reconstruct an individual's cataract-affected view, offering a novel approach for capturing information for screening, diagnosis, and clinical analysis.

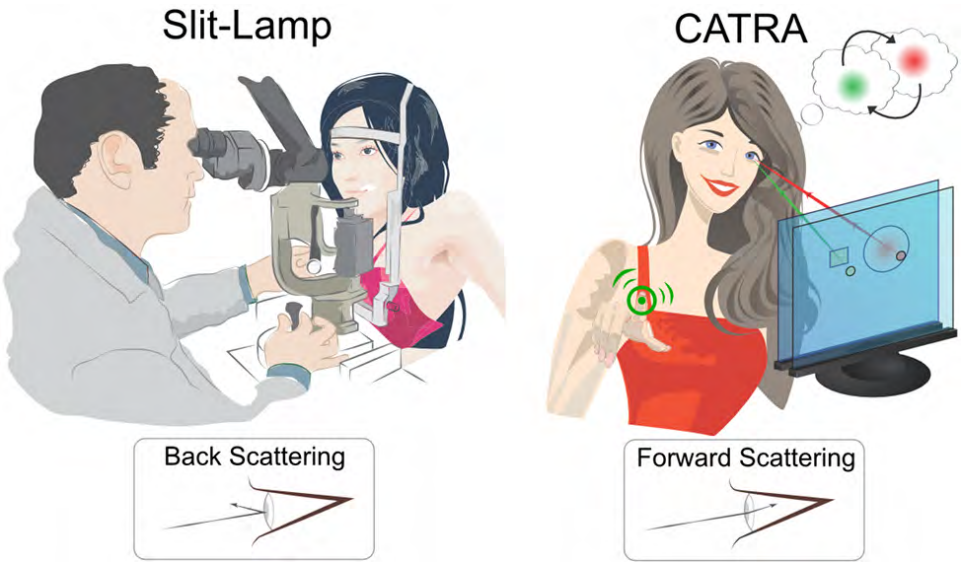

Figure 4.1: Can one create a device that makes people aware of their early cataract condition? Using a modified light-field display, CATRA projects time-dependent patterns onto the fovea. The subject matches these alternating patterns that have passed through scattering (green) and clear (red) regions of the lens. An interactive software measures the attenuation and point-spread function across sub-apertures of the eye. Cataracts' size, position, density, spreading angle and overall scattering profile are then estimated. Differing from standard techniques, which rely on back scattering measurements, CATRA relies on the forward scattering towards the retina.

Cataracts are the leading cause of avoidable blindness worldwide. A cataract-affected eye scatters and refracts light before it reaches the retina. This is caused by a fogging or

clouding of the crystallin. They are generally detected subjectively by locating a white reflex during a slit-lamp examination. Visual acuity tests assess practical symptoms, such as loss of contrast, glare, halo, and general blurriness. Research tools range from high-end Shack-Hartmann (DONNELLY et al., 2004) and femtosecond optical coherence tomography systems (PALANKER et al., 2010), to retro-illuminated image processing techniques (CAMPARINI et al., 2000). In the early stages, cataracts are small and have little impact on vision, but as they grow, they affect color brightness and cause glare and halo-like effects on vision, making driving at night incredibly difficult. They are often associated with age but can also result from medical conditions such as diabetes and ultimately can lead to total blindness (the white blindness).

CATRA, the proposed new method, measures this scattering by allowing one to compare a good light path with a path attenuated by the cataract. It is an interactive and compact solution that goes beyond traditional cataract evaluation procedures by taking advantage of forward scattering to compute quantitative maps for opacity, attenuation, contrast, and point-spread function (PSF) of cataracts. Modified parallax barriers create collimated beams of light to scan the crystallin lens (Figure 4.1). Set up close to the viewers' eye, the device ensures the beams are projected onto the fovea. These beams scatter when the light path hits a cataract, altering the user's experience. To verify their accuracy and precision, study results are cross-referenced utilizing user studies and modified camera optics with partially masked diffusers. This chapter goes a step further reconstructing the individual experience of a cataract-affected view, a method which is currently unexplored by the graphics and vision communities. The dissemination of devices with the ability to estimate intrinsic parameters of the eye may drive the development of future user-sensing technology for displays, and rendering techniques, and more generally improve the current understanding of the human visual experience.

4.1 Contributions

This chapter proposes a novel optical design combined with interactive techniques to measure cataracts based on a view-dependent display. The solution to scan and measure the *forward scattering* of a cataract-affected lens without moving the users' visual point of reference by *creating steady images in the center of the fovea*. The main contributions of this chapter include:

- A co-design of optics and user-interaction that effectively measures optical scattering inside the human eye. Mechanically moving parts are exchanged for moving patterns, on-screen, and forego the need to use external sensors. Off-the-shelf display and simple optical components make the device safe, cheap, and compact;
- Four interactive measurement techniques used to assess the size, position, attenuation, contrast, and point-spread function of scattering spots in imaging systems. These maps quantify and predict the scattering behavior inside the eye, and an image-based technique simulates the individual's eyesight.

The new interactive technique efficiently reduces the search space for the PSF of a subject's eye. The data captured is more detailed than current currently used techniques. Since there is no established gold standard for in-vivo accuracy comparison, the study results in terms of accuracy are related to the doctors ability to locate and rate cataracts in the volunteers. The in-vitro accuracy comparison was discarded. Although the materials to simulate cataract effects exist, but they do not account for localized scattering (WIT et al., 2006; FINE; RUBIN, 1999), which defeats the purpose of this technique. This is the first method to interactively measure a sub-aperture PSF map of an eye, the first to

Techniques / Features	Opacity Map	Attenuation Map	Contrast Map	Sub-apert. PSFs	Scattering	Training Level
Slit Lamp	✓				Back	High
Scheimpflug	✓				Back	High
Retro Illum.	✓	✓			Fwd	Med
Shack-Hartmann	✓	✓		✓	Fwd	Low
OCTs	✓	✓			—	Med
Dynamic Light Scat.	✓	✓			—	High
CATRA	✓	✓	✓	✓	Fwd	Low

Table 4.1: Comparison of CATRA against current available technologies and research tools. It is suspected that Shack-Hartmann, dynamic light scattering, OCTs and retro-illumination, coupled with image processing, are capable of generating maps comparable to CATRA, even though this research is not aware of any such demonstration.

measure sub-aperture contrast sensitivities, and the first to explore an individual cataract-affected view.

4.1.1 Related Works

This chapter complements the contributions of the previous chapter which discussed NETRA (PAMPLONA et al., 2010b). NETRA measures the *required optical correction and focal range* using static clip-ons for high-resolution displays. CATRA computes the *spatial distribution of opacities* inside the crystallin lens and requires programmable high-contrast parallax barriers. NETRA's optics are designed to perform alignment tests, in which accommodation plays a critical role. *CATRA* relies on pattern matching and gaze control, where the alignment of the subject's eye is the main contribution. Unlike NETRA for which several devices provide similar measurements, there is no device capable of measuring quantitative maps for accuracy comparison.

4.1.1.1 Glare Studies and Light-Field Techniques

Isono et al. (1993) introduced dual-stacked LCDs to achieve programmable parallax barriers. CATRA uses a similar hardware setup to measure deficiencies in the human eye. A few researchers have addressed glare removal on coded aperture cameras by resampling the light field image (RASKAR et al., 2008), separating the direct and global components (TALVALA et al., 2007; NAYAR et al., 2006), and adding an LCD to block the glare-affected part of the aperture (HARA; SAITO; KANADE, 2009). Research on CATRA applies an indirect occluder measurement and glare estimation to eyes. With the proposed maps, one can extend these works to correct images for cataract-affected eyes.

4.1.1.2 Simulation of a Subject's View

A number of researchers have ray-traced schematic eyes in order to study the optical importance of each structure. Camp et al. (1990) developed a rendering technique that accounts for eye aberrations based on corneal topography. Kolb et al. (1995) introduced the realistic camera model for computer graphics producing a variety of optical effects. Mostafawy et al. (1997) designed a virtual eye for retinal image visualization using ray tracing techniques. Loos et al. (1998) ray-traced a schematic eye for best fit

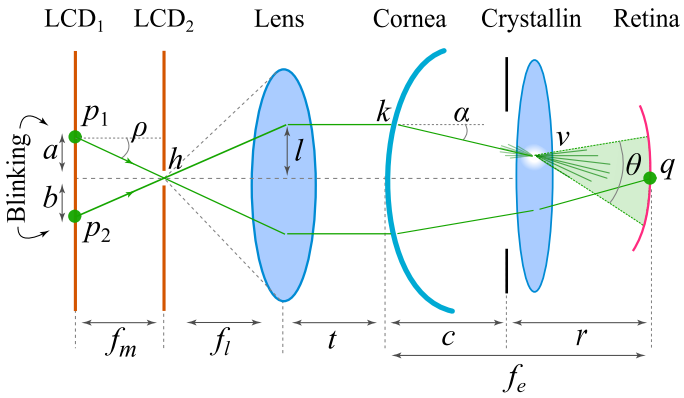

Figure 4.2: Cross-section of *CATRA* optical setup. Two stacked LCDs and a lens create collimated beams of light. If a pinhole is drawn on LCD_2, all bright pixels on LCD_1 will focus at the same spot q on the retina. Thus LCD_1 defines the brightness of each retinal point, while LCD_2 controls the position and shape of q. The lens is positioned at one focal length (f_l) from the display. The distance f_m defines the angular resolution. The setup has a near-Lambertian lightbox placed behind LCD_1.

progressive lenses. Barsky (2004) used wavefront data to simulate the subject's vision. Deering (2005) modeled retinal cones and simulates the perception of displayed digital images. Pamplona et al. (2009) studied the pupil light reflex. Kakimoto et al. (2007) described wavefront tracing in the eye for refractive aberrations. Machado et al. (2010) created a model for the perception of color vision deficients. Schwiegerling et al. (2000) created a diffraction model to find the acuity limit for a standard eye, while (RITSCHEL et al., 2009) developed a diffraction simulator to dynamically compute the PSF of a virtual eye, rendering glare effects in real-time. Although these works achieved their purposes, none developed a test for cataracts dysfunction; and most of them are not targeted toward the simulation of a specific individual's vision.

4.2 Scanning the Crystalline Lens

CATRA turns a parallax barrier into a time-dependent gaze-controlling scanning mechanism in order to explore the intrinsic parameters of the human eye. Figure 4.2 shows a diagram of the setup in flat-land and two applications. Two stacked LCDs create a programmable parallax barrier. An additional lens in front of the display increases light efficiency and reduces diffraction, creating collimated beams that converge to the same point on the retina. The device is positioned very close to the subject's cornea and its components are aligned. The setup on Figure 4.2 traces light from each p_i through many regions of the crystallin, one p_i at a time. Each beam propagates the effect of possible occluders and imperfections to the central point of the fovea. The displayed image disappears on a mostly reflective cataract spot and scatters when the ray finds a semi-transmissive spot. Based on this setup, CATRA computes opacity, attenuation, contrast, and PSF maps of the eye using interactive perceptual pattern-matching functions, which compare clear-path light beams with scattered ones.

The intuition of the design relies on the role of each LCD: each pixel on LCD_1 maps a region on the crystallin and each pixel on LCD_2 corresponds with a retinal position. Patterns drawn on LCD_2 are reflected on the retina, while the brightness of all pixels on LCD_1 are integrated on the same retinal point. A central pinhole in LCD_2 traces rays to the center of the fovea. Positions p_i (Figure 4.2) inside the crystallin are a function of the angle ρ:

$$v(\rho) = f_l \tan \rho - c \tan \alpha, \tag{4.1}$$

where the bending angle α is defined by the optical corneal power at point k. To create patterns on the subject's view, the pinhole on LCD_2 changes to the desired pattern. The position h on LCD_2 is mapped onto the retina as (derived from compound lens equation):

$$q(h) = \frac{(-f_e^2 - f_e f_l)h}{f_l(-f_e - f_l + f_e t)} \tag{4.2}$$

Figure 4.3 illustrates the proposed interactive 6-step method. After measuring the pupil size, which defines the discretization of the pupil area and enables the computation of the cataract size in meaningful physical units, the method sequentially scans the subject's crystallin to identify the presence of cataracts. If cataracts are present, the subject marks the position of opacities and, in a posterior step, measures the light attenuation for each affected sub-aperture of the eye, thus creating opacity and attenuation maps. The measured attenuation values estimate the intensity of the sub-aperture PSF peak. The subject then performs perceptual pattern matching to measure the tail of the PSF. If the light attenuation is too strong, when PSF's is bigger than the fovea, the direct measurement of the PSF by comparison is not reliable. Contrast-sensitivity tests are then used to approximate the PSF. This method's viability relies on the specified order for conducting measurements. The final information achieved is well beyond the results of any currently available clinical device.

4.2.1 Estimating Pupil Size

Figure 4.4 shows a simplified ray diagram to measure pupil size with two light beams in 2D. A circle with radius a of dots p_i is displayed on LCD_1 and a dot (pinhole) is displayed on the center of LCD_2. Parallel rays enter the eye and converge to a single point q on the fovea. Via interactive software, the subject increases a up to a point where the light rays are blocked by the iris and the projected pattern disappears (Figure 4.3(a)). The pupil's radius is given by $d(a) = a - c \tan \alpha$, where c is the anterior chamber depth. It is assumed that the pupil is circular, thus the search method is $1D$.

4.2.2 Screening for Cataracts

In this step, the lens is rapidly scanned to check for the presence of cataracts. At the end of the scan, the user provides input regarding whether they saw any blinking or fading of the light; which indicates the presence of at least one cataract. The rapid scan does not involve user interaction but rather the user waits until the end of the scan to provide input. After subdividing the crystallin into testing regions according to the pixel density of the LCD stack, Equation 4.1, and pupil size, CATRA draws a single dot p_1 on LCD_1 and opens a pinhole on LCD_2. Each move of p_1 scans a different region on the crystallin (Figure 4.3(b)). In this first scanning, p_1 is continuously changing position to cover the visible crystallin. Without pressing any keys, the apparent sudden blinking or fading of the viewed pattern (e.g., case of p_2 in Figure 4.2) reveals the presence of cataracts.

4.2.3 2D Scanning for the Opacity Map

If the subject sees a blinking or fading, the second scanning is initiated (Figure 4.3(c)). The software slows the frequency of changes in p_1 and allows the subject to mark faded regions by pressing keys. Since the subject does not see the pattern moving, audio feedbacks (beeps) indicate every change in p_1. When the scan covers the entire lens, an opacity map is built by concatenating the binary visibility functions for each sub-aperture. An hierarchical procedure for this scanning is left for future research.

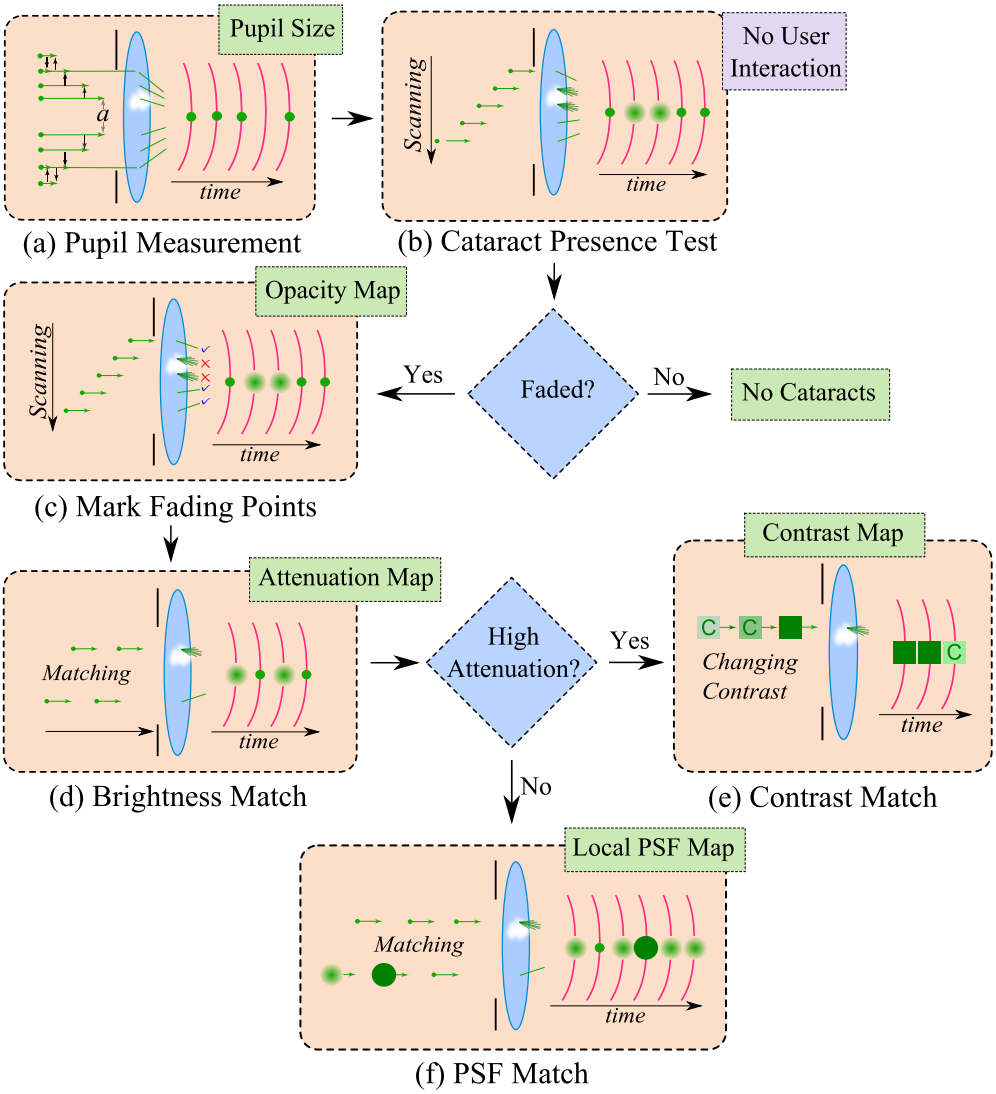

Figure 4.3: Hierarchical method to efficiently measure cataracts. (a) Subject measures pupil size by increasing the distance a while perceiving the green dot. (b) Software automatically scans the lens to check for the presence of cataracts. (c) If a scattering spot is found, the scanning procedure is repeated with the subject's feedback. (d) By matching the brightness of two alternating paths of light, CATRA computes the attenuation map. (e) For a high scattering spot, the sub-aperture contrast-sensitivity test replaces the sub-aperture PSF measurement. In this case, the subject increases the contrast of the displayed pattern up to a point where the letter becomes discernible. (f) Sub-aperture PSF matching is the most detailed mapping; where the peak and Gaussian spread are measured for each scattering spot.

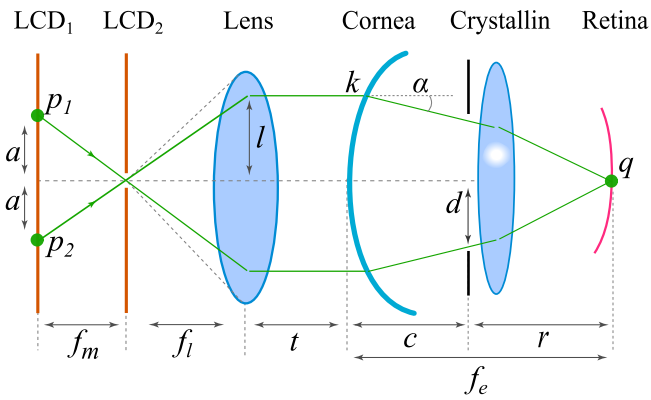

Figure 4.4: Cross-section of *CATRA* schematics for pupil size measurement. The subject chooses the biggest possible "a" while they are still able to see seeing q; Again, the setup has a near-Lambertian light-box placed behind LCD_1.

4.2.4 Brightness Match for the Attenuation Map

The attenuation map measures the relative light attenuation across the crystallin. LCD_1 shows a pair of alternating dots (Figure 4.2). p_1 is computed as the farthest point on the opacity map from the cataract spots. p_2 is a marked spot on the opacity map. Since both are projected on q during distinct time-slices, the subject sees similar patterns with oscillating brightness. As they view these oscillations, the subject decreases the intensity level of the clear-path light beam and thus p_1 brightens until the oscillation stops (Figure 4.3(d)). This same task is executed for all marked regions on the opacity map. In the end, the attenuation map is generated, showing the relative density of the cataracts.

4.2.5 Point-Spread Function Matching

Similar to the brightness matching process, for point-spread function matching, the subject compares and matches alternating patterns p_i on LCD_1 (Figure 4.3(f)). Two patterns are drawn on LCD_2, one for each p_i. The former is a single pixel stimulus that hits the cataract, spreading light onto the retina. The latter is a linear combination of a Gaussian and a box function, which describes a sub-aperture PSF:

$$c(x) = \beta g(\sigma, x) + (1 - \beta)p(x), \tag{4.3}$$

where β is a scaling factor defined by the measured attenuation value, σ is the standard deviation, g is a normalized Gaussian function and p is a normalized box function. In the absence of blur, $\beta = 0$. For each marked spot on the opacity map, the subject changes the values of σ to best match the visualized PSF.

4.2.6 Contrast-Sensitivity Test

A contrast map includes information about how sensitive parts of the eye are to visual contrast. The contrast sensitivity test is a replacement for the PSF measurement procedure, and is well-suited for a high scattering spot. Wider PSFs project their tail out of the fovea and thus the subject may have trouble measuring it reliably. The subject increases the contrast of a displayed pattern up to the point where the displayed pattern becomes discernible. For each attenuated sub-aperture, a single p_i is rendered on LCD_1 and a low-contrast 3 pixel-wide randomly-rotated letter **C** is rendered on LCD_2. At the start, the user sees a white square. The subject increases the contrast until **C** becomes visible (Figure 4.3(e)). The rotation degree (0, 90, 180 or 270) of **C** is marked and noted. This visual acuity test is repeated for each marked sub-aperture, generating a complete map in the end.

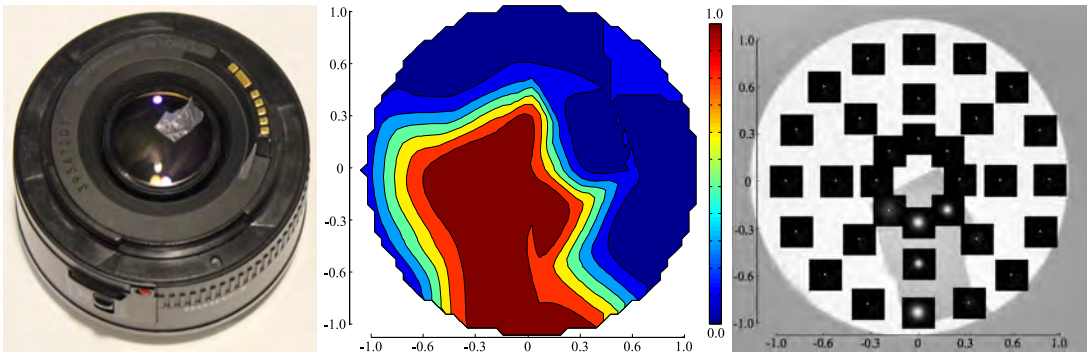

(a) Cataract Simul. (b) Attenuation Map (c) Sub-aperture PSFs

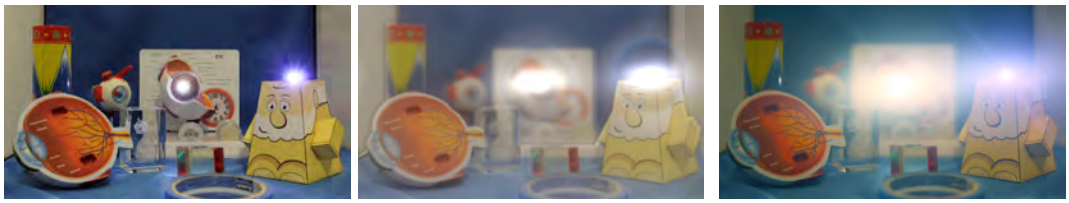

(d) Scene (e) Rendering (f) Picture taken with (a)

Figure 4.5: A strong cataract is simulated by adding an 80-degree diffuser behind a $55mm$ lens of an SLR camera (a). CATRA estimates attenuation map (b) for an aperture of $2.2cm$ and a sub-aperture PSFs map (c) for an aperture of $3cm$. Using (d) as an input image and applying the measured PSFs from (c), the image (e) is rendered, showing effects similar to the picture taken with the cataract-simulated lens (f). Depth information is captured with a Z-camera (Microsoft Kinect).

4.2.7 Implementation Details

Prototypes are built according to the following considerations.

4.2.7.1 Gaze Control and Eye Position

Since all collimated beams are projected onto the fovea, the subject keeps looking at the same point and does not gaze. However, if the subject shifts more than the a pupil diameter, they will no longer see the same image. To help keep the view in the same place, CATRA draws reference points (Figure 4.6) as a circular arrangement of patterns on LCD_2. Part of the circle disappears when the subject moves beyond a certain limit. With this simple trick, the subject detects his movements and can return to the original position.

4.2.7.2 System Resolution

Assuming h is a pinhole, the size of the cross section defined by the collimated light beams between the lens and the cornea is given by $s(p)f_l/f_m$, where $s(p)$ is the radius of the pattern p on LCD_1. Thus the bigger f_m, the smaller the beam radius is. The sampling resolution on the crystallin is defined by the discretization of the angle ρ (Equation 4.1), which is dependent on the pixel size on both LCD_1 and LCD_2. The retinal resolution is defined by pixel pitch on LCD_2 (Equation 4.2). To match the fovea (radius of $\approx 0.92mm$), light rays have to reach the cornea at a maximum angle of $\rho = 2.12°$. Thus, the biggest reliable pattern on LCD_2 has the radius of $f_l \tan(\rho)$.

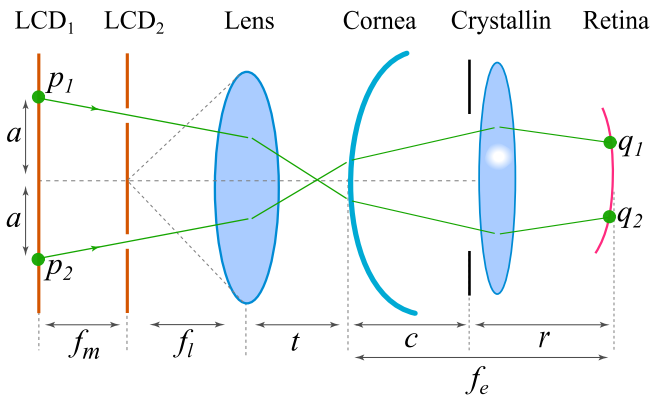

Figure 4.6: Cross-section of *CATRA* schematics for showing reference points (q_1 and q_2) to control eye movement and gaze.

4.2.7.3 Handling Accommodation and Refractive Errors

CATRA's design does not allow the same kind of multi-focus as NETRA, and also do not assemble an image on the subject's retina as the standard parallax barrier does. Instead additional lens on top of the LCD plays an important role in handling accommodation. Subjects can focus on the image displayed by LCD_2 just like any other object seen through a lens. Refractive errors add variations to the position of the patterns on the retina, and can cause the subject to gaze, adding uncertainty to the cataract's position inside the crystallin (e.g., if the scanning moves circularly and the subject happens to have corneal astigmatism, the method is actually measures in an ellipsoidal shape).

4.2.7.4 Required display contrast

In order to match a bright, free path, point-spread-function peak against a dim cataract scattered beam, the display has to be able to decrease the intensity of the former pattern in the perceivable levels of the latter. Assuming a uniform distribution of energy over the scattering angle θ (Figure 4.2), the incidence area on the retina is:

$$Q_s = \pi(r \tan(\theta/2))^2 \tag{4.4}$$

which leads to a required contrast of $(Q_d/Q_s) : Q_d$ on the display, where Q_d is the energy of a non-scattered light beam. This contrast has to match with the contrast of the parallax barrier. By alternating between black frames and patterns, the amount of energy received by the eye is decreased. Due to the slower the integration time when the human eye is looking in dark places, such as occurs in the CATRA prototype, which is about $20hz$, one can increase contrast by 3 times just by adding 2 black frames between each pattern frame.

4.2.7.5 Removing the Residual Black Level

Measured values are scaled according to the residual light emitted by a black-rendered LCD through the parallax barrier. For each point in the retina (h is a pinhole), this black level is:

$$B(x) = \int_{-\tan\eta}^{+\tan\eta} I(f_m \tan\eta) I(h) dh \tag{4.5}$$

where $\tan\eta$ is given by the lens radius over f_l and $I(x)$ is the intensity of the pixel x. Black pixels can be measured in a brightness matching of alternating patterns during a calibration step. There is no pattern drawn on LCD_1 and there is a pinhole that blinks

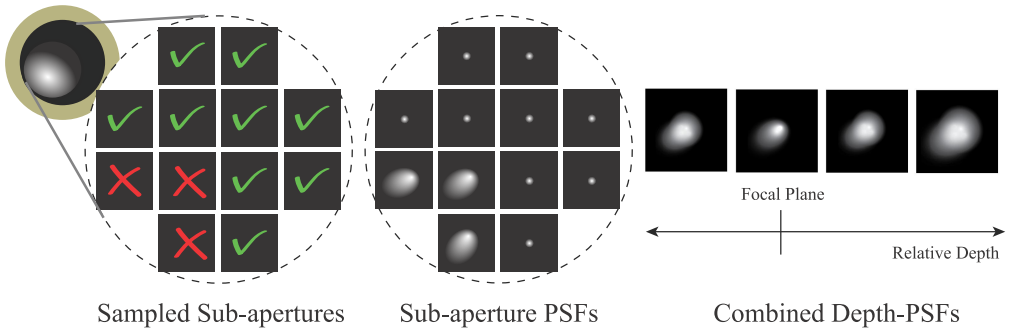

Figure 4.7: Composition of lens' depth-dependent PSFs as the sum of all sub-aperture PSFs (center), shifted and combined in accordance with the relative depth from focal plane and the lens aperture (right). Check marks represent good light paths and Xs are scattering regions marked by the subject on the opacity map (left)

.

on LCD_2 blinking with pixel intensities of 1 and 0.5. The subject adjusts the intensity of all $I(p)$ of the used area A on LCD_1 and eventually the pattern stops blinking. The black level is then: $B = A * I(p)/0.5$

4.2.7.6 Removing Diffraction

The stack of LCDs exhibits inherent diffraction from the liquid crystals. The additional lens, however, bends the diffracted rays on LCD_2 to the same output angle as the light beam. The eye converges them at a single spot. Since diffracted rays are minority of light rays, they are not noticeable.

4.3 Rendering the Subject's View

This section proposes an image-based approach for simulating the vision of a specific individual affected by cataracts. The resulting view can be shown to the subject to make them aware of their condition and how clear it will be after a cataract surgery. The image can also be shown to other people (*e.g.,* the clinician), so that they can see and understand the impaired visual experience their patient or loved one is dealing with. The rendering procedures change according to the maps that are provided as input. If only an opacity map (which says how much of the aperture is blocked by a cataract) is given as input, the aperture structure is transformed into the eye's point spread function, using a simple Fourier transform. If attenuation or contrast maps are provided, they are converted into point spread function maps and then the procedure for converting PSF maps to a cataract-affected view can be applied. Attenuation and contrast values are measured per sub-aperture, like point spread function maps. The PSF for each sub-aperture is a 2D gaussian-like profile (Equation 3) where its standard deviation is proportional to the contrast value and the gaussian maximum intensity to the attenuation value.

An accommodation-dependent convolution of sub-aperture PSFs simulates the view of a cataract-affected eye. Depth-masked patches of the input image are convolved with their corresponding depth-dependent PSFs and combine the results to form the final image. Each depth-dependent PSF is computed by combining the measured sub-aperture PSFs. Figure 4.7(right) illustrates how the combined PSF changes with accommodation. At the focal plane, all sub-aperture PSFs are just superposed and added, averaging their values. The sub-aperture PSFs are shifted from the center according to their distance from the focal plane. Computation of these depth-dependent PSFs can be defined by a sum over

Figure 4.8: Rendering features using measured PSFs from a simulated cataract on a DLSR camera: (A) "Bokeh" effect, the cataract shape projected from out-of-focus bright light sources; (B) picture of the simulated cataract; (C) the estimated attenuation map; (D) the estimated PSF map; Cataract spots scatter light, generating large glare patterns. Depth information captured from the z-buffer. Camera aperture of $4mm$.

all sub-apertures:

$$PSF(B) = \sum_i PSF_i + B\overrightarrow{g_i} \tag{4.6}$$

where B is a depth-offset in diopters (reciprocal of the distance in meters $B = 1/d_m$) from the plane of focus defined by accommodation, $\overrightarrow{g_i}$ is the vector that represents the shift of a given sub-aperture i from the center of the lens. The product $B\overrightarrow{g_i}$ models how the circle of confusion projected through i gets shifted from the center of the image as a function of depth. The final image is given by the sum of the depth-masked patches convolved with their respective PSFs for all depths in the scene:

$$IMG(A) = \sum h(A, B) \otimes PSF(B) \tag{4.7}$$

where $h(A, B)$ gives the depth-masked patch of the input image I for accommodation, A in diopters and is defined pixel-wise by:

$$h_{x,y}(A, B) = \begin{cases} I_{x,y} & \text{if } depth(x, y) = A + B \\ 0 & \text{otherwise} \end{cases} \tag{4.8}$$

where $I_{x,y}$ is the intensity of the pixel x, y, and $depth$ is the distance from the camera to the projected point x, y in diopters. Given sub-aperture PSFs, this depth-based approach renders artifacts similar to those described by cataracts-affected subjects and also computes the expected depth-of-field (Figure 4.5). To account for diffraction from the pupil, lens fibers and cataract opacities, an augmented version of the glare model described in (RITSCHEL et al., 2009) are added to the computed PSF, including the attenuation map as an extra multiplication step to their aperture model. Figure 4.8 shows a simulated night-driving scene with the experimental data used to render it. Cataract's shape (b) can be seen as a mask on the "bokeh" effect of the PSF composition.

The rendering (reconstruct and simulate) of an individual's cataract-affected view may provide a benchmarking analysis for the cataract-affected subject or who would find it useful or insightful. Scenes of daily activities with high and low contrast features, such as driving at night, can be taken using a standard camera. They are then displayed on a

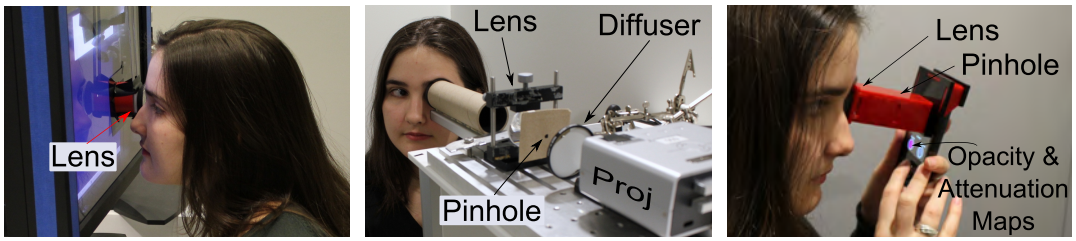

(a) Dual-LCD Monitor (b) DLP Proj.-Mask (c) Cell-Phone-Mask

(d) LCD_1 (e) LCD_2 (f) View (g) Results

Figure 4.9: Prototypes and a scanning procedure example: (a) stack of two LCDs from high-contrast low-resolution monochrome medical monitors; (b) a high-contrast DLP projector plus a pinhole mask, and (c) the cell phone LCD plus a pinhole mask. (d) a picture of the cell phone display on the scanning procedure. Blue dots are reference points. (e) the cell phone pinhole mask. The central pinhole performs the test while others allow for reference points. (f) a simulation for the subject's view (picture). (g) a picture of the cell phone screen showing the opacity and attenuation maps. Because of the absence of color filters, high contrast ratio and a better light box than standard LCDs, (a) is best overall setup. (b) brightest and highest-contrast setup, which allows meaningful scattering projection through high density cataracts; and (c) it is the most portable, comprising of a clip-on for smart-phones.

standard monitor. Using the captured cataract maps, the algorithms convert the displayed picture into the view of an affected individual. The input picture is also displayed on the monitor to establish a benchmark. The interested parties (e.g., a cataract-affected patient or a clinician) can see the effect the cataract is causing in the patient's vision. Since the patient is observing images on a monitor and not the real scenes, the cataracts do not affect the patient's view to the same extent as they affect the real scene. These renderings allow a patient and doctor to share a visual experience, facilitating dialogue and diagnosis. A comparison of the rendering (which approximates the cataract-affected view) and a normal view can be used to help patients decide when to have the surgery, help doctors understand a given patient's condition, and help teaching ophthalmology.

4.4 Prototypes and Evaluation

Different designs for Figure 4.2 that span across size, materials, interface, cost and static contrast were tested. Figure 4.9(top) shows three best CATRA prototypes while Figure 4.10 shows other less efficient prototypes. The *Dual-LCD Monitor* is built using two 18" LCD TFT monochrome medical monitors stacked $f_m = 24mm$ apart, with a brightness of $700cd/m^2$, a contrast ratio of $550:1$, $90DPI$ ($280\mu m$ pixel pitch) and a 20-diopter lens, $50mm$ from the stack (Figure 4.9(a)). A single-pixel pattern on LCD_1 reaches a scanning resolution of $510\mu m$ on the crystallin. Since these LCD panels do not have color filters, the aberrations are smaller than traditional monitors and the high static contrast gives off a smaller residual light level for black pixels.

Since LCD_2 does not change for attenuation and opacity maps, a cheaper version of

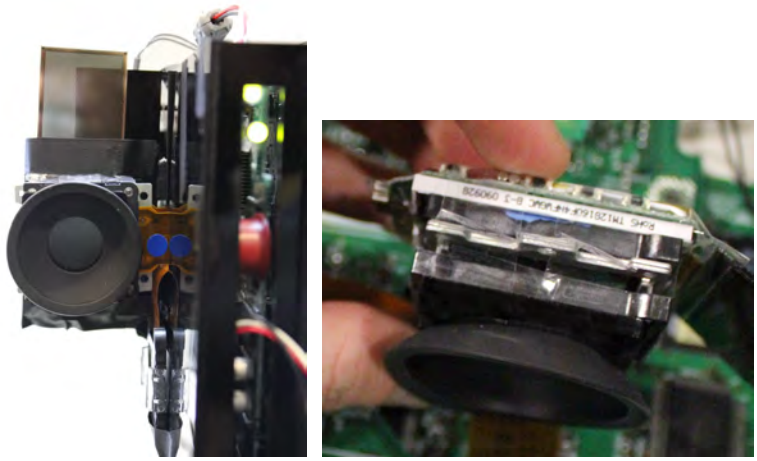

(a) Projector LCD Stack (b) Projector LCD Stack

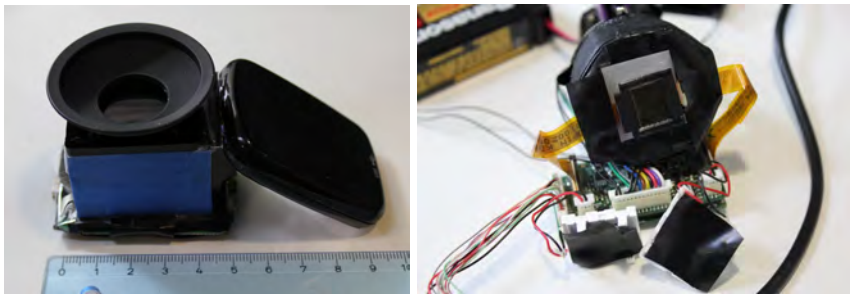

(c) Dual $14.00 Photoframe (d) Dual HMD LCDs

Figure 4.10: Non evaluated prototypes. They suffer from contract issues and produce poor quality of the images. (a,b) stack of LCDs from a monochrome high-resolution low-contrast LCD projector; (c) stack of LCDs using portable low-resolution photo-frames; (d) stack of high-resolution low-contrast LCDs from a head mounted display;

the same optics replaces the LCD for a printed pinhole mask. The setup is still capable of measuring the opacity and attenuation maps, but cannot measure the contrast map or point-spread functions. It can be implemented as a clip-on for any high-contrast spatial light modulator. The *DLP Projector* prototype involves of a Mitsubishi PK10 pocket projector (DMD) and a 50×40mm diffuser as a projection screen, at 800×600 in pixel resolution reaching $62\mu m$ in pixel pitch. A pinhole mask (pinhole radius of $100\mu m$) is placed $60mm$ away from the screen, and a 16-diopter lens is $62mm$ away from the mask. This setup uses a single-pixel pattern and has a scanning resolution of $56\mu m$ on the crystallin (Figure 4.9(b)). The *Cell phone* setup uses a Samsung Behold II (180DPI or $141\mu m$ on pixel pitch - Figure 4.9(c)), with a static pinhole mask (pinhole radius of $100\mu m$) placed $40mm$ from the display, and a 25-diopter lens placed $40mm$ from the mask. Using a 3x3-pixels pattern on LCD_1, the scanning resolution is $370\mu m$ on the crystallin.

The masks are composed of 5 pinholes (Figure 4.9(e)), where the central one performs the measurement and peripheral ones serve as reference points. For instance, for a pupil radius of $\approx 1.5mm$, blue reference points drawn $5mm$ off-center reach the crystallin close to the pupil border and are projected at $0.3mm$ from the foveal center.

4.4.1 Controlled Evaluation

Proposed methods are evaluated using a camera focused at infinity, with diffusers placed at the center of a compound DSLR lens, as shown in Figure 4.5(a). The user manually change patterns seen through a live-view on a PC which is connected to the camera,

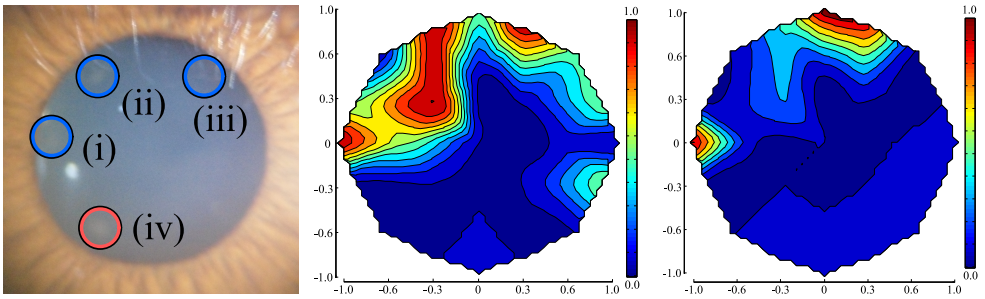

(a) Subject's Picture (b) Opacity Map (c) Attenuation Map

Figure 4.11: Opacity and attenuation maps for one subject. (a) Picture of the cataract-affected eye. (b) Linear interpolated opacity map showing scattering regions highlighted by (i), (ii) and (iii). Spot (iv) cannot be found in measurements. Attenuation map (c) resembles the opacity map and reveals a required increase of 70% on the red parts to allow the subject to observe the same intensity as a beam going through the center of eye. The Subject was asked to rest between opacity and brightness matching tests, requiring a realignment of their position using the reference points.

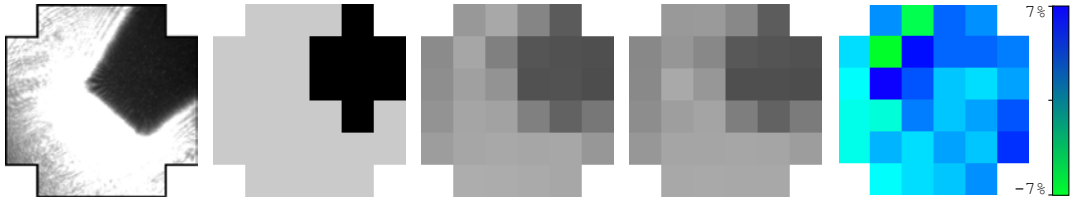

(a) Cataract (b) Opacity (c) Measured (d) Estimated (e) Difference

Figure 4.12: Attenuation comparison for an entire round. Each pixel represents one estimation. (a) Shows the simulated cataract; (b) the estimated opacity map (c) pictures of each measurement spot; (d) the estimated attenuation map and (e) the difference between (c) and (d).

and find the parameter required for optimal matching. Each level of the method is verified independently of the others. For the accuracy tests, captured maps are compared against pictures taken in each estimated position for attenuation and PSF maps. The Canon 5D Mark II with $50mm$ lens and the C-mount Flea Camera from Point Grey Research with $16mm$ lens are used. Luminit diffusers with scattering angles of $5°$ ($7 \times 3mm$), $30°$ ($9 \times 4mm$) and $80°$ ($9 \times 4mm$) and a piece ($9 \times 6mm$) of a diffuse plastic bag are tested. Figure 4.5 shows the attenuation and PSF maps for a simulated cataract and its respective visual effects.

Accuracy of the estimated attenuation maps is tested using the *DLP Proj. plus Mask* with the Flea Camera. Pictures of the scattered and free-path light beam were taken before the user adjusted the brightness level. For 289 measurement spots in 7 rounds randomizing diffusers, the accuracy of the attenuation levels in absolute average error is $1.03\% \pm 4.20\%$. Figure 4.12 shows opacity and attenuation maps for one round. Contrast-sensitivity maps were estimated using the *Dual-LCD Monitor* with the Canon 5D. The repeatability of the contrast value (Range $[0, 1]$) has an average error of 0.03 ± 0.03 for 116 measurements on 4 rounds.

Point-spread function maps were computed for the $80°$ and $5°$ diffusers. Using the Dual-LCD Monitor with a Canon 5D, the repeatability of the measurements in 128 tests points (4 rounds) was 0.03 ± 0.13 in normalized scale. PSF maps also represent the position and size of a cataract. The $80°$ of $36mm^2$ was measured as having $34mm^2 \pm 4.27$ and the $5°$ of $21mm^2$ was measured as having $29mm^2 \pm 8.55$ (Figure 4.13(a)).

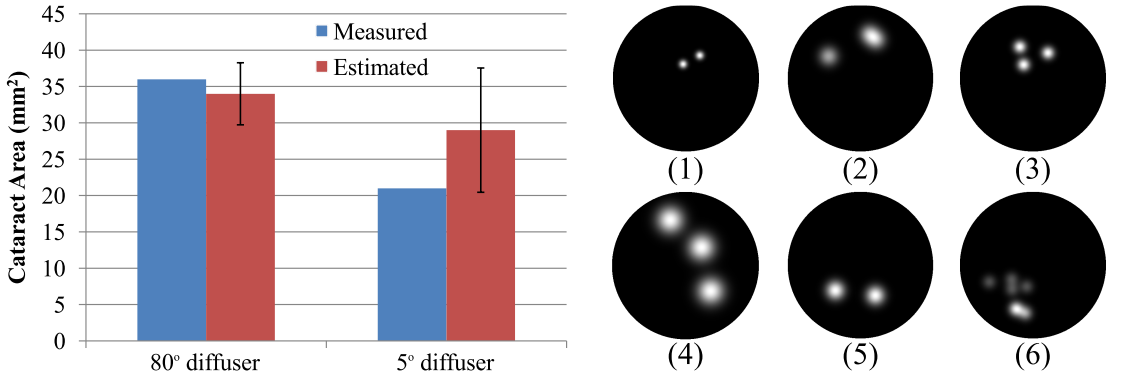

(a) Camera Cataracts (b) Volunteer Results

Figure 4.13: Accuracy comparison for size with two simulated cataracts on cameras (a) and a repeatability analysis in position (b) for subjects of Table 4.2. Each Gaussian represents the centroid (Equation 4.9) of the measured maps for one round with its σ as the standard deviation of centroids throughout subject's maps. The black disks represent the pupil size. (b) shows repeatability as good for (1, 3, 6), reasonable for (2,5) and very poor on (4).

S	Size	Centroid	Compensation
1	1.16 ± 0.07	$(\ \ 0.14, -0.45) \pm 0.23$	
2	0.68 ± 0.09	$(-0.06, -0.85) \pm 0.53$	$146\% \pm 12.29$
3	0.64 ± 0.15	$(-0.06, -0.57) \pm 0.35$	
4	0.36 ± 0.21	$(\ \ 0.21, -0.31) \pm 0.74$	$136\% \pm 2.77$
5	0.27 ± 0	$(-0.08, \ \ 0.45) \pm 0.52$	
6	0.45 ± 0.12	$(-0.43, \ \ 0.82) \pm 0.38$	$135\% \pm 6.9$

Table 4.2: Estimated size (mm^2), position off-center (mm) and attenuation values for 5 early cataract-affected volunteers (1-5^{th}) plus the scratched contact lenses (6^{th}). The compensation values show how much brighter the light ray that passes through the scattering region must be to match the intensity of a clear light path.

Repeatability for the diffuser's centroid is $0.01mm \pm 0.01$, computed by:

$$C = \frac{\sum a_i \overrightarrow{g_i} o_i}{\sum o_i} \tag{4.9}$$

where a_i and o_i are the i-th attenuation and binary opacity values. PSF tests took $\approx 7min$ for full 36-sub-aperture maps on cameras.

4.4.1.1 Cataract-induced contact lenses

A scratched contact lens in a zig-zag pattern generates a $\approx 0.5mm^2$ ($0.5 \times 1mm$) scattering region. Using the contacts, the viewer performed 9 measurements for opacity and attenuation maps. The estimated size of the scratched region is $0.45mm^2 \pm 0.12$ at $(-0.43, 0.82)mm \pm 0.38mm$ off-center. The average of the attenuation maps indicate the need for $135\% \pm 6.9$ of the brightness on the light rays going through the scratch when compared with clear-path brightness. Measurements were taken under a pupil radius of $\approx 1.8mm$. Notice that the contact lens may rotate when the subject blinks during the test. Tests were made using reference points (Figure 4.6).

4.4.2 User Evaluation

Eighteen subjects tested the cell-phone-based prototype (Figure 4.14). Each subject took the test twice for training, and at least twice for data collection. 5 early cataract-

Figure 4.14: Final cell phone prototype for user evaluation showing maps for opacity and density. Picture by Jonathan Williams.

affected volunteers (ages 68 to 76 and one 30-year-old) trained for $\approx 10min$ and tested for $\approx 10-15min$. Subjects with no cataract took $3min$ on the training and testing sessions. A single screening round for the opacity map (no user interaction) runs in $10secs$. Each map measures the observed attenuation for 24 testing points. Estimated values are shown in Table 4.2 and Figure 4.13(b). Figure 4.11 shows the estimated opacity and attenuation maps for a volunteer compared with a picture of his eye. Additionally, 14 healthy eyes were scanned and no cataract was found. Quantitative accuracy tests comparing the captured maps against slit-lamp pictures could not be reliably performed because of low-quality slit-lamp pictures. All tests were made using reference points to control eye motion. User study was performed according to approved procedures for human subjects, and employing de-identified volunteers.

For these experiments, it is assumed that subjects do not have optical aberrations (those who need them took the test wearing his corrective lenses) and a thin lens system[1] for the model of the eye. Thus, α in Equation 4.1 can be approximated by $\tan\alpha = l/f_e$, where f_e is the axial length of the eye, which is the reciprocal of the optical power at point k. $f_e = 25mm$. In these calculations $c = 3.15mm$.

4.5 Clinical Trials

4.5.1 Indian Clinical Trial at the Lotus Eye Hospital

Cataract opacity maps were captured for 80 eyes (mean age 41.61 ± 15.82) using a Samsung Galaxy S cell phone prototype and were compared with 80 slit-lamp pictures. All procedures were executed in August of 2011 in Mumbai, India and hosted by the Lotus Eye Hospital [2]. Inventors were not involved. Instead, patients were instructed by medical students through local translators. The cataract assessment was conducted by an ophthalmologist. There was no interchange of the measured information among inventors, doctors and patients during the test.

Unfortunately, given the low quality of slit-lamp images (*i.e.,* Figure 4.15), it was impossible to measure the size or density of the cataract. Researchers were unable to establish any correlation with this data.

[1] lens with negligible thickness

[2] Collaboration with Neel Patel from MIT Media Lab and Prema K Chande from Lotus College of optometry.

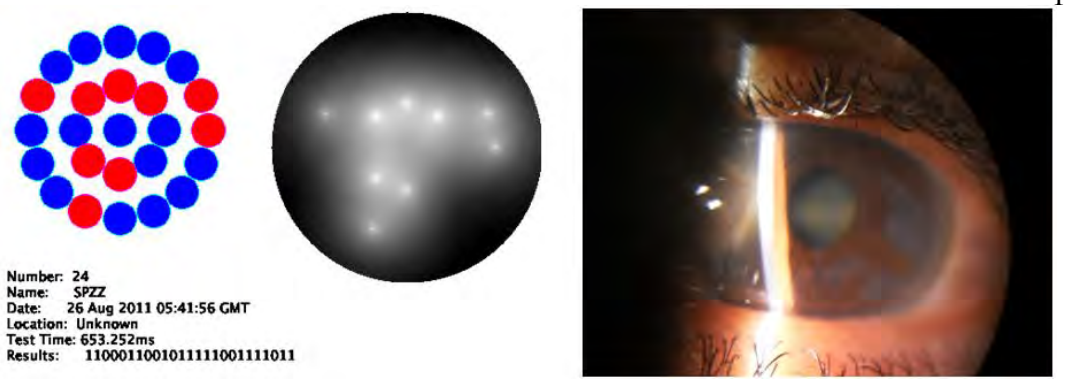

Figure 4.15: Comparison of CATRA results against the best slit-lamp picture of the captured dataset. Red circles indicate a covered subaperture. Although one could qualitativelly compare the results, the lack of high-quality images of the cataract challenges a proper validation of the device.

4.5.2 Mexican Clinical Trial with VOSH

Cataract opacity maps were captured for 47 eyes (age 68.46 ± 13.43) using a Samsung Galaxy S cell phone and were compared with subjective grading (LOCS III). 8 eyes were removed from the analysis due to previous eye surgeries. All procedures were executed in February of 2012 in Sonora, Mexico and were hosted by the Pitic Rotary Club [3]. Inventors were not involved. Patients were instructed by an optical engineer through local translators. The cataract assessment was conducted by an ophthalmologist. There was no sharing of the measured information among inventors, doctors and patients during the test.

In this prototype, the test phone is being controlled by another phone. The patient looks inside the eyepiece and tells the technician when the pattern fades away. The technician marks the region on his device, which captures and stores anonymized data. Captured maps are compiled into the number of sub-apertures along with data on the presence of opacities. It is assumed that the amount of affected sub-apertures is correlated with the doctor's subjective ranking. LOCS III is a common classification of the cataract size and is based on backscattering images of the lens. The clinician grades from 0 - no opacity - to 6 - mature cataract - for the distribution of nuclear (NC) and posterior sub-capsular (PSC) cataracts. Since CATRA measures NC and PSC as one single type an the clinician must indicate the cataract size for each condition, the sum of the LCOS ratings should correlate with the amount of sub-apertures blocked. 25 sub-apertures were measured in the Mexico study. Assuming a linear progression, each LCOS point (12 total) represents 2 sub-apertures.

37 eyes were mapped and then these maps were compared with LCOS III (Figure 4.16). The measurement map from CATRA is well correlated with LCOS ($r = 0.85$) and the two measurements were not statistically significantly different from each other ($p = 0.32$). There are little or no correlation between a difference in the grading and age ($r = -0.04$) or the presence of glaucoma ($r = 0.0$), diabetes ($r = -0.19$), high blood pressure ($r = 0.11$), refractive errors ($r = 0.22$), and current usage of eyeglasses ($r = -0.27$). Of the 37 eyes, 15 were clear on CATRA of which: 6 actually had clear view, 6 had very early posterior sub-capsular cataracts (PSC < 1) and 3 subjects had PSC at level 3 (3 false-negatives). There were no false positives. An additional 16 eyes could not see the dot through the eyepiece. Of these, 8 eyes had severe cataract impairment

[3] Collaboration with Daryl Lim from MIT Media Lab and Geetha Parasuram, Susan Ferguson, Matt Gill, David Stacy from Volunteer Optometric Services to Humanity (VOSH) Arizona.

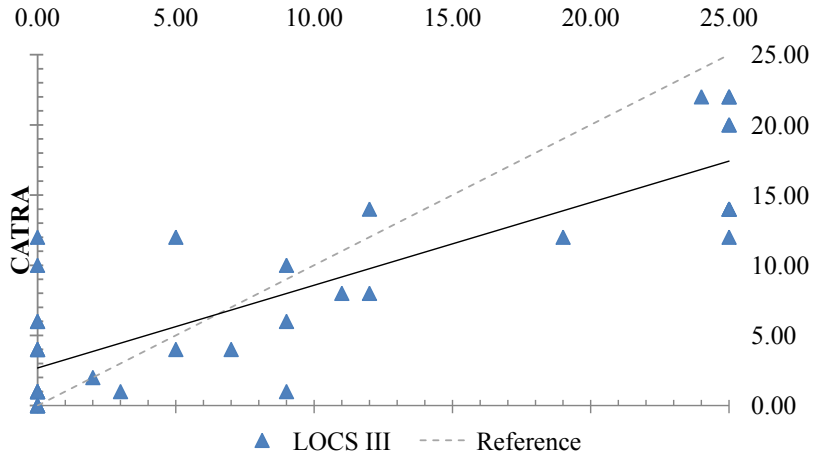

Figure 4.16: Number of occluded sub-apertures measured with CATRA vs LCOS III classification. Dashed line is the ideal case while the solid line is a linear regression on the data.

(NC/PSC > 3), 5 individuals had medium impairments (NC/PSC 2), and only 1 subject had an early PSC (PSC < 1).

4.6 Discussion and Conclusion

This chapter presented an interactive method coupled with an optical design to detect early cataracts using view-dependent, high-contrast displays. Early cataracts are a global health problem that previously required highly-trained technicians and cumbersome equipment to be detected (Table 4.3). This innovation measures the forward scattering profile and creates the PSF of the crystalline with no need of a coherent light source and no mechanical apparatus. *CATRA* ensures the projection of patterns directly onto the fovea to avoid gazing issues. Users look through an eyepiece and interact with a keypad based on what they see. An interactive method scans the subject's crystalline lens to estimate opacities, attenuation levels, contrast-sensitivity, and sub-aperture point-spread functions. Section 4.4.1 validates the optics of the device and the implemented mathematical models. Small variations in attenuation (1%), contrast (3%) and PSF (3%) maps indicate the consistency of the proposed technique. User-driven validation experiments attested to the precision of the method (maximum $\sigma = 0.2mm^2$ in size, $\approx 2\%$ of the pupil area), the forward scattering feature (estimated attenuations on $\approx 140\%$), the gaze control mechanism of the optical design (maximum $\sigma = 0.7mm$ in position, $\approx 20\%$ of the pupil diameter), and the stability of the foveal projection on early cataract-affected elderly subjects (Section 4.4.2). Clinical evaluations in Mexico achieved 85% correlation between CATRA and the clinician's subjective evaluation (LCOS III). This patient-centric device is the first of its kind, providing quantitative results far superior and more consistent than any existing like mechanism. Reasonable repeatability rate and the complete absence of false positives are incentives to continue this investigative research.

This chapter also introduced tools to understand a cataract-affected visual experience, that has been unexplored by the graphics and vision communities. The simple presence of opacities might already indicate glare issues, but a complete contrast, or PSF map, can give a more detailed profile of the effects on how of cataracts on seeing scenes with high dynamic ranges. A PSF mapping tool provides a new opportunity for doctors and patients. Renderings help to improve this relationship through a shared visual experience, which enables a dialogue between doctor and patient that advances the assessment and diagnosis of cataracts.

Features	Slit-lamp Acuity Tests	Scheimpflug	Retro-illumination	Shack-Hartmann	Opt. Coherence Tomography	CATRA
Scattering	Back	Back	Back	Fwd	—	Fwd
Training	High	High	Med.	Low	High	Low
Data Log	No	Comp.	Comp.	Comp.	Comp.	Phone
Mobility	$> 5Kg$	$> 5Kg$	$> 5Kg$	$> 10Kg$	$> 10Kg$	$< 300g$
Speed	Slow	Slow	Fast	Fast	Med.	Fast
Scalability	Costly	Costly	Costly	Costly	Costly	Easy
A.C. Need	Yes	Yes	Yes	Yes	Yes	No
Networked?	No	No	No	No	No	Yes
Self-Eval.	No	No	No	No	No	Yes
Method	Subj.	Subj.	Obj.	Obj.	Obj.	Subj.
Early Cat.	Hard	Hard	Hard	Yes	Yes	Yes
Accuracy	Doc. Skills	Doc. Skills	Doc. Skills	High	High	High
Cost	$\approx 5K$	$\approx 2K$	$\approx 5K$	$\approx 15K$	$\approx 10K$	≈ 302

Table 4.3: Comparison of CATRA technique against current available technologies and research tools. Costs are a very rough estimative for magnitude comparison. Some cheaper options may exist. CATRA does not require high-resolution devices and thus it can be used in the currently available ones. A Smartphone is included in the cost for CATRA.

4.6.1 Limitations

Since *CATRA* requires active user participation, it is limited by the subject's ability to follow instructions. Because it uses perceptual judgment and pattern matching, the technique does not work if a uniform-scattering cataract covers all the visible crystallin, as in advanced cases of the disease (natural aging does not necessarily create uniform scattering). Such uniformity could offset the attenuation and PSF maps, and for opacity maps, subjects would see dim patterns at all times, making it challenging to differentiate between clear and occluded scattering regions. The contrast map, however, should remain accurate and will reflect the regular contrast test that captures one contrast value for the whole pupil.

Pupil size may vary during the test, but these variations are estimated to be very small since the patient's eye is covered by an eye-cup. Retinal diseases may augment the results as well. Just like standard-wavefront-aberration maps of the eye, the proposed maps do not provide information regarding the aberration's depth inside the lens. This screening tool is also sensitive to refractive aberrations. While this could potentially cause problems, detecting conditions other than the target condition, CATRA overcomes this issue by taking aberrations into account and pre-warping light rays accordingly. Further clinical studies with wavefront aberration maps are required to precisely estimate their impact. According to the experiences of test subjects, a few degrees of myopia moves the projected dot or patterns in circles.

The dual-stacked-LCD shares some limitations with other similar designs such as a decrease in brightness and predefined viewing zones (DODGSON, 2009). The time-dependent nature of the solution removes crosstalk that would otherwise happening in static implementations using films instead of displays. The map resolution is a function of pixel density, distance between LCD screens, and the distance from the display to the

eye. Discerning the projected patterns and measuring the PSF may be limited by the current effective static contrast on LCDs. Yet, even with these limitations, the user is still able to obtain reliable, repeatable results.

4.6.2 Experiences shared on the user tests

Testing subjects were generally amazed that they could see their opacity map on a phone screen. One of the cataract-affected subjects had reported struggling to explain the visual effects of cataracts to his family, and the proposed rendering tool could improve communication and understanding in this situation and many others like it. Response from the local community has been very positive. Some users did find the alignment task difficult to understand, yet the captured data still showed a reasonable repeatability. Don Yansen, the CEO of Click Diagnostics, which provides affordable health care in developing countries gave this testimonial: “Village health workers will be able to cheaply and quickly flag early stage cataracts and macular degeneration in order to refer individuals to hospitals, where their vision can be restored before they effectively become blind”. During this research, one of the team members was able to self-diagnose his cataract that went undetected during his eye-exam a few months before the submission and was confirmed afterwards.

4.6.3 Reactions from ophthalmologists

Several researchers and local practicing ophthalmologists have collaborated on this project and are enthusiastic about its quantitative capabilities. Many of them have experimented with the device and they generally agree that reliable quantitative measurements for cataracts are on their own incredibly helpful for screenings. One of them commented that the Shack-Hartmann wavefront sensor, which measures high-order optical distortions of the human eye, had no practical application twenty years ago. Today, however, the high accuracy of these devices provides the only reliable data for LASIK surgery. Widespread availability of devices like CATRA, which generate quantitative data about cataracts, may benefit the future of diagnostic and surgical practice. Since cataracts are correlated with macular degeneration (LIU; WHITE; LACROIX, 1989), many doctors have suggested the use of this device as a side screening tool for other visual impairments. One of the biggest concerns reported by practitioners is what to do if the patient finds out about their condition, but there is no easy access for treatment or surgery. The use of the device, in this cases, may no actually help the subjects to tackle the cataract problem.

A few ophthalmologists reported strong concerns about the complete absence of a glare disability test in order to obtain a driver’s license. For instance, visual acuity tests generally do not detect glare and night driving effects, while tests such as CATRA, which are simpler and cheaper, would identify impairments which currently go unchecked. The overall goal of CATRA is to empower self-awareness about commonly unscreened eye conditions. It is important to stress that this device does not directly diagnose or treat for cataracts, but in the future, methods like this might be able to provide a complete summary of visual performance. The hope is that these early results will encourage future work in developing interactive tools which improve the understanding of the human visual experience.

5 NEUTRALIZING OPTICAL ABERRATIONS

This chapter introduces tailored displays that enhance visual acuity by decomposing virtual objects and placing the resulting anisotropic pieces into a wide range of depths, according to the user's visual needs. The goal is to free the viewer from needing wearable optical corrections when looking at displays. The tailoring process takes existing visual aberrations such as cataracts and refractive errors into account to place objects inside the subject's in-focus range. It splits an object's light field into multiple instances that are each in-focus for a given eye sub-aperture. The integration of these anisotropic light-field pieces projected onto the retina results in improved perception for observing light-field displays with the naked eye. The use of multiple depths to render each point of focus on the retina creates multi-focus, multi-depth displays. User evaluations were performed along with a validation procedure involving modified camera optics. This technology could pave the way for a new wave of devices catered to the user experience. Such advancements could alleviate the need for glasses in many daily tasks, incorporating tailored displays on head-mounted displays, televisions, e-readers, and games. Furthermore, they could be useful for tasks that require multi-focusing such as driving for farsighted individuals (*i.e. looking to the dashboard and to the streets interchangebly*) and the constant check of a portable device while doing other activities that require farsighted eyes.

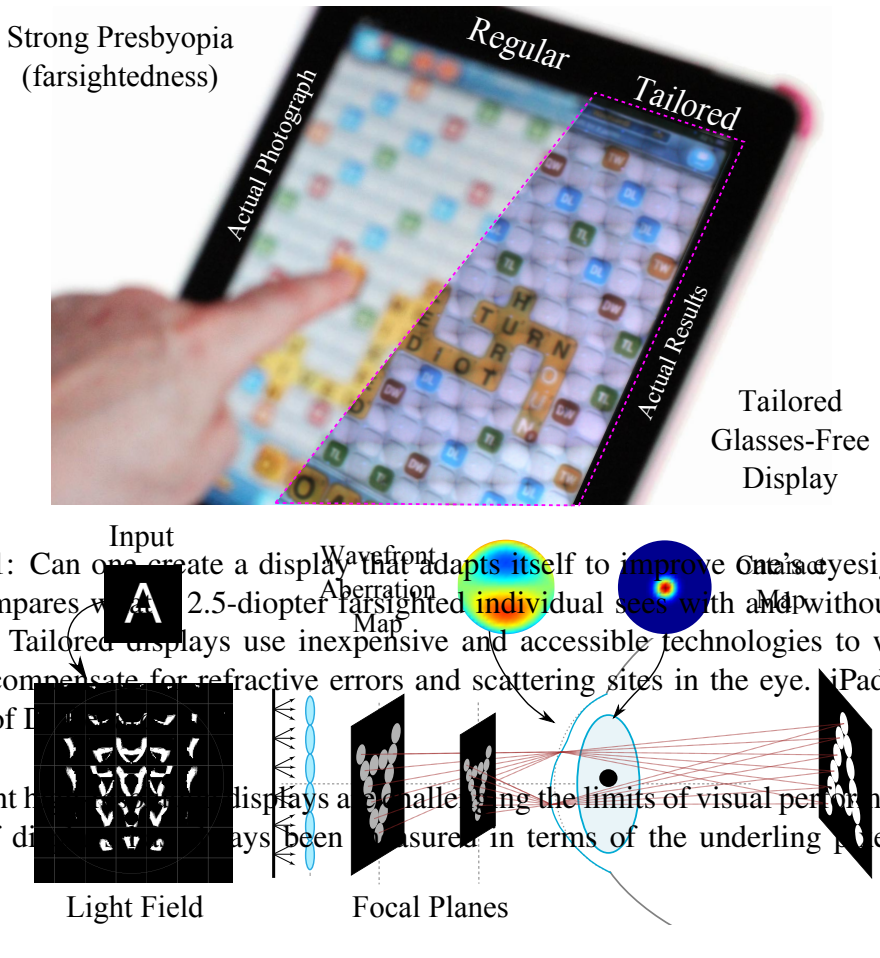

Figure 5.1: Can one create a display that adapts itself to improve one's eyesight? This figure compares what a 2.5-diopter farsighted individual sees with and without tailored displays. Tailored displays use inexpensive and accessible technologies to warp light fields to compensate for refractive errors and scattering sites in the eye. iPad picture's courtesy of I

Current h displays a challe ing the limits of visual performance. The quality of di ays been measured in terms of the underlying pixel density,

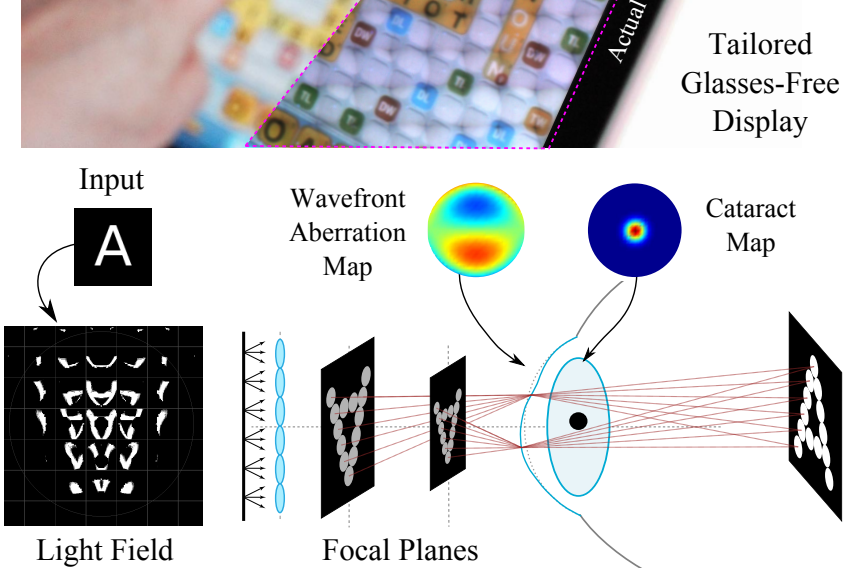

Figure 5.2: A 5-diopter nearsighted subject with nuclear cataracts and optical coma of 2 diopters observes an improved view of the letter ***A***. The device places the letter at two image planes cast to specific sections on the subject's eye.

which is now irrelevant due to the users' own lack visual acuity. Uncorrected eye aberrations decrease one's visual performance, creating sub-optimal, uncontrolled and heterogeneous user experiences. Current acuity enhancement options include wearable devices such as glasses or contacts which, besides providing a fixed correction, can be inconvenient in various daily activities such as sports, and LASIK surgery which is invasive and costly. This chapter explores new image-enhancement techniques based on light-field displays to improve vision without the shortcomings of existing devices. The approach uses holographic images adjusted to the subject's eye conditions. To some extent, this is similar to a adaptive-optics-based contact lenses, which are still under research. (LIANG; WILLIAMS; MILLER, 1997), but applied to the display instead of the eye. Tailored displays account for refractive errors (*e.g.*, nearsightedness, farsightedness, age-related visual degradation, astigmatism, and higher-order aberrations) and avoid scattering media on light paths, such as cataracts (Figure 5.1). Tailored displays have incredible potential for improving the lives of vision-impaired individuals by eliminating the need for inconvenient tools and invasive procedures.

Refractive errors and cataracts can be measured using modified parallax barriers in close range (PAMPLONA et al., 2010b, 2011a), or ophthalmic tools that range from high-end Shack-Hartmann wavefront sensing systems (LIANG et al., 1994; DONNELLY et al., 2004) to low-cost Snellen-chart-based visual acuity tests. Tailored light-fields correct for visual aberrations using a lenslet array on top of a high-resolution display or a small stack of LCDs. Aberration and scattering maps are used to pre-warp a light field, virtually placing the distorted anisotropic images into focused sub-aperture-dependent depths. The result is an enhanced image which is projected onto the retina, with significant decrease of out-of-focus blur. According to the research done for this section, this is the first step ever taken towards a corrective-display without eyewear.

5.1 Contributions

This chapter proposes tailored displays to compensate for spatially varied optical distortions of the human eye. The **contributions** include:

- Multi-depth displays that correct for aberrated vision. They support time-varying optical corrections without moving parts and use off-the-shelf components. These displays exploit current inexpensive technology to provide resolution close to and sometimes higher than a standard retinal resolution;

- A real-time rendering procedure for 3D displays which distributes virtual objects and their light fields into many focal depths according to the wavefront aberrations of the eye's aperture. Virtual objects placed inside one's accommodation range are tailored to compensate for cataract and refractive effects. An extension to support a multi-focus function is also presented;

Tailored Displays were evaluated by human subjects under conditions of myopia, presbyopia, hyperopia, astigmatism, keratoconus (high-order aberration) and cataracts with binary and color pictures. The same evaluations were also performed on cameras.

5.1.1 Previous and Related Works

Existing tools including eyeglasses with simple, bifocal, and multi-focal lenses, pin-hole glasses, contact lenses, LASIK and cataract surgeries, fiber optic tapers, adaptive spectacles (SUGIURA; MORITA, 1993; DOUALI; SILVER, 2004), and adaptive optics (THIBOS; QI; MILLER, 1999; LIANG; WILLIAMS; MILLER, 1997) can be used to enhance visual acuity. However, they require wearing external devices or incisions in the eye. Zooming into images up to the point the smallest detail has enough contrast to stand out against the out-of-focus blur may enhance acuity. However, the lack of high-spatial frequencies disrupts typical eye development and results in an increase in refractive errors (HESS et al., 2006).

5.1.1.1 Eye Modeling and Measuring Techniques

Previous research has looked at schematic eyes to understand the visual importance of their components. Barsky (2004) proposed vision realistic rendering by using wavefront data to render images that simulate the subject's vision. Deering (2005) used a model of cones in the retina to simulate a subject's perception, with their particular aberrations. Camp et al. (1990) developed a rendering technique that accounts for eye aberrations based on corneal topography. Although these works have pushed the scientific frontier by proposing measuring techniques that replicate aberrated vision, none of them proposes a solution to enhance visual acuity, and some do not account for individual variability but only for an average response. Pamplona et al. The previous chapters pointed out a duality between Shack-Hartmann and light-field techniques and showed how computer graphics can be used to measure and model some eye aberrations. Tailored displays tackle the inverse problem of measuring techniques, correcting for the measured aberrations and providing an improved acuity.

5.1.1.2 Vision Enhancement and 3D Displays

Tailored displays use glasses-free 3D display hardware (parallax barriers (IVES, 1903; ISONO; YASUDA; SASAZAWA, 1993) and lenticular-based displays (LIPPMANN, 1908)) generate displays catered to an individual's visual aberrations. Lanman et al. (2010) uses retinal integration to improve cues for convergence, while Wetzstein et al. (2011) recently discussed the benefits of a mask/LCD stack with more than two layers. Rather than addressing convergence cues, this chapter discusses how tailored displays exploit the use of 3D displays to compensate for aberrations on the eye. Multi-focus displays, such as those discussed by Akeley et al. (2004) and Hoffman et al. (2005), can enhance visual acuity by projecting images in the subject's range of accommodation. Goldring et al. (2006) has adapted a display with lenses to focus the image on the center of the eye lens improving readability. Liu and Hua (2009), and Rolland et al. (2000) also introduced dynamic lenses that change the plane of focus and a stack of planes that are selectively illuminated to create volumetric head-mounted displays. These techniques are helpful but inconvenient because they require moving parts and do not account for

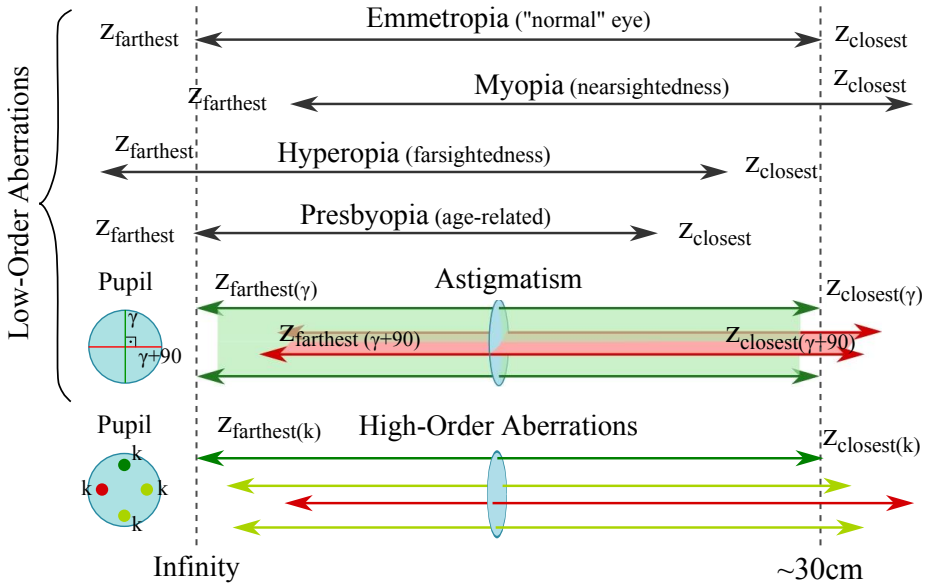

Figure 5.3: The focal range of distinct visual conditions. Myopia shifts the range closer, causing bad far sight. Hyperopia shifts the focal range farther, blurring near sight. Presbyopia reduces the accommodation power due to aging. Astigmatism has two principal focal lengths in perpendicular meridians due a toric curvature of the cornea or lens. Higher-order aberrations such as coma comprise of several focal lengths. Astigmatism and higher-order aberrations cannot project sharp images on the retina, blurring objects inside the subject's focal range.

non-symmetric aberrations, such as astigmatism, higher-order aberrations, and cataracts. Thibos et al. (1999) present wearable liquid-crystal spatial modulators to reshape the wavefront of light. Their work is scientifically sound but limited to 1.5 diopters with current technology. Tippie (2012) have successfully demonstrated, in simulation, the ability to reconstruct images from digital holography data to reflect visual aberrations on a camera. Alonso et al. (2007) use Fourier optics and the Wiener filter to invert the eye's point spread function and display a deconvolved image on a standard monitor, achieving 3% improvement on visual recognition tests. Huang and Barsky (2011) perform simulations of an "inverse blurring" operation to distort an image that would then be blurred by the out-of-focus eye (no cataracts and light fields involved). Creating a prototype based on their concept of a multi-layer display is a complicated task that requires the use of multiple high-dynamic-range transparent displays, which Huang and Barsky acknowledge are not realizable with current technology. This thesis adds to the growing body of glasses-free 3D display research by exploring a new degrees of freedom to the system: the individual's eye aberrations. Super-resolution screens (DIDYK et al., 2010) and superimposed projectors (JAYNES; RAMAKRISHNAN, 2003; DAMERA-VENKATA; CHANG, 2009) used in light-field systems can use tailoring methods to increase individual's acuity beyond average vision.

5.1.1.3 Light-Field Cameras and Refocusing

This work is the dual of previous scholarship on light-field camera correction. The optical basics of anisotropic displays are described in (NG; HANRAHAN, 2006; LEVOY; ZHANG; MCDOWALL, 2009). Isaken et al. (2000) introduce photographic effects in light-field rendering. Synthetic aperture concepts and camera calibration methods are discussed in (VAISH et al., 2004; LEVOY et al., 2004). Ng (2005) and Ng et al. (2005) demonstrate dynamic refocusing using light fields. Dai et al. (2009) and Jeong et al. (2005) propagate wavefront aberrations based on Zernike polynomials. In contrast, tailoring techniques center on the display and add support for refractive errors and cataracts.

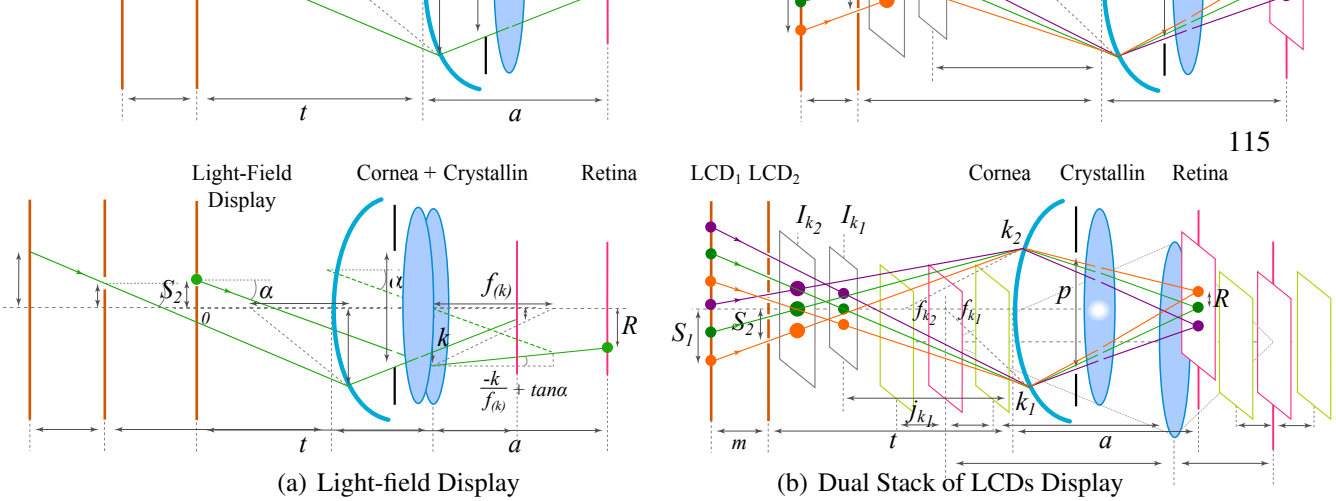

(a) Light-field Display (b) Dual Stack of LCDs Display

Figure 5.4: Schematics for the tailoring optical setup using: (a) an abstract light-field display; and (b) a dual-stack of LCDs. (a) the light-field setup is placed at a distance t from the eye, which has axial length (size of the eyeball) equal to a. A light-field ray from S_2 at an angle α reaches a retinal location R through a corneal point k. The focal length $f(k)$ comes from the eye's wavefront map, given as input, and drives the refraction of the light ray. (b) a dual stack of LCDs, placed m apart, implements a light-field display by showing patterns on LCD_1 and blocking or allowing desired light rays on LCD_2. In this example, the setup creates two image planes I_{k_1} and I_{k_2} (colored dots) to compensate for differences in focal lengths from points k_1 and k_2 in the cornea. Refraction of k_1 is stronger than k_2 ($f(k_1) < f(k_2)$). The distance j_{k_1} points out the depth at which a point conjugates to the retina when going through k_1. j can be seen as the depth at which the subject is focusing, but varying over the cornea. Image planes I_{k_i} are projected at the respective j_{k_i} distances from the eye. j also drives a magnification component ($-a/j_k$): the virtual image I_{k_1} (colored dots) is smaller than I_{k_2}. Each colored dot has its own rays that are cast towards specific sections on the eye.

5.2 Building Tailored Light Fields

The tailoring approach can be described as the projection of depth-dependent anisotropic patterns according to the spatially-distributed optical aberrations of the eye. Optical aberrations are represented as focal lengths on the wavefront map. The depth-dependent patterns are anisotropic images placed virtually at the right point in focus for a given optical power on the wavefront map. Figure 5.4(b) shows two image planes (I_{k_1} and I_{k_2}), each one for a given corneal point (k_1 and k_2). Since the optical power of k_1 is stronger than k_2, I_{k_1} must be placed closer and magnified accordingly. Notice how the individual light rays from respective objects on each image plane are integrated on the retina. Since images are placed at multiple depths to create a single focused image, the system has a *multi-depth* feature. The multi-depth feature breaks an object's light field into several parts and places them virtually into these depths, making sure they are seen only through eye sub-apertures with given refractive powers. Light paths that go through opacities or unpredictable scattering sites, such as cataracts, are not used to cast light. The final result is a light field displayed at a distance t from the eye.

Tailoring is the process of adapting a light field to compensate for an individual's inability to focus. It is performed in two main steps: (i) pairing light-field rays (S_2, k) and retinal positions (R) to designate a measure of raw intensity to each ray; and (ii) normalizing retinal "pixels" to avoid higher intensities in the image center, and noise due to an irregular discretization of the pupil area. An expected image on the retina (I_{Retina}) and wavefront and cataract maps of the subject's eye are input into the mechanism and produce a light field to be shown on a specific display. Using geometric optics and thin lens model, the relation between a ray from point S_2 on the display at an angle α and the

retinal point R is given by (Figure 5.4(a)):

$$\begin{aligned} k &= S_2 + \tan\alpha\, t \\ R(S_2, k) &= a\left(\frac{-k}{f(k)} + \tan\alpha\right) + k, \end{aligned} \tag{5.1}$$

where $f(k)$ is the focal length at position k on the eye's aperture, t is the distance from the light-field display to the eye, and a is the eye's axial length. $f(k)$ is computed from the wavefront map or through the interpolation of the user's prescription data. a is essentially a scaling factor, measured to a specific viewer (alternatively, one can use $23.8mm$, which is the average value of a human eye axial length (SCHWIEGERLING, 2004)). Energy I reaching the retina at point R is the integral of the incoming energy through all corneal points visible through a pupil with diameter p:

$$I_{Retina}(R) = \int_{-p/2}^{p/2} I_{Lightfield}[S_2(R,k),k]\; h(k)\; \mathrm{d}k, \tag{5.2}$$

where function $S_2(k,R)$ is obtained by solving Equation 5.1 for S_2. Values must be clipped afterwards to fit the spatial limits of the display. $I_{Retina}(R)$ is the accumulated intensity at point R on the retina. $I_{Lightfield}(S_2,k)$ is the intensity delivered by the light field through the corneal point k from position S_2 (Figure 5.4(a)). $h(k)$ is a binary visibility function for medium opacities (cataracts).

A trivial solution for Equation 5.2 can be obtained by creating a single light ray from S_2 to each retinal point R. The integral over the pupil would be removed, and only one k, say k_1 on Figure 5.4(b), would be used, creating a one-to-one mapping. The intended result of this equation would be the generating of one image plane (I_{k_1}) which could be seen sharply by the viewer. Although this technique works in theory, it requires a large amount of light for the image to be visible.

The use of many light-field rays to form each pixel on the retina (many-to-one mapping) enhances brightness, but requires a normalization step. The intensity of a light-field ray is then presented as the retinal intensity divided by the number of incoming rays $n(R)$ at each retinal position R:

$$I_{Lightfield}(S_2,k) = \frac{I_{Retina}(R)}{n(R)}, \tag{5.3}$$

5.2.1 Cataracts

Although the point spread function of a cataract can be measured, cataracts make it hard to predict where individual light rays fall on the retina. For this reason, cataract-affected areas are removed from the tailoring procedure using a binary function $h(k)$ on Equation 5.2, which is based on the cataract density function $c(k)$ (PAMPLONA et al., 2011a) and a threshold H. The threshold sets the cataract density so that effects are discreet:

$$h(k) = \begin{cases} 1 & \text{if } c(k) < H, \\ 0 & \text{if } c(k) \geq H. \end{cases} \tag{5.4}$$

The green circles on Figure 5.5(e) and (f) highlight where light rays are blocked by $h(k)$.

5.2.2 Accommodation

Tailored displays are used outside an individual's focal range, which changes with visual aberration (Figure 5.3). While multi-focus displays are mainly generating illusions realistic enough to make the subject accommodate to a given depth, a tailored display only

adjusts itself to project images on which the subject is already focusing. Focal lengths on a standard wavefront map f_{map} are captured with zero accommodation power ($A = 0D$). Since convergence drives accommodation (MADDOX, 1886), the overall environment makes the subject accommodate to the closest possible point on her focal range to the display. When a hyperopic subject converges on a close-by display, she accommodates to focus on the display. She cannot focus from a close range and thus her accommodation stops at the closest possible point of focus behind the display. For a myopic individual, if she converges on a far billboard, her accommodation follows convergence and relaxes the eye up to the most distant point at which she can focus, which happens to be before the billboard. The focal length f required for Equation 5.1 is then $1/f = 1/f_{map} + A$, where A:

$$A = \begin{cases} 0, & \text{if } t > z_{farthest}; \\ \frac{1}{z_{closest}} - \frac{1}{z_{farthest}}, & \text{if } t < z_{closest}; \\ \frac{1}{z_{focus}} - \frac{1}{z_{farthest}}, & \text{otherwise.} \end{cases} \tag{5.5}$$

where, $z_{closest}$, $z_{farthest}$, and z_{focus} are respectively the closest, farthest and the current point in focus for a subject. Nearsighted subjects (first case) have their eyes relaxed when looking at the display. Farsighted subjects (second case) use full accommodative power. In the third case, since the display is inside the accommodation range ($z_{closest} < t < z_{farthest}$), f is adjusted to the current eye focal length (z_{focus}). In this case, one can disable the computation and use a normal display instead.

5.2.3 Matrix Notation

a and t are fixed constants while $f(k)$ is fairly steady for each corneal position k_i over time. Equation 5.1, the S_2-R relation, can be re-written as an affine transformation (Figure 5.4(a)):

$$R(S_2, k) = \frac{-a}{t} S_2 + \left(\frac{-a}{f(k)} + \frac{a}{t} + 1 \right) k \tag{5.6}$$

$$R(S_2, k) = M \; S_2 + B_k, \tag{5.7}$$

where magnification $M = -a/t$ is a constant slope (assuming a is the standard eye axial length), independent of the subject's refractive errors. In matrix notation, the light-field computation is:

$$\begin{bmatrix} R_{1,k_1} & \cdots & R_{r,k_1} \\ R_{1,k_2} & \cdots & R_{r,k_2} \\ \vdots & \ddots & \vdots \\ R_{1,k_n} & \cdots & R_{r,k_n} \end{bmatrix} = \begin{bmatrix} M & B_{k_1} \\ M & B_{k_2} \\ \vdots & \vdots \\ M & B_{k_n} \end{bmatrix} \begin{bmatrix} S_{2_1} & \cdots & S_{2_r} \\ 1 & \cdots & 1 \end{bmatrix}, \tag{5.8}$$

where r is the number of spatial samples on the light field and B_{k_i} is the value for the y-intercept from Equation 5.7 for each sample k_i on the eye's aperture (*i.e.*, pupil). Wavefront maps, as captured by currently available Shack-Hartman systems, sample the aperture with a couple thousands points. Equation 5.8 is point-wise, making it suitable for GPU data-parallel computation. *Since the overall non-linear mapping plus normalization equation functions without image information, it can be pre-computed for a given subject's refractive errors, position and viewing direction.*

5.2.4 Implementation

Given a light-field display setup, wavefront maps $f(k)$, and cataract maps $h(k)$, the tailoring method computes the position R for every pair (S_2, k) by applying Equation 5.8. The number of accesses to each retinal point R are computed and stored. Given a

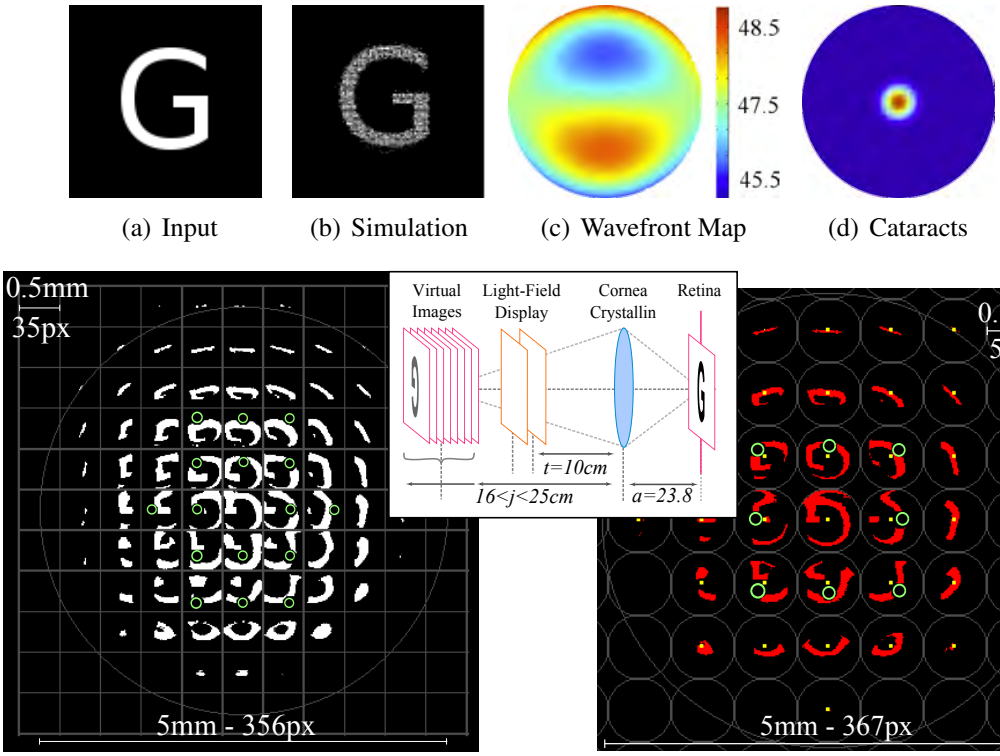

(a) Input (b) Simulation (c) Wavefront Map (d) Cataracts

(e) LCD_1-Lenslets (f) LCD Stack

Figure 5.5: Simulation for the letter ***G*** (a) with height of $\approx 0.90mm$ on the retina of a $2D$-coma, $+5D$-myopia (c), and cataract-affected (d) subject. ***G*** is virtualized at many depths ($16cm < j < 25cm$). (b) is a software simulation of the composed image reaching the subject's retina. (c) Wavefront aberrations best fitted with Zernike polynomials. A standard emmetrope has an optical power of $\approx 42D$ (infinity conjugated with the retina), plus $+5D$ of myopia takes it to $47D$ on average. Coma (blue and red regions on (c)) makes the refractive power change $\pm 1D$, from $46D$ to $48D$. (d) is a scattering density map, red means less than 50% of light passing through. (e) shows LCD_1 for a lenticular based prototype and (f) shows LCD_1 as red and LCD_2 as yellow for a dual stack of LCDs. Small quads in (e) mark the lenslets position and small gray circles in (f) mark its cross-talk limits. Giant gray circle reflects a $5mm$-diameter pupil. Notice how the letter is deformed behind each lenslet. Greenish circles in (e) and (f) highlight the cataract-avoiding feature of the algorithm. For these renderings: $t = 10cm$, $m = 13.8mm$ and $a = 23.8mm$. Retinal image (a) is magnified by $M \approx 8.4$ to $7.56mm$ in height at a distance $j = 20cm$ from the eye. Pinhole pitches ($0.5mm$ and $0.7mm$) are not far from the pixel pitch of a $90DPI$ display ($0.3mm$).

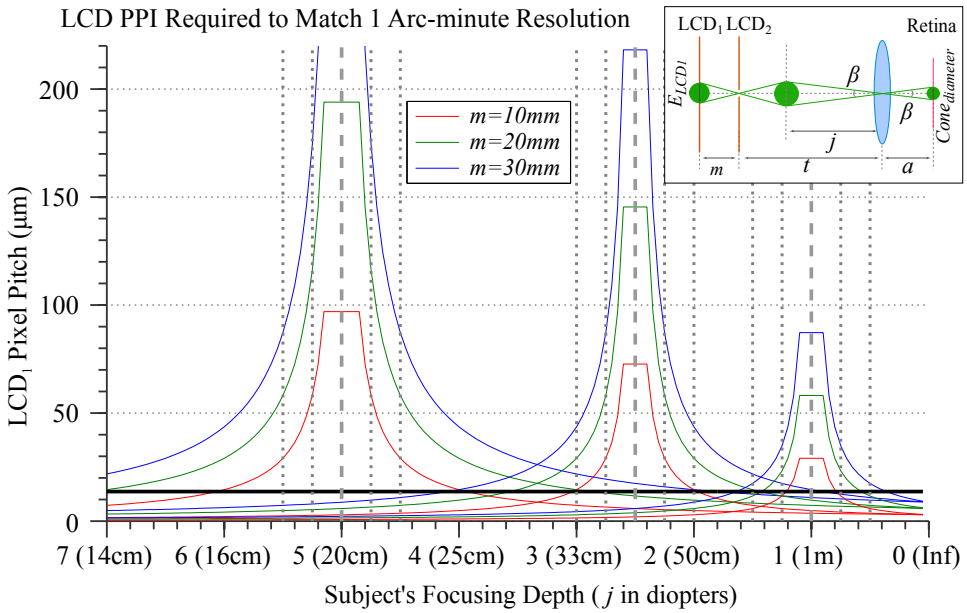

Figure 5.6: This figure shows the pixel pitch required to create virtual images that match the human 1 arc-minute retinal resolution. Nine tailored displays (peaks) positioned at $t = [0.2m, 0.4m, 1m]$ (bold dashed vertical lines), with $m = [10mm, 20mm, 30mm]$ as red, green and blue for each display. Each curve shows the required pixel pitch on LCD_1 for focal points j (Equation 5.9). As the subject's focus j moves away from the display depth t, the required pixel pitch for LCD_1 increases. The thinner dotted vertical lines highlight the subject focus point when the display is at close range, in steps of $.25D$. The horizontal line is the resolution of the LCD_1 of the evaluation prototype (1857 PPI). For focal depths above this line, the display supports virtual images in the eye's resolution. Peaks are cropped when $|1/t - 1/j| < 0.2D$. As m increases and/or t decreases, cheaper LCD panels can be used.

desired retinal image I_{Retina}, the system sets $I_{Lightfield}(S_2, k)$ from $I_{Retina}(R)$ and apply Equation 5.3 to normalize the intensity of each ray defined by $(S2, k)$. These light-field setups can be built using a dual stack of LCDs or with an LCD plus lenticular array. Ray discretization and the choice of ray tracing direction depends on the used technology. To avoid cross-talk, *the dual stack of LCDs uses forward computation*, from the light field to the retina, and (S_2, k) is discretized according to pixel pitch of both LCDs. *Lenticular setups*, on the other hand, *use backward computation* (from the retina and cornea to the light field), and are discretized on the I_{Retina} pixel pitch and the wavefront maps. Figure 5.5 shows how a computed light field looks for a dual stack of LCDs (f) with lenticular arrays (e). Further details are discussed on Sections 5.3 and 5.4.

5.2.5 Tailoring Color Displays

Using color images as input simply requires applying Equations 5.1 or 5.8 for each color channel. Since the pixel pattern must be taken into account, the striped pattern used on standard LCDs is preferred. Horizontal positions are shifted in steps of a third of a pixel to compensate for displacements on the panel. Since refraction is wavelength-dependent (2 diopters from $400nm$ to $800nm$ (CAMPBELL, 2010)), one would expect to have different corrections for each color channel. However, refractive variations among wavelengths also occur naturally in the eye and provide cues to the accommodative procedure. The eye focuses on a specific wavelength, which changes from subject to subject. The use of colors allows the accommodation process to sample two or more image planes and foresee the direction of focus (RUCKER; KRUGER, 2006). Although a tailored cor-

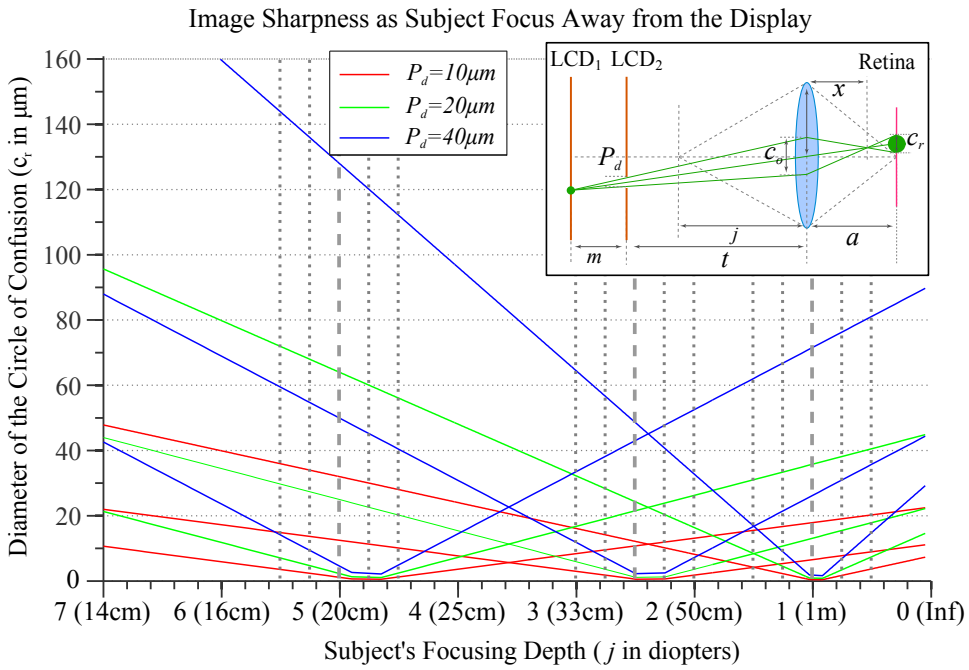

Figure 5.7: Diameter of the circle of confusion c_r created on the retina as a function of where the subject is focusing (j). Three pinhole sizes P_d are shown as red, green, and blue lines. Each circle of confusion line is plotted for three displays using $m = [10mm, 20mm, 30mm]$ and $t = [20cm, 40cm, 1m]$ (bold dashed vertical lines). As the subject's focus moves away from the display, the circle of confusion grows. The growth rate is defined by P_d. Thinner dotted vertical lines illustrates the subject's focal depth in steps of $.25D$

rection for each wavelength may increase visual acuity, to the best of author's knowledge, the eye response to this new stimulus is unknown. Notice that, color channels are not single wavelength but overlap in groups of wavelengths with different profiles among manufacturers. No additional color calibration needs to be performed. The test devices relied on the color calibration supplied by the manufacturer.

5.2.6 System Alignment

Device-eye alignment or calibration is required only for correcting high-order aberrations. For spherical aberrations (farsightedness, nearsightedness and presbyopia), $f(k)$ is constant across the cornea. As the subject's head shifts, the retinal image translates while the light-field pieces integrated on the retina remain aligned. Adjusting for astigmatism does not require translational, but rather rotational alignment. Misplacing the corrected angle of astigmatism (γ) creates undesirable blurriness proportional to the cylindrical power (C). For higher-order aberrations and cataracts, alignment is critical. As is the case with other glasses-free 3D displays, subjects must keep the computed position. In other words, the subject must search for the best angle to see the 3D effect and adjust their position to see the images clearly. For this reason, rendering images based on real-time eye-tracking systems could greatly simplify the user experience.

5.2.7 Resolution

The system resolution is dependent on the angular resolution of the light field, which is defined by the distance m, between LCDs or LCD-lenticular, and the pixel pitch of LCD_1. The Resolution of the system is given by the pixel size by arc-minute resolution of the depth-dependent virtual images (I_k) as they move away from the display. The

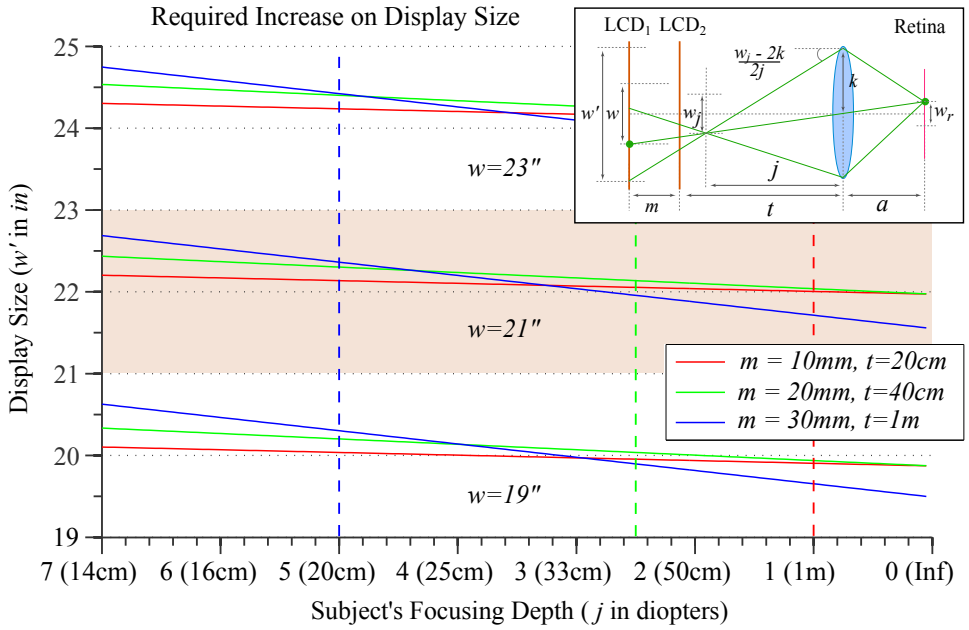

Figure 5.8: Screen size required by tailored displays as a function of the eye's focal point (Equation 5.10). To project an image of size w_r on the retina, a conventional display requires a w-long screen, while the tailored display must have the size of w' (y-axis). 3 screen sizes ($w = [19", 21", 23"]$) are plotted with varying $m = [10mm, 20mm, 30mm]$ and $t = [20cm, 40cm, 1m]$ as red, green and blue respectively. Here, j represents a spherical refractive error. For any given resolution, the optimal tailored display is larger than conventional displays.

LCD_1 pixel pitch required to match 1-arc minute resolution on the retina exists in today's technology (Figure 5.6). The light-field distribution can be placed a few diopters off the screen while the pixel pitch is still inside the retinal visual acuity. Virtual images are magnified by $M = -a/j$ on the retina. Behind each pinhole, segments of the virtual image are magnified by $m/(t-j)$, where j is the distance from the virtual image to the eye and computed by $1/j = 1/f(k) - 1/a$. To match an individual's retinal resolution β (*e.g.*, 1 arc minute), LCD_1 should have a pixel pitch (E_{LCD_1}) of:

$$E_{LCD_1} = \frac{m\, j\, \tan\beta}{t-j}. \tag{5.9}$$

Figure 5.6 shows a plot for Equation 5.9. The best setup parameters are application dependent. For instance, a monitor placed $t = 5m$ from the eye requires larger angular resolution - bigger m - compared to an e-book reader, which can run with a smaller m. Although Figure 5.6 is computed for the best perceivable image (1 arc-minute resolution), the display does not need to perfectly match the equation. For instance, the uncorrected visual acuity of a slightly nearsighted subject ($+1D$) is $\approx$ 13 arc minutes. Even if the display only corrects to 3 or 2 arc minutes, it still improves the visual acuity by 80%.

5.2.8 Display Size

An image displayed on a monitor with a diagonal of $w = 23"$ requires a light-field display with roughly the same size: $w' = w - p\,m/t$, where p is the pupil diameter. Refractive errors add variability to the spatial coverage, but they are insignificant compared to the image's size. The distribution of light among covered pixels follows a quadratic decay when reaching the display border. To minimize this decay, the light-field display

size must be:

$$w'(w) = \max_k \left(\left| \frac{w}{2t} \frac{-k}{j} 2(t+m) + k \right| \right), \tag{5.10}$$

where $1/j = 1/f(k) - 1/a$. Additional brightness decay is caused by the tilt of the available cone of light. Each pixel on the virtual image plane I_k is a cone vertex connected to the pupil border. The pupil and the light-field display planes are conical sections with variable area but become circular when the vertex is on the optical axis, and elliptical when the vertex is off the axis. As the cone vertex moves away from the optical axis, keeping the same depth j, conical sections shrink, dimming the borders of the image by gathering less light from the light field. Both decays are normalized by the loss of brightness as described in Equation 5.3.

5.3 Dual LCD-Stack Tailored Display

Light field displays can be implemented by stacking two off-the-shelf LCD displays. The first LCD shows distorted patterns while the second LCD blocks light in specific directions. Known as parallax barriers (IVES, 1903; ISONO; YASUDA; SASAZAWA, 1993), these hardware setups coupled with smart algorithms are typically used to create 3D stereoscopy by projecting images for the left and right eyes. In this case, however, the algorithms presented for tailored displays do not account for the subject's eye parameters: focal point, low and higher-order aberrations, and cataracts.

On parallax barriers, the transformation is modeled as an image convolution. Given a desired retinal pattern I_{Retina} and a pin-hole array I_{LCD_2}, a cross-talk-avoiding matrix for I_{LCD_1} can be obtained by convolving $I_{LCD_1} = I_{LCD_2} \otimes G$ and cropping the image behind each pinhole. On the presence of eye aberrations, the convolution do not warp the pattern itself, failing to integrate onto the retina. The tailored display uses a similar hardware setup that also warps the pattern as needed to additionally support the aforementioned effects.

A matrix of deformed sections of the desired retinal image is displayed on LCD_1. LCD_2 acts as a pinhole filter to position these sections properly on the retina. The warping transformation is different for each pinhole (Figure 5.5(e) and (f)). For low-order aberrations (nearsightedness, farsightedness, and presbyopia), changing pattern's position and size is enough to make it converge on the retina. For astigmatism, cataract and higher-order aberrations, however, the pattern itself must deform.

On the dual-stacked-LCD setup, the outgoing ray angle is given by $\tan\alpha = (S_2 - S_1)/m$ (Figure 5.4(b)). The pixel intensities on LCD_1 are given by Equation 5.3, while pixels (pinholes) on LCD_2 are set to the maximum intensity. The energy I reaching R is given by the sum of the product of LCD pixel intensities going through the cornea:

$$I_{Retina}(R) = \sum_{k=-p/2}^{p/2} I_{LCD_1}[S_1(k,R)]\; I_{LCD_2}[S_2(k,R)]\; h(k).$$

In practice, the discretization of the LCD pixels creates light rays with an area equivalent to the pixel size of LCD_1. As the pattern distorts, more energy is concentrated on the shrunken parts which will be stretched into bigger sections on the retina. These parts must emit more energy to maintain the brightness once it reaches the retina. The intensity of each light ray is the sum of energies over the area it covers on the retina, normalized by the number of incoming rays $n(R)$ at each retinal position R:

$$I_{LCD_1}(S_2,k) = \int_{R-q}^{R+q} \frac{I_{Retina}(i)}{n(i)}\,\mathrm{d}i, \tag{5.11}$$

where q is the equivalent radius of a single light-field pixel on the retina computed by:

$$q = E_{LCD_1} \frac{a(t-j)}{mj}. \tag{5.12}$$

where E_{LCD_1} is the pixel pitch/size of LCD_1. To avoid repeatedly evaluating the integral, one can use a summed area table to accumulate the intensities of the retinal image pixels. For instance, one can use a trilinear interpolation over a modified mipmapping-like procedure on the retinal image that finds only the sum of energies, on each level of the map instead of averaging them.

5.3.1 Avoiding Cross-talk

The presence of cross-talk creates ghost images, and random noise. Thus the mechanism requires additional computation to re-normalize energies on the retina. Tailoring avoids cross-talk by setting a minimum pinhole pitch (*i.e.*, the separation between two adjacent pinholes) $P_p = pm/t$ of LCD_2, where p is the aperture (pupil) diameter. Since most setups have working distance $t > 20cm$ (and hence $t \gg m$) and the pupil diameter is $9mm$ at most, the possible cross-talk area on LCD_1 is small. The pinhole pitch is usually smaller than $1mm$, close to a 90-PPI display pixel pitch.

5.3.2 Sharpness Analysis

The sharpness of the resulting imagery can be analyzed by measuring the size of the circle of confusion c_r on the retinal plane, which depends on the *pinhole diameter* P_d (Figure 5.7(top)). The diameter of the cone of confusion c_o on the corneal plane is given by $c_o = tP_d/m$ (assuming a locally flat cornea). When $f(k)$ is constant inside c_o, the circle of confusion mimics the one from an object at LCD_1, distance $t + m$ from the eye (Figure 5.7). Then $c_r = c_o(a - x)/x$, where x is the distance to the conjugate plane for LCD_1. Assuming a thin lens system: $1/x = 1/f(k) - 1/(t + m)$.

5.4 Lenticular-based Tailored Display

In this setup, LCD_2 is replaced by a microlens array. Compared to the dual-stacked LCD, it provides wider apertures for LCD_2. As a result, eye captures more light, enhancing brightness while preserving sharp images. Instead of a single ray coming from each pinhole in one direction, the eye lens converges on a bundle of rays (Figure 5.11). When properly designed, the entire bundle is focused into a single point on the retina. The relation among S_1 and R follows Equation 5.1, but $\tan\alpha = (L_c - S_1)/m$ where L_c is the lenslet center.

As a bundle of light rays reaches a sector on the cornea (red ellipse on Figure 5.11) and focuses onto R, the lenslet pitch must match the optical power of a corresponding sector of the eye. Variations on refractive power within the part of the cornea touched by the beam create blur. An optimal beam diameter (lenslet pitch) must expand to a corneal area with variations smaller than $0.16D$ (i.e., unnoticeable blur for 1-arc minute visual acuity). Since refractive aberrations are smooth and continuous, and the sample pitch of a high-quality Shack-Hartmann device reaches $209\mu m$ on the cornea (ROZEMA; DYCK; TASSIGNON, 2005), beam sizes of about $200\mu m$ are expected to cause minimum or no blur. $200\mu m$ microlens pitch is available by many lens arrays manufacturers today.

The bundle of light rays introduces another source of blur called **focus ambiguity**. The eye focuses at the projected image (j) and not at the depth the bundle represents. For instance, if m is equal to the lenslet focal length (f_L), the bundle of light rays becomes parallel (Figure 5.11), simulating an object at optical infinity. If the sector of the eye aperture that receives this bundle is not focusing at infinity, the point becomes blurred on

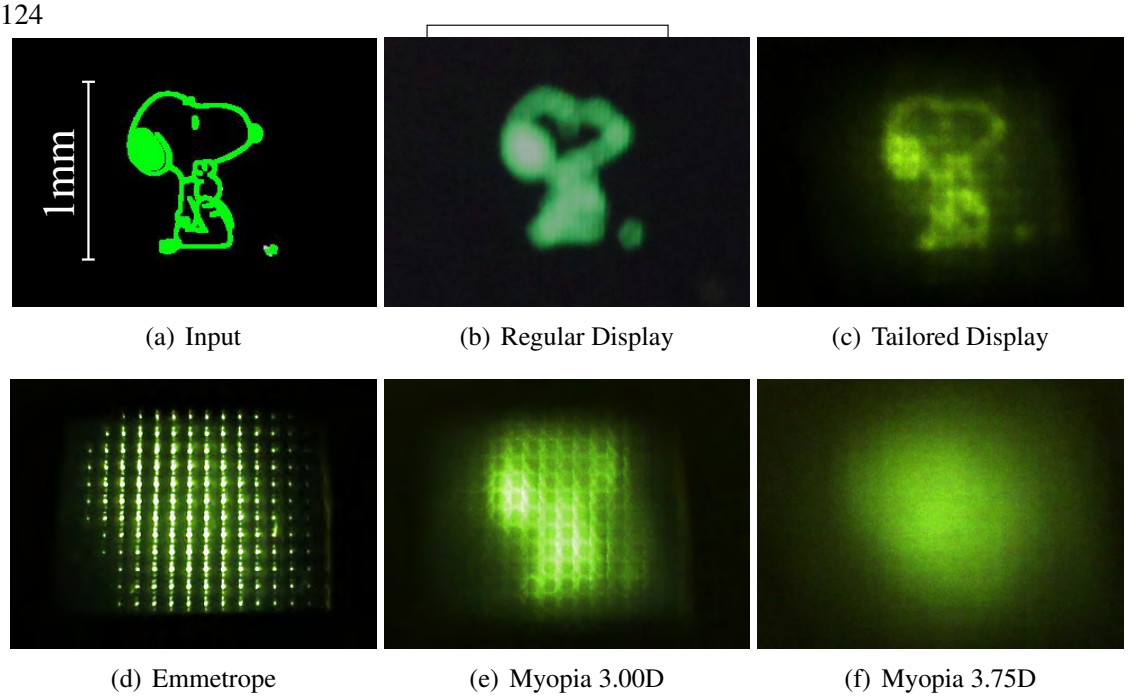

(a) Input (b) Regular Display (c) Tailored Display

(d) Emmetrope (e) Myopia 3.00D (f) Myopia 3.75D

Figure 5.9: Picture (c) reproduces the perception of (a), tailored for a $3.25D$ myopic vision. For comparison, (b) shows how the subject will see the image at a regular display. The tailored image plane is at subject's farthest focal point ($j = 30.7cm$) and the display is placed $t = 37cm$ away from the eye ($0.5D$ difference). This figure shows how precise the prototype is for very small focal changes in small images. To simulate this myopic perception, a $+3.25D$ optometric lens is placed in front of the camera's aperture focusing at infinity. The bottom row shows how subjects that do not match the tailored image perceive it: (d) an emmetrope focusing at the display; (e) a $3D$-myope (slight deviation from the tailored one) which focuses behind the tailored image ($33.3cm$) and (f) a $3.75D$-myope which focuses in front of the tailored image ($26.3cm$). The 150-px-tall image (a) is $\approx 1mm$ tall on the sensor and is magnified by $j/a \approx 5.6mm$ at the focal point. The pixel pitch at the virtual image plane is $\approx 37.3\mu m$ (0.4 arc minute). Pinholes have an area of 3x3 pixels ($P_d = 42\mu m$). This test utilizes small inputs to reach the limits of acuity: 0.55% of the picture area.

the retina. In the ideal scenario, each bundle must represent an object depth at j, which is dependent on the focal length $f(k)$ of the corresponding corneal area:

$$\frac{1}{m} = \frac{1}{f_L} + \frac{1}{j-t}, \tag{5.13}$$

where f_L is the lenslet focal length and m the distance between LCD_1 and the lenticular array. Since m is a parameter of the tailored display (constant for a given prototype), one can adjust it to minimize the blur for a few expected spherical cases (myopia, hyperopia and presbyopia). In the case of a tailored television, placed at $t \approx 5m$ from the eye, m would be very close to f_L since the first term dominates Equation 5.13. A tailored e-book reader, placed $t = 20cm$ from the eye, would have $m < f_L$, when $j > t$ (solving for far-sightedness), and $m > f_L$, otherwise (solving for very strong nearsightedness: $> 5D$ of myopia). As j approaches t, the optimal m becomes more significant. Tailored displays are not recommended when $j = t$. We used the same value of m in all evaluations. Optimizing m for a given device is useful to drive product designers to achieve the sharpest result when using the lenslet array approach and correcting spherical aberrations only. Once the device is built, m does not change.

In the case of astigmatism, cataracts, and higher-order aberrations, m cannot change

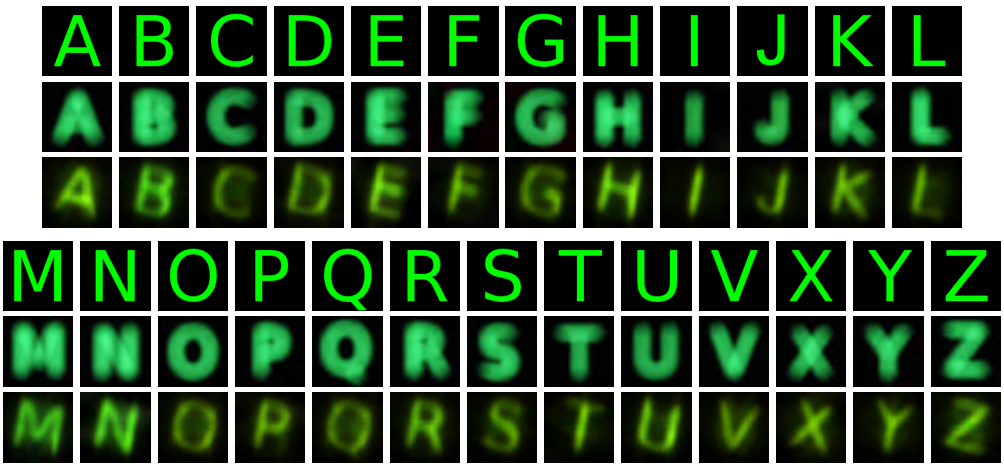

Figure 5.10: (top) Input images to the tailoring process. (middle) Simulated perception by a presbyopic subject of the respective target letters using a regular display. (bottom) Observation of the respective pre-distorted target letters but shown by the tailored display for the same presbyopic aberration. Subject's closest focal point is at $1.6D$ ($\approx 60cm$, behind the display). The camera is placed $38.5cm$ away from the display. $p = 28mm$, $m = 10.7mm$, $a = 70mm$. Images are $1.41mm$ tall on the retina, reaching $\approx 12.6mm$ on the virtual image plane. The pixel pitch at the virtual image is $0.125mm$ (0.69 arc minute resolution). In the trial runs, hardware misalignment produced slanted letters.

among sub-apertures. The bundle also simulates a virtual object through a cone of light that expands its radius as the virtual object depth grows. This allows the light to reach a bigger section of the cornea which may not have constant optical power (*e.g.,* , in the spherical cases). In the tests, m is equal to the lenslet focal length f_L, since beam radius at the corneal plane is constant to the lenslet pitch. The circle of confusion is entirely dependent on the subject's focal point, creating zero blur when focusing at infinity and linearly reaching $\approx 100\mu m$ of blur in extreme cases, such as myopia of $9D$.

To avoid the "ambiguity of focus" (focusing on the laser beam not on the virtual image), the system integrates numerous light bundles onto each retinal point. When subjects view these bundles, they cannot differentiate one from the other and thus does not attain focus on a single bundle stimulus.

5.4.1 Avoiding Cross-talk

Since lenslet pitch cannot be changed, lenslet focal length f_L is carefully chosen to minimize crosstalk using the equation $f_L = L_p t/p$, where p is the pupil diameter and L_p is the lenslet pitch. One can cover all odd (or even) lenses on the array using to reduce m by half and quadruplicate the amount of pixels behind each lenslet.

5.4.2 Energy normalization

For lenslet arrays, the energy I reaching R is the sum of the rays shining through the lenslet pitch L_p:

$$I_{Retina}(R) = \sum_{k=-p/2}^{p/2} \int_{\frac{-L_p}{2}}^{\frac{L_p}{2}} I_{LCD_1}[S_1(k+z, R)]\; h(k+z)\; dz \tag{5.14}$$

In practice, the integral is approximated by the product of the energy of the central light-ray ($z = 0$) by the beam area at the cornea. For spatially-variant refractive powers within $k \pm L_p/2$, such as in larger lenticular pitches, the integral must be computed. In these cases, the energy of a single pixel S_1 on LCD_1 reaches a retinal area around a central

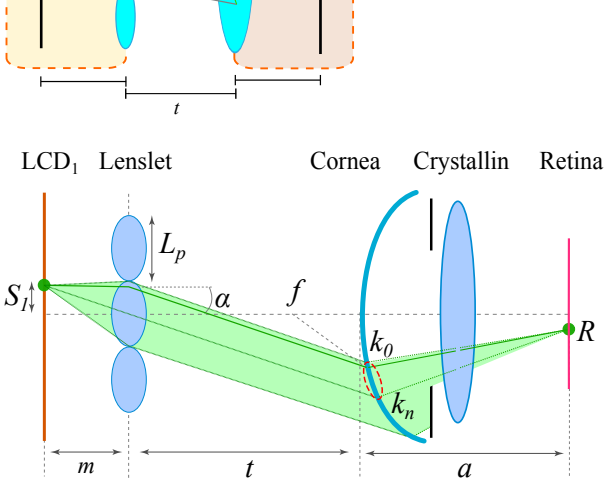

Figure 5.11: Schematics for the optical setup using a lenticular array. An LCD with a lenticular overlay implements a light-field display by drawing patterns on LCD_1 and directing light rays from the lenticular. A collimated bundle of light rays of angle α is focused from a wide region on the eye lens onto R. Variations in focal length inside the red-dot-stroked region ($k_0..k_n$) blurs R. In this scenario, m is one lenslet focal length from LCD_1.

(a) Occlusion (b) Input (c) Clean lens (d) Cataracts (e) Tailored

Figure 5.12: Cataract affected camera (a) sees the green smile (b) without correction (d) and with tailored correction (e). The normalized cataract density map (a) with a threshold of 0.4 (inner circle) is used as input. Rays reaching the sensor through the inner circle are removed. (c) how a non-cataract-affected camera would see (b). (d) decreases on intensity due to the use of pupil borders only. To take the picture $8mm$-tall diffuser is added on top of the camera lens. Here $t = 47cm$ and resolution of 0.87 arc minutes.

point R. $I_{LCD_1}(S_1)$ becomes the sum of I_{Retina} pixels inside the retinal area, with each retinal sample divided by the number of rays reaching it.

5.5 Prototypes and Evaluations

The dual-stack-LCD prototype uses components from an InFocus LP280 economy-class projector (Figure 5.13(a)). Two of the projector's monochrome LCDs ($1,857$ pixels per inch - PPI) are stacked $m = 10.8mm$ apart with three polarizers positioned in front, in between, and behind them. A standard LCD light box is placed behind LCD_1. A Canon T2i DSLR is positioned with the lens pointing towards the display with varying distance t to simulate eye aberrations. Optometric lenses with known optical powers and/or diffusers are added to the front of the camera to simulate refractive and scattering conditions. The head-mounted display prototype (HMD) uses a Vuzix iWear VR 920 for portable user testing (Figure 5.13(b)). Its $1,806$-PPI LCD is placed behind a 500-microns lenslets with focal length $12.5mm$ (Edmund Optics NT64-479). To minimize cross-talk, two 3x3 lenses are placed 1mm away from each other, covering all lenses. Figure 5.5 shows what the images for LCD_1 and LCD_2 look like when they are simultaneously corrected for myopia, cataracts, and coma. The proposed technique was evaluated in three rounds: (i) on small binary images to investigate the suitability of inexpensive LCDs to produce sharp images at retinal resolution for a variety of eye conditions; (ii) on colored

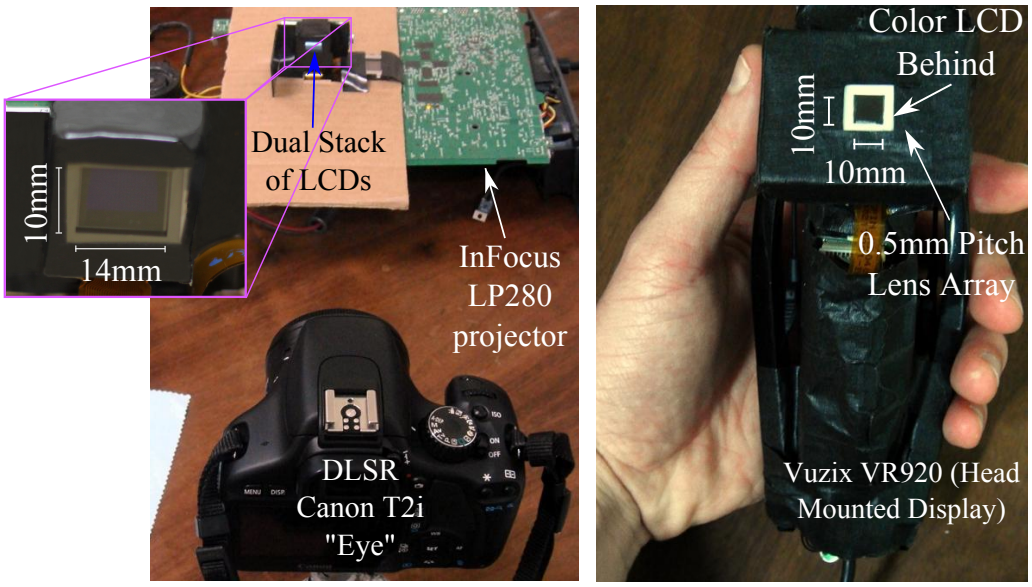

(a) Dual-LCD Projector (b) Lenticular HMD

Figure 5.13: Two of the built prototypes:(a) projector-based monochrome lcd-stacked display, and (b) head-mounted display with a lenticular array. Both LCDs have $\approx 1,800$ PPI and measure about $14x10mm$. The spatial resolution is limited by the small screen size. An array of LCDs is required to replace a standard monitor. The angular resolution, however, nicely fits to tailoring purposes.

light fields to investigate how an array of such LCDs would be captured by the imaging system; (iii) by user evaluations to check their effectiveness in correcting images for human subjects. All steps of the evaluation used small images so that even a tiny deviation (*i.e.,* $0.15D$ in the testes - Figure 5.9) could be easily observed.

5.5.1 Controlled Evaluations

5.5.1.1 Nearsighted evaluation

Figure 5.9(c) shows a picture from the dual-stack-LCD prototype correcting for a nearsighted subject who requires eyeglasses of $3.25D$ and sees the farthest focal point at $j = 30.7cm$. The display is placed at $t = 37cm$ from the eye. To simulate the optical distortion of this myopic subject, a camera is focused at infinity and a $+3.25D$ optometric lens is placed in front of it. (b) shows how the same subject would see the image on a regular monitor. The test image is only 1mm on the retina and the pixel pitch at the virtual image plane is $\approx 37.2\mu m$ (0.4 arc minute). By focusing the camera on LCD_1, one can simulate how an emmetropic individual (perfect vision) (Figure 5.9(d)) sees the same scene.

Figure 5.9 also shows how a subject with $3D$ and $3.75D$ of myopia would perceive the light field corrected for $3.25D$. Figure 5.9(e) and (f) reveal significant out-of-focus effects which contradict with the common ophthalmic understanding that an aberration of 0.5 diopters usually goes unnoticed. Although the system creates a correct image on the subject's focal point, its out-of-focus blur is not expected to be equal to a regular blur. The circle of confusion for a tailored illusion is a coded pattern rather than a uniform distribution of energies. The $1mm$ image, used in this example, enhances this effect, generating the overall blurriness of Figures 5.9(e) and (f). Small variation of .25 diopters strongly affect the visibility of projected images and thus, the success of this evaluation, even while using small images, demonstrates the precision of the setup.

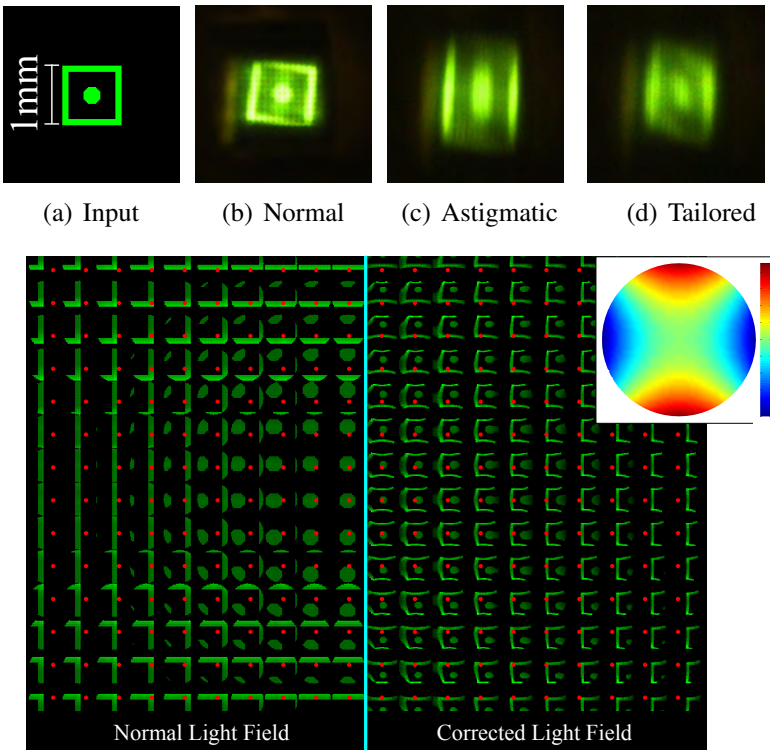

(a) Input (b) Normal (c) Astigmatic (d) Tailored

(e) Uncorrected and Tailored Light Fields

Figure 5.14: How an astigmatic subject sees the original green square (a) without correction (c) and with tailored correction (d). (b) shows how a non-astigmatic subject would see the same square. The light field for these pictures is shown on (e), with the uncorrected field on the left and the tailored light field on the right. The pinholes are the red dots in the images. Notice how in the tailored light field, the pattern deforms under each pinhole. This shows visually that the astigmatic wavefront map has aberrations of $1D$ in cylinder at the 180-degree meridian ($28 < j < 40cm$). While an emmetropic view sees the effects of astigmatism (c), a $1D$ astigmatic view perceives a corrected image (d). Here $t = 47cm$ and the resolution of 1.16 arc minutes.

5.5.1.2 Farsighted evaluation

Using the same evaluation strategy, Figure 5.10 shows 25 letters as seen by a $1.6D$ presbyope (farsighted) individual, for whom the closest point in focus was $j \approx 60cm$. This subject needed $+2D$ or $+3D$ on reading glasses. To imitate this vision using the setup, the camera was set to focus at infinity and a $+1.5D$ lens was inserted in front of it. The virtual image was created behind the actual display and reached 0.68 arc-minute resolution. The setup for hyperopes would be similar since like presbyopes, they cannot focus at close range.

5.5.1.3 Cataract evaluation

Figure 5.12 shows how a cataract-affected camera (a scattering site of $8mm$ diameter on the lens) sees a tailored light field according to Equation 5.4. Additionally, 2.5D myopia ($j = 40cm$) is applied to the camera in this test. Figure 5.12(a) shows the cataract density map. Light rays traveling inside the black circle are strongly scattered and produce glare. The method adjusts for this by generating a light field that passes only through the borders of the aperture, outside the black circle, avoiding scattering. Again, the image being used is small and requires a precise setup for tracing rays. Figure 5.12(d) shows how the cataract affected lens would perceive the pattern without correction. For comparison, (c) shows how a myope-only subject would see the same light field. (e) shows how the

(a) Input Image (b) Regular Display (c) Tailored Display

Figure 5.15: Input images (a) and how they are perceived on a tailored display by a farsighted subject (c). For this experiment, the HMD prototype was placed $t = 20cm$ from the camera which is serving as the eye in this setup. The camera simulated a subject whose closest focal point was $j = 50cm$ (subject using $+3D$ lenses). Picture (b) shows how the subject sees the input image (a), with same size, at the same distance on a standard monitor. Since the setups have small spatial resolution, an array of LCDs is mimicked by changing the displayed image to cover a bigger "retinal" area. (c) is in reality a collage (sum) of 64 combined square patches which create a 3.4 arc-minute image on the retina (each path $= 0.425$ arc minutes). The blue channel of (c) was adjusted to 75% of its captured intensity to remove prototype light leaking.

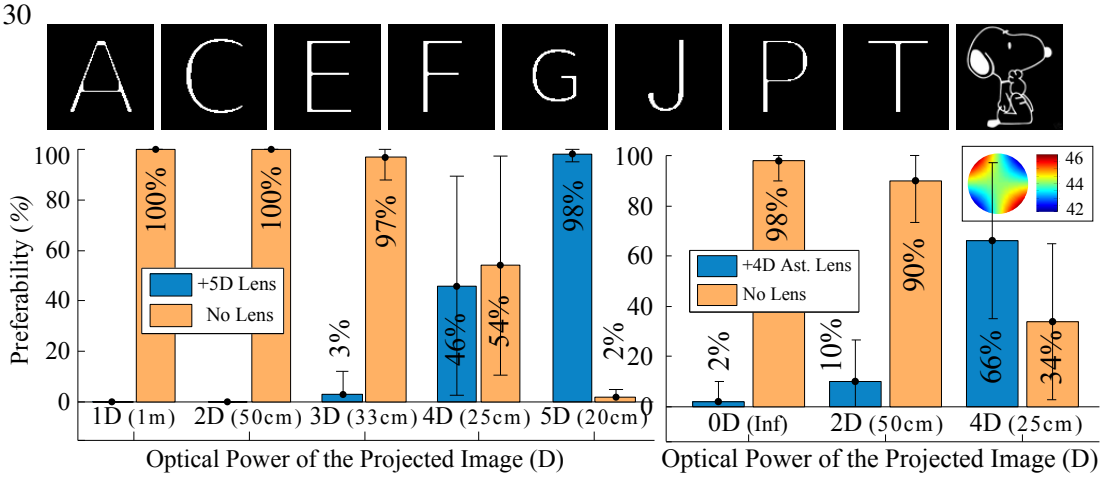

(a) Spherical (b) Astigmatism

Figure 5.16: (a) 13 emmetropes voted for the best readable view, with or without a $+5D$ lens (simulating 5D myopia), for tailored images from $1D$ to $5D$ myopia. As expected, subjects preferred to see images tailored for $5D$-myopia through the $5D$ lens. (b) 10 emmetropes voted for the sharpest view, with or without a $+4D$ astigmatic lens. The HMD prototype was placed $t \approx 7cm$ away from their eyes. A total of 189 votes were taken on (a) and 160 on (b). The 9 images at the top of the graph were shown twice with the two corrections. The error bars represent the standard deviation among subjects.

cataract-affected camera sees the tailored light field. Since the system uses the border of the lenses only, the brightness is diminished. The setup has a resolution of 0.87 arc minute.

5.5.1.4 Astigmatism evaluation

Figure 5.14 corrects for a spherical power of $2.5D$ of myopia plus an astigmatism of $1D$ at 180 degrees. This is a clear case where the virtual object spreads in space, from $j = 28cm$ to $j = 40cm$. The Zernike-fitted wavefront map shows the distribution of refractive aberrations over the eye's aperture. The input image Figure 5.14(a) is tailored for corrected ((e)-right) and non-corrected ((e)-left) scenarios. The pattern distorts under each pinhole. Figure 5.14(c) shows how an astigmatic subject would see a non-corrected light field. The square blurs vertically, following the strongest meridian in optical power. Figure 5.14(b) serves as a comparison, showing how emmetropes would see the uncorrected light field. Figure 5.14(d) shows the tailored light field for this eye condition. Although the prototype alignment between the two LCDs blurred the horizontal lines of the image, one can still see a squarish shape. The setup has a resolution of 1.16 arc minute.

5.5.1.5 Color evaluation

Figure 5.15 validates a color tailoring procedure with the HMD prototype. The images on column (a) are the inputs for the method. Tailored light fields are computed for a farsighted individual who's closest point in focus is at $j = 50cm$. The display is placed $t = 20cm$ from the eye who requires $+3D$ glasses. Column (b) shows how the subject sees the respective image with the same retinal size on a standard monitor at $t = 20cm$, the same distance as the tailored display. (c) shows how the subject sees the tailored light field. Since LCDs being used are very small (14x$10mm^2$), an array of LCDs is mimicked to cover a larger retinal area. The grid-like effect results from the images combining into one group. The resolution for each image pixel is 0.43 arc minutes. Figure 3.1(top) compares the view of a 2.5-diopter farsighted individual in regular and tailored displays. In the case displayed, $t = 38cm$ and the subject can only focus at optical infinity (*i.e.* she

had cataract surgery and her eyes do not accommodate).

5.5.1.6 *Real-time Performance*

The implemented GPU algorithm based on Equation 5.7, which utilizes color, achieves real-time performance (140 frames per second) on a laptop with a GeForce 8400GS on a full 1280x1024 frame. Its surprising ability to tailor videos without pre-processing is only surpassed by the intriguing notion that, if the wavefront aberration map could be measured instantly, tailoring displays could account for variations in teardrops in real time.

5.5.2 User Evaluations

Tailored displays were validated through three user-evaluation trials: spherical only, astigmatism and higher-order aberrations.

5.5.2.1 *Spherical aberration*

13 emmetropes (ages 21 to 27, mean 24 ± 1.88) simulated $5D$ of myopia by placing an optometric lens between their eyes and the HMD prototype. The software randomly showed 16 tailored light fields from $1D$ to $5D$ of myopia. Subjects had to choose which view was clearer, the one with or the one without the lens, for every light field. There were two expected outcomes from this trial: (i) subjects preferred the lens 98% of the time ($\sigma = 3\%$ among subjects) when the light field tailored for $5D$-myopia was shown (Figure 5.16); (ii) subjects chose to avoid the lens on 100% of cases when the light field was non-tailored. The virtual images which were projected from $j = 20cm$ and $j = 25cm$ during the test had resolution of ≈ 0.52 and ≈ 0.42 arc minute below, which below the standard eye acuity.

Interestingly, user preference was not linear with the correction growth (Figure 5.16). For tailored light fields from $1D$ to $3D$, subjects clearly preferred no lens (100%, 100%, 97%, respectively). This is likely because the subjects' eyes accommodate, compensating for distortions of $1D$, $2D$ and $3D$. For $4D$ cases, even though the accommodation power of most subjects increases to $5D$, the accommodation power to focus on a $5D$ tailored image is unsustainable. When subjects add lenses, the eye relaxes and the preference for the lens grows. Diversity in focal ranges among subjects explains the bigger error bars for $4D$.

5.5.2.2 *Astigmatic aberration*

In the second evaluation, 10 emmetropes (ages 23 to 27, mean 24 ± 1.6) selected the best view from a number of images ranging in acuity from a naked eye to a lens displaying astigmatic vision. The software randomly corrects images for infinity ($0D$), $2D$ and $4D$ of astigmatism at 45 degrees. Subjects preferred the lens designed to correct the image being displayed 66% of the time, whereas, they preferred no lens on 44% of the time. ($\sigma = 30\%$ among subjects). Some subjects focused on the spherical equivalent ($S_{eq} = S + C/2$) to overcome the blurriness generated by $2D$ and $4D$ corrected images when viewed without glasses.

5.5.2.3 *Keratoconus aberration*

In the last test, virtual images were tailored to a given keratoconic wavefront map (Figure 5.17(a)) taken from a Shack-Hartmann device. Keratoconus causes individuals to see bright objects doubled. The software displayed tailored and non-tailored light fields at random. A keratoconus-affected subject reported when he saw the double effect. 100% of doubled image reports occured when subject saw the projection of a non-tailored light field (Figure 5.17(b)). Users reported that 92% of the cases appeared to be corrected in

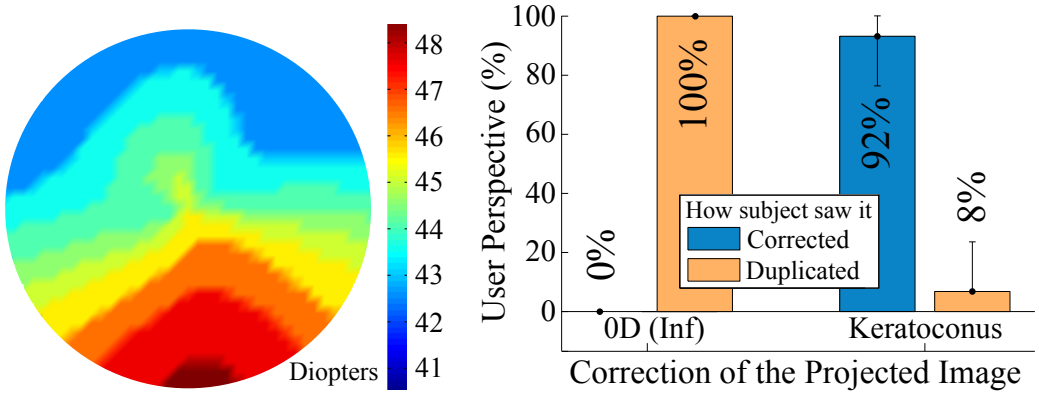

(a) Wavefront (b) Results

Figure 5.17: Subject with keratoconus (wavefront map in (a)) chooses which projection is better: not corrected and tailored for his specific map. Keratoconus is a condition which causes individuals to see bright objects doubled. Tailored displays corrected this effect in 92% of the images ($\sigma = 17\%$ on a 5 round test). A total of 80 votes were computed for source images in Figure 5.16(top).

tailored projections ($\sigma = 17\%$ among 5 rounds of tests with the same subject).

5.6 Multi-Focus and Stereoscopic Add-ons

Multi-focus capabilities for 3D scenes require converging light rays from out of focal range objects into points in front of and behind the retina so that the eye can decide which object to focus by using accommodation (Figure 5.18). Tailored light fields for single-depth projections are computed simply by using information about the subject's eye aberrations and a picture of the expected view only. To add the multi-focus dimension to the system, a depth component for each retinal point R ($I_{dpt}(R)$) must be added to the input. The additional depth coordinate per pixel is added to the axial length the eye (a) on the Equation 5.1.

Since the tailoring process adjusts scene depths to the subject's focal range, the scene depth $I_{dpt}(R)$ representation must be independent of global coordinates. Diopters are best for representing relative distances between object depths in the perceptual space. Refocusing for $1D$ feels similar for different depths. Accommodating from an object at optical infinity ($0D$) to one at $1m$ ($1D$) feels the same as focusing on objects from $33cm$ ($3D$) to $25cm$ ($4D$). Furthermore, accommodation speed is measured in diopters per second, which dissociates velocity from a global coordinate (CHARMAN; HERON, 2000). $I_{dpt}(R)$ in diopters preserves the affine transformation. Thus, a in Equation 5.1 changes to $1/(1/a + I_{dpt}(R))$, where I_{dpt} is the scene-depth map. Equation 5.7 supports the scene depth as:

$$\begin{bmatrix} S_{2_1}k_1 & \cdots & S_{2_r}k_1 \\ S_{2_1}k_2 & \cdots & S_{2_r}k_2 \\ \vdots & \ddots & \vdots \\ S_{2_1}k_n & \cdots & S_{2_r}k_n \end{bmatrix} = \begin{bmatrix} \frac{-t}{a} & tk_1 & -t & B_{k_1} \\ \frac{-t}{a} & tk_2 & -t & B_{k_2} \\ \vdots & \vdots & \vdots & \vdots \\ \frac{-t}{a} & tk_n & -t & B_{k_n} \end{bmatrix} \begin{bmatrix} R_1 & \cdots & R_r \\ I_{dpt}(R_1) & \cdots & I_{dpt}(R_r) \\ R_1 I_{dpt}(R_1) & \cdots & R_r I_{dpt}(R_r) \\ 1 & \cdots & 1 \end{bmatrix}$$

$$B_k = \frac{tk}{a} - \frac{tk}{f(k)} + k,$$

where positive values on I_{dpt} bring objects closer to the viewer. All units are in meters. Figure 5.18 also shows two examples of tailoring with multi-focus. To discover where

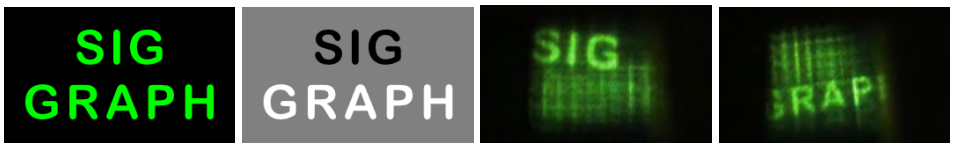

(a) Retinal Image (b) Depth Map (c) Simul. -0.5D (d) Simul. +0.5D

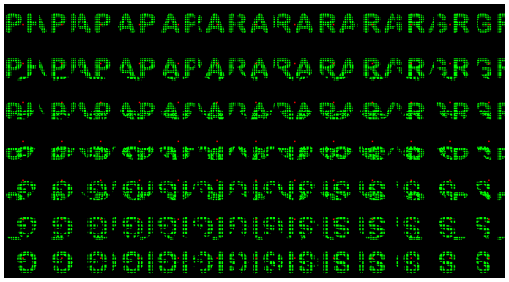

(e) LCD_1 (red) - LCD_2 (yellow)

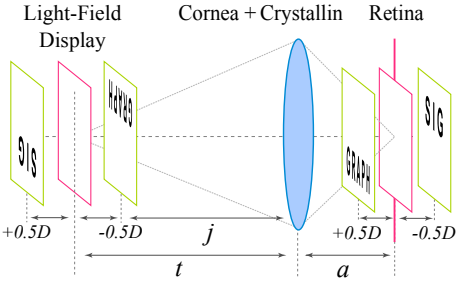

(f) Tailoring Optical Diagram

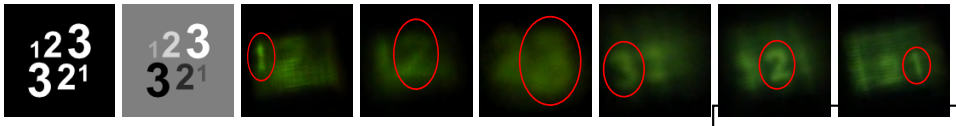

(g) Inp (h) Dpt (i) -0.5 (j) -1 (k) -1.5 (l) +1.5 (m) +1 (n) +0.5

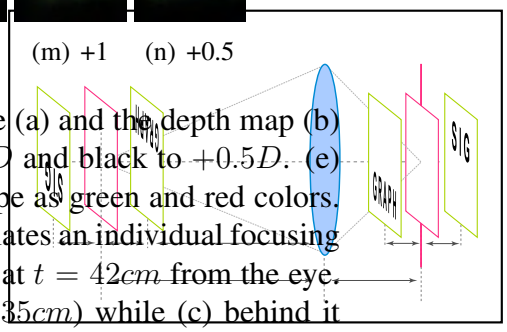

Figure 5.18: Multi-focus tailored light field. The retinal image (a) and the depth map (b) are inputs to the method. White pixels in (b) represent $-0.5D$ and black to $+0.5D$. (e) shows the LCD_1 and LCD_2 images for the projector prototype as green and red colors. Both depths are rendered on top of each other. (c) and (d) simulates an individual focusing $0.5D$ in front and behind the display. The display was placed at $t = 42cm$ from the eye. Virtual image of (d) is created in front of the display ($j = 35cm$) while (c) behind it ($j = 53cm$), inverting ***SIG*** on Figure (e). The bottom row shows a multi-focus correction for figure (g) with 6 levels ((i)-(n)) on the depth map (h): from $1.1m$ (k) to $25cm$ (l) from the eye ($t = 42cm$). Images are scaled for best visualization.

subjects are focusing, one can show numbers at different depths (Figure 5.18, bottom row) and ask the subject which number he sees.

Stereoscopy can be achieved by projecting two warped images per LCD pin-hole. For the sake of simplicity, the derivation presented has up to now assumed that the eye is centered with the light-field display (optical axis). For stereoscopy, the system will be aligned with the nose instead of each eye's optical center. Equation 5.1 must be adjusted accordingly.

5.7 Conclusion and Discussion

This chapter proposes novel multi-depth displays to compensate for visual aberrations and improve visual acuity sans glasses or contact lenses. It supports optical corrections for spacial disorders (higher-order aberrations and cataracts) and time-varying optical corrections (*e.g.*, daily changes on refractive error from diabetes). It has no moving parts and uses off-the-shelf components to accommodate for aberrations in real time. To the best of the author's knowledge, this is the first display technology capable of adjusting itself to subject's visual conditions. Tailored displays decompose virtual objects in many focal depths according to wavefront aberrations which exist in various sectors of the eye's aperture. As a single point of focus is distributed into many depths, it creates multi-focus multi-depth displays. Parallelization on GPUs is straightforward. Virtual objects are carefully placed inside one's accommodation range and warped to compensate for eye

aberrations.

The validation procedures and mathematical equations provided in this chapter have demonstrated that existing high-resolution displays can create colored virtual objects with a resolution around 1-arc minute, the standard acuity of the human eye. The prototypes used a modified LCD-stacked or lenticular-based light-field displays. User experiments confirm the system's ability to create corrected versions of virtual objects to target given eye aberrations.

The system is validated with small binary images and bigger colorful scenes in several environments: (i) presbyopic, where the subject cannot focus close (Figure 5.10); (ii) myopic, where the subject cannot focus far (Figures 5.9 and 5.15); (iii) astigmatic, where subject cannot sharply focus (Figure 5.14), and (iv) cataracts (Figure 5.12). User evaluations with spherical (Figure 5.16(a)), astigmatism (Figure 5.16(b)) and high-order aberrations (Figure 5.17) reveal users' preference for the tailoring technique.

The main takeaway from this chapter is that it is very simple to create holograms for the visually impaired. Since the subject is not focusing on the display, the system does not need to drive accommodation, which would be required to create realistic out-of-focus blur, and thus the need to produce an optical transfer function (2-dimensional Fourier transform of the point spread function of the image that is being created by the display) with negative values.

5.7.1 Limitations

One limitation of the tailored display is that like existing glasses-free 3D displays, the tailoring approach requires the subject's eyes (and thus head) to be fixed relative to the tailored display. Thus, real-time eye-tracking technology would increase the usability and range of uses for tailored display. Secondly, as is the case with similar designs, the dual stacked LCD has some limitations with regards to brightness, contrast, diffraction, and spatial vs. angular resolution tradeoffs, which are directly affected by the resolution capacity of the technology to which tailor display is applied (DODGSON, 2009). This is because the virtual image resolution is a function of the display's angular resolution and the distance from the display to the eye. Tailored displays require high-resolution pixel panels in terms of pixel-per-inch. Thirdly, retinal and other ocular diseases, along with changes in pupil size, which can distort the brightness equalization, may affect the presented results. However, these variations are easily trackable with a single camera or predicted with models for pupil light reflex (PAMPLONA; OLIVEIRA; BARANOSKI, 2009). The lack of total sharpness in the results from validation tests was due to: (i) lack of precision in the assembly of the hand-made prototypes, and (ii) the usage of only a tiny portion of the camera's sensor. Most of the results were cropped images that used only 0.55% of the area of the camera's sensor. Lastly, relatively long viewing distances are presumed so that one can assume: (i) a locally flat cornea, (ii) a flat retina or, similarly, a curved focal plane, (iii) isotropic distribution of light among cast rays, and (iv) an eye modeled as a calibrated thin lens system.

5.7.2 Applications

This work could be applied immediately for several uses without significant technological advances. These uses include head-mounted displays, digital wrist devices, tracking and monitoring tools, small-screen cell phones, and music players. All of these can be efficiently built with the inexpensive LCD panels used in our prototypes. Tailored displays have the potential to impact all daily tasks where eyewear is inconvenient. For example, checking the time or speed while running is hard for farsighted individuals, who cannot easily slip on reading glasses. By applying tailored displays to phones and wrist watches, they could eliminate the need for reading glasses and the cumbersomeness of

pulling them on and off every time the phone beeps with texts or emails. Tailored displays could also be used for several activities where a multi-focus function is necessary but currently undoable, such as tailoring the car dashboard. For people with high-order aberrations or cataracts, which cannot be corrected for with eyeglasses, tailoring displays are an interesting alternative to surgeries, which are invasive and may be inadvisable for patients with heart conditions, etc.

Tailored monitors would require near giga-pixel displays (23" on $1,857$-PPI requires 800-megapixel LCDs) and consequently several improvements in current hardware and software. Although the LCD panel industry is not evolving as fast as its digital camera sensor counterpart, the new uses for ultra-high-resolution giga-pixel displays presented in this work show that there is a clear market to be explored. Since the ever-increasing market value for high-quality 3D displays and HD-ready mobile phones is expected to make higher-resolution LCDs ubiquitous, tailoring methods are expected to expand in the near future.

5.7.3 Future Works

The proposed method contributes to the scholarship available to develop future multi-focal techniques that avoid the mismatch between convergence and accommodation on parallax barriers. Tailored displays could diminish the eye strain caused by current displays for those with visual aberrations. Time-multiplexed displays (LANMAN et al., 2010) could be used to eliminate loss of spatial resolution. Other methods for optimizing LCD_1 and LCD_2 for brightness such as matrix factorization remain for future research. The tailoring process could also account for the Stiles-Crawford effect and for anisotropic light boxes that may which could potentially perception. Other conditions, such as color vision deficiencies (MACHADO; OLIVEIRA; FERNANDES, 2009), retinal displacement and detachment (sensor warping) could be corrected on a tailored display. Eye tracking systems and physiologically based models for the eye (PAMPLONA; OLIVEIRA; BARANOSKI, 2009) can provide real-time data, such as the eye-display distance, eye angle and pupil size for the best possible tailored display experience. Further user evaluations are needed to assess dynamic contents, a quantitative error analysis of diffraction (beyond geometric optics), and the 3D perception/accommodation of stereo/multi-focus prototypes.

Additional research is necessary to apply tailored displays to multi-user interactive environments (*e.g.*, several eyes looking at a public tailored display) and to maximize the search for the best viewing angle by expanding the number of points where the image is seen clearly. Color calibration of the wavelength profiles of red, green and blue channels would also enhance the image being displayed. New technologies for displaying light-fields, such as an array of nano antennas (YU et al., 2011), or DNA-based displays (WEI; DAI; YIN, 2012) could lead to new trends in our field. Interactive measuring techniques for refractive errors (PAMPLONA et al., 2010b) could also be improved by applying tailoring to distort their displayed patterns in real time. A wavelength-dependent tailoring process could provide new insights into the eye accommodation behavior for natural scenes wherein refractive variations among wavelengths are close to null.

Can tailored displays replace eyeglasses? Eyeglasses provide better image quality than our current tailored displays and provide enhanced acuity in all environments, not only to displays. Yet tailored displays still fill a current need as an acuity enhancement option that can be used to see electronic displays during activities where glasses are inconvenient. Thus, this chapter does not assert that tailored displays make glasses obsolete, but that they can be used in special circumstances. Some lenses, like hard contacts for keratoconus, are prescribed to help treat a given visual condition. Studies on how tailoring displays could be used for additional purposes are left for future research.

6 CONCLUSIONS AND DISCUSSIONS

This thesis proposed, created, and validated hardware and software to demonstrate how light-field displays can be used to measure and enhance visual acuity. The proposed interactive methods for estimating refractive conditions (NETRA) and model lens opacities (CATRA) are the first devices in a set of solutions that can establish the field of computational diagnostics, or ophthalmatics. The subject's ability to focus on virtual objects, interactively align displayed patterns, and detect variations in shape and brightness allows for the estimation of the eye's point spread function and lens' accommodation range. Adding this interactive component to optical measurement and correction devices could significantly decrease the cost of diagnostic solutions, maximizing the capabilities of the subject involved to reduce the need for complex hardware. The light-field techniques being applied to mobile phones are able to measure retinal deformations (*e.g.,* retinal detachment, macula degeneration), to image and display retinal conditions (*e.g.,* glaucoma), to compute frame parameters (*e.g.,* interpupillary distance and angling), to capture the corneal topography and to measure the degree of color vision deficiencies. Furthermore, the device provides straightforward methods for staying informed and for customizing solutions for an individual's eye health.

Similar optical setups could be used to assess a variety of health conditions such as hypertension, diabetes, stroke and cholesterol, multiple sclerosis, certain types of cancer including brain tumors and breast and some psychological conditions. The established network for mobile phones allows the creation of ubiquitous patient-centric medical record systems. Data analytics of the collection of individual medical inputs could help specialists assess and handle public health situations and anticipate outbreaks.

Generating tailored displays for enhanced visual acuity on digital devices was proposed in this thesis. The easy-to-spread feature of computational diagnostics is key for these tailored user experiences. Instead of targeting an average individual, which is not optimal, its proposed a user experience that creates the same effect or feeling for a wide range of individuals, including outliers. Applying knowledge of the optical properties of an eye allows traditional displays to go beyond an individual's visual acuity, presenting images that are in focus even without corrective eyeglasses. The idea builds on major trends of: ubiquitous glasses-free 3D displays and their increasing power for high end diagnostics, and consumer-based interactive healthcare (people want to know what is wrong with them). It also addresses the ever-increasing demand for comfort, individually catered products, and the growing demand for high-quality visual corrections. Since the used hardware is similar to glasses-free 3D displays (dual stack of LCDs), the industry already has the technology to easily add some tailoring features to their manufacturing conduit. Yet tailoring is not currently being utilized currently. Implementing new tailored display methods could be the next technological wave once 3D technology saturates the market.

In summary, the main contributions of this paper are three novel methods for using light-fields:

- **NETRA** measures refractive errors without moving parts or retinal illumination by implementing a dual of a Shack-Hartmann system. A co-design of optics and interactive software creates an effective, low-cost interface sensitive to refractive parameters of the human eye. NETRA enables the measurement of the farthest and closest focal point by changing the pattern's position on screen. The unusual configuration leads to the exploration of a variety of patterns, and a signal processing approach provides greater freedom to create view-masks and patterns. The adaptive two-step process allows one to estimate the relaxed-state aberrations via alignment of lines as well as the focusing range via accommodation patterns. Our evaluations showed $< 0.3D$ accuracy and a $0.18D$ repetition rate on a mobile phone display without cycloplegia.

- **CATRA** measures the forward scattering profile and builds the point spread function of the crystallin with no need of a coherent light source. It ensures the projection of patterns directly onto the fovea to avoid gazing issues. There is no existing method which produces comparable quantitative results. In clinical tests, the observed correlation between CATRA and the clinician's subjective evaluation (LCOS III) was 85%.

- **Tailored displays** render virtual objects in a wide range of depths and pre-warp images to enhance visual acuity without moving parts. Using measured data from NETRA and CATRA, this new class of displays adjusts according to the user's needs. It supports nearsightedness, farsightedness, astigmatism, presbyopia, coma, keratoconus, other higher-order aberrations and any type of cataracts. Multi depths render each point of focus on the retina which produces multi-focus, multi-depth displays. The goal of tailored displays to eliminate the need for glasses in activities where they are especially cumbersome. This thesis demonstrates that high-resolution displays can create virtual images at a resolution close to the eye's standard acuity.

CATRA and NETRA substitute mechanically moving parts with moving patterns on a digital screen. This requires careful consideration of the impact of asymmetric aberrations, such as astigmatism, and opacities, such as cataracts. The designed 2D patterns and their movement mimic virtual sources and allow intuitive manipulation users who are not tech-savvy.

Renderings which display an individual's aberrated view promise to improve understanding and open dialogue between patients and their family, friends, and doctor. A more open dialogue could also improve the diagnosis of cataracts and refractive errors. The creation of closed-loop solutions - modeling, measuring and rendering - for visual effects should inspire a new range of research and real world solutions in eye care. Built with low-cost technology, these kind of *hardware apps* achieve an ideal of low cost and high availability. Individual-catered content matching algorithms, such as tailored displays, help educate individuals on their eye health so they can understand their own aberrations and seek proper attention. It has incredible potential as a public health tool.

One promising direction for NETRA and CATRA would be to make the interactive user process into a digital game. A video game interface could increase user focus and thus provide more accurate information, addressing one of the major shortcomings with the data (CHEN, 2007). Consistent focus has been shown to produce better results in past research (CSIKSZENTMIHALYI, 2008) It would also make the interface more enjoyable, easier to use, and appealing to young children.

All of the clinical evaluations in this paper followed the Declaration of Helsinki and were approved by the review boards in host countries. NETRA, CATRA and Tailored Displays created using filters over standard LCD panels, a system which does no damage to the eye health of the testers, partners, and volunteers.

Figure 6.1: NETRA and CATRA attracted the attention of the $36th$ President of Brazil and the first woman to hold the office, Dilma Rousseff. She was very interested in using the clip-ons in the Brazilian Public Health system (SUS).

6.1 Publications and Impact

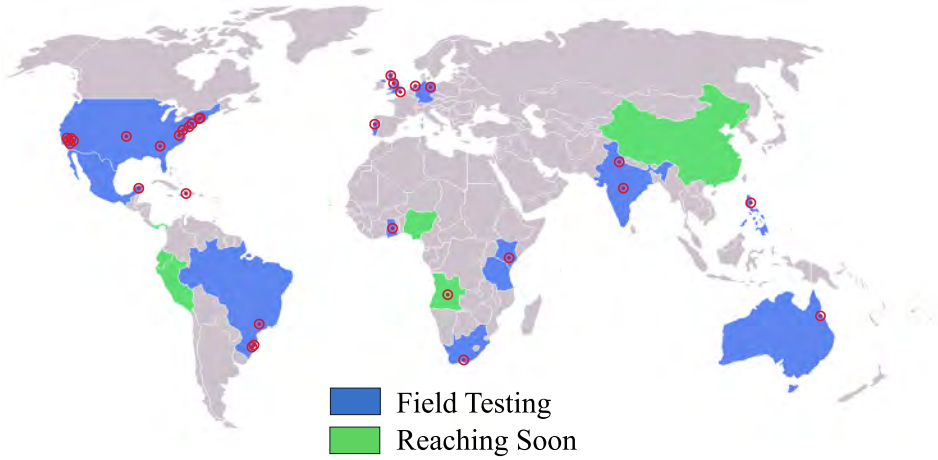

Figure 6.2: Worldwide collaboration and distribution of NETRA during this thesis. Several research institutions have reported usability feedback.

NETRA's scientific idea was published at the prestigious ACM SIGGRAPH 2010 (PAMPLONA et al., 2010b), following a patent on the USPTO (PAMPLONA et al., 2010c) and a less complex version of the concept with more results was presented at the Frontiers in Optics conference (PAMPLONA et al., 2010a). CATRA was published in the ACM SIGGRAPH 2011 (PAMPLONA et al., 2011a), USPTO patent (PAMPLONA et al., 2012) and Tailored Displays on SIGGRAPH 2012 (PAMPLONA et al., 2012), INPI/BR patent (PAMPLONA; OLIVEIRA, 2012).

Clinical evaluations were published at the Annual meeting of the American Academy of Optometry (AOA) (PAMPLONA et al., 2010d), with results from a Tufts/NECO partnership; which includes the Association for Research in Vision and Ophthalmology (ARVO)

2011 (PESALA et al., 2011), and the L.V. Prasad Eye Institute in India. Research on NETRA was also published at the Pan-American Congress of Ophthalmology (PAKTER et al., 2011CPO), Brazilian Congress of Ophthalmology (PAKTER et al., 2011), at ARVO 2012 (LANG et al., 2012) with Brazilian evaluations, and at AOA 2012 (MOORE et al., 2012) with a bi-ocular design and no cycloplegia.

CATRA and NETRA researchers were invited to present at TEDxBoston 2011 (RASKAR; PAMPLONA, 2011), TEDxGateway 2011 (RASKAR, 2011), mHealth Summit 2010, mHealth Summit 2011, WHCC Latin America Health Care Congress 2011 (PAMPLONA et al., 2011b) and the Mobile Health Expo 2011 (PAMPLONA, 2011). NETRA and CATRA won first place ($\$300K$) in the Vodafone Wireless Innovation competition. NETRA won the Lemelson-MIT Award in the MIT Ideas Competition 2010, the NASA LAUNCH: the Health Challenge Award of 2010, the Google's Innovation Grant, the Deshpande's Ignition Grant, and was awarded the second place in the Thomas Edison's Best New Product Award of 2012. CATRA won the "Best of What is New Award" in 2011 from Popular Science Magazine, the MIT Ideas Award 2011 and MIT Global Challenge Public Choice Award 2011. NETRA was a finalist for the Index Award 2011, Boston Angel Boot Camp 2010, MIT $\$100K$ 2010, MassChallenge 2010 and won the Morgenthaler DC2VC in 2011 as the one of the "most promising health IT startups".

Figure 6.2 and 6.3 show the worldwide collaboration that went into NETRA. The first bags of prototypes were sent to 29 research teams in 14 countries. Today, there are 936 entities in line waiting to receive NETRA. It has been mentioned by a variety of visual media outlets including (Figure 6.4): Bom Dia Brasil, Jornal da Band, Jornal da Record, SBT Brasil, AlJazeera, NASA, CNN, BBC, BusinessWeek, PC World, IDG, IBN Live, Fox News, NPR, NBC, ABC and Olhar Digital. Main mentions on the written and printed press include: Singularity Hub, New Scientist, NPR (2x), FastCompany (3x), TechCrunch, Duttie, The Atlantic, CNET (2x), Gizmodo (2x), Wired, Mashable (2x), Make, Crazy Engineers, MIT News (2x), Pop-Sci, New Scientist, Discovery News, Slashdot, Endgadget, The New York Times, Boston Globe, BBC, CNET, ABC News (2x), Time and AOL. The main Brazilian news sources where it has received mention are: Veja (3x), Isto É, Jornal de Santa Catarina, Universo Visual, IG Ciência, Pesquisa Fapesp, Galileu, UOL, Estadão (3x), Star, Jornal da Ciência, CNPq, Baguete, Instituto Ciência Hoje and Gazeta do Povo.

The device has also been looked at by world leaders such as the President of Brazil (Figure 6.1) and the UN Champion of the Earth, the 2010 presidential candidate Marina Silva (Figure 6.5).

6.2 Computational Diagnostics and Hardware Apps In Practice

NETRA and CATRA make it so that eye evaluations can be performed outside of the office without the help of a trained professional (*e.g.,* , home, schools, nursing homes, pharmacies, retail stores, health clinics, rural eye camps, and anywhere an optometrist is not available or is too expensive). They bring affordable and accurate eye diagnostics to hundreds of millions around the world who previously could not afford such simply lacked access to eye specialists. The fact that they use displays that are already in the market, ensures deep penetration. When compared to the state-of-the-art, the proposed solution stands out in terms of:

- **Cost**: NETRA and CATRA have the potential to be the most affordable objective measurement tools for refractive errors and cataracts ever made. They can cost as low as $3 dollars to make, assuming that every potential user has a cell phone which is becoming increasingly common even in rural and developing locations, with 5

Figure 6.3: Shared experiences during this graduate experience.

Figure 6.4: Media response to the NETRA and CATRA.

Figure 6.5: (left) Stephen Wolfram, (center) YouTube Founder Chad Hurley, and (right) Nobel Peace Prize Muhammad Yunus testing CATRA. (bottom) Marina Silva visiting NETRA's manufacturing facilities.

billion cell phones worldwide. This is significantly cheaper than the sophisticated auto-refractometers and aberrometers that cost $\$15,000$ dollars apiece, and is even more affordable than the eye chart which can cost up to $\approx \$200$ dollars with a trial

set of lenses.

- **Minimum Training**: The clip-ons do not use moving parts or require specialized training to maneuver, and the custom software application utilizes a simple user interface. This interface is made yet simpler through a training program which provides clear directions so that almost anyone can take the test accurately. Since the test is conducted by the patient and can be managed by anyone, the training can be performed by deskilled refractionists instead of a professional optometrist;

- **Accuracy**: Tests have revealed that NETRA's accuracy is comparable to industry standards. Unlike the Snellen chart, which relies on the patient's ability to discern blur and yields to variable results, NETRA relies on a simple alignment task by the patient which has produced consistent, highly repeatable results (Vernier test – hyperacuity). CATRA provides even more quantitative information for detecting cataracts than any device currently used. Both methods avoid error-prone and enable more effective treatment, significantly better collection and analysis of data, and rapid data transfer through mobile networks;

- **Data Integration**: All of the current eye examination methods in the developing world involve handwritten methods of data collection which are highly prone to human error. The design of the hardware app, on the other hand, uses the mobile platform to collect a patient's name, location, and prescription and send it to a central medical records repository;

- **Speed**: Conventional hybrid methods of diagnosis require two steps: the former automatically estimates the disorder and the latter determines the prescription. Since NETRA introduces a patient-driven and combined subjective-objective approach, it can do both steps together in less than 5 minutes;

- **Scalability**: Based on the typical trajectory of technology, it can be assumed that the cost of high-resolution screens will decreases and their quality will increase. Furthermore, as smart phones continue to penetrate the world market, the cost for the phone will likely bottom out. With these changes, the accuracy of devices will be much higher.

- **Safety**: Since these optical widgets do not use lasers and involve no moving parts, safety concerns are reduced, specialized training is nearly superfluous, and there is little chance of damage in transit;

- **Mobility**: Relying on the hardware of a mobile phone, hardware apps can be built and transported anywhere. They remain highly useful for days even with minimal human management. The current tools simply cannot be transported easily or used as quickly in remote areas where electricity may not be available;

- **Self evaluation**: Ultimately, NETRA and CATRA designs allow for periodic self-evaluation by users, while other methods do not.

It is important to reiterate that, although the proposed measuring methods are designed for self-assessment, they are not intended to replace optometrists or ophthalmologists. Instead, the goal is to build accessible screening and measuring tools, similar to modern electronic devices used to promote self awareness by measuring body temperature, blood oxygenation, or blood sugar. The smartphone-clip-on solution may turn mobile devices into one of the most viable options for providing diagnostic services worldwide. From a public health perspective, the new low-cost and easy-to-use techniques and the ability

to quantitatively track the evolution of eye disorders over time represents a significant jump in eye care. These features greatly increase the amount of available data to correlate risk factors and predict the evolution of deformations, as well as prevent future individual complications.

Hopefully, the ever-increasing need for 3D printing and home manufacturing will produce the ideal scenario for the deployment of computational diagnostics. It is not hard to imagine a hardware app store where designers submit their own work or variations of these devices and the local population prints them at a given cost and quality. A world where designers can print out their work and there is increased access to new health-related measuring devices. The store would remove the commercial barriers between countries and the high shipping costs, making health devices available worldwide instantly.

6.3 Display Tailoring as a Global Trend

The continuing evolution of tailoring technology will lead to tailorable designs to assess more areas of health and better user experiences. Tailoring displays were inspired by consumer light-field cameras when researchers realized that exceeding sensor resolution was redundant and could instead be exploited for refocusing. The current trend in display resolution will also lead to redundant angular resolution for human consumption and it can instead be used to provide new functionality (*e.g.,* vision corrected displays). Convergence-based 3D displays with multi-focus and tailoring features could lead to a new ultra-resolution vision-enhancing 3D technology.

The ultimate tailored display would equalize a designed user experience among an audience. Each individual interprets sensory stimuli in slightly different ways. The computer's ability to enhance an individual's focusing dexterity could be applied to hearing, taste, smell, touch, temperature, and time. The individually-enhanced stimuli would compensate for variations in one's ability to accurate sense them.

REFERENCES

Access Economics. **The Global Economic Cost of Visual Impairment**. 2010. 79p.

AKELEY, K. et al. A Stereo Display Prototype with Multiple Focal Distances. In: SIGGRAPH 2004. **Anais...** [S.l.: s.n.], 2004. p.804–813.

Alonso Jr., M.; BARRETO, A.; ADJOUADI, M. Development and Evaluation of a Custom Display Compensation Method for Computer Users Based on Individual Visual Characteristics. In: INT. CONF. COMP., 16. **Anais...** [S.l.: s.n.], 2007. p.804–813.

American Optometric Association. **Understanding the Difference Between Vision Screenings and Vision Examinations**. 2010.

ANSARI, R. R.; DATILES, M. B.; KING, J. F. A new clinical instrument for the early detection of cataract using dynamic light scattering and corneal topography. **SPIE Ophthalmic technologies X**, [S.l.], v.3908, p.38–49, 2000.

ARTAL, P. et al. Compensation of corneal aberrations by the internal optics in the human eye. **J. of Vis.**, [S.l.], v.1, p.1–8, 2001.

ASBELL, P. A. et al. Age-related cataract. **The Lancet**, [S.l.], v.365 (9459), p.599–609, 2005.

ATCHISON, D. et al. Useful variations of the Badal Optometer. **Optom Vis Sci**, [S.l.], v.72(4), p.279–284, Apr 1995.

BADAL, J. Optomètre mètrique international Pour la mesure simultané de la réfraction et de l'acuité visuelle même chez les illettrés. **Annales d'Oculistique**, [S.l.], v.75, p.101–117, 1876.

BARSKY, B. A. Vision-realistic rendering: simulation of the scanned foveal image from wavefront data of human subjects. In: APGV 2004. **Anais...** ACM, 2004. p.73–81.

BELT, T. H. V. D. et al. Definition of Health 2.0 and Medicine 2.0: a systematic review. **J Med Internet Res**, [S.l.], v.12(2), 2010.

BERGER, I. et al. Testing the FOCOMETER - A New Refractometer. **Optometry & Vision Science**, [S.l.], v.70, n.4, p.332–338, 1993.

CAMP, J.; MAGUIRE, L.; ROBB, R. An efficient ray tracing algorithm for modeling visual performance from corneal topography. In: VIS. BIOMED. COMP. **Anais...** [S.l.: s.n.], 1990. p.278 –285.

CAMPARINI, M. et al. Retroillumination vesus reflected-light Images in the photographic assessment of Posterior Capsule Opacification. **Invest. Ophthalmol. Vis. Sci**, [S.l.], v.41, n.10, p.3074–3079, 2000.

CAMPBELL, C. Observations on the optical effects of a cataract. **J. Cataract Refract Surg.**, [S.l.], v.25, p.995–1003, 1999.

CAMPBELL, C. Relative importance of sources of chromatic refractive error in the human eye. **J. Opt. Soc. Am. A**, [S.l.], v.27(4), 2010.

CHARMAN, W.; HERON, G. On the linearity of accommodation dynamics. **Vision Research**, [S.l.], v.40(15), p.2057–2066, 2000.

CHEN, J. Flow in games (and everything else). **Commun. ACM**, [S.l.], v.50, 4, p.31–34, 2007.

CHYLACK, L. T. et al. The Lens Opacities Classification System III: longitudinal study of cataract study group. **Arch Ophthalmol**, [S.l.], v.111(6), p.831–836, 1993.

CORBOY, J. M. **The Retinoscopy Book**: an introductory manual for eye care professionals. [S.l.]: Slack Incorporated, 2003.

CSIKSZENTMIHALYI, M. **Flow**: the psychology of optimal experience. [S.l.]: Harper Perennial Modern Classics, 2008.

CUSHMAN, W. B. **Small, simple and cost-effective scheiner-principle optometer with computer interface for automated assessment**. 1993.

DAI, G. ming et al. Wavefront propagation from one plane to another with the use of Zernike polynomials and Taylor monomials. **Applied Optics**, [S.l.], v.48, n.3, p.477–488, 2009.

DAMERA-VENKATA, N.; CHANG, N. L. Display supersampling. **ACM Trans. Graph.**, [S.l.], v.28, p.9:1–9:19, 2009.

DAVE, T. Automated Refraction: design and applications. **Optometry Today**, [S.l.], p.28–32, June 2004.

DAY, M. et al. The Relationship Between Object Spatial Profile and Accommodation Microfluctuations in Emmetropes and Myopes. **Journal of Vision**, [S.l.], v.9 (10), p.1–13, 2009.

DEERING, M. F. A photon accurate model of the human eye. In: SIGGRAPH. **Anais...** [S.l.: s.n.], 2005. v.24(3), p.649–658.

DEUBEL, H.; BRIDGEMAN, B. Fourth Purkinje image signals reveal eye-lens deviations and retinal image distortions during saccades. **Vision Research**, [S.l.], v.35(4), p.529–538, 1995.

DIDYK, P. et al. Apparent Display Resolution Enhancement for Moving Images. In: ACM SIGGRAPH'10. **Anais...** [S.l.: s.n.], 2010.

DODGSON, N. Analysis of the viewing zone of multi-view autostereoscopic displays. In: SPIE STEREOSCOPIC DISPLAYS AND APPLICATIONS XIII. **Anais...** [S.l.: s.n.], 2009. v.4660, p.254–265.

DONNELLY, W. J. et al. Quantifying scatter in Shack-Hartmann images to evaluate nuclear cataract. **Journal of refractive surgery**, [S.l.], v.20(5), p.S515–S522, 2004.

DOUALI, M. G.; SILVER, J. D. Self-optimised vision correction with adaptive spectacle lenses in developing countries. **Ophthalmic Visual Optics**, [S.l.], v.24, 2004.

DOUTHWAITE, W. A.; EVARDSON, W. T. Corneal topography by keratometry. **Br J Ophthalmol**, [S.l.], v.84, p.842–847, 2000.

DROVER, J. et al. Vernier acuity cards: examination of development and screening validity. **Optom Vis Sci**, [S.l.], v.87(11), p.E806–12, 2010.

ESSILOR. **2009 Registration Document**. [S.l.: s.n.], 2009. (1).

FINCHAM, E. F. The coincidence optometer. **Proc. Phys. Soc.**, [S.l.], v.49(5), 1937.

FINE, E. M.; RUBIN, G. S. Effects of Cataract and Scotoma on Visual Acuity: a simulation study. **Optometry and Vision Science**, [S.l.], v.76(7), p.468–473, 1999.

FOSTERA, P. J. et al. Risk factors for nuclear, cortical and posterior subcapsular cataracts in the Chinese population of Singapore. **Br J Ophthalmol**, [S.l.], v.87, p.1112–1120, 2003.

GOLDRING, E. et al. Enhanced visual experiences and seeing hardware for reduced vision: a pilot study. **J Optometry**, [S.l.], v.77, p.88–92, 2006.

HARA, T.; SAITO, H.; KANADE, T. Removal of Glare Caused by Water Droplets. In: CVMP. **Anais...** [S.l.: s.n.], 2009. p.144–151.

HAYASHI, K. et al. In vivo quantitative measurement of posterior capsule opacification after extracapsular cataract surgery. **Am J Ophthalmol**, [S.l.], v.125, p.837–843, 1998.

HESS, R. et al. What image properties regulate eye growth? **Curr. Biol.**, [S.l.], v.16(7), p.687–691, 2006.

HOFFMAN, D. M. et al. Vergence-accommodation conflicts hinder visual performance and cause visual fatigue. **J. Vis.**, [S.l.], v.5, n.10, p.834–862, 2005.

HOLDEN, B. A. Uncorrected refractive error: the major and most easily avoidable cause of vision loss. **Community Eye Health**, [S.l.], v.20(63), p.37–39, 2007.

HOWLAND B, H. H. **Photographic method for the study of vision from a distance**. [S.l.]: MIT Research Laboratory of Electronics. Q Prog Res Lab Electron, 1962. (67).

HOWLAND, H. C. Photorefraction of Eyes: history and future prospects. **Optometry and Vision Science**, [S.l.], v.86(6), p.603–606, 2009.

HUANG, F.-C.; BARSK, B. A. **A Framework for Aberration Compensated Displays**. [S.l.: s.n.], 2011. (UCB/EECS-2011-16).

HUGHES, B.; JOSHI, I.; WAREHAM, J. Health 2.0 and Medicine 2.0: tensions and controversies in the field. **J Med Internet Res**, [S.l.], v.10(3), 2008.

ISAKSEN, A.; MCMILLAN, L.; GORTLER, S. J. Dynamically reparameterized light fields. In: ACM SIGGRAPH'00. **Anais...** [S.l.: s.n.], 2000. p.297–306.

ISONO, H.; YASUDA, M.; SASAZAWA, H. Autostereo-scopic 3-D display using LCD-generated parallax barrier. **Electr. and Comm. in Japan**, [S.l.], v.76(7), p.77–84, 1993.

IVES, F. E. **US Patent 725.56**: parallax stereogram and process of making same. 1903. n.725,56.

J, H. Objektivuntersuchungen. **Zeitschrift fuer Instrumentenkunde**, [S.l.], v.24, p.1–32, 1904.

JAYNES, C.; RAMAKRISHNAN, D. Super-resolution composition in multi-projector displays. In: IEEE PROCAMS. **Anais...** [S.l.: s.n.], 2003.

JEONG, T. M.; KO, D.-K.; LEE, J. Generalized ray-transfer matrix for an optical element having an arbitrary wavefront aberration. **Optics Letters**, [S.l.], v.30, n.22, p.3009–3011, 2005.

KAKIMOTO, M. et al. Interactive Simulation of the Human Eye Depth of Field and Its Correction by Spectacle Lenses. **Comp. Graph. Forum**, [S.l.], v.26, p.627–636, 2007.

KER, D. A. **Principle of the Split Image Focusing Aid and the Phase Comparison Autofocus Detector in Single Lens Reflex Cameras**. [S.l.: s.n.], 2005. (5).

KIM, S.; BRESSLER, N. M. Optical coherence tomography and cataract surgery. **Curr Opin Ophthalmol**, [S.l.], v.20, p.46–51, 2009.

KOCH, S. Home telehealth - Current state and future trends. **International Journal of Medical Informatics**, [S.l.], v.75, n.8, p.565–576, 2006.

KOLB, C.; MITCHELL, D.; HANRAHAN, P. A Realistic Camera Model for Computer Graphics. In: ACM SIGGRAPH. **Anais...** [S.l.: s.n.], 1995. p.317–324.

KORETZ, J. F. et al. Scheimpflug and high-resolution magnetic resonance imaging of the anterior segment: a comparative study. **JOSA A**, [S.l.], v.21(3), p.346–354, 2004.

LANG, M. P. et al. Comparison of a Cell Phone-Based Refraction Technique (NETRA) With Auto-Refraction. **ARVO**, [S.l.], 2012.

LANMAN, D. et al. Content-adaptive parallax barriers: optimizing dual-layer 3d displays using low-rank light field factorization. **ACM Trans. Graph.**, New York, NY, USA, v.29, n.6, p.163:1–163:10, 2010.

LASA, M. et al. Scheimpflug photography and postcataract surgery posterior capsule opacification. **Ophthalmic Surg.**, [S.l.], v.26, p.110–113, 1995.

LEVI, D.; KLEIN, S.; CARNEY, T. Unmasking the mechanisms for Vernier acuity: evidence for a template model for vernier acuity. **Vision Res**, [S.l.], v.40(8), p.951–72, 2000.

LEVOY, M. et al. Synthetic aperture confocal imaging. **ACM Trans. Graph.**, New York, NY, USA, v.23, p.825–834, August 2004.

LEVOY, M.; ZHANG, Z.; MCDOWALL, I. Recording and controlling the 4D light field in a microscope. **Journal of Microscopy**, [S.l.], v.235, n.2, p.144–162, 2009.

LI, H. et al. A Computer-Aided Diagnosis System of Nuclear Cataract. **IEEE Trans. Bio. Eng.**, [S.l.], v.57(7), p.1690–1698, 2010.

LIANG, J. et al. Objective measurement of wave aberrations of the human eye with the use of a Hartmann-Shack sensor. **JOSA A**, [S.l.], v.11, p.1949–1957, 1994.

LIANG, J.; WILLIAMS, D. R.; MILLER, D. T. Supernormal vision and high-resolution retinal imaging through adaptive optics. **J. Opt. Soc. Am. A**, [S.l.], v.14, n.11, p.2884–2892, Nov 1997.

LIPPMANN, G. Épreuves réversibles donnant la sensation du relief. **Journal of Physics**, [S.l.], v.7, p.821–825, 1908.

LIU, I.; WHITE, L.; LACROIX, A. The association of age-related macular degeneration and lens opacities in the aged. **Am.J. of Public Health**, [S.l.], v.79(6), p.765–769, 1989.

LIU, S.; HUA, H. Time-multiplexed dual-focal plane head-mounted display with a liquid lens. **Optics Letters**, [S.l.], v.34, n.11, p.1642–1644, 2009.

LIUA, Z.; HUANGA, A. J.; PFLUGFELDERA, S. C. Evaluation of corneal thickness and topography in normal eyes using the Orbscan corneal topography system. **Br J Ophthalmol**, [S.l.], v.83, p.774–778, 1999.

LL, L. et al. Prevalence of myopia in Taiwanese schoolchildren: 1983 to 2000. **Ann Acad Med Singapore.**, [S.l.], v.33(1), p.27–33, 2004.

LOOS, J.; SLUSALLEK, P.; SEIDEL, H.-P. Using Wavefront Tracing for the Visualization and Optimization of Progressive Lenses. **Comp. Graph. Forum**, [S.l.], v.17, p.255–265, 1998.

MACHADO, G. M.; OLIVEIRA, M. M. Real-Time Temporal-Coherent Color Contrast Enhancement for Dichromats. **Comp. Graph. Forum**, [S.l.], v.29, n.3, p.933–942, 2010.

MACHADO, G. M.; OLIVEIRA, M. M.; FERNANDES, L. A. F. A Physiologically-based Model for Simulation of Color Vision Deficiency. **IEEE Trans. Vis. Comp. Graph.**, [S.l.], v.15(6), p.1291–1298, 2009.

MADDOX, E. E. Investigations in the Relation between Convergence and Accommodation of the Eyes. **J Anat Physiol**, [S.l.], v.20(Pt 3), 1886.

MARK, H. H. On the accuracy of accommodation. **Brit. J. Ophthal.**, [S.l.], v.46, p.742–744, 1962.

MOORE, B. D. et al. Comparison of a Novel Cell Phone-based Refraction Technique (NETRA-G) with Subjective Refraction. In: AOA 2012. **Anais...** [S.l.: s.n.], 2012.

MORENO-BARRIUSO, E. et al. Comparing Laser Ray Tracing, Spatially Resolved Refractometer And Hartmann-Shack Sensor To Measure The Ocular Wave Aberration. **Optometry and Vision Science**, [S.l.], v.78, p.152–156, 2001.

MORGAN, I. G.; OHNO-MATSUI, K.; SAW, S.-M. Myopia. **The Lancet**, [S.l.], v.379: 1739-48, 2012.

MOSTAFAWY, S.; KERMANI, O.; LUBATSCHOWSKI, H. Virtual Eye: retinal image visualization of the human eye. **IEEE CGA**, Los Alamitos, CA, USA, v.17, p.8–12, 1997.

NAOR, M.; SHAMIR, A. Visual Cryptography. In: EUROCRYPT 1994. **Anais...** [S.l.: s.n.], 1994. p.1–12.

NAVARRO, R.; LOSADA, M. Aberrations and relative efficiency of light pencils in the living human eye. **Optometry & Vision Science**, [S.l.], v.74, p.540–547, 1997.

NAYAR, S. et al. Fast Separation of Direct and Global Components of a Scene using High Frequency Illumination. **ACM TOG**, [S.l.], v.25(3), p.935–944, 2006.

NG, R. Fourier slice photography. **ACM Trans. Graph.**, New York, NY, USA, v.24, p.735–744, July 2005.

NG, R. et al. **Light Field Photography with a Hand-Held Plenoptic Camera**. [S.l.: s.n.], 2005.

NG, R.; HANRAHAN, P. Digital Correction of Lens Aberrations In Light Field Photography. In: SPIE INTERNATIONAL OPTICAL DESIGN CONFERENCE. **Anais...** [S.l.: s.n.], 2006. v.6342.

NIH-EDPRSG. Prevalence of Cataract and Pseudophakia/Aphakia Among Adults in the United States. **Arch Ophthalmol**, [S.l.], v.122, p.487–494, 2004.

ONG, J. Influence of a pinhole on the accommodative response. **Australian Journal of Optometry**, [S.l.], v.51(12), p.337–343, 1968.

OPTIOPIA. **Optiopia, INC**. OptiOpia.

PAKTER, H. M. et al. NETRA: auto-refrator portátil adaptado a telefone celular: validação de protótipo. **Congresso Brasileiro de Oftalmologia 2011**, [S.l.], 2011.

PAKTER, H. M. et al. Auto-refrator: validação instrumento portátil adaptado a telefone celular. **Congresso Panamericano de Oftalmologia**, [S.l.], 2011CPO.

PALANKER, D. V. et al. Femtosecond Laser-Assisted Cataract Surgery with Integrated Optical Coherence Tomography. **Science Translational Medicine**, [S.l.], v.2, n.58, p.58ra85, 2010.

PAMPLONA, V. NETRA: cellphone-based optometry solution using inverse shack hartmann technique. In: MOBILE HEALTH EXPO 2011. **Anais...** [S.l.: s.n.], 2011.

PAMPLONA, V. et al. CATRA: cataract mapping tool with snap-on for mobile phones. In: WHCC LATIN AMERICA HEALTH CARE CONGRESS 2011. **Anais...** [S.l.: s.n.], 2011.

PAMPLONA, V. et al. Tailored Displays to Compensate for Visual Aberrations. In: ACM SIGGRAPH 2012. **Anais...** [S.l.: s.n.], 2012.

PAMPLONA, V. F. et al. Dual of Shack-Hartmann Optometry Using Mobile Phones. In: FRONTIERS IN OPTICS (FIO) , OPTICAL SOCIETY OF AMERICA TECHNICAL DIGEST., New York, NY, USA. **Proceedings...** [S.l.: s.n.], 2010. p.Paper FTuB4.

PAMPLONA, V. F. et al. NETRA: interactive display for estimating refractive errors and focal range. **ACM TOG**, New York, NY, USA, v.29(4), p.77:1–77:8, 2010.

PAMPLONA, V. F. et al. **Methods and Apparatus for Measuring Refractive Errors and Focal Range of the Human Eye**. 2010.

PAMPLONA, V. F. et al. Low-cost and Portable tool for Measuring Eye Refractive Disorders using Active Participation. **Proc. of 88th Annual Meeting of the American Academy of Optometry**, [S.l.], 2010.

PAMPLONA, V. F. et al. CATRA: interactive measuring and modeling of cataracts. In: ACM SIGGRAPH'11. **Anais...** [S.l.: s.n.], 2011. p.47:1–47:8.

PAMPLONA, V. F. et al. **Methods and Apparatus for Cataract Detection and Measurement**. 2012.

PAMPLONA, V. F.; OLIVEIRA, M. M. **Dispositivos de Aberração Configuráveis para Compensar Aberrações Visuais**. 2012.

PAMPLONA, V. F.; OLIVEIRA, M. M.; BARANOSKI, G. Photorealistic models for pupil light reflex and iridal pattern deformation. **ACM TOG**, [S.l.], v.28(4), p.106, 2009.

PESALA, V. et al. Comparison of a Novel Cell Phone-Based Refraction Technique (NETRA) With Objective Clinical Retinoscopy. In: ARVO 2011. **Anais...** [S.l.: s.n.], 2011.

PORTERFIELD, W. **A Treatise on the Eye**: the manner and phenomena of vision. [S.l.]: Edinburgh, Hamilton and Balfour, 1759. 251p. v.2.

RASKAR, R. **Eye Exams**: there's an app for that. 2011.

RASKAR, R. et al. Glare aware photography: 4d ray sampling for reducing glare effects of camera lenses. In: ACM SIGGRAPH. **Anais...** [S.l.: s.n.], 2008. p.56:1–56:10.

RASKAR, R.; PAMPLONA, V. **Eye Exams**: there's an app for that. 2011.

RITSCHEL, T. et al. Temporal Glare: real-time dynamic simulation of the scattering in the human eye. **Comp. Graph. Forum**, [S.l.], v.28, n.2, p.183–192, 2009.

ROLLAND, J. P.; KRUEGER, M. W.; GOON, A. Multifocal Planes Head-Mounted Displays. **Applied Optics**, [S.l.], v.39, n.19, p.3209–3215, 2000.

ROORDAA, A.; BOBIERA, W. R.; CAMPBELLA, M. C. An infrared eccentric photooptometer. **Vision Research**, [S.l.], v.38(13), p.1913–1924, 1998.

ROYSTON, J. M.; DUNNE, M. C. M.; BARNES, D. A. Measurement of the posterior corneal radius using slit lamp and Purkinje image techniques. **Ophthalmic and Physiological Optics**, [S.l.], v.10(4), p.385–388, 2007.

ROZEMA, J. J.; DYCK, D. E. V.; TASSIGNON, M.-J. Clinical comparison of 6 aberrometers. Part 1: technical specifications. **JCRS**, [S.l.], v.31, n.6, p.1114 – 1127, 2005.

RUCKER, F. J.; KRUGER, P. B. Cone contributions to signals for accommodation and the relationship to refractive error. **Vision Research**, [S.l.], v.46, p.3079–3089, 2006.

SALMON TO, T. L.; A, B. Comparison of the eye's wave-front aberration measured psychophysically and with the Shack-Hartmann wavefront sensor. **J Opt Soc Am A**, [S.l.], v.15, p.2457–2465, 1998.

SCHACHAR, R. A. Growth patterns of fresh human crystalline lenses measured by in vitro photographic biometry. **Journal of Anatomy**, [S.l.], v.206, p.575, June 2005.

SCHAEFFEL, F. Myopia: the importance of seeing fine detail. **Curr. Biol.**, [S.l.], v.16(7), p.R257–R259, 2006.

SCHWIEGERLING, J. Theoretical limits to visual performance. **Survey of ophthalmology**, [S.l.], v.45, n.2, p.139–146, 2000.

SCHWIEGERLING, J. **Field guide to visual and ophthalmic optics**. [S.l.]: International Soceity for Optical Engineering, 2004.

SHACK; PLATT. Production and use of a lenticular Hartmann screen. **JOSA**, [S.l.], v.61, p.656, 1971.

SMITH, G.; GARNER, L. F. Determination of the radius of curvature of the anterior lens surface from the Purkinje images. **Ophthalmic and Physiological Optics**, [S.l.], v.16(2), p.135–143, 1995.

STRUTT, J. W.; RAYLEIGH, L. Some applications of photography. **Nature**, [S.l.], v.44 (1133), p.249–254, 1891.

SUGIURA, N.; MORITA, S. Variable-focus liquid-filled optical lens. **Appl Opt.**, [S.l.], v.32(22), 1993.

TALVALA, E.-V. et al. Veiling glare in high dynamic range imaging. **ACM TOG**, [S.l.], v.26(3), 2007.

THIBOS, L.; BRADLEY, A. Use of Liquid-Crustal Adaptive-Optics to alter the Refractive State of the Eye. **Optometry and Vision Science**, [S.l.], v.74, p.581–587, 1997.

THIBOS, L. et al. Statistical variation of aberration structure and image quality in a normal population of healthy eyes. **J Opt Soc Am A Opt Image Sci Vis**, [S.l.], n.19(12), p.2329–48, 2002.

THIBOS, L.; QI, X.; MILLER, D. T. Vision Through a Liquid-Crystal Spatial Light Modulator. In: ADAPTIVE OPTICS FOR INDUSTRY AND MEDICINE. **Anais...** World Scientific Press, 1999.

TIPPIE, A. E. **Aberration Correction in Digital Holography**. 2012. Tese (Doutorado em Ciência da Computação) — University of Rochester.

TKACZYK, E. R. et al. Cataract diagnosis by measurement of backscattered light. **Optics Letters**, [S.l.], v.36(23), p.4707–4709, 2011.

TSCHERNING, M. Die Monochromatischen aberrationen des Menschlichen Auges. **Z. Psychol. Psysiol. Sinn.**, [S.l.], v.6, p.456–471, 1894.

VAISH, V. et al. Using plane + parallax for calibrating dense camera arrays. In: IN PROC. CVPR. **Anais...** [S.l.: s.n.], 2004. p.2–9.

WAARD, P. W. T. de; IJSPEERT, J. K.; BERG, P. T. V. M. d. J. Thomas J. T. P. van den. Intraocular light scattering in age-related cataracts. **IOVS**, [S.l.], v.33, n.3, p.618–625, 1992.

WEBB, R.; PENNEY, C.; THOMPSON, K. Measurement of ocular wavefrontdistortion with a spatially resolved refractometer. **Applied Optics**, [S.l.], v.31, p.3678–3686, 1992.

WEI, B.; DAI, M.; YIN, P. Complex shapes self-assembled from single-stranded DNA tiles. **Nature**, [S.l.], v.485, p.623–627, 2012.

WESTHEIMER, G. Visual acuity and hyperacuity. **Investigative Ophthalmology**, [S.l.], v.14, n.8, p.570–572, 1975.

WETZSTEIN, G. et al. Layered 3D: tomographic image synthesis for attenuation-based light field and high dynamic range displays. **ACM Trans. Graph.**, New York, NY, USA, v.30, n.4, 2011.

WHO. **State of the world's sight**: vision 2020, the right to sight: 1999-2005. 2005.

WIT, G. C. de et al. Simulating the straylight effect of cataracts. **J. Cataract Refract Surg.**, [S.l.], v.32, p.294–300, 2006.

YOUNG, T. On the mechanics of the eye. **Philosophical transactions of the Royal Society of London**, [S.l.], v.91(23), 1801.

YU, N. et al. Light Propagation with Phase Discontinuities: generalized laws of reflection and refraction. **Science**, [S.l.], v.334 (6054), p.333–337, 2011.

APPENDIX A MEDIDAS INTERATIVAS E TELAS AJUSTÁVEIS PARA ABERRAÇÕES ÓPTICAS EM OLHOS HUMANOS

Resumo da Dissertação em Potuguês

Aberrações oculares não corrigidas diminuem as capacidades visuais, criando uma experiência de usuário sub-óptima e inconsistente. A falta de ferramentas para diagnóstico de saúde ocular de baixo custo cega a busca da população por um melhor desempenho visual. Por exemplo, algumas partes da Índia ainda acreditam que a catarata, ou cegueira branca como eles chamam, é uma etapa necessária da vida ao invés de uma condição visual simples que pode ser resolvida com uma cirurgia de três dólares. Os erros de refração, ou visão desfocada, são aceitos como uma limitação natural por todas as crianças. Por isso o choque que a maioria percebe quando vestem os primeiros óculos. Centros especializados para exames oftalmológicos são escassos e muitas vezes vistos como serviços super-faturados e bens supérfluos pelas comunidades carentes. Ao permitir a medida e correção das condições refrativas em tempo real, esta tese tem como objetivo aumentar os padrões mundiais de qualidade da visão e da acessibilidade de informação.

A maioria dos dispositivos de medição da acuidade usam equipamentos sofisticados para estimar as aberrações ópticas com precisão. Opções para aprimoramento da acuidade visual variam entre simples óculos até próteses ópticas e óptica adaptativa. Tendências emergentes em monitores de campo de luz portáteis proporcionam novas oportunidades para criação de instrumentos de baixo custo e fácil utilização que capturam dados médicos confiáveis para medir e neutralizar as aberrações ópticas. Esta tese propõe métodos de pré-deformação para monitores de campo luz para estimar as aberrações refratavas (*NETRA*), opacidade do cristalino *CATRA* e compensar as deformações ópticas de um indivíduo (*Tailored Displays*). NETRA e CATRA têm o potencial de aumentar a conscientização sobre condições visuais. Monitores adaptados pela tecnologia de Tailored Displays podem melhorar a acuidade visual, libertando o espectador dos inconvenientes óculos e adiando a necessidade de substituições ópticas e incisões desnecessárias no olho.

Desde a introdução do disco de Scheiner, em 1619 - dois furos em um disco onde os objetos distantes duplicam quando erros de refração estão presentes - ferramentas oftálmicas evoluíram para instrumentos caros, de altíssima precisão e automáticos projetados para clínicos com mais de quatro anos de treinamento. Esta tese retorna aos primórdios da oftalmologia e reutiliza um poder computacional ubíquo para criar versões do século XXI do teste da Scheiner. Lasers e sensores de alta resolução são substituídos por procedimentos de interação do usuário. As ferramentas propostas permitem que uma pessoa tome suas próprias medidas e exporte os dados para centros clínicos que então podem fornecer soluções para a condição encontrada. *NETRA* e *CATRA* medem aberrações óp-

(a) Nairobi - Kenia (b) Hyderabad - Índia

(c) Teresina - Brasil (d) NASA's Kennedy Space Center - USA

Figura A.1: NETRA sendo testado no (a) Quênia, (b) Índia (c) Brasil e (d) no Centro Espacial Kennedy da NASA. Este protótipo é um clip-on óptico que é colocado sobre a tela de um telefone celular. O usuário olha através dele e, de forma interativa, alinha linhas vermelhas e verdes. O número de cliques necessários para alinhar indica o erro refrativo.

ticas espacialmente distribuídas utilizando um conceito de anisotropia programável. Os aplicativos utilizam telefones celulares amplamente disponíveis para os cálculos (Figura A.1). Em vez de um sistema automatizado, os métodos propostos envolvem o usuário no processo de diagnóstico. O usuário olha para o monitor do celular através de uma mascara e alinha uma série de padrões (*e.g.,* linhas por exemplo) várias vezes. O procedimento resulta em valores quantitativos para as aberrações de refração em termos de índice esférico, cilíndrico, eixo de astigmatismo, scopo de foco, e quatro representações gráficas 2D para cataratas: mapas de opacidade, atenuação, contraste e pontos de espalhamento. Estes testes eliminam a necessidade de um médico treinado para compreender as condições visuais pessoais.

O conhecimento das propriedades ópticas de um olho permite que as telas eletrônicas tradicionais ir além da acuidade visual de um indivíduo. As telas de alta resolução são limitadas pelo sistema visual do indivíduo. Melhorias na resolução dos monitores são ineficazes porque só beneficiam uma pequena fração da população: aqueles com visão acima do padrão atual para acuidade visual (*i.e.,* visão 20/20). O mesmo hardware disponível em televisores 3D sem óculos pode ser usada para projetar uma imagem em foco para um indivíduo com miopia ou deformar uma imagem de acordo com a condição de um olho específico e, portanto, para compensar a visão desfocada. Monitores de campos de luz adaptados compensam as aberrações de maneira que os raios de luz se desviam de opacidades e são emitidos para compensar a deformação refrativa na lente do paciente. O procedimento usa mapas de aberração e cataratas de entradas. Ele divide campo de luz de um objeto em várias instâncias que estão cada um em foco para uma determinada sub-abertura do olho. O display projeta ilusões anisotrópicas gerando

Figura A.2: Esta tese propõe dois novos métodos subjetivos centrada no paciente para medir parâmetros ópticos do olho humano. Neste protótipo, o acessório para celular (esquerda) cria um campo luz limitado, projetado para medição de erros refrativos em termos de valor esférico, cilíndrico e eixo de astigmatismo (direita). Foto por Jonathan Williams.

objetos em muitas profundidades da mesma que uma holografia. A integração da luz na retina remonta a imagem em foco. O uso de várias profundidades para criar cada ponto na image em foco cria um sistema multi-focal inédito. Estes monitores que atuam sob medida para o usuário têm aplicação em tarefas diárias onde os óculos não são desejados ou quando a função de multi-foco é necessária (*e.g.,* dirigindo). Os monitores oferecem uma alternativa confortável e conveniente para a correção de acuidade visual. Sistemas de registos médicos futuros serão atualizados constantemente e serão essenciais para a normalização/acessibilidade de uma interface computacional.

Esta abordagem de utilizar monitores anisotrópicos e a interface com o usuário para medir e compensar errors refrativos é única a esta tese. Esses dispositivos criam uma nova família de ferramentas de diagnóstico baseados na ubiquidade de dispositivos móveis com alta resolução de tela, tornando a oftalmologia mais acessível para a população. Além disso, este trabalho apresenta novas representações quantitativas para medição de catarata e um método simples de medir os limites de foco de uma pessoa. Os dados podem ser capturados e processados ??para simular a visão de um indivíduo, incluindo todos os defeitos de refração. Esta tecnologia pode redefinir a relação médico-paciente por meio da experiência compartilhada de visão.

A.1 Oftalmologia Computacional: Aplicativos para Diagnóstico Médico

Todas as soluções desenvolvidas ao longo deste trabalho combinam hardware anisotrópico (ou seja, monitores de campo de luz) e software interativo. O controle da direção dos raios de luz individualmente permite a divisão da pupila em setores de teste e, com o feedback do usuário, as medições de suas aberrações ópticas individuais. Os displays de alta resolução projetam objetos virtuais em diferentes profundidades e fornece uma maneira para explorar habilidades foco do usuário (Figura A.3). Durante o decorrer deste texto, explora-se a óptica geométrica e conceitos de interação para otimizar a usabilidade geral e viabilidade em hardware e software para as técnicas de medição.

Como a tecnologia de campo de luz em alta resolução ainda não está disponível, é necessário a criação de acessórios ópticos para os monitores padrão (Figura A.2). Essas

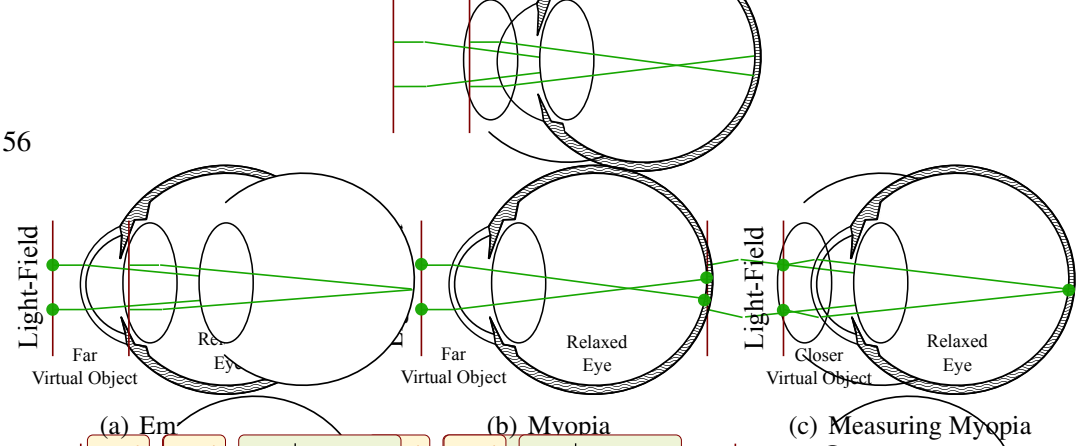

(a) Em (b) Myopia (c) Measuring Myopia

Figura A.3: O NETRA é um monitor de campo de luz programável que, quando colocado perto de um olho, cria uma gama de interatividade que é extremamente sensível aos parâmetros ópticos do olho humano. O usuário observa os padrões e altera o monitor para alinhá-los. Com o alinhamento completo, o celular computa o erro refrativo. Neste exemplo, a alteração do ângulo de saída dos raios de luz cria um objeto virtual a uma distância finita do olho. O inverso desta distância equivale ao poder óptico requerido nos óculos.

configurações ópticas são essencialmente um monitor de campo de luz destinados a tarefas específicas como, por exemplo, a medição refrativa. Eles atingem um ideal de brilho e resolução angular encontrado em telefones celulares (300 pontos por polegada). Estes acessórios são passivos e não são destinados a criar monitores de campo de luz completos, mas sim telas multi-focais otimizadas para uma finalidade específica. Análogo ao desenvolvimento de software livre, os recentes avanços da tecnologia de impressão 3D permite a qualquer pessoa, em qualquer lugar para fornecer soluções personalizadas para as necessidades locais.

A.2 Um Termômetro para o Desempenho Visual

O campo da oftalmologia hoje reflete fotografia em meados dos anos 1960. Naquele tempo, a fotografia exigia equipamentos caros e volumosos. Os custos de manutenção eram altos, medidas eram repetidas muitas vezes, e imagens poderiam levar uma semana para serem impressas. O fotógrafo também era um químico. Os produtos utilizados na revelação do filme permitiam ajustar a cor, brilho e contraste. Os clientes tinham que visitar lugares específicos para serem fotografado. A portabilidade era nula. Os avanços na fotografia através das últimas décadas levaram a uma prática muito mais conveniente e acessível. Hoje as câmeras portáteis estão em toda parte. Apesar disso, os fotógrafos profissionais não estão obsoletos. A profissão mudou. A transição permitiu a criação de artistas de tempo integral que lidam principalmente com a iluminação, enquadramento e processamento digital. A câmera hoje tem o simples papel de captar os dados brutos em qualquer lugar. Profissionais são utilizados para medições de alta qualidade e por sua interpretação da qualidade do que será capturado e seu uso.

O campo da medicina tem seguido a mesma tendência (HUGHES; JOSHI; WAREHAM, 2008; BELT et al., 2010). A maioria dos profissionais já acreditam que o seu impacto principal é sobre interpretação de dados ao invés de sua captura (KOCH, 2006). No entanto, a própria classe ainda detém posse sobre dispositivos de imageamento, que são volumosos, caros e exigem treinamento especial para operar. Isso leva a uma dependência destes profissionais e o gasto excessivo de tempo em tarefas simples demais para o nível de treinamento presente. Com os novos aparelhos, tenta-se acelerar a popularização de ferramentas de imagens médicas usando dispositivos de uso geral como plataformas para instrumentos científicos. O NETRA não substitui os dispositivos atuais, mas sim permite direcionar e medir os erros de refração em qualquer lugar, aumentando o número crescente de soluções para atendimento domiciliar. O aplicativo campos de luz apropriados

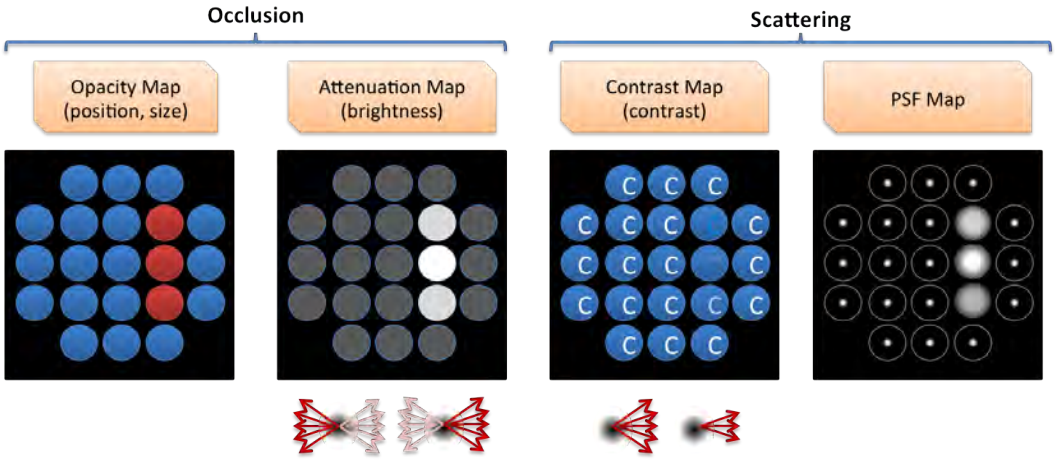

Figura A.4: Quatro mapas propostos para medir e modelar cataratas. Cada círculo representa um sub-abertura do olho. Da esquerda para direita: (i) mapa de opacidade avalia a posição e o tamanho da catarata (círculos vermelhos representam as sub-aberturas afetadas pela catarata); (ii) mapas de atenuação estimam a densidade da catarata que, por sua vez, determina a quantidade de luz que chega até a retina; (iii) mapas contraste estimam quão grande é o ângulo do espalhamento de um único raio luz; (iv) funções de propagação do ponto de luz para cada sub-abertura do olho. Estes quatro mapas não existem em nenhum outro aparelho na oftalmologia atual.

para automatizar disco de Scheiner e compila os dados de refração em termos de poderes esférico, cilíndrico e eixo de astigmatismo. Baseando-se em testes interativos de Vernier (LEVI; KLEIN; CARNEY, 2000; DROVER et al., 2010) - alinhamento de linhas ao invés de classificação de imagens borradas - as medidas do Netra são notavelmente precisas. Assim como um termômetro que mede a temperatura corporal e não prescreve medicamentos, o NETRA mede o erro refrativo para lentes (imageamento), mas não prescreve uma correção. Em outras palavras, o dispositivo só captura as informações do corpo e não interpreta os dados. Como o termômetro, o NETRA permite o monitoramento das condições oculares para que eles possam procurar cuidados médicos se os números excedem um ponto crítico. Com cerca de dois bilhões de pessoas em todo o mundo usando óculos e seiscentos milhões de pessoas com erros de refração não corrigidos (WHO, 2005), esses anexos ópticos de baixo custo para celulares podem ??ajudar a resolver um problema de saúde global, e são ferramentas ideais para partes remotas do mundo.

A.3 Um Radar para Cataratas

CATRA modela e mede mapas quantitativos de opacidade, atenuação, contraste e funções de espalhamento de ponto (PSF) do olho. As técnicas para identificar cataratas atribuem uma pontuação subjetiva que varia de baixo (1) até completamente bloqueada (6). A representação proposta é equivalente a um radar para a cobertura dos pontos onde a catarata mais afeta o olho. Em vez de uma classificação subjetiva para a gravidade da catarata, o software apresenta informações quantitativas, espaciais e de densidade (Figura A.4). O mapa de opacidade é um mapa binário que mostra o tamanho e a posição das cataratas. O mapa de atenuação exibe as densidades de cada sub-abertura. O mapa de espalhamento e contraste determina como a luz está sendo espalhada pelos sub-aberturas afetadas. O procedimento interativo proposto navega estes mapas e reduz o espaço de busca para a função de propagação do ponto total do olho. Juntos, esses novos mapas codificam a informação necessária para estimar o quão afetado está a visão do indivíduo.

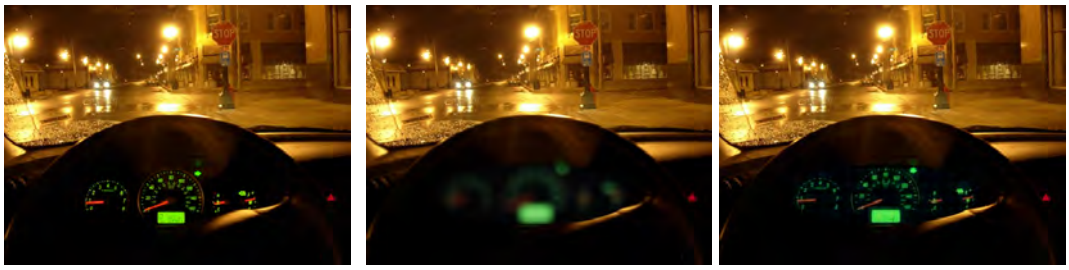

(a) Imagem Original (b) Painel Não Corrigido (c) Painel Corrigido

Figura A.5: Diferença na visão de um indivíduo com presbiopia ao dirigir usando um painel regular (b) e com um monitor personalizado para suas deficiências visuais (c). A imagem (a) mostra como um emmetrope veria o mesmo painel.

Tecnologia esta que não existe em nenhum outro aparelho.

A cirurgia é a única solução para a catarata e, assim, os médicos enfrentam geralmente um dilema binário: se está ou não na hora da remoção cirúrgica do cristalino. Em sua versão atual, os mapas propostos contêm mais informações do que o que os médicos precisam para tomar essa decisão. No entanto, o sensor de frente de onda de Shack-Hartmann foi criado para maper as distorções ópticas de alta ordem mesmo sem ter aplicação prática. Hoje, a alta precisão desses dispositivos fornece os dados para a cirurgia LASIK. A ampla disponibilidade de dispositivos como o proposto, que geram dados quantitativos pode beneficiar o futuro da prática diagnóstica e cirúrgica, bem como aumentar a saúde e consciência da população para suas próprias condições visuais.

A.4 Monitor adaptado para compensar as aberrações visuais

Monitores adaptados aqui propostos melhoraram a acuidade visual de acordo com as necessidades visuais do usuário (Figura A.5). Eles evitam a necessidade de óculos quando olhando para o monitor. Assim como qualquer correção visual, os valores refrativos são essenciais para esta abordagem. Mapas de aberração e de cataratas são usados ??para pré-calcular um campo de luz que emite sinais de luz anisotrópicos para sub-aberturas da pupila de maneira que compensem a aberração visual. Como um único ponto de foco pode ser distribuído em várias profundidades, o novo aparelho além de ser multi-focal também é multi-profundidade. O resultado é uma projeção em foco na retina. Estas novas telas personalizadas são sugeridas para uso em tarefas diárias onde os óculos não são desejados (por exemplo, quando se utiliza aparelhos eletrônicos para esportes, trabalho, leitura, etc) ou quando uma função multi-foco é necessária (por exemplo, condução, reuniões, aulas, etc). Displays 3D baseados em convergência com características multi-foco e com adaptação para aberrações visuais podem ser o próximo estágio da tecnologia 3D encontrada hoje no comércio.

A.5 Conclusão

Esta tese demonstra a criação de três aparelhos para medição e correção de aberrações visuais. O NETRA é um acessório para celular barato que mede erros refrativos para miopia, hipermetropia e astigmatismo. Foi testado em várias partes do mundo e alcança uma acurácia de 0.3 dioptrias e uma repetabilidade de 0.18 dioptrias. O CATRA cria mapas para monitorar a presença de cataratas. É a primeira plataforma a gerar resultados tão detalhados sobre as opacidades de uma lente *in-vivo*. CATRA alcança uma correlação de 85% contra a análise subjetiva de medicos. Os monitores sob medida permitem a

correção de erros refrativos no monitor ao invés do uso de óculos. Estes monitores tem uma resolução comparável a acurácia do olho humano de 1 arco minuto.

A evolução contínua da tecnologia permitirá uma melhor experiência do usuário, mantendo todas as pessoas, com erros de refração, cataratas e outras condições visuais, nas mesmas condições de competição. Este projeto foi inspirado por câmeras de campo de luz, cujos fabricantes entenderam que a resolução excessiva pode ser utilizada para gerar outras características previamente desconhecidas. A tendência é que os monitores sigam o mesmo modelo e que descubram novas características provenientes da resolução excessiva dos produtos. O sonho em longo prazo é criar esta correção visual para outros sentidos do corpo. Audição, paladar, olfato, tato, temperatura e tempo são sentidos que podem ser afetados por tecnologias como as discutidas durante este trabalho.